Self-assembly, dimensional control and application of supramolecular 1D- and 2D- materials

Dissertation

zur Erlangung des akademischen Grades eines
Doktors der Naturwissenschaften (Dr. rer. nat.)
in der Bayreuther Graduiertenschule für Mathematik
und Naturwissenschaften (BayNAT)
der Universität Bayreuth

vorgelegt von

Christoph Steinlein

geboren in Bayreuth

Bayreuth, 2020

Der experimentelle Teil der vorliegenden Arbeit wurde in der Zeit von Oktober 2013 bis Juli 2018 in Bayreuth am Lehrstuhl Makromolekulare Chemie I unter Betreuung von Herrn Prof. Dr. Hans-Werner Schmidt angefertigt.

Vollständiger Abdruck der von der Bayreuther Graduiertenschule für Mathematik und Naturwissenschaften (BayNAT) der Universität Bayreuth genehmigten Dissertation zur Erlangung des akademischen Grades eines Doktors der Naturwissenschaften (Dr. rer. nat.).

Dissertation eingereicht am:	23.10.2020
Zulassung durch das Leitungsgremium:	18.11.2020
Wissenschaftliches Kolloquium:	22.03.2021

Amtierender Direktor: Prof. Dr. Markus Lippitz

Prüfungsausschuss:

Prof. Dr. Hans-Werner Schmidt	(Gutachter)
Prof. Dr. Josef Breu	(Gutachter)
Prof. Dr.-Ing. Volker Altstädt	(Vorsitz)
Prof. Dr. Jürgen Senker	

Die vorliegende Arbeit ist als Monographie verfasst.

Teile der Arbeit sind bereits in den folgenden Publikationen erschienen.

Controlling the Aspect Ratio of Supramolecular Fibers by Ultrasonication

Christoph Steinlein, Klaus Kreger, Hans-Werner Schmidt

Macromol. Mater. Eng. 304, 1900258 (**2019**)

Diese Publikation ist in der vorliegenden Arbeit mit der Literaturstelle [127] zitiert.

I*mproved compression properties of polypropylene extrusion foams by supramolecular additives*

Michaela Mörl, Christoph Steinlein, Klaus Kreger, Hans-Werner Schmidt, Volker Altstädt

Journal of Cellular Plastics 54, 483-498 (**2018**)

Diese Publikation ist in der vorliegenden Arbeit mit der Literaturstelle [191] zitiert.

List of abbreviations and symbols

1D	one-dimensional
2D	two-dimensional
3D	three-dimensional
AFM	atomic force microscopy
BTA	1,3,5-benzenetrisamide
CBA	chemical blowing agent
CTA	1,3,5-cyclohexanetrisamide
CNTs	carbon nanotubes
D	platelet thickness/thickness of 2D-objects
d	monolayer thickness
DMF	dimethylformamide
DTA	differential thermal analysis
(μ-)DSC	(micro) differential scanning calorimetry
EtOH	ethanol
F	force
SEC	size exclusion chromatography
H-bond	hydrogen bond
HMN	2,2,4,4,6,8,8-heptamethylnonane
i-PP	isotactic polypropylene
(FT)IR	(Fourier-transform) infrared spectroscopy
MAS	magic angle spinning
MCH	methyl cyclohexane
MeOH	methanol
MFI	melt flow index
NMP	*n*-methyl-2-pyrrolidone
NMR	nuclear magnetic resonance
o-DCB	*ortho*-dichlorobenzene
p	pressure
PBA	physical blowing agent
pc	Pearson coefficient

PE	polyethylene
PolMic	polarized light microscopy
ppm	parts per million (here: used as weight fraction)
PS	polystyrene
PTFE	polytetrafluoroethylene
rpm	revolutions per minute
SEM	scanning electron microscopy
T	temperature
T_c	crystallization temperature
T_m	melting temperature
TGA	thermogravimetric analysis
THF	tetrahydrofurane
V	volume
WAXS	wide-angle X-ray scattering
(P)XRD	(powder) X-ray diffraction
ρ	density

All other symbols used in equations are explained in the respective context.

Table of contents

Summary

Supramolecular chemistry is supposed to become one of the significant research fields in material science of the 21st century. This is attributed to the manifold self-assembly processes resulting in distinct supramolecular architectures with specific functionalities. However, several issues are still not easy to solve. For example, tailoring supramolecular architectures with precise dimensions via bottom-up approaches remains challenging. Therefore, this work is dedicated to *self-assembly, dimensional control and application of supramolecular 1D- and 2D- nanomaterials* based on 1,4-bisamides and 1,3,5-trisamides.

The first part addresses the *self-assembly of 1,4-benzene- or 1,4-cyclohexanebisamides into 2D-nanoobjects*. These novel 1,4-bisamides are designed with different fluorocarbon or *tert*-butyl substituents resulting in symmetrical or asymmetrical substitution patterns. Within each substitution pattern, the length of the fluorocarbons was varied from C_3F_7 over C_5F_{11} to C_7F_{15}. A symmetric 1,4-bisamide with *tert*-butyl groups was used as reference. All bisamides proved to feature sufficient thermal stability allowing self-assembly experiments at elevated temperatures. In this context, an important aspect was the structural elucidation by X-ray diffraction, solid-state NMR and IR spectroscopy, as these methods reveal the H-bonding pattern, which typically reflects the shape of nano-objects on the mesoscale. In cooperation with the department of Inorganic Chemistry III at the University of Bayreuth, it was shown that bisamides without *tert*-butyl substituents form rows of molecules connected by H-bonds. These rows align into layers, which stack to form platelets. By contrast, bisamides comprising at least one *tert*-butyl substituent connect to four neighbors to form layers, which also stack into platelets. Based on this finding, a reference bisamide was used to evaluate different self-assembly processes and to tune self-assembly conditions to obtain thinner nano-platelets. Transferring and further optimizing these results to the symmetric and asymmetric 1,4-bisamides with fluorocarbon substituents it was found that an asymmetric bisamide formed the thinnest platelets, featuring an average thickness of around 32 nm, which equals 15 layers. In addition, a reduction of platelet thickness with longer fluorocarbon chains was revealed. Moreover, contact angle measurements of two fluorocarbon substituted bisamides revealed that the surfaces of their 2D-objects are highly hydrophobic.

The second part focuses on *dimensional control of supramolecular fibers* of 1,3,5-benzene¬trisamides via a top-down approach. In particular, length control of such fibers was

addressed via ultrasound. For this, supramolecular submicron fibers of 1,3,5-benzene¬trisamide were produced in large amounts by self-assembly upon cooling of solutions in high-boiling hydrocarbons. For later systematic sonication experiments, several dispersion media for supramolecular submicron fibers such as *n*-hexane, methyl cyclohexane and anisole were explored. A systematic screening of sonication parameters such as sonication time, ultrasonic power amplitude, medium, cooling bath temperature and concentration of BTA fibers revealed their influence on the final fiber dimensions. For instance, the applied ultrasonic energy is the major factor for the length of the obtained fibers. By contrast, raising the concentration or lowering the temperature gave only slightly shorter submicron fibers. Remarkably, the used medium during sonication altered fibers' length as well as their aspect ratio. This way, it was possible to vary the aspect ratio from 3.7 to 6.8 and the fiber length from 0.66 to 0.98 µm. In this context, the fiber lengths were successfully correlated with the viscosity of the media revealing shorter fibers in more viscous media even after a long sonication time demonstrating the control over the fibers' dimensions.

In the third part, *supramolecular nanofibers* were applied to improve the foam morphology and mechanical properties of *extruded polypropylene foams*. This work was realized in cooperation with the department of Polymer Engineering at the University of Bayreuth. Conceptually, the homogeneously dissolved BTAs self-assemble during cooling in the extrusion process into solid nanofibers, which act as finely dispersed nucleation sites for the foam cells and consequently control the foam morphology. To realize this, three different BTAs at different concentrations were compounded into an isotactic polypropylene (*i*-PP) grade and injection molded. The specimens were thoroughly investigated and, based on these results, compounds comprising different concentrations of the three BTAs were chosen for foam extrusion. Talc at different concentrations was used as reference. Foam extrusion was realized in a tandem extrusion line using CO_2 as physical blowing agent. It was found that the density and the morphology of extruded foams can be significantly altered by the presence of BTAs. With BTAs, the foam density is strongly reduced by more than 40% to 0.09 g/cm^3 compared to neat *i*-PP. Also, the average foam cell diameter was reduced by more than 40%, reaching an optimum diameter of 27 µm. Such homogenous foams with small cell sizes could not be achieved with the talc reference foams. Moreover, it was demonstrated that the specific compression moduli of foams with BTA could lead to an improvement of more than 100% compared to neat *i*-PP and more than 65% compared to the talc reference foam. This finding is attributed to a reinforcing effect of BTA fibers.

Zusammenfassung

Die Supramolekulare Chemie wird voraussichtlich zu einem der bedeutenden Forschungsfelder der Materialwissenschaften des 21. Jahrhunderts werden. Dies ist den vielfältigen Selbstassemblierungsprozessen, die zu unterschiedlichen supramolekularen Architekturen mit spezifischen Funktionalitäten führen, geschuldet. Dabei verbleiben jedoch bisher einige ungelöste Aufgaben. Beispielsweise stellt die Schaffung supramolekularer Strukturen mit maßgeschneiderten Dimensionen durch *bottom-up*-Ansätze weiter eine Herausforderung dar. Deshalb befasst sich diese Arbeit mit *Selbstassemblierung, Dimensionskontrolle und Anwendung supramolekularer 1D- und 2D-Nanomaterialien* auf Basis von 1,4-Bisamiden und 1,3,5-Trisamiden.

Der erste Abschnitt behandelt die Selbstassemblierung von 1,4-Bisamiden auf Basis von Benzol oder Cyclohexan zu 2D-Nanoobjekten. Diese neuartigen 1,4-Bisamide tragen Perfluorcarbon- oder *tert*-Butylsubstituenten, was eine symmetrische oder asymmetrische Substitution erlaubt. Innerhalb jedes Substitutionsmusters wurde die Länge der Kohlenwasserstoffsubstituenten von C_3F_7 über C_5F_{11} hin zu C_7F_{15} variiert. Als Referenzverbindung wurde ein symmetrisches 1,4-Bisamid mit *tert*-Butylsubstituenten verwendet. Alle Bisamide zeigten eine für Selbstassemblierungsexperimente bei höheren Temperaturen ausreichende thermische Stabilität. Für die behandelten Fragestellungen war die Strukturaufklärung über Röntgenstreuung, Festkörper-NMR und IR-Spektroskopie von großer Bedeutung, da diese Methoden die Aufklärung des Musters der Wasserstoffbrückenbindungen erlauben. Dieses spiegelt typischerweise die Form der mesoskopischen Nanoobjekte wieder. In Zusammenarbeit mit dem Lehrstuhl für Anorganische Chemie III der Universität Bayreuth wurde festgestellt, dass Bisamide ohne *tert*-Butylsubstituenten durch Wasserstoffbrückenbindungen verknüpfte Reihen von Molekülen bilden. Diese Reihen ordnen sich zu Schichten an, welche wiederum Stapel bilden, wodurch Nanoplättchen entstehen. Im Gegensatz dazu bilden Bisamide mit mindestens einem *tert*-Butylsubstituenten Bindungen zu vier Ihrer Nachbarn aus und formen so Schichten, die sich ebenfalls zu Nanoplättchen stapeln. Ausgehend von diesem Ergebnis wurden mithilfe eines Referenzbisamids verschiedene Selbstassemblierungsprozesse verglichen und die Prozessparameter hin zu dünneren Nanoplättchen optimiert. Die so gewonnenen Erkenntnisse wurden auf die symmetrischen und asymmetrischen 1,4-Bisamide mit Perfluorcarbonsubstituenten übertragen und weiter optimiert. Dabei bildete ein

asymmetrisches Bisamid die dünnsten Plättchen mit einer durchschnittlichen Dicke von ca. 32 nm, was 15 Schichten entspricht. Zudem wurde ein Sinken der Plättchendicke mit zunehmender Länge der Perfluorcarbonsubstituenten festgestellt. Darüber hinaus zeigten Kontaktwinkelmessungen an 2D-Objekten zweier Bisamide mit Perfluorcarbonsubstituenten stark hydrophobe Oberflächeneigenschaften.

Der zweite Abschnitt befasst sich mit der *Kontrolle der Dimensionen von supramolekularen 1,3,5-Benzoltrisamidfasern* mittels eines *top-down*-Ansatzes. Mithilfe von Ultraschall wurde insbesondere eine Kontrolle der Faserlänge angestrebt. Dazu wurden supramolekulare Fasern eines 1,3,5-Benzoltrisamids (BTAs) in größeren Mengen durch Selbstassemblierung beim Abkühlen ihrer Lösungen in hochsiedenden Kohlenwasserstoffen synthetisiert. Für spätere systematische Ultraschallexperimente wurde mehrere geeignete Dispersionsmedien wie beispielsweise *n*-Hexan, Methylcyclohexan und Anisol identifiziert. Eine systematische Untersuchung der Parameter Beschallungszeit, Ultraschallleistung, Medium, Kühlbad-temperatur und Konzentration der BTA-Fasern zeigte den jeweiligen Einfluss auf die finalen Faserdimensionen. Beispielsweise ist die applizierte Ultraschallleistung der Faktor mit dem größten Einfluss auf die Länge der erhaltenen Fasern. Im Gegensatz dazu führte eine Erhöhung der Konzentration oder eine Senkung der Temperatur nur zu geringfügig kürzeren Submikrofasern. Das zur Beschallung verwendete Medium beeinflusste bemerkenswerter-weise nicht nur die Länge der Fasern, sondern auch ihr Aspektverhältnis. Dadurch konnte das Aspektverhältnis im Bereich von 3,7 bis 6,8 und die Faserlänge zwischen 0,66 und 0,98 µm variiert werden. In diesem Zusammenhang wurde die Faserlänge erfolgreich mit der Viskosität des Mediums korreliert. Viskosere Medien führten selbst nach langen Beschallungszeiten zu kürzeren Fasern, was gleichzeitig die erfolgreiche Steuerung der Faserdimensionen verdeutlicht.

Im dritten Abschnitt wurden *supramolekulare Nanofasern* zur Verbesserung von Schaum-morphologie und Mechanik von *extrudierten Schäumen* aus Polypropylen eingesetzt. Dieses Projekt wurde in Kooperation mit dem Lehrstuhl für Polymere Werkstoffe der Universität Bayreuth realisiert. Das zugrundeliegende Konzept sieht homogen gelöste BTAs vor, die durch Abkühlen im Extrusionsprozess zu Nanofasern selbstassemblieren. Diese wirken als gut verteilte Nukleierungskeime für Schaumzellen und bestimmen so die Schaum-morphologie. Um dieses Konzept zu verwirklichen wurden zuerst drei verschiedene BTAs in ein isotaktisches Polypropylen (*i*-PP) eingemischt und spritzgegossen. Die erhalten Probe-körper wurden gründlich untersucht und auf Basis dieser Ergebnisse wurden Compounds mit

verschiedenen Konzentrationen der drei BTAs für die Schaumextrusion ausgewählt. Als Referenz wurde Talk in verschiedenen Konzentrationen verwendet. Für die Schaumextrusion wurde eine Tandem-Extrusionsanlage mit CO_2 als physikalischem Treibmittel verwendet. Es wurde festgestellt, dass die BTAs Dichte und Morphologie der extrudierten Schäume deutlich veränderten. Mit BTAs wurde die Schaumdichte gegenüber reinem *i*-PP um mehr als 40%, auf 0.09 g/cm^3 verringert. Der mittlere Durchmesser der Schaumzellen wurde ebenfalls um mehr als 40% auf bis zu 27 µm reduziert. Solche homogenen Schäume mit geringen Zellgrößen konnten bei den talkhaltigen Referenzschäumen nicht erreicht werden. Zudem wurde gezeigt, dass die spezifischen Kompressionsmoduln von Schäumen mit BTAs vergleichen mit reinem *i*-PP maximal um bis zu mehr als 100% und verglichen mit den talkhaltigen Referenzschäumen um mehr als 65% gesteigert werden konnten. Dieses Resultat wird auf einen verstärkenden Effekt der BTA Fasern zurückgeführt.

1. Introduction

Nanomaterials have attracted broad interest for many years due to their outstanding properties related to their large surface area, which differ from bulk materials featuring the same composition. Owing to these size-dependent properties, dimensional control is of paramount importance for nanomaterials. Therefore, nanomaterials featuring structures of defined size are supposed to play a significant role in industry and daily life in the future. Notably, this big impact of such materials is reflected in large research programs intended to foster research and technology transfer to industry and to practices. For example, the government of the United States of America has launched the "National Nanotechnology Initiative", having the vision of *"a future in which the ability to understand and control matter at the nanoscale leads to a revolution in technology and industry that benefits society."*[1] Similarly, the European Union also enclosed nanotechnology into its "Horizon 2020" research and innovation program. It is based on the expectation that *"nanotechnologies […] will help address key societal challenges such as climate change, reducing carbon emission, developing renewable energies, more efficient use of resources and addressing medical needs of an ageing population."*[2]

1.1. Nanomaterials – Definition and examples

According to the most common definition, a nanomaterial is a *"material with any external dimensions in the nanoscale or having internal structure or surface structure on the nanoscale".*[3] The nanoscale is generally understood as the range between 1 and 100 nm.[3,4] Nanomaterials often consist of many objects, which frequently feature a size distribution. As a rule, 50% of the objects should feature at least one dimension on the nanoscale for the whole material to be referred to as a nanomaterial.[3] Depending on how many of the object's dimensions are on the nanoscale, three morphologies are distinguished, as Figure 1 illustrates. If all three dimensions are on the nanoscale and feature comparable dimensions, the objects are called nanoparticles. If two dimensions are on the nanoscale, nanofibers result. They feature a third dimension significantly larger than the two others. If only one dimension is on the nanoscale, nanoplatelets, which are also referred to as nano-plates or nanosheets result. These feature two dimensions significantly larger than the other one.[4] In this context, nanofibers may also be called 1D-nanoobjects. In a similar manner, nanoplatelets may be referred to as 2D-nanoobjects. These terms are used synonymously in this thesis.

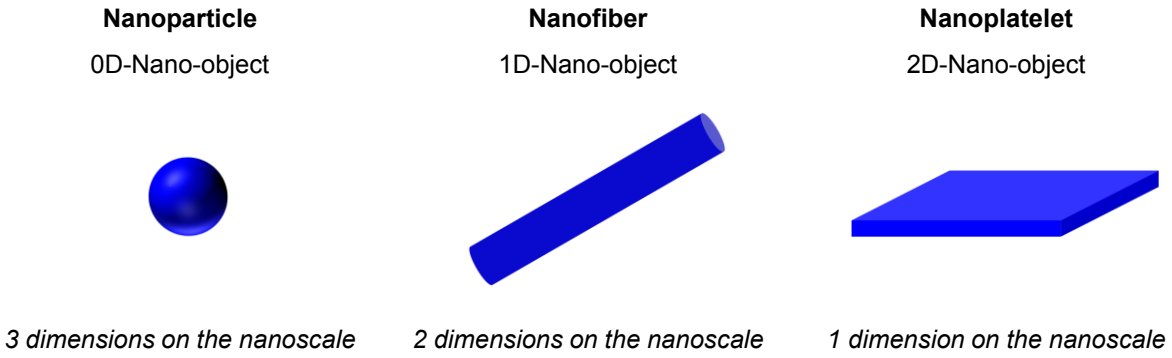

Figure 1: Shapes and nomenclature of nanoobjects.

There is a plethora of nanoparticles known from different material classes. Prominent examples are nanoparticles of metals, e.g. gold[5] or silver[6], or nanoparticles of metalloid oxides such as TiO_2[7], ZrO_2[8] or SiO_2[9]. As this thesis focuses on 1D- and 2D-nanoobjects, these two other classes will be discussed in the following.

Examples of 1D-nanoobjects made of different materials are metallic silver nanowires, carbon nanotubes and polymeric poly(lactic acid) nanofibers, as shown in Figure 2. To achieve this kind of structures, top-down as well as bottom-up approaches are viable. A common way, e.g. for metallic nanowires, is a template-directed growth, as shown for silver nanowires in Figure 2A. In this bottom-up process, silver is released from a precursor such as $AgNO_3$ in solution and due to its insolubility it starts growing into crystals. To achieve 1D-structures, some crystal faces have to be selectively covered with the templating substance such as poly(vinyl pyrrolidone). This hinders further growth on same faces and results in an anisotropic growth into 1D-nanoobjects.[10] Another example of a bottom-up preparation technique for 1D-nanomaterials are carbon nanotubes prepared via electric-arc discharge as shown in Figure 2B. By the electric-arc discharge, carbon is evaporated from the graphite anode and deposits as carbon nanotubes on the graphite cathode.[11] A top-down method frequently applied to polymers, although not limited to these, is electrospinning. Here, a charged thread is pulled from a solution of a material by an applied electric field. After evaporation of the solvent, the final fiber is obtained. Under appropriate conditions, very thin fibers can be produced this way, as shown for electrospun poly(lactic acid) nanofibers in Figure 2C.[12]

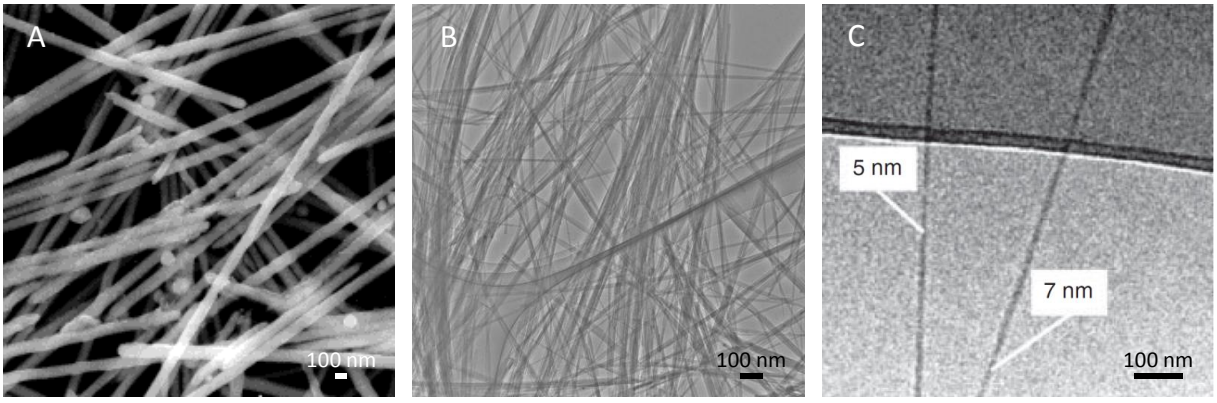

Figure 2: Examples of 1D-nanoobjects. A: Silver nanowires (Sun et al. 2002)[10], B: carbon nanotubes (Ajayan und Ebbesen 1997)[11] C: Poly(lactic acid) nanofibers (Hou et al. 2002)[12] *Reprinted with permission from refs. © (2002) American Chemical Society and (1997) IOP Publishing.*

For 2D-materials, also a plethora of substances is known, of which the probably most famous one is graphene. Besides, several transition metal dichalcogenides such as MoS_2[13] or layered silicates such as sodium hectorite[14] are used to obtain nanosheets. Figure 3 shows three examples of nanosheets representing these materials' classes alongside with their respective top-down synthesis routes. Very typically, nanoplatelets are produced from layered materials, particularly inorganic ones, by liquid exfoliation, a top-down process.[15]One way to obtain nanoplatelets via liquid exfoliation is sonication in appropriate media. Here, surfactant solutions are applied, as in the case of the single layer graphene presented in Figure 3A.[16] Alternatively, solvents with matched surface energy are used in a surfactant-free process, as it was done to prepare the MoS_2 nanoplatelets shown in Figure 3B.[13] A second way of liquid exfoliation is based on intercalated ions. The presence of appropriate ions, either introduced by intercalation or ion exchange or already present in the pristine material, facilitates exfoliation to a great extent. This is due to the osmotic pressure induced by the charges, when the material is in contact with water. This pressure allows water to move between the layers and, thus, swells the material, which increases the interlayer distance. Upon that, spontaneous delamination is possible, as it was shown for the sodium hectorite nanoplatelets presented in Figure 3C.[14]

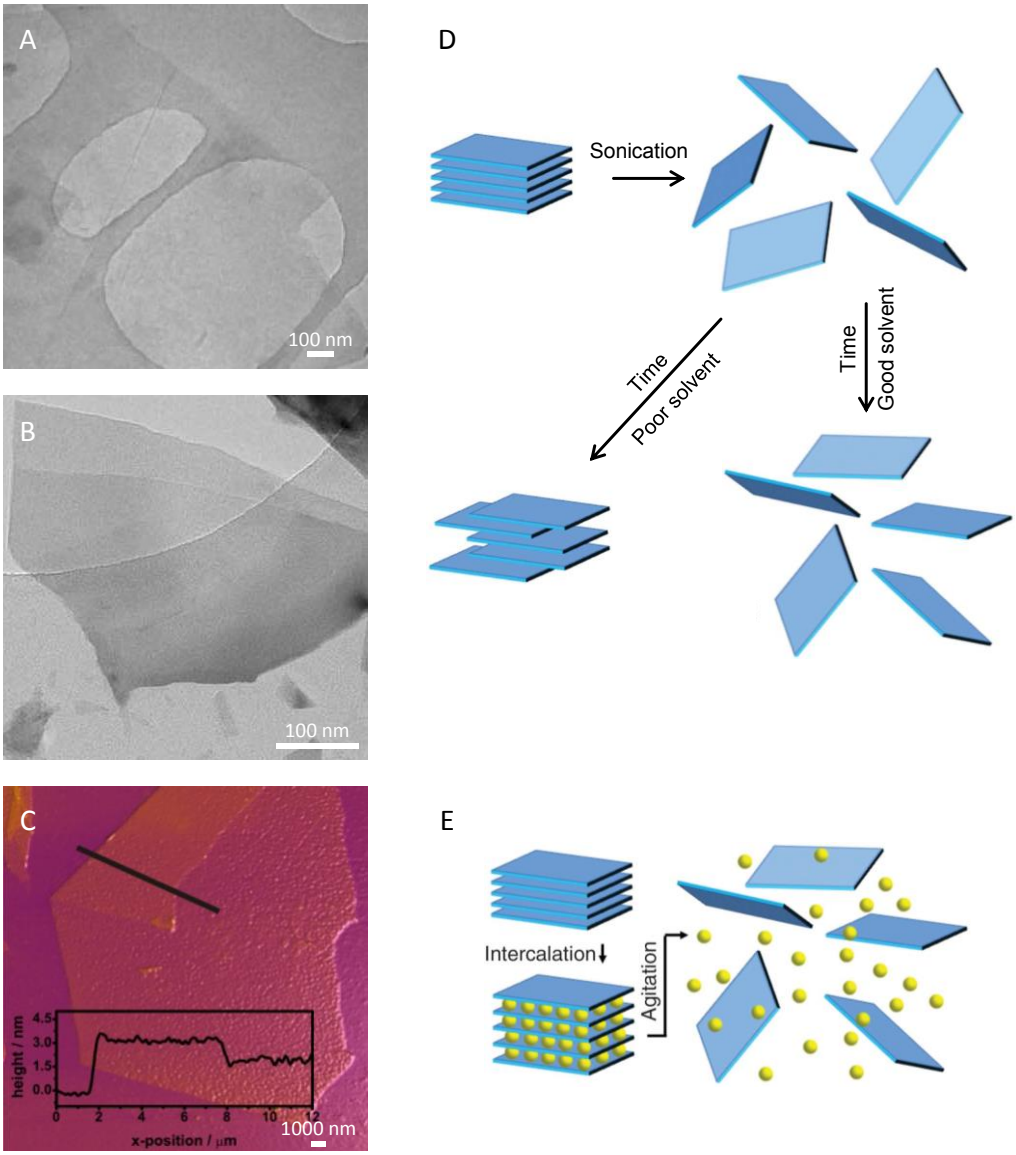

Figure 3: Examples of 2D-materials and schematic representations of their exfoliation routes. A: Single layer graphene (Lotya et al. 2009)[16], B: MoS_2 nanoplatelets (Coleman et al. 2011)[13] and C: sodium hectorite nanoplatelets (Stöter et al. 2013) [14]. A and B were exfoliated by sonication (scheme (scheme D). To avoid agglomeration of nanosheets, for A a surfactant and for B a medium with matched surface energy were applied. C was exfoliated from an intercalated material upon application of external force, i.e. shearing. This easy separation of layers is possible as intercalation with proper ions weakens the interaction between the individual layers of the material. Intercalated materials can be generated by intercalation of ions (yellow) (scheme E) into suitable layered materials or direct synthesis as intercalated material. Schematics were adopted from Nicolosi et al. 2013[15]. *Reprinted with permission from refs. © (2009 and 2013) American Chemical Society and (2011, 2013) The American Association for the Advancement of Science*

1.2. Properties and applications of nanomaterials

Nanomaterials have properties different from those of the corresponding bulk materials. For example, tin features a melting point of 232 °C in the bulk, which is decreased to 14 °C, when the material is present as particles of a size of 6 nm.[17] Another prominent example for this phenomenon is gold, which changes from a golden inert bulk material to a red material with catalytic activity in the form of nanoparticles.[17] Obviously, the threshold of a possible change of properties with decreasing dimensions depends on the material. However, it does not necessarily correspond to the common definition of 100 nm for nanoobjects presented above.[17]

Due to their novel or uncommon properties, nanomaterials have found their way into many applications: For example, they are used in industry as antimicrobial agents, catalysts, in (opto)electronics and in sensors.[18] Nanomaterials are present in a broad variety of consumer products, for example in personal care products, clothing, cosmetics, sporting goods, automotives and many more.[19] This plethora of current applications, alongside with other applications expected in the future, makes nanomaterials an emerging research field.

The shape of nanoobjects plays a significant role in many applications. For example, 1D-objects have been shown to allow longer blood circulation times compared to their spherical analogues. This effect, which increases with object length, may be an important feature in drug delivery applications.[20] Also for applications related with nano-electronics, the objects' shapes are relevant: 1D-nanoobjects may be applied as nanowires[21], while 2D-nanoobjects can serve as insulating layers.[22] Furthermore, in barrier applications, the 2D-morphology of applied nano-materials is a profound advantage. In this context, also a high aspect ratio is required.[14] These examples show that control of morphology and size of nanoobjects is of paramount importance in many applications.

1.3. Supramolecular nanomaterials

According to J.-M. Lehn, *"supramolecular chemistry is the chemistry of the intermolecular bond, covering the structures and functions of the entities formed by association of two or more chemical species"*[23]. This *"chemistry beyond the molecule"*[23] relies on different non-covalent interaction ns to form larger structures, typically via bottom-up approaches. These

non-covalent interactions can be divided into dipole-dipole, ion-dipole, ion-ion, ion-π and π-π interactions and van der Waals forces.[24] Hydrogen bonding as a special case of dipole-dipole interactions is the most frequently utilized interaction in supramolecular chemistry. Commonly, hydrogen bonds are formed between a donor group and an acceptor group. Donor groups comprise an H-atom covalently bond to an electronegative atom like e.g. oxygen in hydroxyl groups or nitrogen in the case of amide groups. The acceptor group is subsequently an electronegative atom like e.g. oxygen in carbonyl groups, nitrogen in imine groups or fluorine in fluorocarbons. H-bonds can achieve remarkable strength with typical binding energies between 4 and 60 kJ/mol[24]. In supramolecular chemistry, building blocks are very often designed in a way that hydrogen bonds facilitate directed interactions to build-up anisotropic structures. Supramolecular nanoobjects based on small molecules and held together by hydrogen bonds often feature a one- or two-dimensional morphology.

1.3.1. Supramolecular 1D-nanoobjects

Supramolecular 1D-nanoobjects can also be found in nature. For example, the tobacco mosaic virus consists of a strand of RNA and 2130 protein units. When mixed under physiological conditions, these components self-assemble into the virus's shape. This shape of a 1D-nanoobject features a length of 300 nm and a diameter of 18 nm, as shown in Figure 4A. The strand of RNA acts as a template, directing the protein units to form a well-defined helical assembly around it.[25]

An example of artificial supramolecular 1D-nanoobjects are the nanowires reported by Khalily *et al.*. These electrically conductive nanowires are made up from p- and n-type peptide-chromophore conjugates via alternating co-assembly. The formed objects, which are shown in Figure 4B, feature diameters of around 11 nm and lengths of several micrometers. The self-assembly into nanowires in this case is mainly driven by the formation of hydrogen bonds.[26] Another example are nanofibers based on the sorbitol derivative 1,3:2,4-di(4-acylhydrazide)-benzylidene sorbitol. This compound self-assembles into nanofibers via hydrogen bond formation upon cooling of a hot aqueous solution, subsequently yielding a hydrogel, as depicted in Figure 4C.[27]

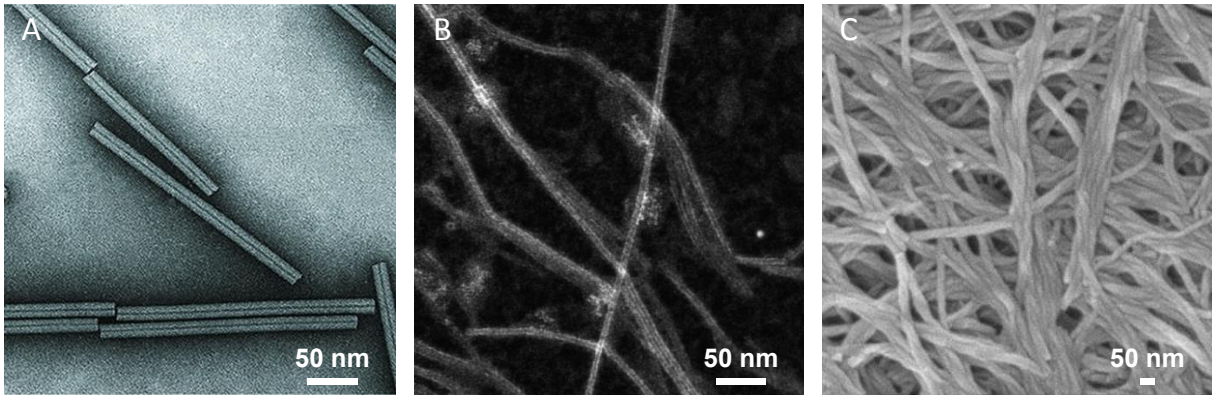

Figure 4: Examples of 1D-Nanomaterials. A: Tobacco mosaic virus (Adams et al. 2017)[25], B: self-assembled nanowires consisting of peptide-chromophore conjugates (Khalily et al. 2017)[26] and C: self-assembled nanofibers consisting of a sorbitol derivative (Howe et al. 2015)[27]. *Adopted with permission from refs. © (2017) Microbiology Society, (2017) American Chemical Society and (2015) Royal Society of Chemistry*

1.3.2. Materials class of 1,3,5-benzene- and 1,3,5-cyclohexanetrisamides

A prominent class of compounds with a well-known ability to form supramolecular 1D-nano-objects are 1,3,5-benzenetrisamides (BTAs) and 1,3,5-cyclohexanetrisamides (CTAs). Since the first report of compounds with this structure[28], BTAs and CTAs have been subject to research by various research groups. Owing to the versatility of this supramolecular building block with three hydrogen bonding groups, many applications have been discovered. Prominent examples are liquid crystals, gels, polymer additives and microcapsules for drug delivery based on these building blocks.[29]

In particular, BTAs are also applied in two chapters of this thesis. Hence, this most interesting chemical class is briefly introduced providing (i) the general molecular design of these compounds and possible variations, (ii) the self-assembly behavior of trisamides and supramolecular structures generated therefrom and (iii) a short overview of selected properties and applications of BTAs and CTAs.

A schematic representation of the general molecular structure of 1,3,5-trisamides is presented in Figure 5. These molecules feature (i) a C_3-symmetrical central core, (ii) hydrogen bond forming amide groups and (iii) a periphery. The central core can either be benzene or cyclohexane, resulting in 1,3,5-benzenetrisamides (BTAs) or 1,3,5-cyclohexane-trisamides (CTAs). It is symmetrically substituted with three amide groups (1,3,5-substitution). The amide groups can be linked to the core either by their C-atom or by their

N-atom. Among other research groups, the influence of the linkage of the amide groups to the core was studied by Albuquerque *et al.*. They found that the negative heat of formation for stacks of BTAs increases with more amide groups being connected to the core by their N-atoms.[30] Abraham *et al.* found the solubility of compounds with one or two inverted amide groups to exceed the one of their analogues featuring symmetrical amide substitution.[31] Hence, the orientation of amide groups is a valuable tool to tune the properties of BTAs and CTAs. Finally, the peripheral substituent is also a decisive part of the molecular design and can be easily varied to a very large extent. By this substituent, solubility and thermal properties of the molecules can be adjusted.[32,33] In particular, a great variety of hydrocarbon substituents have been used in numerous investigations.[30,32,34,35,36]

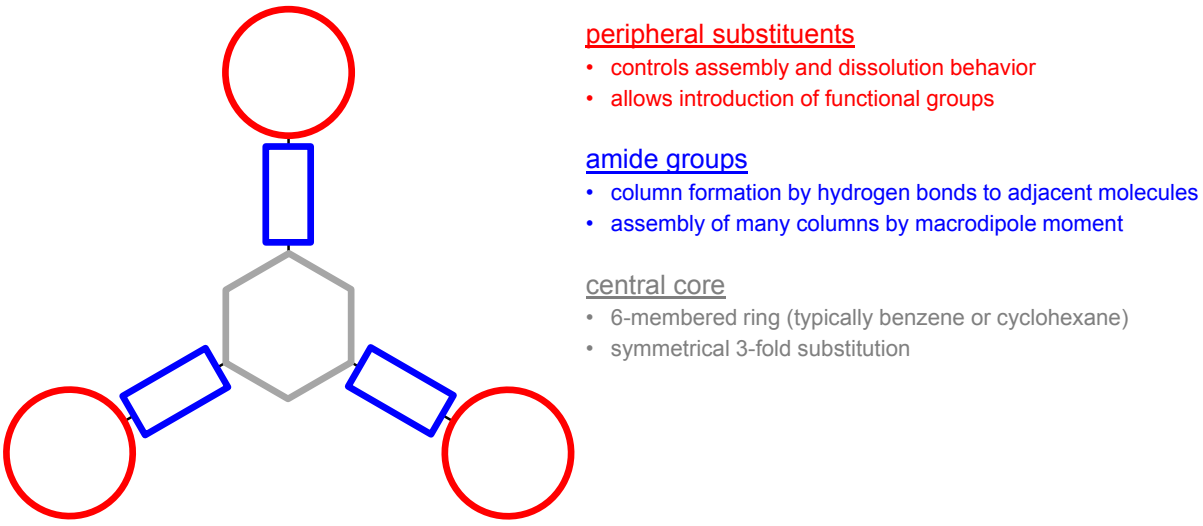

Figure 5: General molecular structure of BTAs and CTAs.

The driving force for the self-assembly of BTAs and CTAs is mainly the formation of strong and directed intermolecular H-bonds. Typically, these molecules assemble in supramolecular columns with their cores being placed directly above each other. As depicted in Figure 6, BTAs assemble with each molecule rotated about 60° relative to its neighbors in the column. Each individual column in BTAs is held together by three helical chains of H-bonds.[37] The strength of the H-bonds is widely determined by the ability of amide groups to rotate into the column's length axis. This can be seen when comparing BTAs and CTAs: In BTAs, amide groups participate in the π-conjugation of the aromatic core. Hence, their rotation out of the core's plane is limited to retain the π-conjugation. By contrast, in CTAs the core provides no conjugated system and thus the amide groups are free to rotate. In this case, the amide

groups are positioned almost perpendicularly to the core's plane and form H-bonds almost parallel to the column's length axis.[30] This leads to several phenomena: H-bonds in CTAs generally are shorter and stronger than those in comparable BTAs, rendering CTAs less soluble than BTAs. In addition, the H-bond direction along the column's length axis enables the CTAs to assembly directly above each other. This parallel assembly evokes repulsions between the core's axial atoms and increases the interdisc distance compared to BTAs.[30]

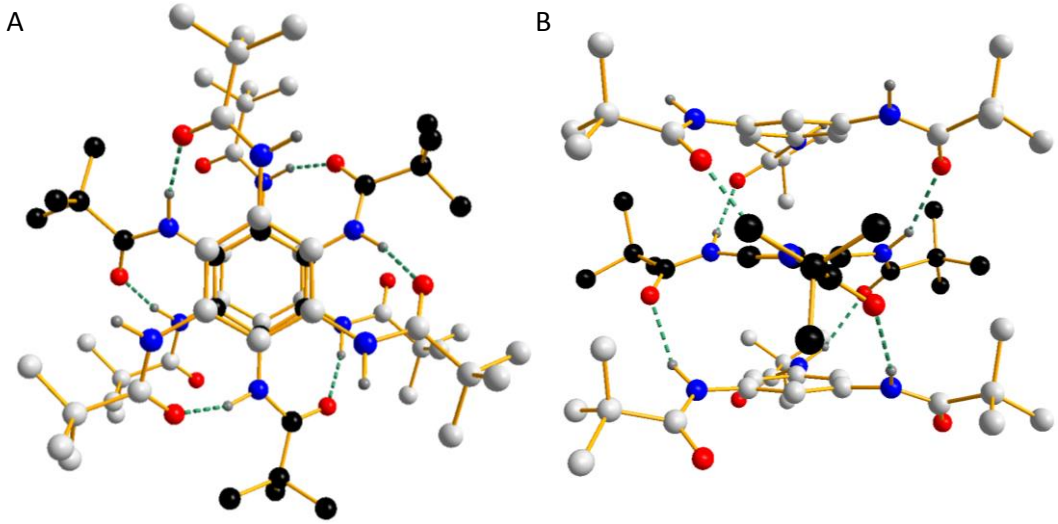

Figure 6: Columnar stacking of BTAs at the example of a BTA bearing *tert*-butyl substituents. A: view from top. B: view from side. H-bonds are indicated by green dashed lines. For the sake of clarity, H-atoms not involved in H-bonds are omitted and carbon atoms of the second molecule are colored black. *The figure is based on data from Schmidt et al. (Schmidt et al. 2012)*[39].

The parallel and directed orientation of amide groups results in a dipole moment of a single BTA molecule. Within a column these dipole moments sum up to a macrodipole moment, i.e. the column features a supramolecular macrodipole.[30] To compensate this macrodipole, other columns align next to the first one in an antiparallel manner, as it is depicted in Figure 7A.[38] Depending on the peripheral substituents and the applied conditions, BTAs and CTAs typically assemble in more or less thick fibers or needles rather than in single columns. From a crystallographic point of view, a (pseudo)hexagonal stacking of columns is favored.[38,39] However, the hexagonal arrangement does not allow all columns to align in the favored antiparallel orientation relative to all nearest neighbors, as shown in Figure 7B, which result in a so called geometric frustration. To compensate this geometric frustration, ferroelectric domains form in the mesoscopic assembly of BTAs, as Zehe *et al.* reported.[38]

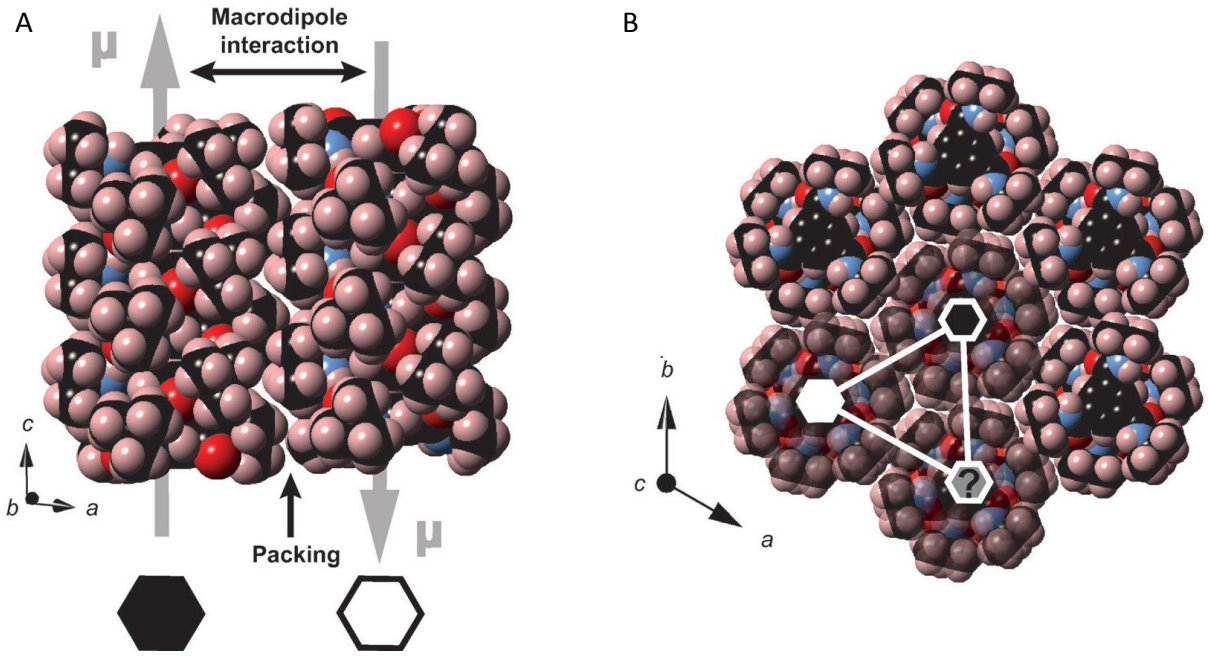

Figure 7: A: Antiparallel alignment of neighboring columns of a BTA in side-view. This alignment compensates their macrodipole moments μ. The direction (up or down) of each column and subsequently of its macrodipole moment is symbolized with white or black hexagons. B: Top view on an assembly of seven columns. For any triangle of three columns, two can assume the favorable antiparallel orientation (black and white hexagons), while the third one is geometrically frustrated (grey hexagon). *Reprinted with permission from ref (Zehe 2017)[38]. © (2017) The authors.*

Finally, the chemical nature of the substituents also plays an important role in tuning self-assembly. The size of the substituents determines the diameter of the column and thus the distance of columns to each other. Thus, it determines the dipolar interactions and also the size of ferroelectric domains.[38] When the substituents are bulky carbohydrates, solid materials with high melting points are obtained.[29,31,34] BTAs with long alkyl chains show thermotropic liquid crystalline behavior.[29] For a BTA featuring *n*-octyl substituents also a non-columnar, sheet-like modification has been reported.[40]

Typically, self-assembly upon cooling of hot solutions is the process most widely reported in literature. In the first step of this process, the respective 1,3,5-trisamide is mixed with the solvent (which can be a polymer melt) and the mixture is heated. At elevated temperatures, depending on the molecular structure of the 1,3,5-trisamide used, the 1,3,5-trisamide dissolves in the solvent or melt. In this step, diffusion of the dissolved 1,3,5-trisamide units results in homogeneous dispersion of those. Upon cooling, self-assembly into primary aggregates, i.e. columns, and, finally, into supramolecular nanofibers is induced.[29,32] This

self-assembly process is reversible, i.e. dissolution and self-assembly can be repeated by applying the heating and cooling cycle once again. Self-assembly upon cooling is typically affected by several parameters, which are given in Figure 8.

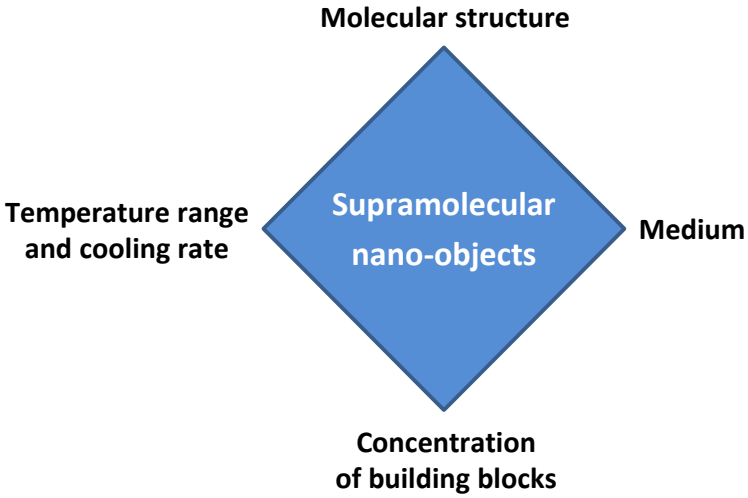

Figure 8: Parameters influencing the formation of supramolecular nanoobjects via self-assembly upon cooling.

When these parameters are tuned well, supramolecular nanoobjects can be obtained reproducibly. Hence, BTAs can self-assemble into nanofibers, as it is demonstrated by an example from the group of E.W. Meijer in Figure 9.[41]

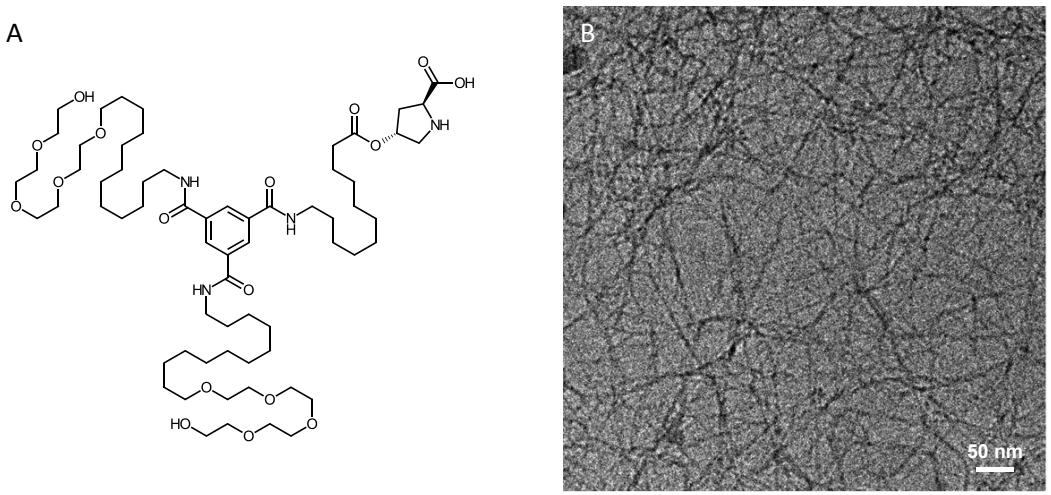

Figure 9: Molecular structure of a BTA ((2S,4R)-4-((11-(3,5-Bis((1-hydroxy-3,6,9,12-tetraoxatetra-cosanyl)-carbamoyl)benzamido)undecanoyl)oxy)pyrrolidine-2-carboxylic acid) and nanofibers of it. The fibers were prepared via self-assembly in water. Dark spots in the cryo-TEM image are non-vitrified water. The scale-bar represents 100 nm. *Reprinted with permission from ref (Neumann 2015)[41]. © (2015) The Royal Society of Chemistry.*

The most important property of BTAs and CTAs is their robust columnar self-assembly, which results in supramolecular nanofibers. Such nanofibers assembled from suitable solvents feature good mechanical stability, as Kluge *et al.* demonstrated.[42,43] This allows applications requiring a mechanical stability of the fibers, e.g. in air filtration.[44,45] Moreover, 1,3,5-trisamides featuring a wide range of substituents can be synthesized. This makes 1,3,5-trisamides suitable for applications requiring adjustment of the substituent and, hence, the fiber surface, like gelation of organic media[46] or water[47,48]. The supramolecular 1D-packing induced by the 1,3,5-trisamide motif also allows for advanced functionality of nanofibers, if appropriate substituents are introduced. This is the case for "flexible" single columns of BTAs synthesized by the group of E.W. Meijer, which were also referred to as *"supramolecular polymers*". Meijer et al have demonstrated that these *"supramolecular polymers"* showed catalytic activity, when functionalized with L-prolin.[41] With another system, consisting of several differently substituted BTAs, L. Albertazzi *et al.* demonstrated assembly into *"supramolecular copolymers"*. Furthermore, they reported, that the monomer sequence of these structures could be controlled by external stimuli.[49] This shows, that self-assembly of 1,3,5-trisamides is a versatile tool to tailor structures of high complexity.

Another outstanding property of BTAs and CTAs is the combination of a relatively simple synthesis with good chemical and thermal stability. This provides access to industrial applications, e.g. as polymer additives. BTAs have successfully been applied to nucleate the crystallization of semi-crystalline polymers like poly(vinylidene fluoride) (PVDF)[50], poly(butylene terephthalate) (PBT)[51] and isotactic poly(propylene) (*i*-PP)[31,32,34]. In the case of *i*-PP, selected BTAs nucleate the β-phase of *i*-PP[32], which results in improved mechanical properties due to toughening of the material.[52,53] Besides, selected BTAs improved the optical properties of *i*-PP by manipulation of the crystallization process, acting as clarifiers.[32] Moreover, BTA nanoobjects present in *i*-PP were demonstrated to enhance electret properties of the material.[54]

1.3.3. Supramolecular 2D-nanoobjects

From the plethora of systems forming supramolecular 2D-nanoobjects, three will be presented in the following exemplarily. The first example deals with nanosheets of peptoid polymers reported by Nam *et al.*. Upon mixing of the peptoids depicted in Figure 10A the nanosheets shown in Figure 10B spontaneously form as bilayers in aqueous solution. The

driving force for bilayer formation is the poor interaction between the hydrophobic parts of the molecules and the polar medium. Ultimately, the hydrophobic parts face each other in the center of the bilayer, as the model in Figure 10C illustrates. Each single layer consists of alternating chains of positively charged and negatively charged peptoids. Thus, the structure is stabilized by electrostatic interactions, while the hydrophobic groups drive bilayer formation.[55]

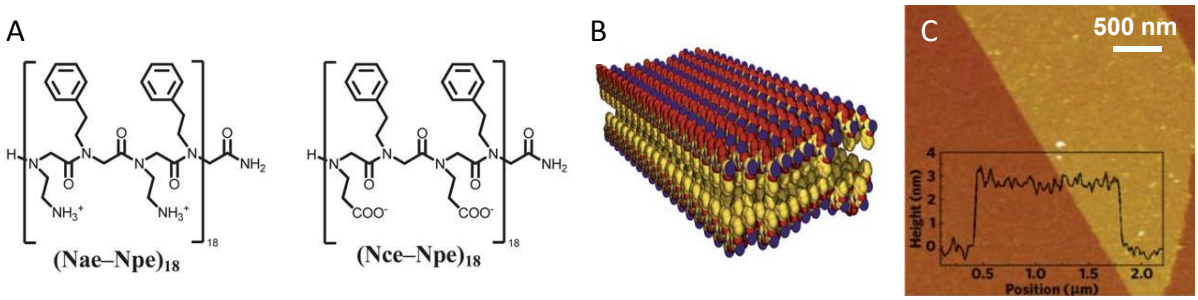

Figure 10: A: Molecular structures of peptoids (Nae-Npe)$_{18}$ and (Nce-Npe)$_{18}$. These peptoids form bilayers with a thickness of approx. 3 nm, as the AFM image (C) and the molecular model (B) show. (Nam et al. 2010)[55] *Adapted with permission from ref. © (2010) Springer Nature.*

A different system relying on similar interactions to form 2D-nanoobjects was reported by Wu *et al.*: They investigated the self-assembly of positively charged polycyclic aromatic hydrocarbon salts. Figure 11A exemplarily shows the molecular structure of an anion-cation combination applied. These compounds are able to form nanosheets in water/methanol solutions, as shown in Figure 11B. These nanosheets feature a thickness of around 20 nm. A schematic representation of the assembly pattern is given in Figure 11C. As in the first example, electrostatic interactions within the hydrophilic parts of the molecules guarantee stable layers. Here, particular stability is achieved by the bifunctional disulfate anions (DSA) linking the polycyclic aromatic hydrocarbon cations (PQP cations). The hydrophobic parts of the structure lead to the formation of bilayers.[56] An important difference between the two systems presented is the stacking of bilayers to thicker nanoplatelets occuring in the second example.

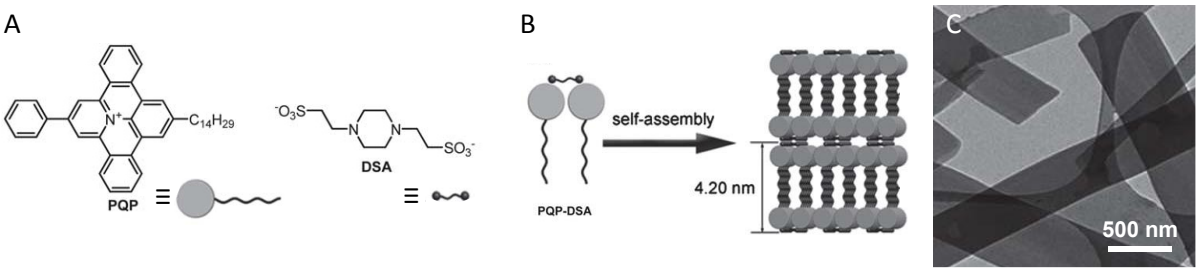

Figure 11: A: Polycyclic aromatic hydrocarbon cations (PQP) linked by disulfate anions (DSA) also self-assemble into 2D-nanoobjects (C). B: Scheme of the self-assembled structure. Here, bilayers are formed by the hydrophobicity of the PQP's carbohydrate chain in a methanol/water solvent system. This structure is stabilized by the bifunctional DSA.(Wu et al. 2011)[56] *Adopted with permission from ref. © (2011) John Wiley and Sons.*

As a third example of supramolecular 2D-nanoobjects, a system featuring intermolecular hydrogen bonds is presented, namely bisacylurea derivatives investigated by the Zentel group. These molecules comprise two bisacylurea groups connected by a flexible hydrocarbon spacer. Both bisacylurea groups carry a peripheral spacer, as shown in Figure 12A. When self-assembled upon cooling of a hot solution, each bisacylurea group forms hydrogen bonds to two neighboring molecules. As both bisacylurea groups within one molecule can twist due to the flexible spacer, they are part of hydrogen bond strands pointing in different directions. Hence, a layer is formed, as schematically depicted in Figure 12B. Several of these layers stack to form multilayered nanosheets, as shown in Figure 12C.[57,58]

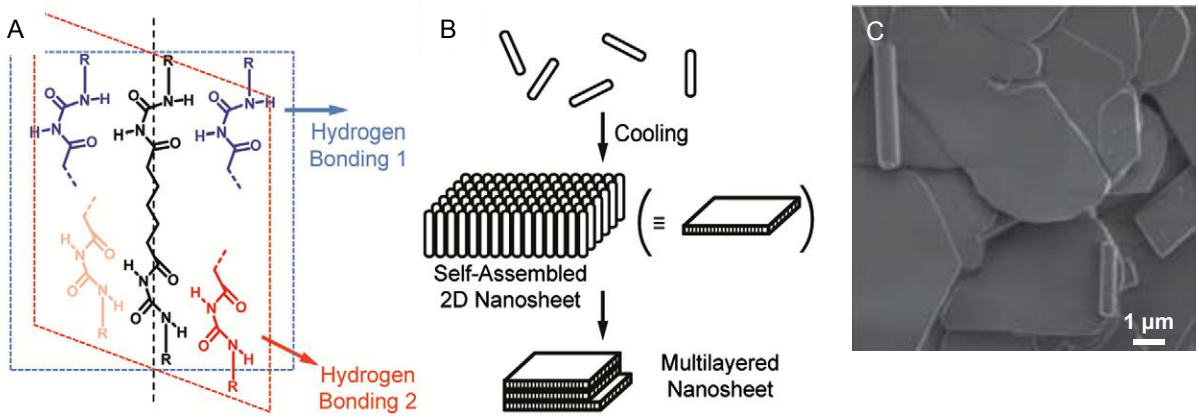

Figure 12: A: Bis-acylurea derivatives form intermolecular hydrogen bonds in two different directions. B: Schematic representation of the resulting self-assembly into nanoobjects.(Kim et al. 2011a)[57] C: SEM-image of the resulting multilayered nanosheets.(Davis et al. 2007)[58] *Reprinted with permission from refs. © (2010) Royal Society of Chemistry and (2007) John Wiley and Sons*

1.3.4. Materials class of 1,4-benzene- and 1,4-cyclohexanebisamides

Another class of compounds capable of forming 2D-nanostructures via self-assembly are 1,4-benzene- and 1,4-cyclohexanebisamides. In this work only bisamides with a 1,4-substituted core are used, therefore they will be treated in the following. This section is partitioned into three parts: Firstly, the general molecular structure of these compounds is presented and possible variations are discussed. The second part features a brief introduction into the self-assembly of bisamides and supramolecular structures generated therefrom. The latter are treated more in detail in the appropriate place in chapter 3. Finally, the third part gives an overview of properties and applications of bisamides.

The molecular design of 1,4-bisamides comprising (i) a central core, (ii) two amide groups in 1,4-position and (iii) a periphery is shown in Figure 13. In this class, the central core is either based on a benzene or a cyclohexane unit. The core spatially separates the neighboring amide groups and provides the molecule stiffness. In 1,4-position, the core is typically C_2-symmetrically substituted with amide groups. The arrangement of amino groups can be altered by using different cores based on e.g. terephthalic acid or 1,4-diaminobenzene. The type of attachment to the core has significant impact on compound properties such as melting point and solubility, as Mohmeyer *et al.* showed.[59] Each amide group is connected to a peripheral substituent, which widely influences the solubility of the respective compound. In literature, hydrocarbons are mostly used as substituents.[59,60,61,62]

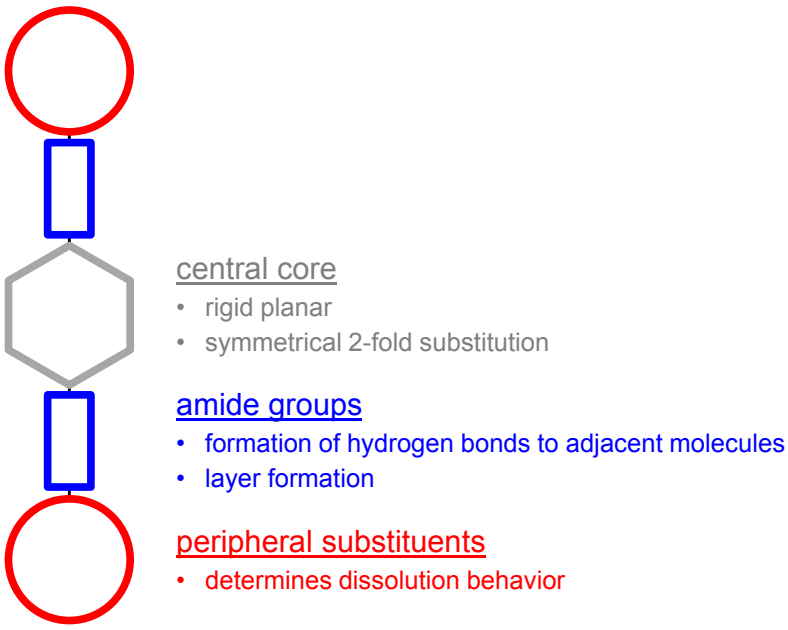

Figure 13: General molecular structure of 1,4-bisamides with hexagonal core.

Bisamides with a 1,4-substituted core are known to self-assemble into objects from hot solutions of organic solvents or from polymer melt.[59,63] In both cases, self-assembly typically is induced upon cooling. The temperature at which self-assembly occurs depends (besides solvent and concentration) on the molecular structure of the respective bisamide. For example, Mohmeyer *et al.* found a 1,4-bisamide with asymmetrically attached amide groups, i.e. one attached with the N-atom and one with the C-Atom, to be more soluble and to self-assemble at lower temperatures than its analogues with symmetric amide group substitution.[59] The peripheral substituents also influence the self-assembly conditions: For example, the longer the linear hydrocarbon chain of the substituent is, the lower is its self-assembly temperature.[60,61]

Regarding the morphology of the objects formed by self-assembly processes, several results are reported: For 1,4-benzene bisamides with cyclohexane substituents self-assembled in *i*-PP, Mohmeyer *et al.* observed supramolecular objects regardless the orientation of amide groups.[59] For the *trans*-1,4-cyclohexyl bisamide with *tert*-butyl substituents, Schmidt *et al.* reported large 2D-objects. The crystal structure of this compound shows a layered structure.[63] Furthermore, crystal structures of both symmetric 1,4-benzene bisamides with *tert*-butyl substituents, which differ in the orientation of amide groups, have been reported. Both compounds show layered structures in the solid state.[64,65] The assembly of the molecules and the H-bond connectivity will be discussed more in detail in chapter 3, alongside with the results of this work.

If hydrocarbons are used as peripheral substituents, 1,4-benzene- and 1,4-cyclohexane-bisamides feature good chemical and thermal stability. For example, Mohmeyer *et al.* reported melting temperatures above 280 °C without degradation.[59] This makes this class of compounds interesting for the use as supramolecular polymer additives, where they must withstand temperatures around 250 °C during polymer processing. Cyclic 1,4-bisamides were found to improve electret properties[59] and to nucleate the β-phase of *i*-PP.[59,62] When cooled from solution, bisamides form very fine structures.[59,60,61] Such microfibrils are a prerequisite for gelators. Hence, such bisamides also were successfully applied as organo-gelators, e.g. for *p*-Xylene at concentrations down to 0.2 wt% of bisamide.[60,61] All these applications are strongly related to the morphology of the structures formed. Yet, there is still a lack of a full understanding how to control the morphology of bisamide structures.

2. Aim and motivation

The main focus of this thesis is the formation of supramolecular nanoobjects by self-assembly of low-molecular weight building blocks, such as benzene- or cyclohexane-based 1,4-bis- or 1,3,5-trisamides. The self-assembly process is typically initiated by variation of parameters such as temperature or concentration. For a rational application of supramolecular nanostructures formed via self-assembly processes, control of their morphology and dimensions is crucial. Therefore, the first two chapters of this work deal with the dimensional control of self-assembled 1D- or 2D-nanoobjects. The third chapter deals with the formation of supramolecular nanoobjects in *i*-PP and their use as cell nucleating agents during foam extrusion.

2.1. Supramolecular 2D-nanoobjects via self-assembly

Whereas numerous investigations were performed with respect to the formation and properties of supramolecular nanofibers (1D-nanoobjects), much less is known about the formation of supramolecular 2D-nanoobjects. 2D-nanoobjects, which are also referred to as nano-platelets, feature a small thickness, typically in the range below 100 nm, compared to their lateral dimensions. In this context, self-assembly of 1,4-benzene or 1,4-cyclohexane bisamides to supramolecular 2D-nanoobjects will be investigated. Moreover, the peripheral groups will be varied resulting in symmetric and asymmetric 1,4-bisamides with chemically different groups such as hydrophobic and fluorophilic moieties. For the preparation of supramolecular nanoobjects, self-assembly upon cooling is a common approach, because this allows for a reasonable control of processing parameters. To gain a better understanding of the self-assembly, the processing parameters are systematically varied and the resulting morphologies are investigated. This chapter is divided into four sections. In the first one, the molecular design, synthesis and properties of all symmetric and asymmetric 1,4-bisamides are discussed. In the second one, crystal structures of the compounds are revealed and correlated to the respective molecular structure. The results of this section were obtained in cooperation with the department of Inorganic Chemistry III at the University of Bayreuth. In the third section, self-assembly upon cooling is optimized. Finally, in the fourth section, the molecular structure of the bisamides is optimized with respect to the thickness of formed self-assembled nanoobjects and their property profiles.

In this context, the following main scientific questions will be addressed:

- How does the molecular structure of bisamide compounds affect their packing pattern in the solid state?
- How can the thickness of supramolecular bisamide-based 2D-nanoobjects be reduced by molecular design of symmetric or asymmetric bisamides?
- How must conditions for the self-assembly process be selected to optimize the thickness of resulting 2D-nanoobjects?

2.2. Length control of supramolecular 1D-nanoobjects via ultrasound

Supramolecular nanofibers can typically be prepared by a bottom-up approach, i.e. self-assembly upon cooling. However, to obtain fibers with a defined morphology reproducibly, control of their dimensions, i.e. fiber diameter and fiber length is of paramount importance. It has already been shown, that the diameters of trisamide fibers can be adjusted by tuning the cooling process during self-assembly.[66] By contrast, control of fiber length during such a process is hard to achieve, since the trisamide columns forming the nanofibers are supposed to grow faster with increasing column length.[30] The aim of this work is to make use of a top-down, post-treatment process such as ultrasound and to evaluate how the nanofibers' dimensions, i.e. length and diameter can be controlled. In this context, the influence of important process parameters like sonication time, ultrasonic power amplitude, medium, temperature and concentration of the BTAs in the dispersion on the fiber dimensions will be systematically investigated. This chapter is divided into three sections. In the first section, supramolecular 1,3,5-trisamide fibers are prepared via self-assembly. In the second section, different media are investigated to identify suitable systems for sonication experiments. In the third section, selected systems are treated with ultrasound and correlations between chosen process parameters and dimensions of resulting nanoobjects are established.

In this context, the following main scientific questions will be addressed:

- Does the application of ultrasound reproducibly result in supramolecular nanoobjects with defined dimensions?
- Which parameters dominate the sonication process?
- Can the influence of the most relevant process parameters be correlated with known underlying physical processes?

2.3. Supramolecular cell nucleating agents for foam extrusion of *i*-PP

Rigid polymer foams become increasingly important due to their lightweight and improved insulation properties. In this context, isotactic polypropylene features a beneficial property profile in terms of mechanical and dimensional stability as well as a higher end use temperature in contrast to PE and PS. Progress in this field can be achieved by preparing foams with more homogeneous and finer cells. Most approaches to reduce the cell size in polymeric foams are based on the modification of the polymers used, on optimization of the foam processing machinery or on the use of insoluble cell nucleating agents.[67] To achieve this goal a different approach is chosen in this thesis, based on supramolecular nanoobjects as cell nucleating agents. As polymer grade a linear *i*-PP is selected, since it is of great practical importance. As supramolecular cell nucleating agents, distinct 1,3,5-benzene trisamides (BTAs) will be selected and applied. As processing technique foam extrusion with CO_2 is selected, as it is a highly relevant method for foam processing. Accordingly, this project was realized in cooperation with the department of Polymer Engineering at the University of Bayreuth. This chapter is divided into five sections: In the first section, the applied *i*-PP is characterized. In the second section, compounds which are composed of selected BTAs and *i*-PP are investigated with respect to the self-assembly behavior of the BTAs. In the third section, promising compounds are processed by foam extrusion. Subsequently, in the fourth section, the morphology of the resulting foams is investigated. Finally, the fifth section is focused on the compression properties of these foams.

In this context, the following main scientific questions will be addressed:

- To which extent can BTAs be used to control the morphology of polymer foams produced via foam extrusion?
- How can the role of BTA nanoobjects be visualized and evaluated to draw conclusions on the resulting foam morphology?
- How are the mechanical properties of polymer foams affected by the use of supramolecular cell nucleating agents?

3. Supramolecular 2D-nanoobjects via self-assembly

3.1. 2D-nanoobjects

2D-nanoobjects, also known as nanoplatelets or nanosheets, have attracted great interest due to their versatile properties like high specific surface area, flexibility and 2D-anisotropy.[68,69,70] Nanosheets are defined as structures consisting of one or multiple layers of a 2D-material, i.e. a material, which features covalent or supramolecular bonding of similar strength along two directions and much weaker interactions along the third one.[69] If these nanosheets become sufficiently thin, their properties may alter significantly. For example, graphene exhibits an anomalous room-temperature quantum Hall effect, contrasting to the corresponding 2D-material graphite.[69] Owing to these exceptional properties, nanosheets are either already used or are supposed to find use, for example, in gas barrier applications[71], to improve the flame retardancy of polymers[72], for catalysis, in sensors and as biomaterials.[73] Moreover, nanosheets providing electronic conductivity may be employed in e.g. optoelectronics, batteries and supercapacitors.[69,73]

In principle, there are two ways of preparing nanosheets: Firstly, in a top-down approach, a 2D-material can be exfoliated to obtain nanosheets, which in the case of complete exfoliation consist of single layers. Secondly, via the bottom-up approach, smaller building blocks can be arranged in a way that they directly build up nanosheets. In the bottom-up approach, surfaces can be used as templates for nanosheet growth.[69] Since this templated growth is limited in synthetic as well as in design flexibility[73], it is not discussed in the following. The other approaches are presented in more detail and examples are provided.

3.1.1. Top-down approaches to 2D nanoobjects

Many studies on exfoliation deal with graphene, which probably is the most prominent nanosheet material. Although there are many ways to produce graphene, exfoliation of graphite dispersions is of special interest since it is cheap and easily scalable.[74] Lotya *et al.* managed to partly exfoliate graphene by simple sonication of graphite in an aqueous solution of the surfactant sodium dodecylbenzene sulfonate. After sonication in a low power ultrasonic bath for 30 min, the dispersion was centrifuged to remove non-exfoliated graphite particles. Thus, they yielded flakes with diameters around 1 µm, of which 3% were mono-layers and 40% featured less than 5 layers.[16] However, this method results in nanosheets

covered with surfactant, which is disadvantageous for some applications. Hence, exfoliation must be realized in a surfactant-free process. Typically, exfoliation is hindered by the enthalpy for generating a new surface ΔH_{Mix}, which is described, e.g. for graphene by equation 1.[75]

$$\frac{\Delta H_{Mix}}{V} \approx \frac{2}{N}\left(\sqrt{E_S} - \sqrt{E_G}\right)^2 \phi_G \quad (1)$$

By this equation, ΔH_{Mix} is given for a dispersion of the volume V featuring a known volume fraction of graphite Φ_G. N denotes the thickness of the exfoliated graphene sheets (number of layers) and E_s and E_G are the surface energies of solvent and graphene. For successful exfoliation ΔH_{Mix} has to be minimized or, at best, eliminated. This is achieved if the surface energies of solvent and graphene E_s and E_G become equal.[75] In this context, Hernandez *et al.* reported exfoliation of graphene to work best for solvents with surface energies close to the one of graphene, which is 47 mJ/m^2, as reported by Wang *et al.*.[76] For example, *N*-methylpyrrolidone (NMP) allowed the exfoliation of 1 wt% of the initial graphite into monolayer graphene upon only 30 min of treatment in a low power ultrasonic bath.[77]

This liquid phase exfoliation was successfully transferred to layered metal chalcogenides, which are another intensely investigated class of inorganic 2D-materials. The most popular material of this class is MoS_2, for which Coleman *et al.* obtained nanosheets with lateral dimensions between 50 and 1000 nm and thicknesses between 3 and 12 nm, which equals 3 to 12 layers, using NMP as solvent.[13] Though liquid phase exfoliation works well for a plethora of materials[15,69,78], it can be further improved by prior intercalation of ionic species between the material's individual layers. Intercalation increases the layer spacing and reduces the energy barrier for exfoliation.[15] This phenomenon is commonly utilized for layered silicates, where intercalated ions induce an osmotic pressure resulting in additional intercalation of neutral solvent molecules.[79,80] Based on this, Stöter *et al.* reported the production of sodium hectorite nanosheets featuring lateral dimensions of several micrometers and a thickness around 1 nm. Hence, these single layer nanosheets reached exceptional aspect ratios up to 20,000.[14]

3.1.2. Bottom-up approaches to 2D nanoobjects

Bottom-up approaches, which represent the second pathway to nanosheets, are often applied for organic compounds.[73] For example, Govindaraju *et al.* used self-assembly of cyclic dipeptides in a solvent mixture of chloroform and trifluoroacetic acid to obtain nanosheets with a thickness of only 60 nm.[81] Also for derivatives of naphthalenediimide, an organic n-type semiconductor material, self-assembly to 2D-structures with lateral dimensions up to 100 µm was reported, yet the thickness of these objects was not determined.[82,83] For a similar material, 2-aminooctane-functionalized naphthalenediimide, Wang *et al.* showed self-assembly into platelets with lateral dimensions in the range between 2 and 7 µm. They induced the self-assembly process by injection of a solution of the naphthalenediimide in ethyl acetate into a mixture of the poor solvents methanol and water. Apparently, the self-assembly process was highly dependent on the water content in the mixture of poor solvents.[84] They also applied this method to a solution of 9,10-bis(phenylethynyl)-anthracene in dichloromethane as good and isobutyl alcohol as poor solvent. The 2D structures prepared this way featured lateral dimensions of several hundred micrometers and a thickness around 600 nm.[70] In another study, Hou *et al.* obtained very thin nanosheets of a 1,3,5-benzene trisamide featuring *n*-octyl substituents upon injection of acetone solutions either into water or into heptane. They demonstrated that the nature of the non-solvent influenced the morphology of formed nanosheets, but did not alter the crystal structure. They also showed that the injection approach is important for nanostructure formation. For example the simply dried sample from acetone yielded thicker and larger 2D structures.[40]

For complexes of positively charged polycyclic aromatic hydrocarbons and platinum ions Yang *et al.* observed self-assembly into nanosheets via another process: Here, self-assembly occurred directly after synthesis of the insoluble complexes in a mixture of DMF and MeOH. The obtained nanosheets featured a thickness of 23 nm, while lateral dimensions of several hundreds of nanometers were reported.[85] Lai *et al.* demonstrated direct assembly during synthesis for perylene. Hereto, they released perylene from perylene perchlorate in an aqueous hexadecyltrimethylammonium bromide (CTAB) solution. Since CTAB is surface active in aqueous solutions, it adsorbed to the top and bottom planes of the perylene nuclei and thus blocked the thickness growth of the formed nanosheets. By this elaborated approach, nanosheets featuring a thickness below 10 nm were produced successfully.[86]

For the generation of 2D-structures from bis-acylureas the Zentel group applied an approach relying on self-assembly upon cooling: A hot solution of the respective bis-acylurea was allowed to cool to room temperature, which resulted in precipitation of nanosheets. The bis-acylureas feature two acylurea groups connected by a flexible pentyl spacer, as shown in Figure 14. The flexible spacer allows torsion of the acylurea groups relative to each other (Figure 14A). Hence, H-bonds in two different planes to four neighboring molecules in total can be formed, resulting in a nanosheet connected by H-bonds.[58] In further studies, the Zentel group functionalized bis-acylureas prior to self-assembly and found the morphology formed to be highly dependent on the functional substituents. Bulky or thiol substituents hinder regular self-assembly, which results in morphologies other than sheets. Nevertheless, for a large variety of functional groups, nanosheets were obtained.[57,87] Furthermore, they reported successful assembly of a bis-acylurea asymmetrically substituted with a pyridine end group into nanosheets upon cooling of hot ethanol solutions. These nanosheets were several hundred nanometers thick and featured lateral dimensions of several micrometers. Due to the pyridine groups at the nanosheet surfaces, gold nanoparticles could be immobilized on the nanosheets, demonstrating the versatility of this approach.[88]

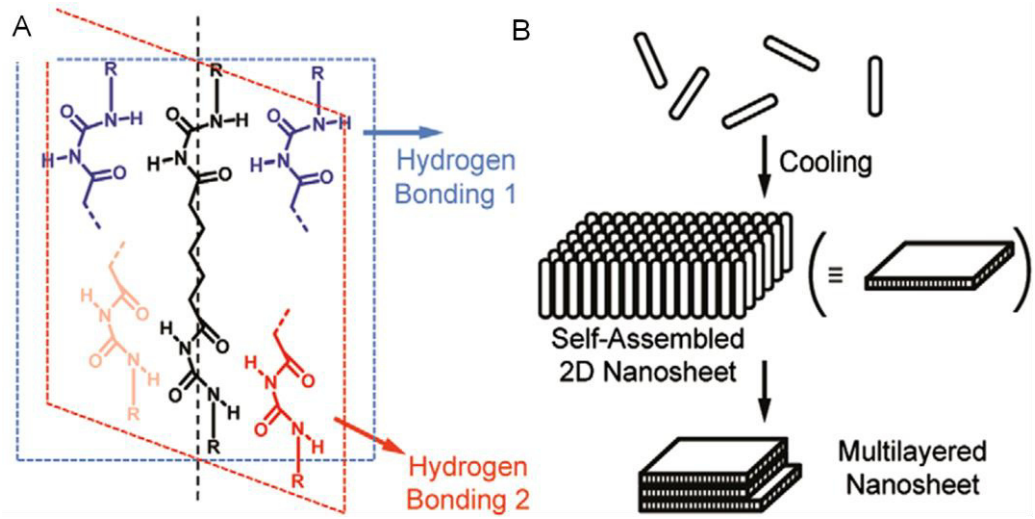

Figure 14: A: Biaxial hydrogen bonding of bis-acylurea. B: Self-assembly to nanosheets upon cooling and stacking to multilayered nanosheets. *Reprinted with permission from ref.(Kim et al. 2011a)[57]. © (2010) Royal Society of Chemistry*

Ray *et al.* investigated 1,4-benzenebisamides with methyl esters of amino acids as substituents. With the stiff benzene spacer, no tilt of each molecule's amide groups is

possible anymore. Hence, each molecule is involved in two antiparallel strands of hydrogen bonds. Molecules directly connected by a hydrogen bond are tilted by 90°. These structures are stabilized by C-H···π interactions, as depicted in Figure 15. From this, corrugated layers of connected molecules result. Ray *et al.* denoted this structure as 'nanostaircases'.[89]

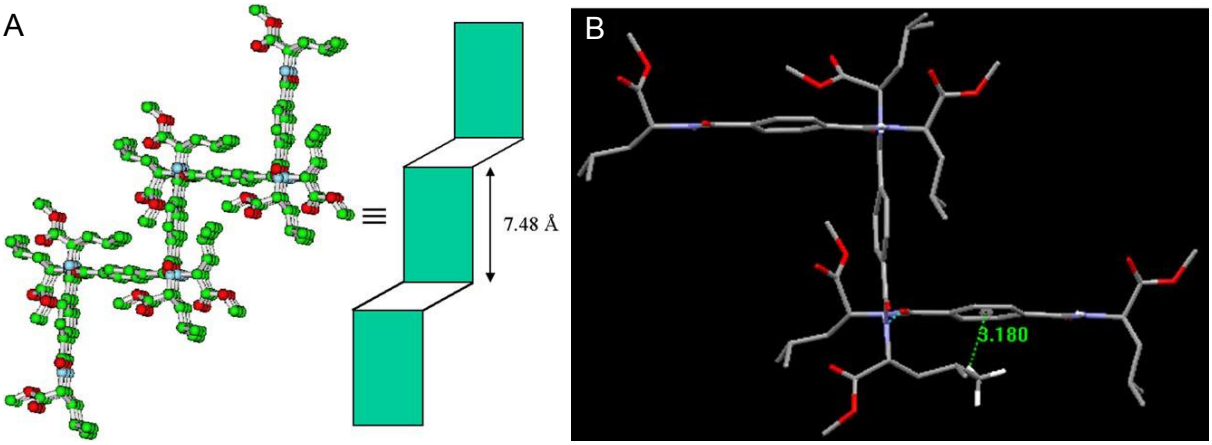

Figure 15: A: Nanostaircase assembly of a bisamide with amino acid methyl ester substituents. Molecules in this structure are connected by hydrogen bonds. Molecules connected this way feature a tilt of 90°, yielding the staircase structure. B: Crystal packing with C-H···π interactions stabilizing the tilt. *Reprinted with permission from ref.(Ray et al. 2006)[89]. © (2006) Elsevier*

In a previous publication, we investigated similar compounds, which feature a rigid cyclohexane core instead of the benzene core used by Ray *et al.*.[63] Again, this rigid core hinders twisting of the two hydrogen bonding groups. The investigated compounds comprised amide (Figure 16), urea or acylurea units as hydrogen bonding groups and *tert*-butyl substituents. The bisamide from this publication is used as starting point and comparison in this work and hence denoted as bisamide 1.

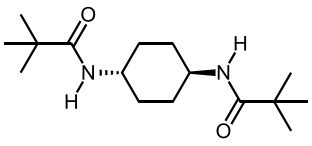

Figure 16: Molecular structure of the *trans*-1,4-cyclohexane bisamide 1.

All three compounds also self-assembled into large and thick sheets upon cooling of hot solutions. For the bisamide 1 and the bis-urea derivative a similar crystal packing into layered materials was determined by combination of powder X-ray diffraction and NMR

crystallographic methods.[63] It is discussed more in detail at the example of the bisamide 1 in the following.

Figure 17 shows the packing pattern of bisamide 1 from several perspectives, based on the published data.[63] As it is visible from Figure 17C, the crystal is made up of molecules, which are tilted relatively to each other along the b-axis. Viewing along the b-axis (Figure 17B), chains of H-bonds along the c-axis become visible. By this H-bond pattern, each molecule is connected to four others. Since these four are tilted in the other direction than the initial one, the structure is simultaneously built up in two directions by the H-bonds. In the third dimension, only Van der Waals interactions connect the formed layers. The resulting structure is schematically depicted by a stack of thin layers (A), where (B) and (C) then represent side views on the stacking from two directions. In the space-filling representation (D) it becomes clear, that the *tert*-butyl-substituents of adjacent layers are densely packed. Additionally, this representation helps to illustrate the molecules' alternating tilt mentioned above.

Guo *et al.* solved the crystal structure of a benzene-based bisamide, which also bears peripheral *tert*-butyl substituents. Here, the same structure is observed, although the authors proposed a different H-bond pattern, which implies each molecule being connected to only two neighboring molecules by two hydrogen bonds, respectively.[64] The structure described is based on the stiff molecules tilting relatively to each other in both studies.[63,64]

In this work, 1,4-bisamides with rigid core moiety were used to self-assemble nanosheets. These experiments were performed without use of any surfactants to avoid coverage of obtained nanosheets with these surfactants. As an alternative to self-assembly, the production of bisamide nanosheets via top-down approaches was also performed and evaluated. To learn about the influence of the molecular structure on the morphology of self-assembled structures, 1,4-bisamides with symmetric and asymmetric substitution were synthesized. Here, substituents with big differences in their chemical nature, i.e. fluorocarbons and hydrocarbons, were applied. Crystal structures of all utilized 1,4-bisamides allowed comparison of their packing patterns in the solid state.

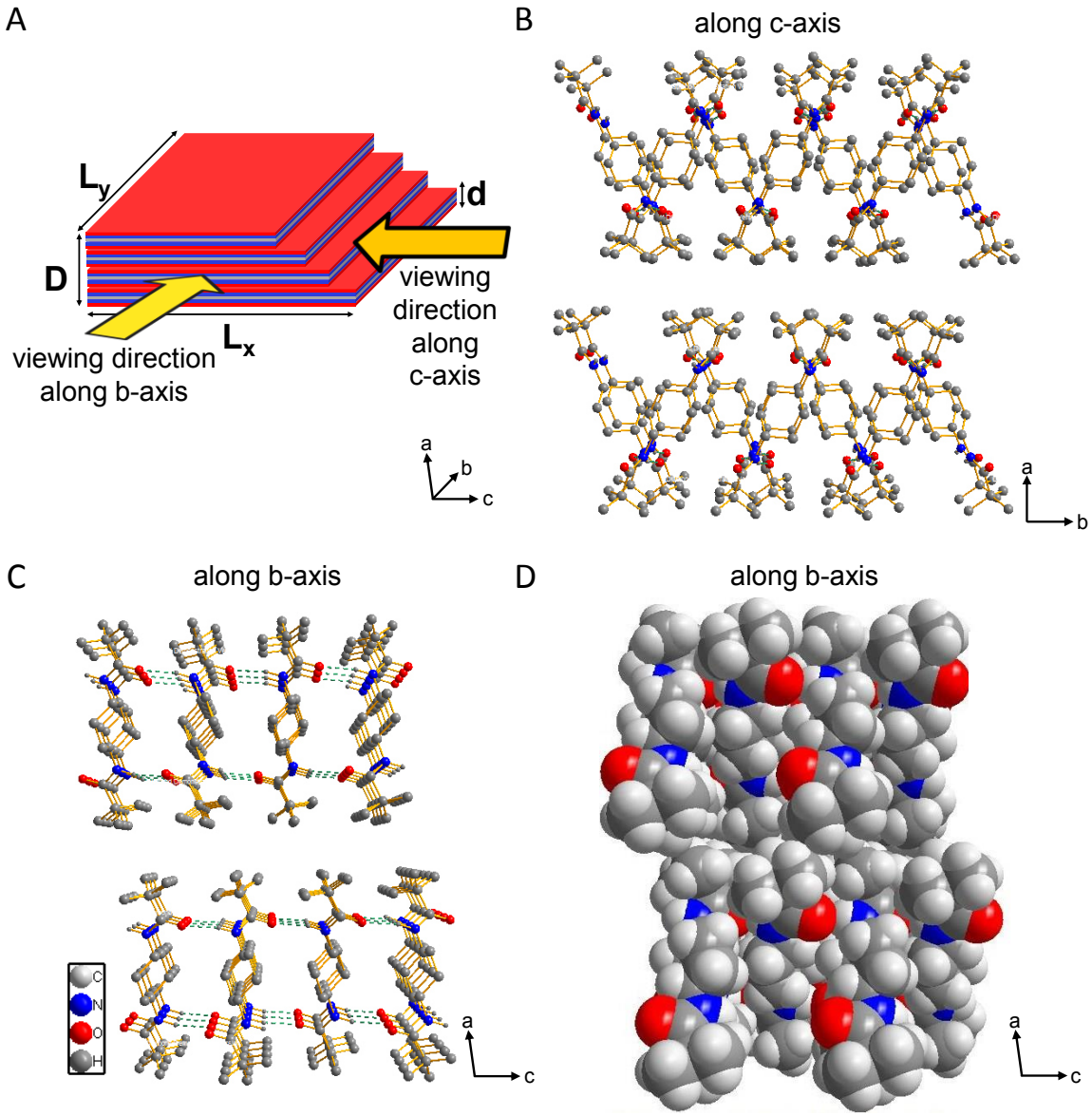

Figure 17: Crystal packing of compound 1. A: Model of a platelet made up from several layers. The arrows indicate viewing directions along b- and c-axis shown in B, C and D. Corresponding side views on the crystal packing along the c-axis (B) and the b-axis (C, D) are provided. In B and C, two layers are displayed as ball-and-stick models with H-atoms not involved in hydrogen bonds omitted for clarity. D: The space filling model along the b-axis shows the dense packing of the layers and illustrates the alternating tilting direction of the molecules, i.e. molecules' tops slightly direct either away from or towards the viewer. *Own representation based on published data (Schmidt et al. 2013).*[63]

3.2. Concept and selection of bisamides

One major aim of this chapter is thickness reduction of self-assembled 2D-objects (also called platelets) by molecular design of the applied bisamides. In this context, two design approaches were pursued. The intended mechanism for thickness reduction by these modifications is strongly connected with the molecular packing in the solid and therefore is discussed alongside with it below. On the one hand, fluorine-containing groups were introduced. These groups were chosen, because it is well-known, that fluorocarbons feature weaker interactions and are more easily sheared compared to hydrocarbons.[90,91] On the other hand, asymmetric substitution of bisamides was applied. Here, a shift to benzene-based bisamide was made to grant easier access to asymmetrically substituted bisamides:
The latter can be obtained in a facile synthesis via three-steps. (I) Attaching one peripheral substituent to 4-nitroaniline, (II) subsequent reduction of the nitro-group and, finally, (III) reaction with the second substituent in the form if an organic acid. As a consequence of these deliberations, a set of seven benzene-based bisamides, as shown in Figure 18, was used. The three compounds of series 3 are expected to yield thinnest platelets, as both approaches to thinner platelets were applied to them, i.e. fluorocarbon groups and asymmetric substitution. To distinct between the effects of fluorocarbons and asymmetric substitution, the molecules of series 4, which are symmetrically substituted by two perfluoroalkyl chains each, were designed. In series 3 and 4, the length of perfluorocarbon chains was varied to be able to detect possible additional effects arising therefrom. Finally, reference compound 2, symmetrically substituted with *tert*-butyl groups, is intended to link series 3 and 4 to compound 1, discussed above, and to shed light on the influence of the fluorocarbon chains.

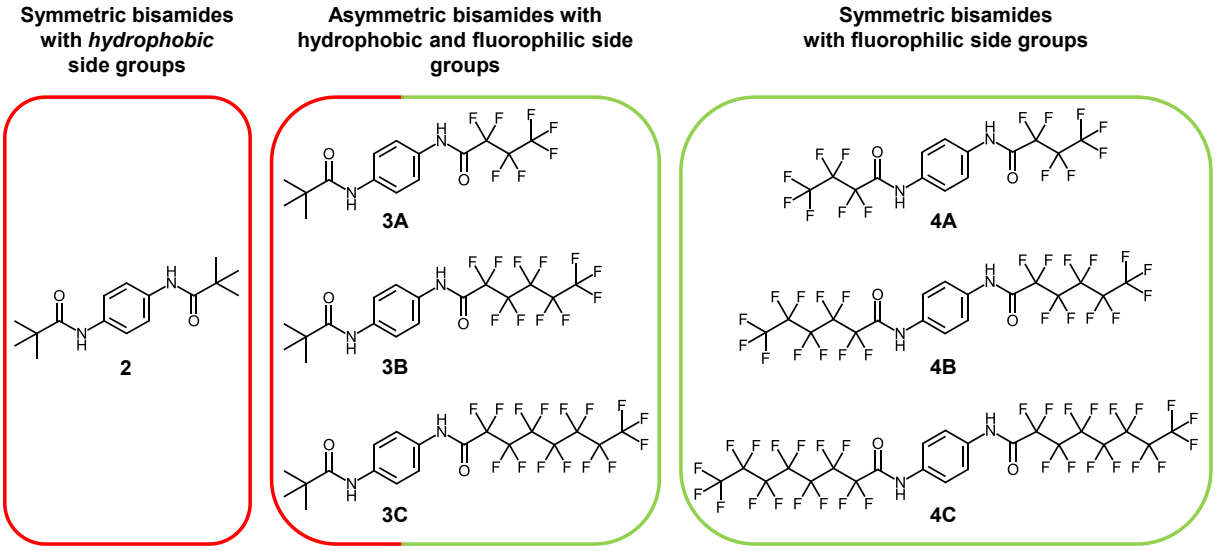

Figure 18: Molecular structures of investigated symmetric and asymmetric 1,4-benzene bisamides with different hydrophobic and fluorophilic side groups.

The factor mediating between molecular structure and platelet shape is crystal packing. Hence, the correlation between molecular structure and crystal packing of 1,4-bisamides is another major question addressed in this chapter. Compound 1 demonstrates a sheet-like packing according to its crystal structure reported in literature.[63] From its packing pattern, four models, as shown in Figure 19, can be derived. As bisamide 2 is only distinct from 1 by its aromatic core, it is supposed to from platelets with a packing pattern similar to that of 1. Here, the *tert*-butyl groups are expected to be exposed to the platelets top and bottom surfaces (Figure 19A). Consequently, a comparable pattern is expected for series 4, resulting in fluorocarbon surfaces (Figure 19D). For series 3, two different packing patterns are possible. On the one hand, all molecules in a layer may assemble with their fluorocarbon substituents pointing to one side of the layer, avoiding energetically unfavorable hydrocarbon/fluorocarbon interfaces. This ultimately would result in every layer to feature one fluorocarbon and one hydrocarbon surface. The additional layers then would stack in such a way, that only surfaces with the same surface chemistry are in contact (Figure 19B). On the other hand, substituents made up of *tert*-butyl groups and those with linear fluorine-containing groups may form alternating rows to counterbalance the higher spatial demands of the bulky *tert*-butyl groups. This then will lead to layers featuring surfaces with mixed contributions of hydrocarbon and fluorocarbon rows (Figure 19C). For these two possible patterns, slowed thickness growth of the platelets is expected: If a new layer is formed during self-assembly, this has to start with a nucleus on the surface of the existing platelet.

Since the interaction of surfaces built of fluorinated substituents is weak[91], nuclei are supposed to form slower, resulting in remarkably retarded thickness growth. At the same time, following the concept, growth of individual layers will not be slowed down significantly. As a result, thinner platelets with higher aspect ratio are expected to form by self-assembly of molecules from series 3. To test this hypothesis, the symmetric reference compounds are investigated parallel to the asymmetrically substituted ones.

To the best of my knowledge, all compounds of series 3 are new, i.e. not reported in literature yet, although a crystal structure solution has been reported for 2.[64] 4B is also new, while 4A and 4C are known in literature, yet not in the context of self-assembly or crystal structure.[92,93,94,95]

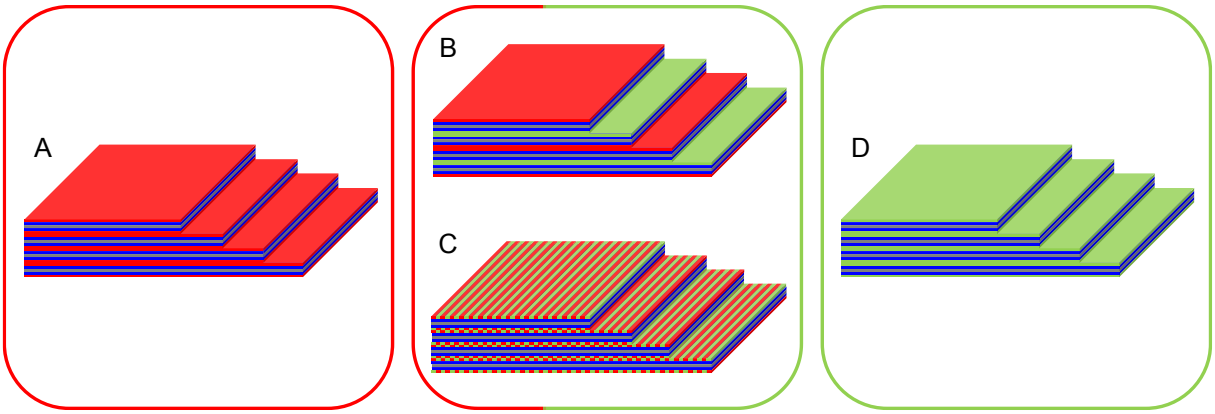

Figure 19: Possible sheet structures of symmetric (A, D) and asymmetric (B, C) bisamides. Red and green planes and stripes represent areas made up of *tert*-butyl-substituents or fluorocarbon substituents.

Besides molecular structure and crystal packing, self-assembly conditions are another important factor guiding the platelets' shape. Thus, the third major topic in this chapter is reducing the thickness of 1,4-bisamide based platelets by adjusting self-assembly conditions The main process selected for this purpose is self-assembly upon cooling. For this investigation, bisamide 1, which is shown in Figure 16, was applied. This is due to bisamide 1, a 1,4-*trans*-cyclohexane bisamide with *tert*-butyl-substituents, being known to easily form platelets via self-assembly. In addition, its crystal structure has already been solved.[63] Moreover, it can be synthesized in amounts sufficient for comprehensive testing and evaluation of various self-assembly conditions.

3.3. Synthesis and thermal properties of bisamides

The synthesis of all bisamides described here was done by the technicians Jutta Failner and Sandra Ganzleben under my supervision. A detailed synthesis protocol for each compound is provided in the experimental section. They also performed basic analytic procedures like ^{1}H-NMR and TGA for each compound under my supervision. Analysis and interpretation of the corresponding data was carried out by me.

For the symmetrically substituted benzene bisamides 2, 4A, 4B and 4C, a facile one-step synthesis was selected, as it is shown schematically in Figure 20. 1,4-phenylenediamine was reacted with the respective acid chloride in THF as solvent. To remove HCl formed during the reaction, an acid scavenger like triethylamine or pyridine was added. This synthesis is similar to the one of the 1,4-*trans*-cyclohexane bisamide 1, which has been reported in literature.[63]

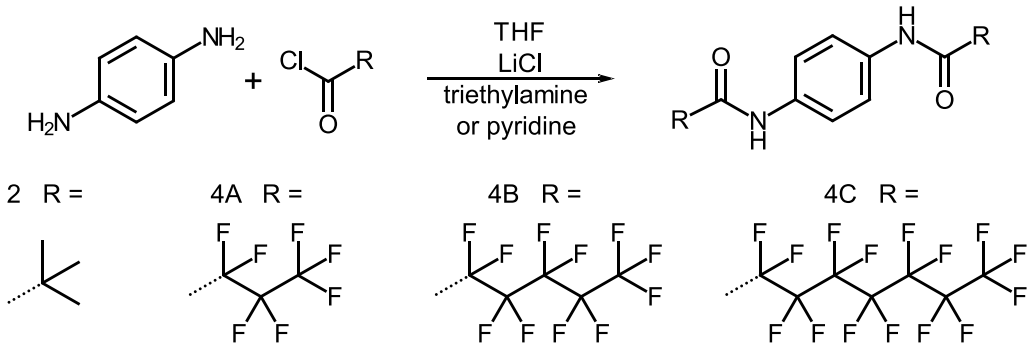

Figure 20: Schematic synthesis of the symmetrically substituted benzene bisamides 2 and 4A - C

To successfully synthesize the asymmetrically substituted bisamides 3A, 3B and 3C, three steps were necessary, as shown in Figure 21. In the first step, the *tert*-butyl-substituent was attached to a 4-nitroaniline core. Next, the nitro-group was reduced with H_2 using palladium on activated charcoal as catalyst to obtain the corresponding amine group. In the third step, the respective fluorocarbon acid chloride was reacted with this amine group to finally obtain the asymmetric bisamides.

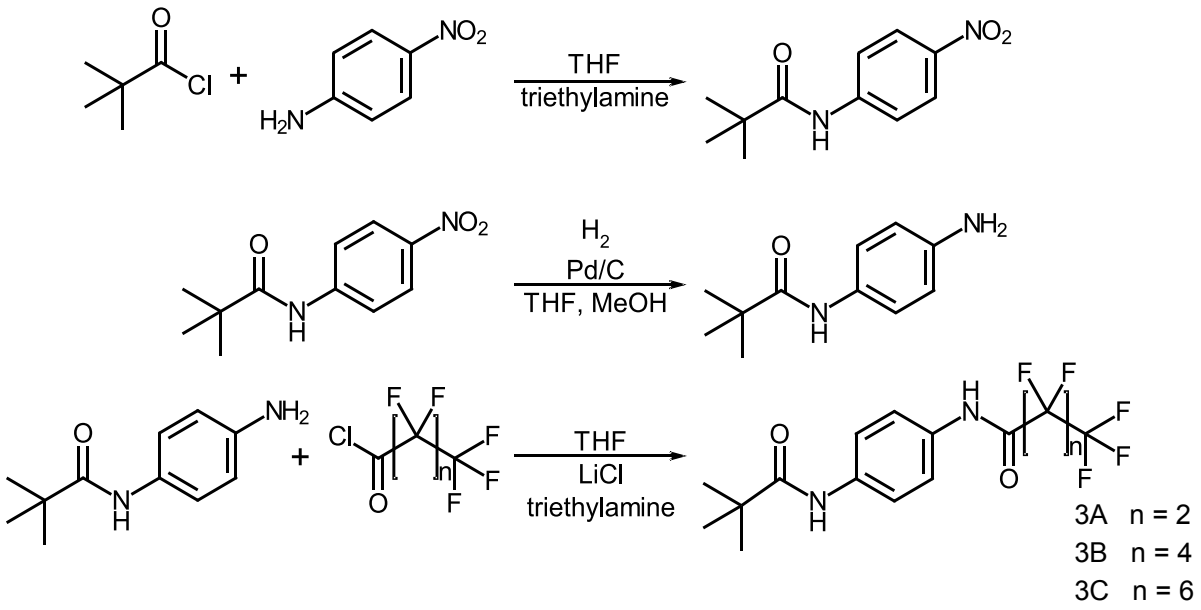

Figure 21: Schematic synthesis of asymmetrically substituted bisamides 3A - C.

After synthesis, all bisamides were purified by crystallization from methanol, ethylacetate or THF. All bisamides were obtained as crystalline white solids in good yields, which are listed in Table 1.

Table 1: Yields of 1,4-benzene bisamides after crystallization. For asymmetric bisamides, the relative yield takes only the last step of the synthesis into account.

compound	2	3A	3B	3C	4A	4B	4C
rel. yield [%]	77	64	20	84	94	43	81

Molecular characterization and purity of all synthesized bisamides was determined by NMR and mass spectroscopy. The respective data for each compound are given in the experimental section.

The thermal behavior of the synthesized 1,4-benzene bisamides was evaluated by means of TGA and DSC. This is important, as in this work self-assembly is mostly done upon cooling of hot bisamide solutions in this thesis. The thermal characterization is necessary to ensure the stability of the bisamides under these conditions, e.g. at 120 °C when using *o*-DCB as solvent. TGA curves of all applied bisamides are displayed in Figure 22. The TGA curve of the reference bisamide 1 is given in the experimental section. Apparently, all investigated bisamides are thermally stable up to at least around 210 °C. All of them show a one-step

mass loss from 100% to 0%, which is indicative for an evaporation of the compounds rather than a decomposition process. The curves of 2 and 4A feature very little kinks around 90% mass. Therefore, the temperature at 5% mass loss is applied as TGA temperature. These temperatures are provided in Table 2. The TGA of bisamide 1 reveals a one-step mass loss during heating with 10 K/min under N_2. A weight loss of 5% is reached at 267 °C. The benzene bisamide 2, which comprises no fluorine, is the most stable material with 5% mass loss at 295 °C. All three compounds of series 3 show a mass loss of 5% at the same temperature, namely at 221 °C.

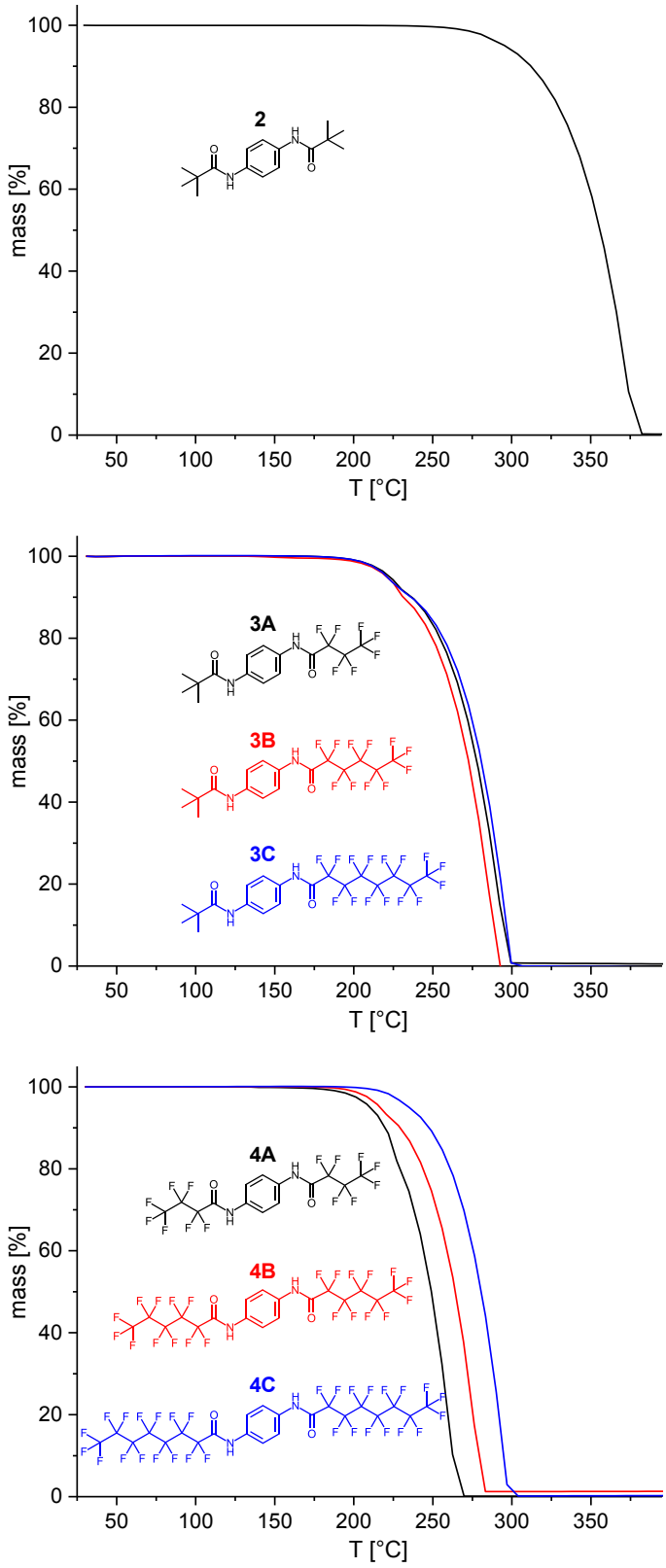

Figure 22: TGA curves of all seven investigated 1,4-benzene bisamides. Measurements were performed with a heating rate of 10 K/min under N_2.

For later self-assembly experiments it is also important to know about the phase behavior, especially melting and crystallization temperatures, because melting during self-assembly

experiments may result in a system with two liquid phases. In such systems, assembly may occur in a phase with larger bisamide content, which is detrimental to a proper self-assembly investigation. Thus, the thermal transitions of the compounds were measured via DSC. The results are shown in Figure 23 alongside with those of the reference bisamide 1.

The fluorine-free bisamides 1 and 2 melt above 270 °C. By contrast, all six fluorine containing bisamides melt between 200 and 250 °C. Upon cooling, 2 crystalizes at 265 °C, which is at a much higher temperature than all other bisamides investigated. Notably, bisamide 1, which features the same substituents, shows no sharp crystallization peak. Here, crystallization occurs in a broad range around 160 °C, which is scarcely visible in the cooling curve. All bisamides of series 3 and 4 crystallize between 190 and 220 °C.

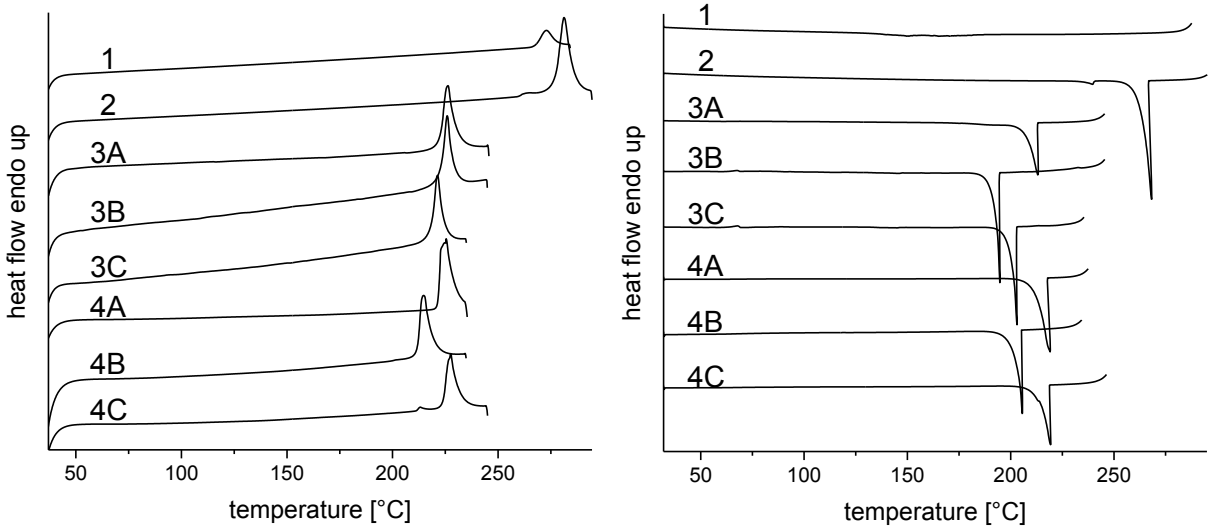

Figure 23: DSC second heating (left) and cooling (right) curves of all seven investigated benzene bisamides. Measurements were performed with a heating/cooling rate of 10 K/min in a sealed high-pressure pan.

For comparison, Table 2 lists melting and crystallization temperatures of the compounds. The discrepancy between the decomposition temperatures of the TGA and the melting temperatures of the DSC T_m can be explained by the different procedures of the two methods. In particular, the DSC measurements were performed in a high-pressure pan, preventing the compounds from evaporation as it takes places in the TGA, where additionally a significant nitrogen flow of 75 mL/min is applied. In the sealed pan applied in DSC, the bisamides of series 3 also melt in a close temperature range from 221 to 226 °C. Nevertheless, their crystallization temperatures T_C range from 194 to 213 °C with 3A

crystallizing at the highest and 3B at the lowest temperature. So, in this series, no trend of T_C with increasing fluorocarbon chain length is apparent. In series 4, temperature at 5% mass loss increases with the length of the substituent from 212 °C for 4A to 235 °C for 4C. Contrary to this, T_m and T_C exhibit another pattern: 4B features lowest T_m and T_C, while 4A and 4C melt and crystallize roughly at the same temperature. Most interestingly, this pattern with the compound bearing a fluorinated C_5-chain providing lowest T_C of the series is the same as in series 3. Yet, to prove this rule, investigation of more compounds would be necessary, which is beyond the scope of this work.

Table 2: Thermal properties of all seven 1,4-benzene bisamides investigated. The 1,4-cyclohexane bisamide 1 is listed for comparison. Temperatures at 5% mass loss were taken from TGA measurements under N_2. Peak melting (T_m) and crystallization (T_c) temperatures and melting enthalpy (ΔH_m) were measured by DSC in a sealed pan. T_m and ΔH_m were determined during second heating and T_c was measured during first heating. Heating and cooling rate was 10 K/min for all measurements.

Compound	M [g/mol]	$T_{5\%\ mass\ loss}$ [°C]	T_m [°C]	ΔH_m [kJ/mol]	T_c [°C]
1	282	267	272	6.4	~ 160
2	276	295	281	32.5	265
3A	388	221	226	3.8	213
3B	488	221	226	9.8	194
3C	588	221	221	11.0	203
4A	500	212	225	38.9	219
4B	700	216	215	58.7	206
4C	900	235	228	61.6	219

To sum up the results from thermal characterization, all eight investigated bisamides are thermally stable beyond 200 °C and do not melt upon heating in this range. Therefore, they all appear suitable for self-assembly upon cooling from hot solutions, at least, as long as the temperature of the hot solution does not exceed 200 °C.

The thermal characterization of each individual compound is also provided in the compound data sheets in the experimental part.

3.4. Crystal structure elucidation of 1,4-bisamides

The knowledge of the arrangement of the bisamides are in the solid state is of vital importance, as it may influence the morphology of nanoobjects on the mesoscale formed by self-assembly. All crystal structures discussed here are based on powder or single crystal X-ray diffraction experiments. The crystal structure solutions of 1,4-benzene bisamides along with the respective diffraction experiments were done by Kasper van der Zwan at the department of Inorganic Chemistry III of the University of Bayreuth. The images displaying the crystal packing were made by me using the program Diamond 3.0 by Crystal Impact.

To draw conclusions about bisamides with a still unclear crystal structure, solid state NMR experiments were also done by Kasper van der Zwan. The results are provided in the experimental section.

Moreover, a summary of the investigated bisamides' most important crystallographic data is also given in Table 14 in the experimental section.

3.4.1. Symmetrically substituted 1,4-bisamides with tert-butyl-substituents

The crystal structure of bisamide 1 has already been determined by combination of powder X-ray diffraction and NMR crystallographic methods. Figure 17 (see section 3.1) shows its packing pattern from several perspectives, based on the published data.[63]

The crystal structure of compound 2 has already been reported in literature by Guo *et al.*.[64] This crystal structure solution was reproduced using powder X-ray diffraction. A monoclinic crystal system with space group P21/c was found. The packing of 2 in the crystal is illustrated in Figure 24. This crystal packing of 2 is similar to the one of compound 1 presented above, which may be attributed to the small difference between both molecules' structure.

Figure 24B gives a schematic representation of the layered structure of 2. The platelet thickness D and layer thickness d, which will be important later on, are appointed. As it is visible from Figure 24C, the crystal is made up of molecules, which are tilted relative to each other along the b-axis. Viewing along the b-axis (Figure 24B), chains of H-bonds along the c-axis become visible. By this H-bond pattern, each molecule is connected to four others. Since these four are tilted in the other direction than the initial one, the structure is simultaneously built up in two directions by the H-bonds. In the third dimension, only Van

der Waals interactions connect the formed layers. The resulting structure is schematically depicted by a stack of thin layers (B), where (C) and (D) then represent side views on the stacking from two directions. The resulting platelet features two hydrocarbon surfaces, as proposed before. Following the top layer in Figure 24D from left to right, the first molecule's top end points away from the viewer, while the one of the second molecule points towards the viewer. The third one is parallel to the first one; the fourth one is parallel to the second one and so on. This packing pattern results in a solid consisting of layers with a thickness d of 12,25 Å. In the space-filling representation (E) it becomes clear, that the *tert*-butyl-substituents of adjacent layers are densely packed. Additionally, this representation illustrates the molecules' alternating tilt mentioned above.

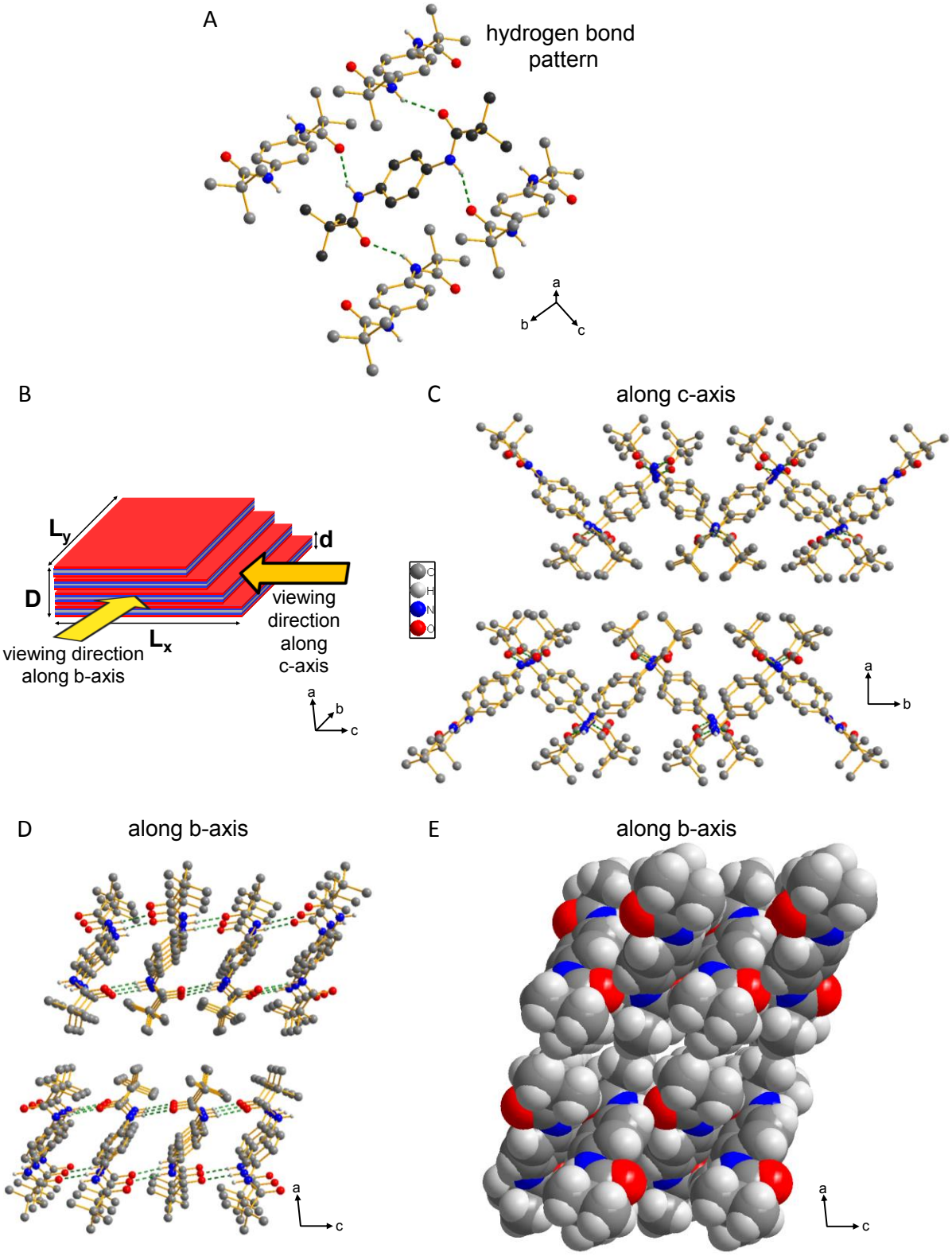

Figure 24: Crystal packing of compound 2. A: Model of a platelet made up from several layers. The arrows indicate viewing directions along b- and c-axis shown in C, D and E. A: Illustration of one molecule with all four adjacent ones, to which it is connected by one hydrogen bond each. Carbon atoms in the central molecule are colored black for clarity. C-E: Side views on the crystal packing along the b-axis (D, E) and the c-axis (C). In C and D, two layers are displayed as ball-and-stick models with H-atoms not involved in hydrogen bonds omitted for clarity. E: The space filling model along the b-axis shows the dense packing of the layers and illustrates the alternating tilting direction of the molecules: Molecules' tops slightly direct either away from the viewer or towards the viewer.

3.4.2. Asymmetrically substituted 1,4-bisamides

To solve the crystal structure of the asymmetric bisamides 3A and 3B single crystals were grown and analyzed via single crystal XRD. For the third asymmetric bisamide 3C, no suitable single crystals could be obtained to date. Hence, PXRD was measured and a structure solution from the resulting powder data was performed. For all three asymmetric bisamides, a monoclinic crystal system with space group P21 was determined.

As a representative example for these asymmetric bisamides, the crystal structure of 3A is presented in Figure 25. Here, the arrangement of the molecules and the hydrogen bond pattern are similar to the ones of 1 and 2 discussed above. Again, rows of parallel molecules diagonal to the layer's lateral extension are formed, which stack to layers with parallel rows via H-bonds. The striking difference to the aforementioned structures is due to the asymmetric substitution of 3A: Within one row, all the molecules' fluorocarbon groups point into the same direction, i.e. up or down. In the two neighboring rows, they are orientated in the opposite way. If, for example, when viewing along the a-axis (Figure 25C), all fluorocarbon substituents in the first row point to the bottom right, then, in the second row, they point to the top right. In row three, the structure of row one is repeated and so on. As a result, each layer's surface is made up from alternating rows with hydrocarbon or fluorocarbon character, as Figure 25B schematically shows. Since the hydrocarbon rows are formed by *tert*-butyl groups, which are shorter than *n*-undecafluoropentyl groups, these rows' level is deeper than the level of the fluorocarbon rows, causing a corrugated surface pattern of each layer. In the platelet, neighboring layers assemble in such a way, that each fluorocarbon row of one layer is covered by a hydrocarbon row of the other layer and vice versa. This ensures close packing in the solid state. Nevertheless, as *n*-undecafluoropentyl groups are sterically less demanding than *tert*-butyl groups, still very small voids exist between two layers, which can be seen from the space-filling representation in Figure 25E. This ordering into alternating rows may be attributed to the different spatial demands of both substituents: If the more bulky *tert*-butyl groups were on the same side of a platelet and, at the same time, the distance between the cores was kept constant to keep the energetically favorable short H-bonds, a sphere would be the resulting morphology, as it is well-known in micelle formation of surfactants.[96] In such a situation, the molecule can be imagined as a 2D-wedge. When all wedges' tips point in one direction, close packing results in a circle, whereas alternating tip orientation gives a straight line of wedges. So, 3A exhibits

the packing pattern suggested in Figure 19C, whereas the model with layers featuring pure hydrocarbon and fluorocarbon surfaces (Figure 19B) has been refuted. From the packing pattern of 3A thinner platelets should emerge upon self-assembly than from the structure of 2. This expectation is based on the fact that in the structure found all the layer-to-layer contact planes are between hydro- and fluorocarbons, which show weaker interactions than two hydrocarbons.[91]

Structure solution of the remaining two asymmetric bisamides was possible from single crystal diffraction data (3B) or from powder diffraction data (3C). Both data sets show that these two bisamides exhibit the same crystal packing pattern as 3A. Therefore, the hydrogen bonding pattern and schematic representation presented in Figure 25 are also valid for 3B and 3C. The layer thickness d derived from the respective crystal structure was found to be 15.36 Å for 3A, 18.56 Å for 3B and 20.68 Å for 3C.

To provide further evidence of the similarity of crystal packing patterns in series 3, solid state NMR spectroscopy was performed. The results, which are shown in the experimental section, also support results of XRD with respect to the crystal packing of these compounds.

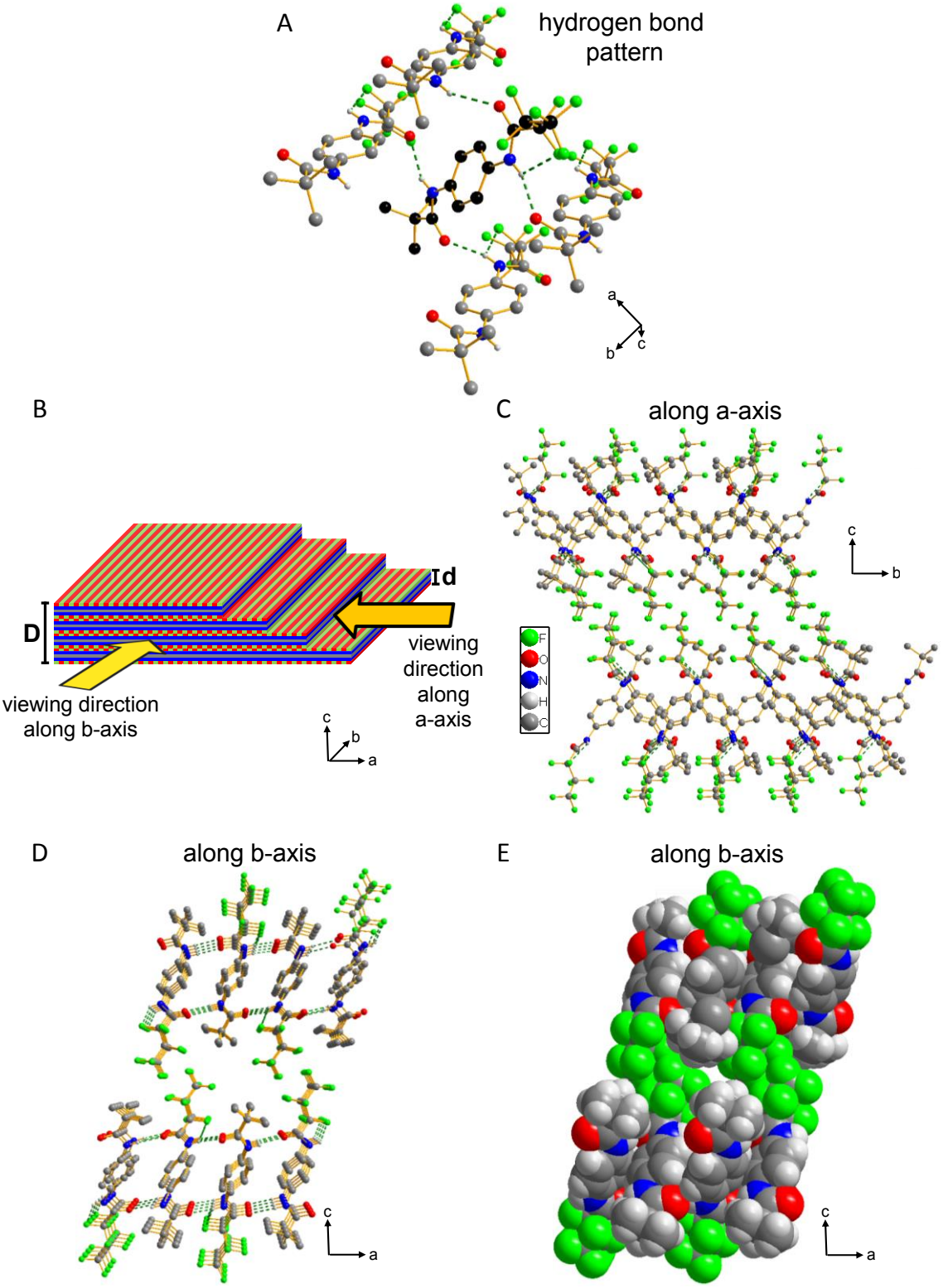

Figure 25: Crystal packing of compound 3A. A: Model of a platelet made up from several layers. The arrows indicate viewing directions along a- and b-axis shown in C, D and E. B: Illustration of one molecule with all four adjacent ones, to which it is connected by one hydrogen bond each. Carbon atoms in the central molecule are colored black for clarity. Side views on the crystal packing along the b-axis (C) and the a-axis (D and E) are provided. In C and D, two layers are displayed as ball-and-stick models with H-atoms not involved in hydrogen bonds omitted for clarity. E: The space filling model along the a-axis shows that small voids exist between the *tert*-butyl-groups of neighboring layers and illustrates the alternating tilting direction of the molecules, i.e. molecules' tops slightly direct either away from or towards the viewer.

3.4.3. Symmetrically substituted 1,4-bisamides with fluorocarbon substituents

For the crystal structure solution of 4A, single crystals were grown and analyzed via single crystal XRD. However, no suitable single crystals could be obtained for both other bisamides symmetrically substituted with fluorocarbon substituents. Hence, PXRD was measured and evaluated. For 4B, the structure was successfully solved this way, whereas for 4C only cell parameters could be determined via PXRD until now.

As an example for these symmetric bisamides with fluorocarbon substituents, the crystal structure of 3A is presented in Figure 26. This crystal packing of 4A significantly differs from the other packing patterns: Viewing along the a-axis, i.e. along the hydrogen bonds, all molecules in the crystal are oriented parallel to each other. Each row made up from these parallel molecules is connected by two antiparallel hydrogen bond strands. The space-filling model in Figure 26E demonstrates that no voids of significant size exist between the individual layers in this structure. All in all, the structure found for 4A follows the scheme initially expected for this compound. Yet, in this structure, molecules are only connected by hydrogen bonds in one direction (along the a-axis) within each layer. Perpendicular to that (along the b-axis), only van der Waals interactions are present. In consequence, the layers are bound more stable in one direction than in the other. This finding also implies different growth rates along the lateral extensions of the platelets, with much faster growth along the hydrogen bonds due to stronger binding in that direction, which should result in elongated platelets.

Considering all crystal structures shown, it appears that the bulky *tert*-butyl group directs assembly of bisamides into a structure with crossed molecules as found for 1, 2 and 3A to 3C. If no bulky substituents are present, as for 4A, a parallel assembly of all molecules occurs, as seen in Figure 26.

The general packing pattern motif of 4A has also been found for 4B. Both compounds crystalize in a triclinic crystal system with space group $P\bar{1}$. The layer thickness d is 16.02 Å for 4A and 21.10 Å for 4B. A transfer of these results to the third bisamide in series 4, 4C, cannot easily be made, because no full crystal structure solution was possible for that compound yet. Nevertheless, the indication of a unit cell was successful, indicating a monoclinic crystal system with space group P2.

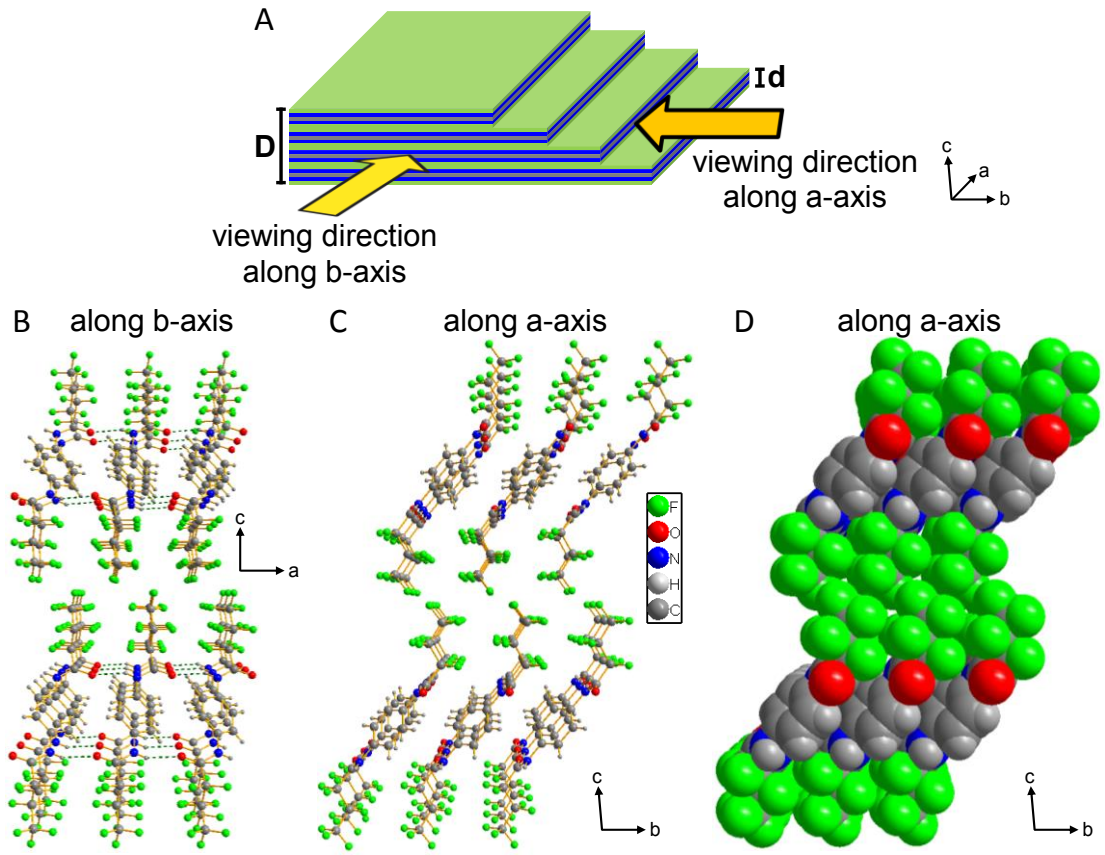

Figure 26: Crystal packing of compound 4A. A: Model of a platelet made up from several layers. The arrows indicate viewing directions along a- and b-axis shown in B, C and D. Side views on the crystal packing along the a-axis (C, D) and the b-axis (B) are provided. In B and C, two layers are displayed as ball-and-stick models with H-atoms not involved in hydrogen bonds omitted for clarity. D: The space filling model along the a-axis shows the dense packing of the layers.

As described before, NMR crystallography was also applied to the symmetric 1,4-benzene bisamides 4A – C supporting the results of the XRD evaluation (see experimental section). By contrast, the crystal structure of 4C, which has not been solved yet, appears to be distinct, as it features two different positions for the molecules in the solid-state NMR measurements.

The finding of the packing of 4C to be distinct also reflects in the cell parameters presented in Table 14 in the experimental section (6.5.): For 4C, the length of the a-axis is approximately doubled, compared to 4A and 4B. This is attributed to two molecules being included in one cell of 4C along this axis instead of one, as for 4A and 4B. By contrast, the length of the second short axis, which is the b-axis for 4A and 4B and the c-axis for 4C, is comparable. The third axis performs a noteworthy length growth from around 16.1 nm for 4A to around 21.2 nm for 4B and to around 27.0 nm for 4C. This correlates very well with the increase in chain length between these molecules when assuming all-*trans* configurations for the stiff

fluorocarbon chains. Thus, it points to a similar orientation of all three compounds in their unit cells. Based on these findings, it is concluded that all three molecules pack in an overall similar way, though 4C shows some differences compared to the others, as discussed above. As the precise orientation of the molecules is unknown, no value for d can be derived for 4C.

Another method to gain insight into the solid-state structure of bisamides is infrared (IR) spectroscopy, as it provides information about hydrogen bonds, which are the main force for the assembly of bisamides in the solid state. In this context, absorption bands of the amide groups are of interest, in particular the N-H stretching vibration around 3300 cm^{-1} and the C=O stretching vibration in the area between 1700 and 1650 cm^{-1} (Amide I).[97] The strength of the hydrogen bond can be deduced from the N-H stretching vibration band, as it has been shown for 1,3,5-benzene trisamides[98]: Stronger hydrogen bonds weaken the N-H bond. This weaker covalent bond features lower activation energy and hence the associated band is shifted to lower wavenumbers.[98]

FTIR spectra of all seven 1,4-benzene bisamides were recorded and are presented in Figure 27. Bisamide 2 exhibits a N-H stretching vibration band at 3295 cm^{-1}, which is the lowest wavenumber of all seven compounds and, therefore, 2 is concluded to show the strongest hydrogen bonds. All molecules of series 3 provide a vibration band at 3365 cm^{-1}. This high wavenumber indicates that hydrogen bonds are relatively weak in solids of these compounds. Compounds of series 4 show bands at different wavenumbers, i.e. at 3305 cm^{-1} for 4A, at 3313 cm^{-1} for 4B and at 3317 cm^{-1} for 4C. Hence, it is concluded, that the hydrogen bond is slightly weakened with increasing length of the fluorocarbon chain within this series. Nevertheless, the strength of hydrogen bonding of series 4 still is between the ones of compound 2 and series 3. The weaker hydrogen bonding observed in the IR spectra of series 3 is in accordance with the behavior in solubility tests, where compounds of series 3 are dissolved more easily than the other bisamides. A remarkable finding of the FTIR spectra is, that molecules of the asymmetric series 3 just seem to form only hydrogen bonds with a similar energetic level in the solid state, as indicated by the single N-H stretching vibration. This matches the solid state structure of series 3 (illustrated in Figure 25 at the example of 3A) very well, where only H-bonds between substituents of different nature are formed. In the hypothetic case of asymmetric bisamides forming layers with all fluorocarbon substituents pointing to one side and all *tert*-butyl-substituents pointing to the other side (Figure 19B), two different N-H stretching vibrations would be expected: One for hydrogen

bonds between fluorocarbon substituents and another one for those between *tert*-butyl-substituents. Thus, the finding of just one kind of hydrogen bonds for asymmetric bisamides in IR supports the crystal structures found and leads to the rejection of the suggested packing pattern with pure fluorocarbon and pure *tert*-butyl surfaces (Figure 19C).

The position of the C=O stretching vibration bands reflects the chemical nature of the respective substituent, which is in direct vicinity to the amide C=O group. For bisamide 2, this band is located at 1650 cm^{-1}, which is the lowest value of all seven compounds. The three compounds of series 4, which also are symmetrically substituted, provide one band at 1695 cm^{-1}. As expected, all compounds of series 3, which bear two different substituents, accordingly feature two bands at 1700 and 1665 cm^{-1}. The one with lower wavenumber is roughly at the position found for bisamide 2 and therefore is attributed to the *tert*-butyl substituted C=O groups. The C=O stretching vibrations of series 3 at higher wavenumbers are at the same position as the ones of series 4 and hence are attributed to the C=O groups with fluorocarbon substituents.

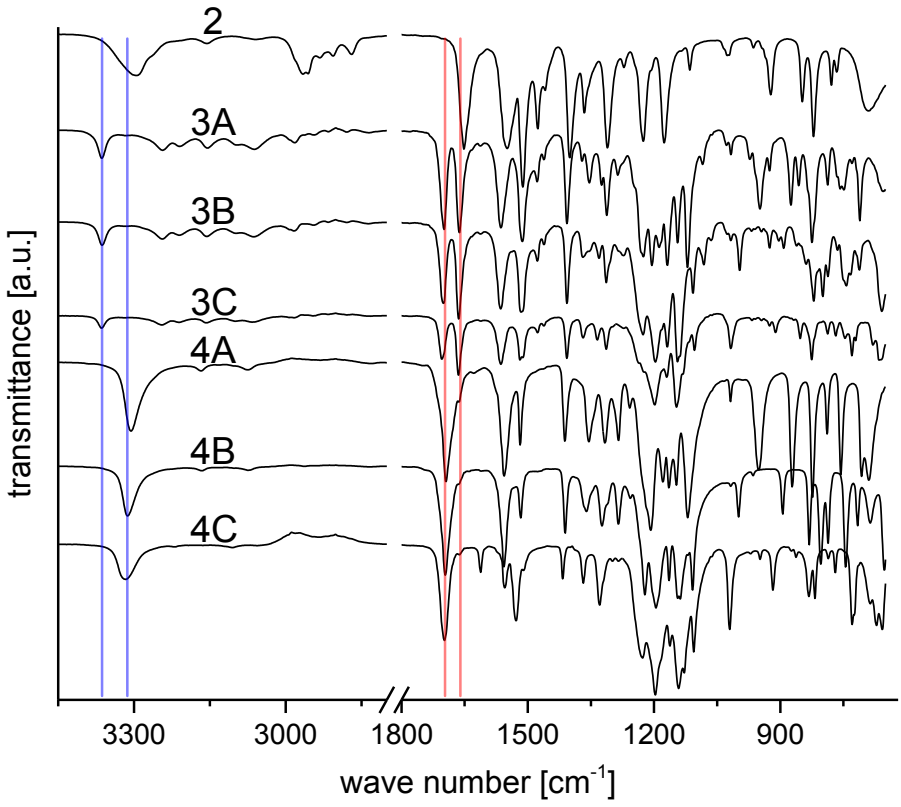

Figure 27: FTIR spectra of all seven investigated benzene bisamides in the solid state. For orientation, guiding lines mark N-H (blue) and C=O (red; Amide I) stretching vibration bands of fluorine containing bisamides.

3.5. Self-assembly to 2D-nanoobjects

3.5.1. Procedures for self-assembly at the example of a cyclohexane bisamide.

The bisamide platelets known up to now, which were e.g. used for crystal structure analysis, feature thicknesses d in the range of hundreds of nanometers. The aim of this section is to demonstrate the ability of bisamide compounds to form supramolecular nano-structures featuring thicknesses below 100 nm. Therefore, suitable preparation routes have to be developed and evaluated. In preliminary experiments, grinding with mortar and pestle and ultrasonic treatment were tested as top-down approaches. Both methods did not yield well-defined supramolecular nano-platelets. Hence, bottom-up approaches based on self-assembly are exclusively applied here. In this context, the influence of processing conditions was investigated to gain a deeper understanding of the nano-platelet formation and to be able to control the dimensions of the formed nanoobjects. The *trans*-1,4-cyclohexane bisamide 1 was chosen as model compound for these experiments, since it was already known to form stable 2D-objects.[63]

To initiate self-assembly of bisamide 1 from solution, there are different triggers such as increasing the concentration by evaporation of solvent, addition of a non-solvent to the solution, and decreasing the solution's temperature. In the following, self-assembly is predominantly done by cooling hot bisamide solutions, since this method is highly reproducible. As a second method, addition of non-solvent was used. By contrast, self-assembly upon solvent evaporation requires precise control over several parameters governing the evaporation rate during the whole experiment, which is hard to achieve. In addition, solvent evaporation occurs exclusively at the liquid's surface, adding additional surface phenomena to the self-assembly process. Consequently, this method was not applied in this work to have self-assembly influenced by as few factors as possible and to achieve the highest possible reproducibility.

The surface energy difference between material and medium is the most important factor, when trying to produce thin platelets. To find good solvents for the self-assembly into thin platelets, surface energies of the bisamides must be known. The surface energy of many media is reported in literature, yet for most solids like e.g. bisamide 1 it has to be determined. A common method to achieve this is contact angle measurement with different media on the surface of the solid sample. As single platelets of 1 are by far too small for this method, tablets of 1 with a diameter of 12 mm were pressed. Due to the fact, that the top

area of platelets is much bigger than the side ones, it is assumed, that the tablet's surface is dominated by such top areas. Therefore, surface energies determined on top of the tablets are assumed comparable to the ones of the top surface of bisamide stacks.

Contact angle measurements using only one test liquid are often uncertain. Hence, the method following Owens, Wendt, Rabel und Kaelble (OWRK-method), which uses contact angles of several liquids, is applied to calculate the surface energy here. The OWRK-method uses the total surface tension of each test liquid σ_L alongside with its both components, i.e. polar and disperse contributions σ_L^P and σ_L^D to calculate the polar and the disperse contribution to the sample's surface energy, σ_S^P and σ_S^D, from the measured contact angle Θ for each liquid. These variables are brought in the form of a linear equation, as equation 2 shows.[99]

$$\underbrace{\frac{\sigma_L(1+\cos\,\theta)}{2\sqrt{\sigma_L^d}}}_{y} = \underbrace{\sqrt{\sigma_S^P}}_{m} \cdot \underbrace{\frac{\sqrt{\sigma_L^P}}{\sqrt{\sigma_L^D}}}_{x} + \underbrace{\sqrt{\sigma_S^d}}_{t} \qquad (2)$$

$$y = m \cdot x + t$$

Surface energy contributions for each solvent can be found in literature (see Table 11 in the experimental section) and the determined contact angles are presented on the left side of Figure 28. Plotting these data in the form indicated by equation 2, a straight line can be fitted to the data, as shown on the right side of Figure 28. Slope *m* and intercept *t* of this line finally yield the polar and the disperse part of the sample's surface energy. For bisamide 1, the polar contribution σ_S^P is 0.5 ± 0.7 mJ/m^2 and the disperse one is 31.3 ± 2.9 mJ/m^2, resulting in a total surface energy of approximately 32 mJ/m^2. The small value of the polar contribution supports the assumption, that the non-polar top and bottom surfaces of the bisamide platelets dominate the surface of the tablet. If the side surfaces of the nanoplatelets were predominant, a bigger polar contribution would be expected due to the amide groups on these surfaces.

Medium	θ [°]
Water	78.9 ± 5.5
Formamide	77.8 ± 1.4
Glycerol	75.7 ± 3.9
Ethylene glycol	69.2 ± 1.8
Diiodo-methane	55.1 ± 1.8
Aniline	51.2 ± 1.3

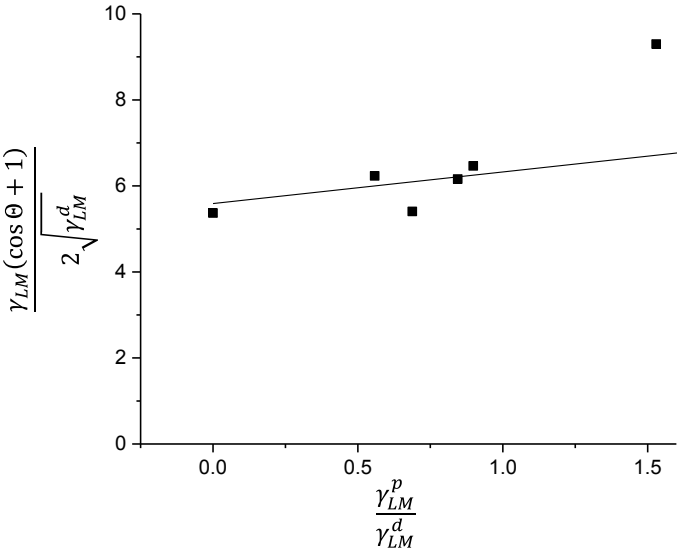

Figure 28: Left: Contact angles *Θ* of bisamide 1 measured by the sessile drop method with six different test liquids. Averages and standard deviations for each test liquid are based on at least five measurements each. Right: OWRK-plot for bisamide 1. Literature values of the liquids are plotted on the x-axis, while the y-axis is determined by liquid literature values as well as by the determined contact angles *Θ*. The solid line represents a linear fit of all six data points.

Generally, the self-assembly process should be exothermic. Therefore, DSC-measurements in solution were performed. Since the soluble amount of bisamide in the solvent is typically low (e.g. 500 ppm), a very small signal is expected, which makes the use of a very sensitive so-called µ-DSC necessary. As solvent, *o*-dichlorobenzene (*o*-DCB), which is the most frequently applied solvent for self-assembly in this chapter, was used. For the measurement, the sample cell was filled with the dispersion at ambient temperature and the reference cell was filled with a comparable amount of pure *o*-DCB. Both cells were heated to 110 °C, shortly kept at this temperature to make sure that the bisamide is completely dissolved and then cooled with cooling rates of 0.1, 0.5 or 1.0 K/min. The cooling curves recorded this way are presented in Figure 29. In all heating curves no dissolution peaks were observed, hence these curves are not shown here. All cooling curves with exception of the second cooling curve at 1 K/min show a weak exothermic peak, which is attributed to self-assembly of the bisamide. In the first cooling curves, the peak is shifted to lower temperatures with increasing cooling temperature. Since supersaturation must occur at the same temperature for the same solution from a thermodynamic point of view, this shift must stem from a kinetic hindrance. This means, that supercooling of the solution is increased at higher cooling rates. So, the cooling rate will most likely influence self-assembly of bisamide 1. On

the contrary, both second cooling curves featuring exothermic signals show their peaks approximately at the same temperature.

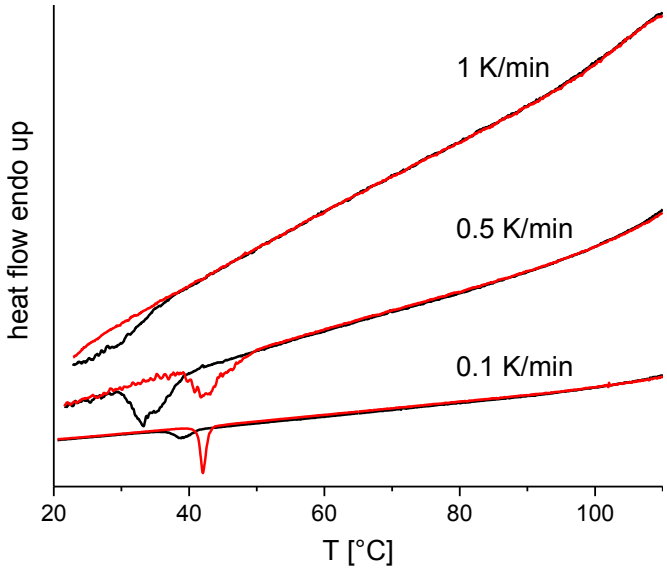

Figure 29: Cooling curves of 500 ppm of compound 1 in *o*-DCB measured via µ-DSC. Measurements were conducted with cooling rates of 1 K/min, 0.5 K/min, 0.1 K/min. Black lines indicate the first cooling, red lines indicate the second cooling of the sample.

In a next step, the influence of various solvents as media on this process was tested. Several solvents were pre-selected for this study with respect to the requirements of self-assembly experiments: The solvent should feature a melting point clearly below ambient temperature, to allow cooling to low temperatures without freezing the solvent. Furthermore, the boiling point must be high enough to allow dissolution of the bisamide at high temperatures. Moreover, the liquid must feature a certain vapor pressure at ambient temperature to enable drying of samples under vacuum. Finally, at high temperatures (below the boiling point), a sufficient amount of bisamide must be soluble. Here, a minimum solubility of 50 ppm was selected. Table 3 lists solvents meeting these requirements alongside with selected properties. Solubility tests were conducted in all of these solvents. Some solvents show a very high solubility of bisamide 1 even at low temperature, which is in the following referred to as residual solubility. This is undesirable, since substance remaining in solution after cooling will self-assemble upon solvent evaporation during later SEM sample preparation, which is be a process different from the desired self-assembly upon cooling. Thus, solvents featuring a high residual solubility like e.g. chloroform were discarded. Hence, six solvents, namely toluene, anisole, *o*-DCB, cyclohexanone, 1,4-dioxane and 1-heptanol, which exhibit

surface energies in the same region as the bisamide (approx. 32 mJ/m^2) were selected. Subsequently, bisamide solutions were prepared in these solvents by heating the dispersions. Details on the preparation of bisamide solutions are given in the experimental section. Self-assembly experiments were performed by cooling the hot solutions to room temperature.

Table 3: Selected properties of solvents applied for self-assembly experiments with compound 1. Values are sorted by increasing surface energy and are determined at 25 °C, if not stated otherwise.[100,101,102]

Medium	Surface energy [mJ/m^2]	Freezing point [°C]	Boiling point [°C]	Viscosity [mPa*s]
Ethanol	22.0	-114.1	78.4	1.074
Butanone	24.0	-86.7	79.9	0.405
1-Pentanol	25.4	-77.6	138.9	3.619
Chloroform	26.7	-63.5	61.3	0.537
THF	26.9	-108.5	65.9	0.456
Toluene	27.9	-95.0	110.6	0.560
Acetonitrile	28.7	-43.8	81.7	0.369
1-Heptanol	32.0	-34.0	174.9	5.810
Chlorobenzene	32.9	-45.2	132.0	0.753
1,4-Dioxane	32.9	11.8	101.2	1.177
Cyclohexanone	34.4	-31.15	154.9	2.017
Anisole	35.0	-4.4	153.6	1.056
Benzyl alcohol	36.8	-15.3	204.9	5.474
***o*-Dichlorbenzene**	38.1	-17.0	180.6	1.324
1,2,4-Trichlorobenzene	40.6	17.0	213.6	2.08 [20 °C]

Figure 30 shows supramolecular structures formed by bisamide 1 upon cooling in the six different solvents. For these experiments, the bisamide concentration was adapted to the solubility in the respective solvent. Bisamide 1 forms platelets in all six solvents. For toluene and anisole, the large platelets formed look quite similar: They measure more than 20 µm across and predominantly exhibit regular, straight edges. Also, *o*-DCB yields single platelets, althought with less regular edges. Upon self-assembly in cyclohexanone, a thin layer rather than distinct platelets is formed. This indicates that assembly may occur during drying of the sample, which means that the residual solubility in this solvent still is too high. In 1,4-dioxane, platelets with wavy edges are formed, which also feature a rough, wavy surface.

The platelets formed in 1-heptanol again feature straight edges, but seem to be quite thick. Besides the defined shape of the platelets, *o*-DCB was chosen for further experiments due to its superior combination of properties, namely low melting point, high boiling point, high bisamide solubility (more than 1000 ppm at 120 °C) and low residual solubility.

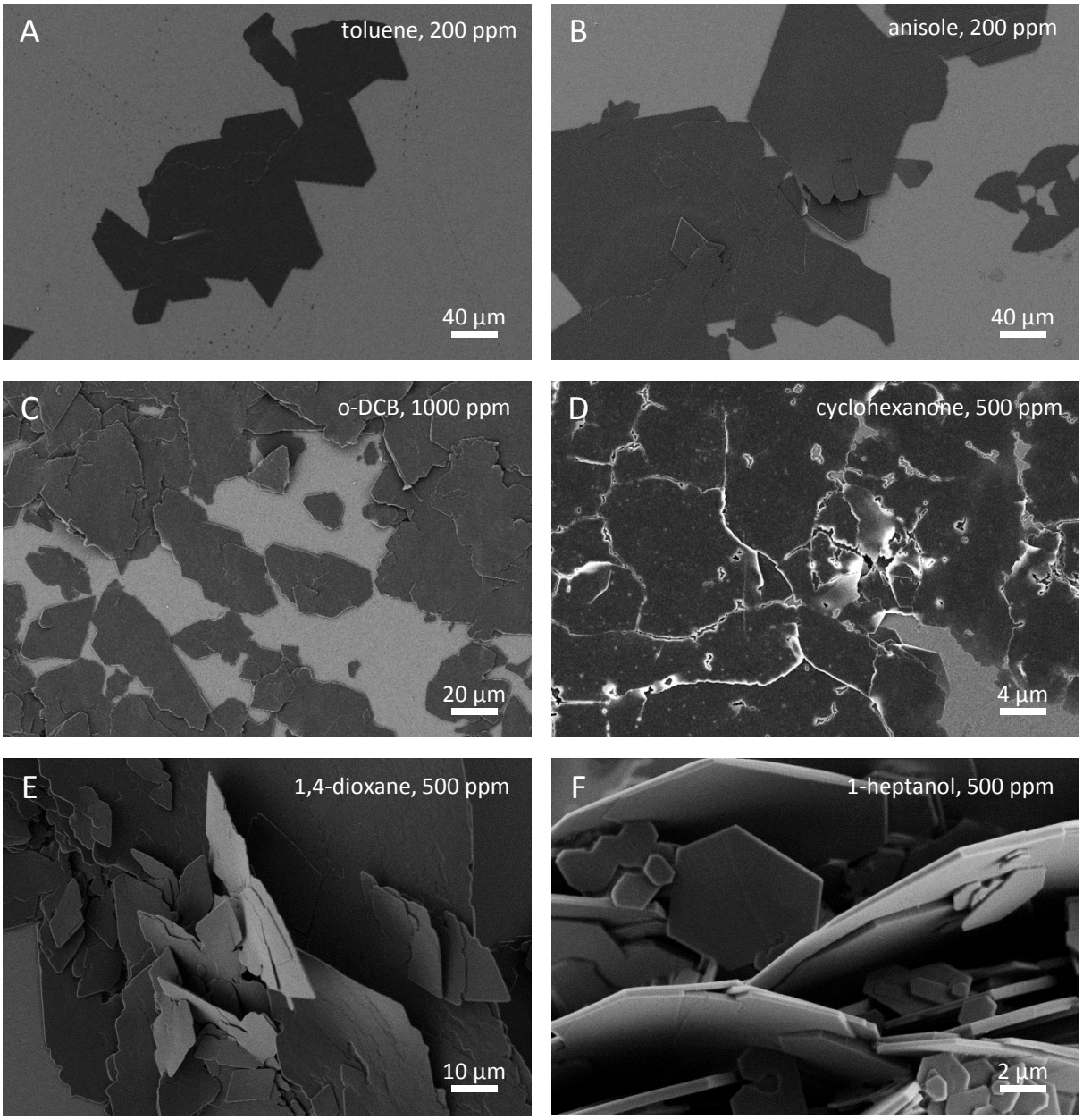

Figure 30: SEM images of structures formed by self-assembly of bisamide 1 in various solvents upon cooling. Concentrations were adapted to the solubility in each hot solvent: A: 200 ppm in toluene, B: 200 ppm in anisole, C: 1000 ppm in *o*-DCB, D: 500 ppm in cyclohexanone, E: 1000 ppm in 1,4-dioxane and F: 500 ppm in 1-heptanol.

The second factor influencing self-assembly is the cooling rate. In general, smaller and thinner platelets are expected at higher cooling rates. In µ-DSC experiments, no cooling rates of more than 1 K/min are possible. Therefore, other setups were used, which allow higher cooling rates and at the same time allow processing of several milliliters of solution in one single experiment. The latter is important, since, due to the low bisamide concentrations used, smaller samples increase the concentration error, when preparing the different solutions. The use of 4 mL-glass vials with screw cap turned out to meet these requirements. For each experiment, 2.5 mL of the respective bisamide dispersion were placed in a vial. The vial was screwed tightly and placed in a heated metal block, which could be moved by a shaker, and the bisamide was dissolved upon heating. Subsequently, different cooling rates were achieved by applying six different methods: I) Allowing the hot solution in the vial to cool in the shaker's metal block. II-IV) Shaking the vial in in three different cooling baths, which feature different temperatures, respectively. V) Dropping the hot solution into a water/ice bath. VI) Dropping the hot solution onto a nitrogen-cooled wafer. All six applied methods are discussed in the following.

The first four methods of cooling the hot solutions, i.e. switching off both heating and the shaker and leaving the vial to cool in the metal block or shaking the vial in different cooling baths are shown in Figure 31. For self-assembly by cooling in the shaker (method I), heater and shaker were simply turned off and the respective hot solution remained in the hot metal shaker block until block and sample reached ambient temperature. For self-assembly by immersion of the hot sample vial in three different cooling baths (methods II-IV) the hot vial containing the sample was vigorously shaken in the respective cooling bath by hand for one minute and subsequently stirred with a magnet stirrer for 5 min vigorously. Cooling baths were prepared by either mixing water and ice or letting enough dry ice sublime from an ethanol bath to reach the bath temperature of 20, 0 or -60 °C, respectively.

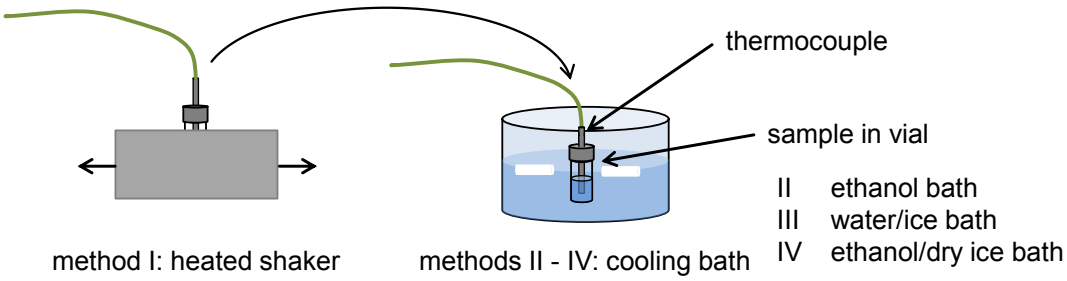

Figure 31: Schematic representation of the setup for the measurement of temperature profiles. After heating to 120 °C (in the case of *o*-DCB) under shaking the vials are immersed in the cooling bath. The temperature of the sample liquid is determined by a thermocouple.

During these processes, the temperature of the sample liquid can be monitored with a thermocouple, which is introduced into the vial through a septum and a hole in the screw cap. By use of ethanol or ethanol in combination with dry ice, different cooling bath temperatures were adjusted. Variation of cooling bath temperature (20, 0 and -60 °C) results in different cooling rates, as shown in Figure 32. For comparison, also profiles for cooling in the shaker's metal block and in a water/ice bath are displayed. The temperature profile for the sample remaining in the shaker exhibits a very flat decline of temperature. E.g., a temperature of 40 °C is only reached after more than 50 min (3000 s). The use of cooling baths drastically accelerates the cooling process: All samples cooled in baths exhibit cooling rates in the range between 7 and 12 K/min above 80 °C. At lower temperatures, the bath temperature becomes increasingly relevant. In contrast to the experiments in the µ-DSC, whereby self-assembly only took place between 30 and 40 °C at cooling rates up to 1 K/min, , self-assembly is assumed in this case to take place between 20 and 30 °C due to the higher cooling rates. Therefore, to estimate the cooling rate during self-assembly, the slopes of the cooling curves in the area around 25 °C are compared. Using a cooling bath at 20 °C, a relatively low cooling rate around 20 K/min is reached, which is nevertheless still 200 times higher than the highest one in the µ-DSC. The use of a 20 °C colder ethanol/dry ice bath (T = 0 °C) significantly raises the cooling rate to the region of 110 K/min. If a water/ice bath is used instead, approximately 140 K/min are reached. Yet, the curves for both cooling bath compositions at 0 °C feature a similar shape, which means that the lower heat capacity and slightly higher viscosity of ethanol compared to water[103] does not play a major role. Using an ethanol/dry ice bath with a temperature of -60 °C, a cooling rate around 330 K/min is measured between 20 and 30 °C.

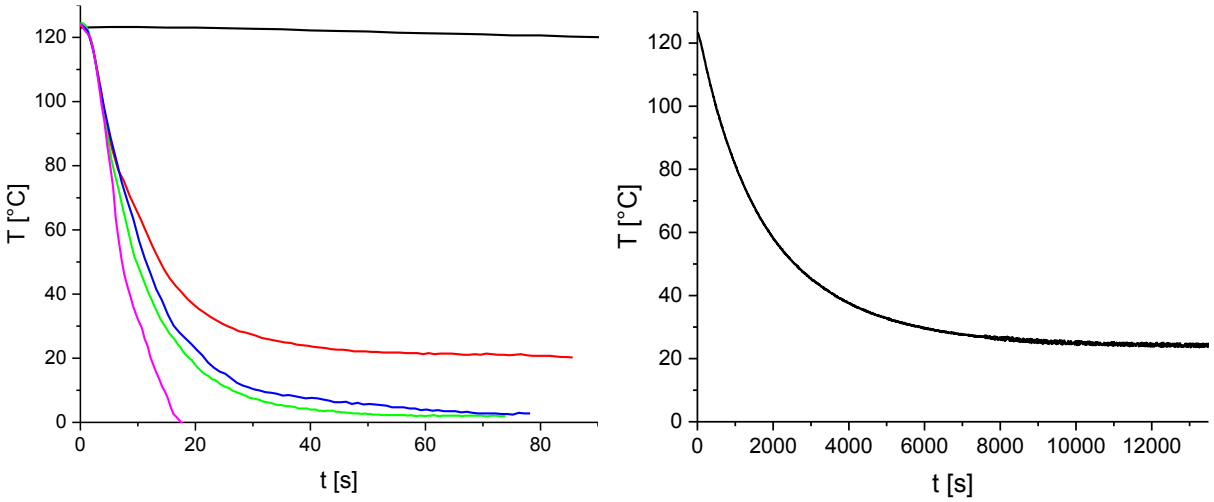

Figure 32: Temperature profiles of vials filled with *o*-DCB. Cooling was done by keeping the sample in the shaker (black) and by shaking in an ethanol bath at 20 °C (red), in an ice bath (green), in an ethanol/dry ice bath at 0 °C (blue) and in an ethanol/dry ice bath at -60 °C (magenta). The left side shows all profiles during the first 120 s, while the right side shows the whole profile for the slow cooling in the shaker.

With this setup comprising a 4 mL glass vial and a cooling bath, it is hard to achieve higher cooling rates. Thus, two other procedures for extreme cooling speeds were developed. This was achieved by improving the heat transfer with setups featuring a higher surface per volume of the solution. In addition, the omission of a container wall between cooling medium and sample will further accelerate the heat transfer and thus increase the cooling rate.[103] These considerations led to simply dropping of the hot solution into or onto the cooling medium. An ice bath or a wafer cooled by liquid nitrogen were chosen as cooling media. Both setups are schematically shown in Figure 33.

On the left side, dropping into a water/ice bath (method V) is illustrated. For the handling of the 120 °C hot solution, a preheated glass pipette was used. Some drops of the solution were carefully dropped into an ice bath without any stirring. Doing so, the pipette's tip had to be immersed into the bath to avoid swimming of the drops on the surface due to the water's surface tension. As *o*-DCB features higher density than water, the released drops sink to the bottom of the bath, where they form an organic phase. Subsequently, this phase containing the nanoobjects is collected for further investigation.

In the case of method VI, a wafer piece (approx. 1*1 cm) was placed on a solid steel block, which in turn was surrounded by liquid nitrogen in an insulation dish (Figure 33). The nitrogen is used to exclusively cool the steel block. In contrast to method V, method VI is

preferable, since it avoids the so called Leidenfrost effect: If a mass is placed in contact with a liquid and the temperature of the mass is far above the liquid's boiling point, the liquid will boil and the formed vapor will thermally insulate mass and liquid. Hence, the transport of thermal energy into the liquid will decrease drastically.[103] To rule out issues related to the Leidenfrost effect, the sample was dropped into the wafer, wafer and block remained in the liquid nitrogen for at least 5 min to allow them cooling to liquid nitrogen temperature despite the slower cooling. Subsequently, 2 – 3 drops of the hot solution were dropped onto the wafer with a preheated glass pipette. When the sample was dropped on the wafer, the drop froze almost immediately. Next, block and wafer were moved into a desiccator and high vacuum was applied to remove the frozen solvent.

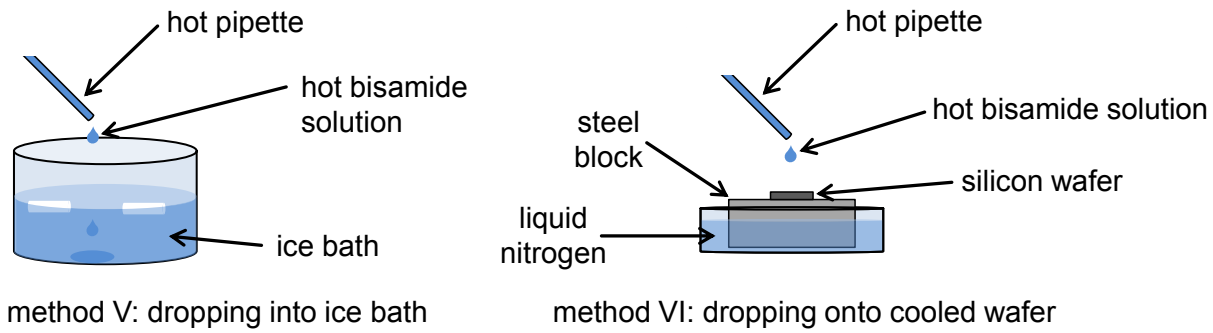

Figure 33: Schematic representation of sample cooling by dropping into an ice bath (left) or onto a silicon wafer cooled by liquid nitrogen (right). The hot (120 °C in the case of o-DCB) solution is carefully dropped into the ice bath or onto the wafer, respectively, with a preheated pipette. Drops of dispersion in *o*-DCB sink in water, forming a liquid phase at the ground of the ice bath.

Freezing means, that the sample is at least cooled to the melting point of *o*-DCB, which is at -17 °C[100]. Taking a time of approximately 1 s for freezing of the formerly 120 °C hot solution, a cooling rate of at least 137 K/s, which equals 8220 K/min, was achieved. This value is just a rough estimate, as the time until freezing is not determined precisely. The main reason for this is that a testing probe in contact with the small drop volume would most likely alter the results significantly. Moreover, the cooling rate is likely to vary within the sample drop, since the lower layers insulate the upper ones from the wafer and thus lower their cooling rate.

The methods described cover a wide range of cooling rates from below one to several thousands of K/min in the relevant temperature range for self-assembly of bisamide 1 in *o*-DCB. These methods were applied in the self-assembly process. The resulting nano-platelets

were investigated in the SEM and resulting micrographs are shown in Figure 34. Upon self-assembly, bisamide 1 forms nano-platelets for all cooling rates applied. When cooling the solution slowly in the metal block of the shaker, large platelets with lateral dimensions in the range of tens of micrometers are formed. They feature smooth edges and regular shape and appear quite thick. When increasing the cooling rate by use of an ethanol/dry ice bath at 20 °C, significant smaller platelets with less regular shape, which appear much thinner, form. Further acceleration of cooling by a bath temperature of 0 or -60 °C enhances this effect, i.e. platelet size decreases with increasing cooling rate. This is in agreement with classical nucleation theory, according to which nucleation of new objects competes with the growth of existing ones. Stronger and faster supersaturation boosts nucleation and thus results in the formation of more and smaller objects.[104] Surprisingly, when the hot solution was dropped into an ice bath, larger platelets formed, despite the higher cooling rate expected for this experiment, as discussed above. Self-assembly under extreme cooling rates achieved by dropping onto a wafer at liquid nitrogen temperature surprisingly yields thick platelets with lateral dimensions of tens of micrometers, which exhibit either smooth or jagged edges. As described above, for cooling rates as high as the ones achieved by this setup, extremely small and thin platelets were expected. Yet, the precise process, which leads to such big objects at this extreme cooling rate, remains unclear. Since the gained platelets are far from the desired shape anyway, this cooling process is not relevant for this work any further and therefore was not investigated more in detail.

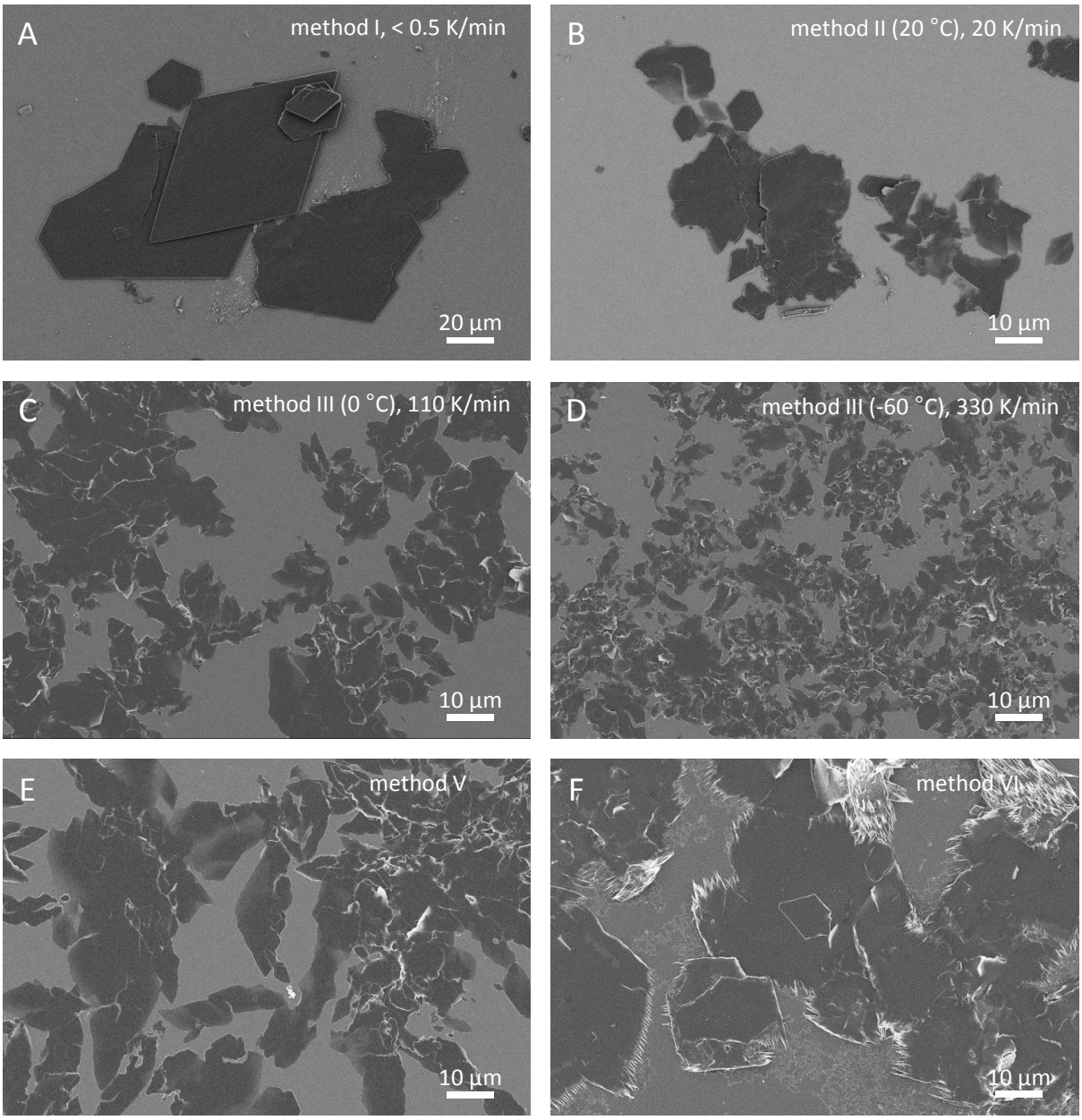

Figure 34: SEM images of structures formed by self-assembly of bisamide 1 upon cooling with different cooling rates. Vials containing the hot solutions were cooled at ambient conditions in the shaker (A) or in ethanol/dry ice baths at 20 °C (B), 0 °C (C) and -60 °C (D). Further, hot solutions were dropped into an ice/water bath (E) or onto a silicon wafer cooled with liquid nitrogen (F). Cooling rates for the latter two methods can only be estimated and hence are not given here. Solutions consisted of 500 ppm of bisamide 1 in *o*-DCB.

Summarizing, the cooling rate was found to affect the dimensions of formed platelets to a great extent. For the experiments in which cooling was done in a vial, a clear trend towards smaller objects with higher cooling rate was observed. When the cooling was done by dropping in a cold liquid or onto a cold solid, this trend was not continued, and again larger objects were obtained despite further increase of cooling rate. Therefore, for the

investigation of platelet thickness, the most promising samples, i.e. the ones from cooling baths at 0 and 60 °C were selected. For comparison, a sample prepared by dropping into an ice bath, was also investigated.

Up to now, only the lateral dimensions of the platelets formed have been investigated, since they are easily accessible via SEM. With all platelets lying flat due to their high aspect ratio, their thickness cannot be measured looking from the top, as it is done in SEM. To investigate platelet thickness despite that, AFM was applied. Figure 35 exemplarily shows results from a measurement done with the purpose of gaining information about the thickness of platelets.

On the left side, an AFM height image of a sample self-assembled by cooling in an ethanol/dry ice bath at -60 °C is shown. Big agglomerates as well as single platelets are visible in the image. For thickness measurements, only the isolated single platelets are used to avoid accidental measurement of several platelets stacked together. For each platelet, a cross-section along the scanning direction of the AFM was measured. In the example presented, three of these cross-sections are marked with colored lines. On the right, the height profile along each of these lines is displayed. Platelet heights measured from the profiles are illustrated with arrows.

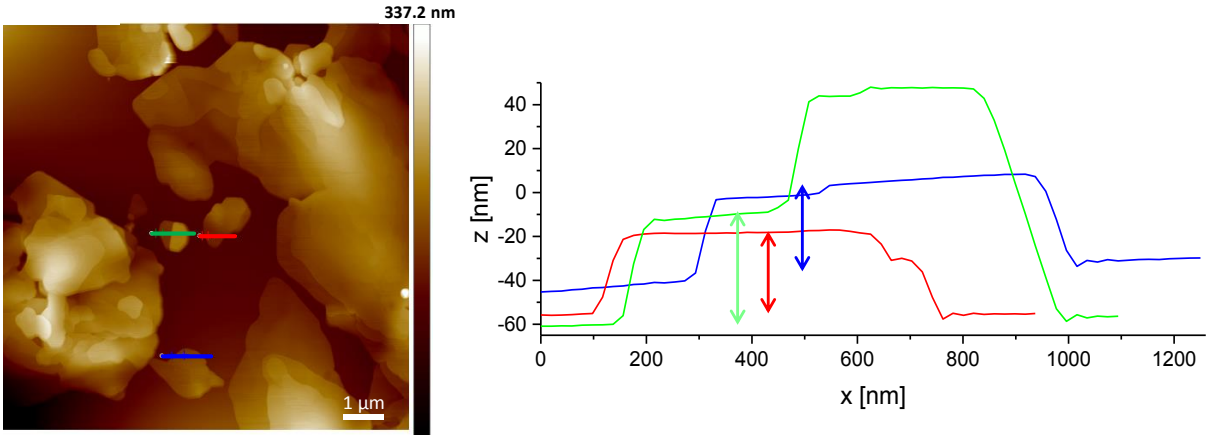

Figure 35: Measurement of platelet thickness at the example of bisamide 1 in *o*-DCB cooled with an ethanol/dry ice bath at -60 °C. On the left an AFM image with three cross-sections marked by colored lines is shown. Corresponding height profiles are displayed on the right. Arrows mark measured platelet heights.

For each sample, several SEM images were evaluated to get at least 12 platelets' heights per sample. Table 4 lists average thicknesses for the samples cooled with a bath at 0 or -60 °C and for the one prepared by dropping into an ice bath.

From both cooling bath experiments (methods II and III), nano-platelets with average thicknesses below 50 nm are obtained. Using a bath at 0 °C, 48 nm are achieved. With the layer thickness d of 1.4 nm, which has been determined via XRD, as described above, this thickness equals a stack of 34 layers. Faster cooling with a bath at -60 °C results in a thickness of 38 nm, which equals 27 layers. Dropping into an ice bath (method 5) results in significantly thicker platelets, as it has already been suggested by the SEM pictures discussed above. Here, the average platelet thickness is 119 nm (85 layers), which is more than twice as thick as the platelets from cooling baths.

Table 4: Platelet thickness as determined via AFM for 500 ppm solutions of bisamide 1 in *o*-DCB cooled with an ice bath, an ethanol/dry ice bath at -60 °C and after dropping the solution into an ice bath.

Sample	average thickness [nm]	standard deviation [nm]	number of measurements
Method II (0 °C bath)	48	17	15
Method III (-60 °C bath)	38	7	18
Method V (dropping into 0 °C bath)	119	53	12

In all subsequent experiments, method II (water/ice bath) was used, as it is easy to reproduce and to handle. Moreover, it gives similar results as the -60 °C bath, which is more difficult in terms of handling and reproducibility.

The concentration of bisamide 1 in the hot solution is also known to influence the dimensions of self-assembled nano-platelets from preliminary experiments. There are two adversary effects expected to cause this influence: On the one hand, an increase in concentration shifts self-assembly to higher temperatures. There, the cooling rate is higher (see Figure 32) and therefore smaller platelets are expected to be formed due to a resulting increase of nucleation density, as discussed above. This effect has already been published for another self-assembly system.[66] On the other hand, an increase in concentration means more bisamide per volume, i.e. more material per nucleus, if the nucleation density remains unchanged. This should result in larger platelets. To elucidate the effect of concentration, samples comprising 1000, 500 and 50 ppm of bisamide 1 in *o*-DCB were prepared. Cooling was done by shaking of the vial containing the 120 °C hot solution in an ice bath. Figure 36

shows SEM micrographs of nano-platelets resulting from these experiments. Apparently, self-assembly from all three investigated solutions results in thin platelets. From the 50 ppm solution, regularly shaped rhombi are formed, whereas the 500 ppm solution yields a less defined platelet shape. At 1000 ppm, a mixture of small regular shaped platelets and bigger and less regular ones is found. The platelet size decreases with the concentration, yet the samples with 500 and 1000 ppm of bisamide 1 feature a broad platelet size distribution. The increase of platelet size with raised concentration indicates that increased nucleation density due to higher supersaturation caused by a shift of self-assembly temperature towards higher temperatures, as discussed above, does not play a dominant role in this process. However, the presence of more bisamide per nucleus (assuming roughly constant nucleation density) due to increased concentration, explains the finding very well: Every nucleus or growing crystal will grow, until so much of the surrounding solved bisamide is consumed, that the supersaturation is gone. The more solved bisamide is present, the larger the object can grow until reaching that point. Since this deliberation matches the results, this effect is concluded to be the dominant one.

In conclusion, lowering the bisamide concentration decreases object size, although this effect is much smaller than e.g. the influence of the previously discussed cooling rate. As higher concentration on the other hand means, that more material can be processed in the same volume, dimensional control via cooling rate appears to be the preferable parameter for size adjustment in the production of bisamide nano-platelets.

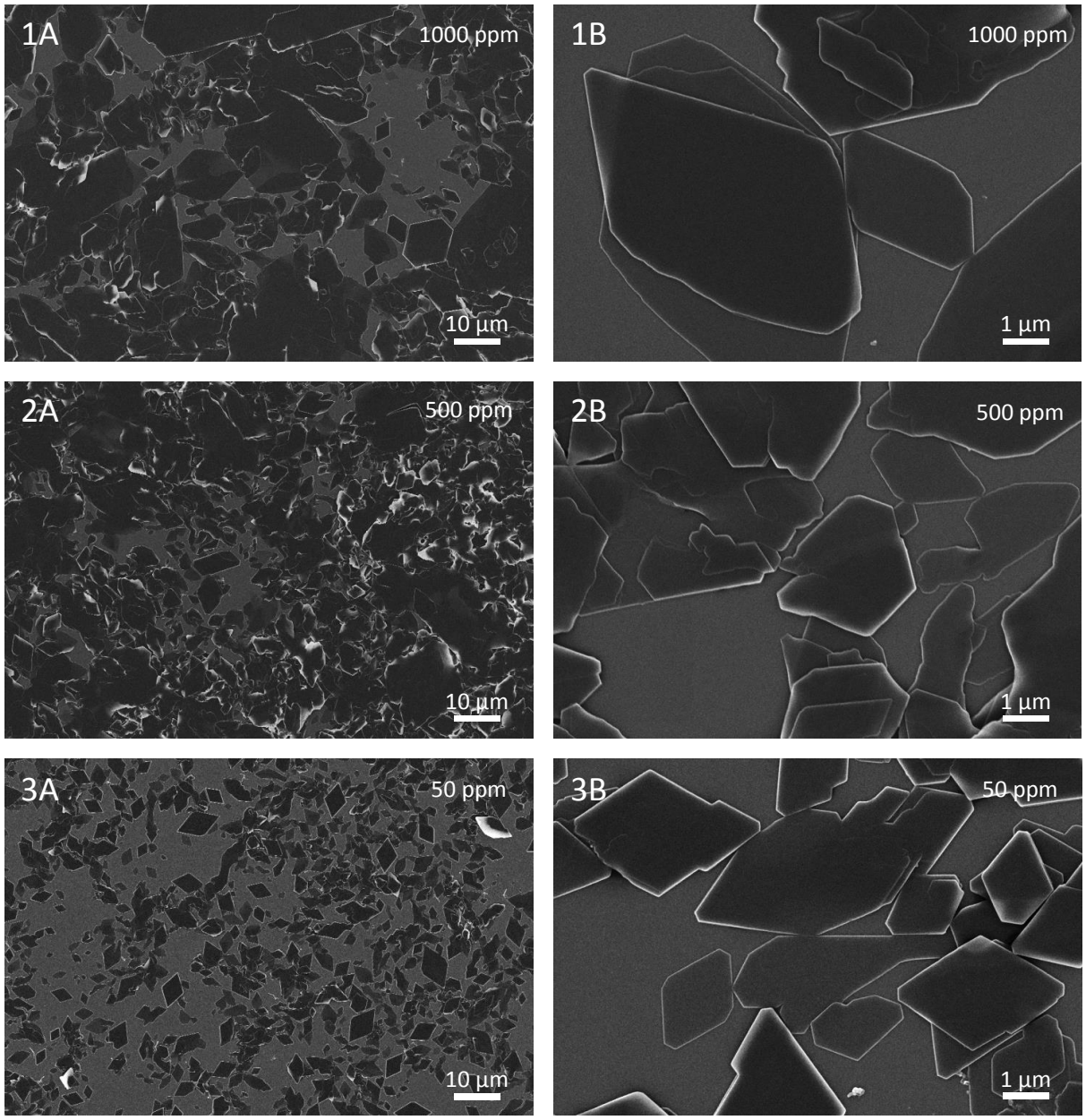

Figure 36: Structures formed by self-assembly of compound 1 upon cooling of hot solutions with different concentrations in *o*-DCB. Vials containing the hot solutions were cooled in an ice bath. Solution concentrations were 1000 ppm (1), 500 ppm (2) and 50 ppm (3). SEM images at low (A) and high magnifications (B) are given respectively.

The systematic study presented in the first part of this section solely relies on self-assembly upon cooling. Nevertheless, there are other methods like self-assembly upon removal of the solvent or addition of non-solvent to the solution. The latter can be realized by injection of the hot solution into a non-solvent at ambient temperature. By this procedure, object morphologies different from the ones formed upon cooling can be gained, as it has successfully been demonstrated by Hou *et al.*.[40]

For such experiments, non-solvents for bisamide 1 had to be found. Here, it is crucial that no residual solubility exists at ambient temperature, because even a very low solubility would result in dissolution of a great share of 1 in the big non-solvent volume used. Solubility tests revealed that water as a polar medium and *n*-heptane as a non-polar medium meet this criterion. Subsequently, a solvent, which solves a sufficient amount of bisamide 1 at elevated temperature and, at the same time, dissolves well in both non-solvents had to be selected. In this case, ethanol was found well suited for that purpose. For self-assembly, a saturated solution of 1 in ethanol was prepared at 75 °C by removal of non-dissolved solid from the liquid with a preheated syringe filter. 100 µL of this hot solution was injected into 10 mL of the respective non-solvent (water or *n*-heptane) under vigorous stirring. Then, the liquid was further stirred for 10 min, before a sample for SEM preparation was taken. Figure 37 presents SEM micrographs synthesized by injection into water and *n*-heptane.

Injection of a hot saturated solution of bisamide 1 in ethanol into water yielded elongated platelets featuring very smooth surfaces. Apparently, they possess high thickness and a low aspect ratio. Platelets self-assembled by use of *n*-heptane as non-solvent by contrast are less elongated. Obviously, injection into non-solvents yields a different platelet shape, featuring a much lower aspect ratio, compared to the one from the cooling experiments.

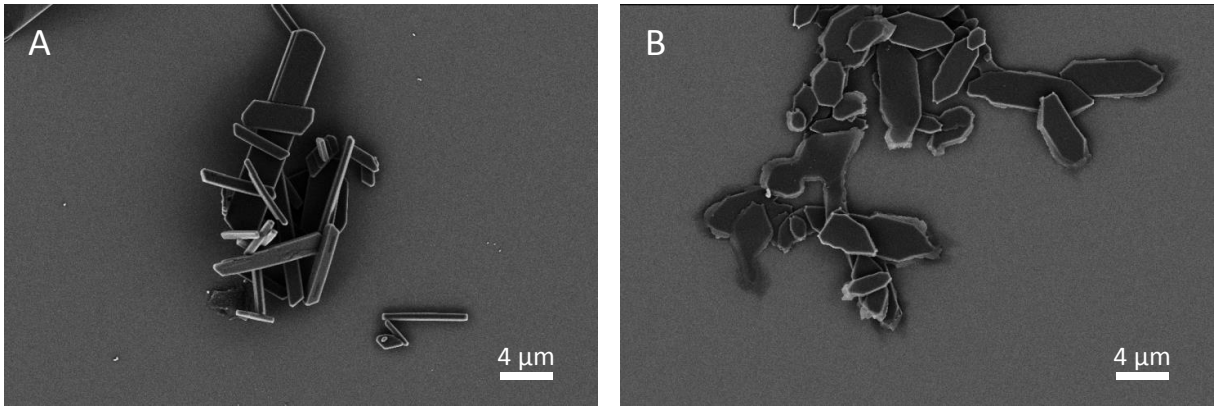

Figure 37: SEM images of supramolecular structures formed by injection of a hot saturated solution of bisamide 1 in ethanol into A: water or B: *n*-heptane.

The generation of platelets with high aspect ratio is one major aim of this chapter. With respect to this, self-assembly upon cooling clearly outperformed the tested approach of self-assembly upon addition of non-solvent. Hence, self-assembly upon cooling is exclusively applied in the following sections.

3.5.2. Self-assembly of fluorine-containing benzene bisamides

To get a first impression of the object morphology, all six fluorine containing bisamides were recrystallized from suitable solvents after synthesis and the formed solid state structures were investigated by SEM. Figure 38 shows SEM micrographs of these structures. All six bisamides assemble into flat structures, as it had been predicted from their crystal structures, as discussed above. 4A, 3B and 4B form particularly thin platelets with very smooth and defined edges.

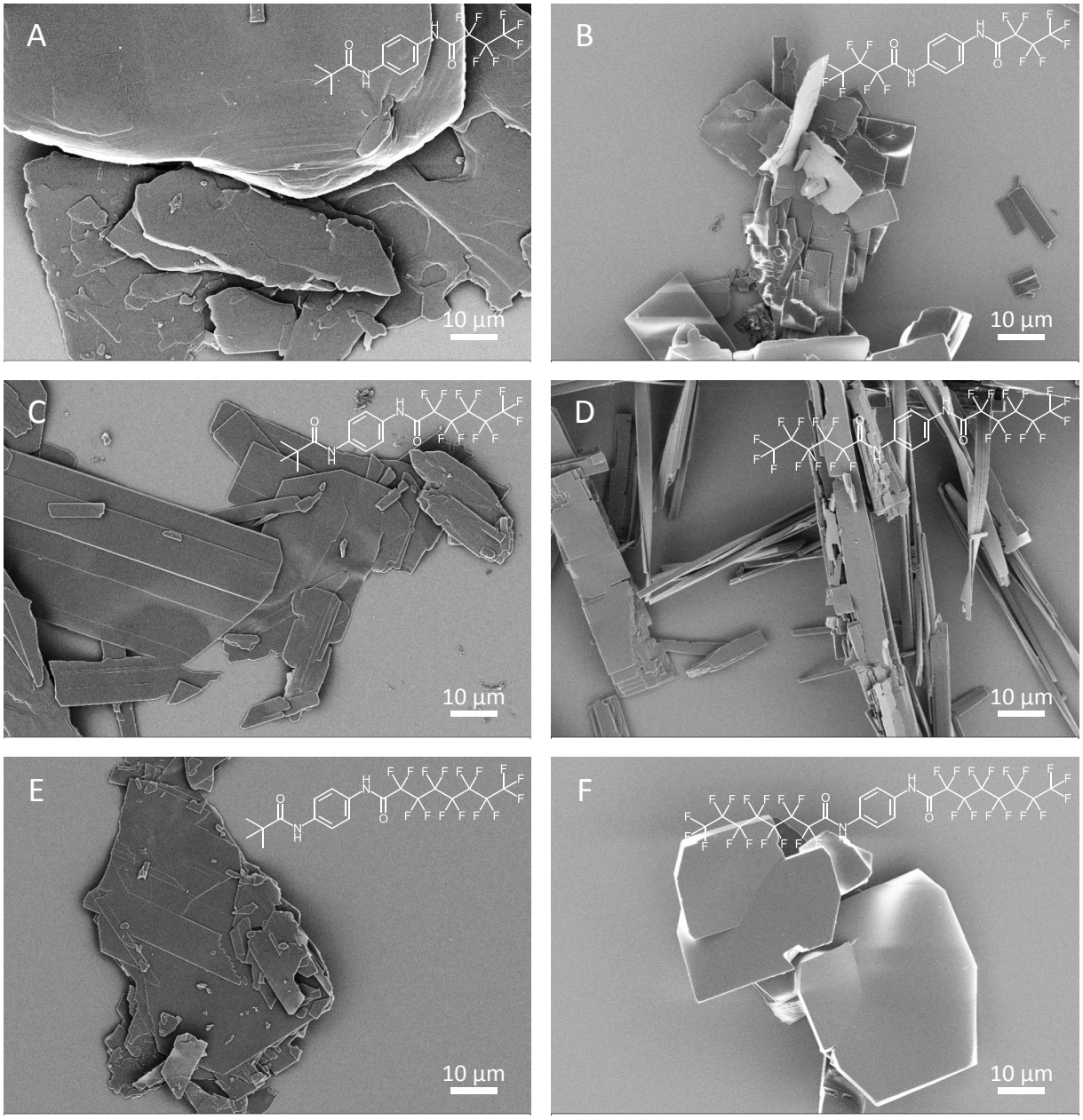

Figure 38: SEM micrographs of structures formed by the fluorine containing bisamides 3A (A), 4A (B), 3B (C), 4B (D), 3C (E), 4C (F) by recrystallization from methanol (A-D), ethyl acetate (E) or DMF (F) during synthesis.

All in all, the objects formed by this poorly controlled process feature quite large lateral dimensions of 20 or more micrometers. Also, these objects appear to be quite thick.

Therefore, a method with better parameter control is needed to reduce platelet dimensions significantly. In chapter 3.5.1., such a method has been developed for a similar bisamide. There, self-assembly upon cooling with the aid of an ice bath was found to be a suitable method for the preparation of thin 2D-objects. Consequently, each fluorinated bisamide alongside with the non-fluorinated reference bisamide 2 was dissolved in *o*-DCB at 120 °C in a glass vial with screw cap to obtain a clear solution with a bisamide concentration of 500 ppm. Subsequently, each filled vial was shaken in an ice bath for one minute to cool the solution and to induce self-assembly, which turned the liquids in the vials turbid. After that, the vials were allowed to rest in the ice bath for additional 15 min under stirring, before samples were prepared by dropcasting onto silicon wafer pieces. Figure 39 shows SEM micrographs of the objects obtained from the reference bisamide 2 and the asymmetrical bisamides of series 3 by this procedure. The non-fluorinated reference bisamide 2 forms big platelets with lateral dimensions up to several micrometers wide. 3A forms much smaller objects, which measure around 1 µm across. Platelets of both compounds exhibit relatively smooth and regular edges. For some platelets of 3A, an underlying hexagonal shape can be observed. Increasing the fluorocarbon chain length renders the obtained structures smaller, as can be seen from Figure 39 B to D. Moreover, both compounds with larger fluorinated substituents, 3B and 3C, exhibit rough platelet edges with no noticeable underlying regular shape.

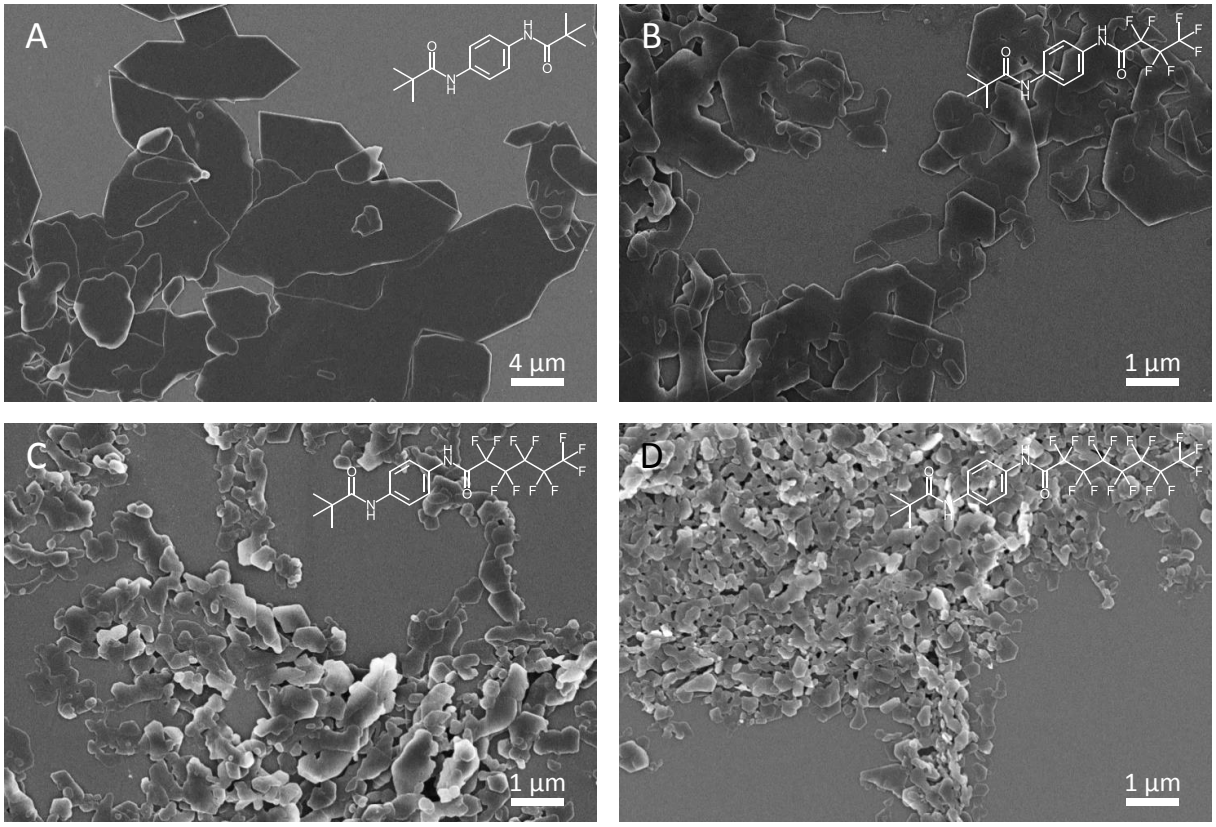

Figure 39: SEM micrographs of structures formed by self-assembly upon cooling of the asymmetrically substituted bisamides 3A (B), 3B (C) and 3C (D). For comparison, the reference compound 2 is also shown (A). Samples were prepared by rapidly cooling a 120 °C hot solution of 500 ppm of the respective bisamide in *o*-DCB by means of an ice bath.

Figure 40 compares SEM images of the three symmetric fluorinated bisamides of series 4 (prepared the same way as described above) to one image of the reference bisamide 2. All three bisamides of series 4 form elongated platelets upon self-assembly, contrasting to the asymmetric bisamides. The platelets of bisamides 4A – C feature lengths up to more than ten micrometers, while their diameters measure 2 µm maximum. Formation of such elongated structures already has been proposed based on their crystal structures: It is supposed, that the long lateral dimension is parallel to the strong hydrogen bonds in the structure, while the shorter lateral dimension is cross to it. In the latter direction, only relatively weak van der Waal forces are present. Thereby, the different growth speeds are attributed to the higher amount of crystallization enthalpy released upon growth along the hydrogen bonds. The platelets formed by series 4 still appear to be thin, yet much thicker than the ones formed by the asymmetric bisamides.

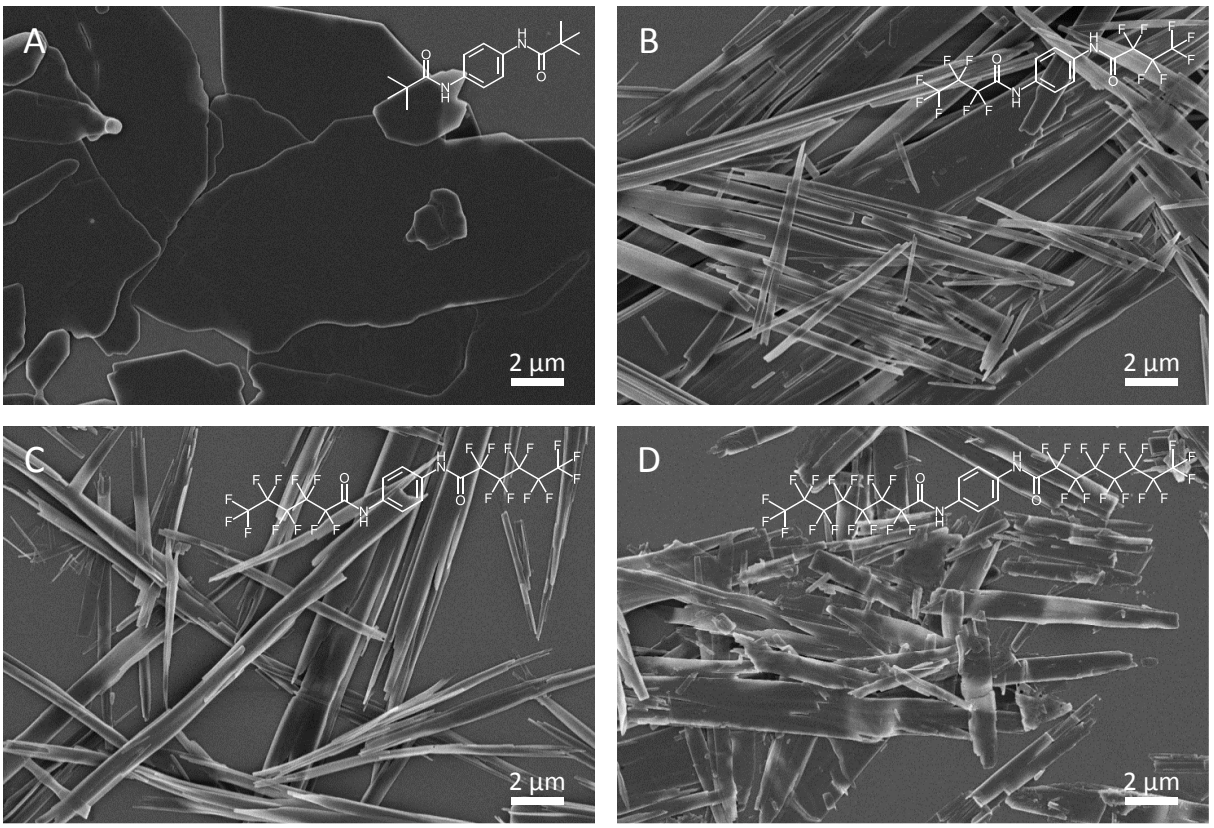

Figure 40: SEM micrographs of structures formed by self-assembly upon cooling of the symmetrically substituted bisamides 2 (A), 4A (B), 4B (C) and 4C (D). Samples were prepared by rapidly cooling a 120 °C hot solution of 500 ppm of the respective bisamide in *o*-DCB by means of an ice bath.

To obtain precise information about the thickness of platelets formed by these seven bisamides, platelets self-assembled from *o*-DCB solutions upon cooling in an ice bath were measured via AFM. Figure 41 illustrates such a measurement at the example of the asymmetric bisamide 3C. On the left side, a hight image of platelets of 3C is shown. Most platelets are agglomerated to form one big structure. For thickness measurements, only isolated single platelets around the agglomerates are used to avoid accidental measurement of several stacked platelets together. All aggregated platelets are ignored, assuming both, isolated and aggregated platelets, to feature equal average thickness. For each platelet taken into account, a cross-section along the scanning direction of the AFM was analyzed. In the example shown in Figure 41, three of these cross-sections are marked with colored lines. On the right, the height profile along each of these three is displayed. The platelet heights determined from the profiles are illustrated with arrows.

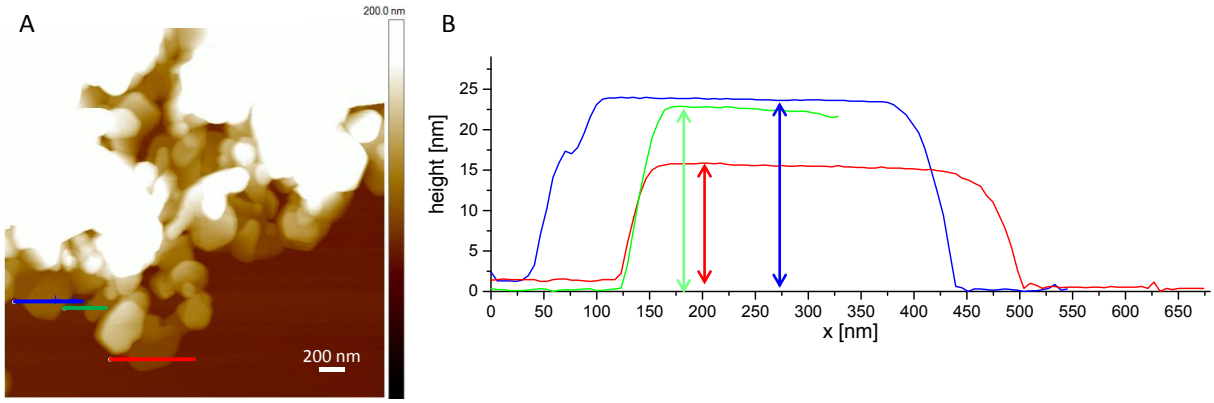

Figure 41: Measurement of platelet thickness at the example of compound 3C self-assembled in *o*-DCB upon cooling with an ice bath. On the left an AFM image with three cross-sections marked with colored lines is shown. The corresponding height profiles are displayed on the right. Arrows illustrate the measured platelet heights.

For each sample, several height images were evaluated to get at least 12 platelets' height values per sample. Table 5 lists average thicknesses *D* for the respective samples of bisamide 2 and of all six fluorinated bisamides.

The average platelet thickness of all seven bisamides is in the nanometer range. All three asymmetric bisamides 3A to 3C feature much thinner platelets than their symmetric analogs. Remarkably, the platelet thickness in series 3 decreases with the fluorocarbon chain length from around 50 nm for C_3F_7 to around 30 nm for C_7F_{15}. The symmetric fluorinated bisamides 4A – C yield thick platelets, even when compared to the symmetric bisamide 2, bearing two *tert*-butyl substituents. Nevertheless, the reduction of platelet thickness with increased chain length is also found here: With C_3F_7 substituents an average thickness of around 710 nm is achieved, while C_5F_{11} reduces this value to around 250 nm and C_7F_{15} finally yields platelets as thin as 130 nm. This effect of the chain length may be explained by the increasing mobility of the fluorocarbon chain: The longer the chain becomes the less defined and softer will the platelet surface become. This lack of defined structures is supposed to hamper epitaxial growth of additional layers on this surface. A second possible explanation for this phenomenon is based on energetic considerations: The motion of chains is associated with increased entropy and is therefore energetically favorable. If these chains are covered by another layer, they will lose degrees of freedom, since some previously available space is now covered by the new chains (see Figure 26 for the packing pattern), which fix each chain in a certain position in the crystal. This loss in entropy reduces the total

energy released by assembly of additional molecules on the top surface of an existing platelet and hence slows down thickness growth of the platelets. From the data of series 3 and 4, this effect of decreased platelet thickness with longer fluorocarbon chains can be expected to continue with further elongation of fluorocarbon chains.

Table 5: Platelet thickness *D* as determined via AFM for all seven benzene bisamides. Samples were prepared by self-assembly from 500 ppm solutions in *o*-DCB upon cooling with an ice bath.

Compound	D [nm]	st.dev. [nm]	Number of measurements
2	142	52	21
3A	53	21	21
3B	36	15	18
3C	32	22	12
4A	713	339	15
4B	253	148	18
4C	130	95	17

3.5.3. Determination of the height of bisamide single layers

Up to now, only the total height of bisamide platelets has been investigated. Yet, the crystal structures suggest, that the platelets consist of much thinner layers. Measurements of these layers help to connect crystal structure and platelet shape. To determine this layer thickness *d* of 2D-nanoobjects, AFM can also be employed. This is necessary, as the values of *d (XRD)* indicate that the orientation of the layers is along the planes predicted from the crystal structures, which has not been proven yet. In other words, the assumed relative orientation of unit cells and platelets has not been confirmed yet. To obtain the *d* values via AFM, the surface of a platelet is scanned. In some regions of the 2D-nanoobjects terraces are observed. They form, when layers do not cover the entire platelet surface (as in the schemes in Figure 19). The height difference between two neighboring terraces equals *d (AFM)*.

Figure 42 shows the measurement of such terraces at the example of a platelet of bisamide 3C. In the height image depicted on the right side, several terraces can be distinguished. The terrace heights are in the range of one to two nanometers, a range in which the noise of AFM measurements becomes relevant. To diminish the effect of this noise, many parallel

horizontal lines are considered and for every point along these lines the average height is calculated from all lines. In the example shown in Figure 42 all lines contained in the white box on the right image are considered in this method. A disadvantage of this method is the smoothing of steps. This happens, if the steps are not perpendicular to the lines, which is observed in the average height profile on the left side of Figure 42. In this height profile, three layers can be distinguished, although the level between the two lower layers is very short. In the example of the upper layer, which is very distinct, lines along the levels and their distance, from which the layer thickness is read out, are marked.

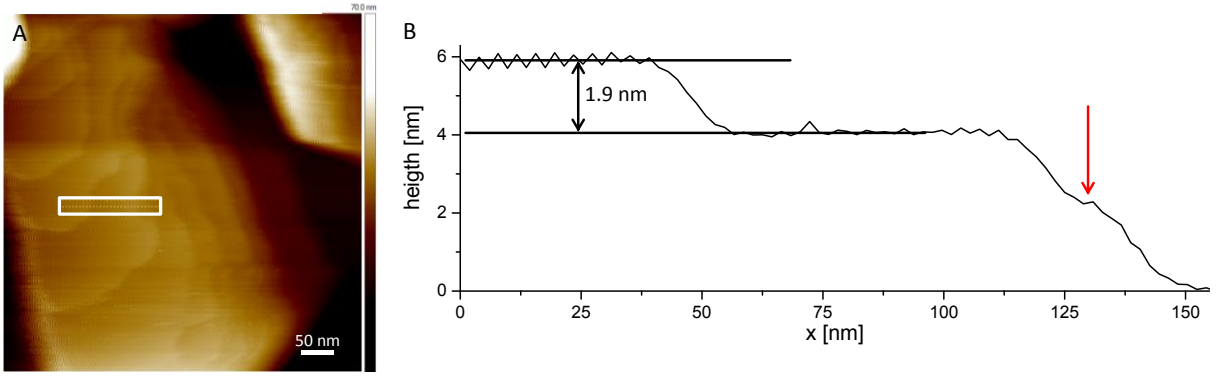

Figure 42: Determination of layer thickness via AFM at the example of compound 3C. A: AFM height image of the surface of a platelet formed by cooling of a solution in *o*-DCB with an ice bath. The white frame marks the measured area. B: Mean heights for each point along the frame (x). The diagram shows four different levels, yet the third level (red arrow) is very short and undefined. Therefore, only the thickness of the top layer is provided.

The layer thickness *d (AFM)* for each benzene bisamide was determined as shown at the example of Figure 42. The results are listed in Table 6. For some bisamides, exact measurements were extremely difficult and ambiguous. Therefore, in these cases the range of measured values for *d (AFM)* is given in these cases. For both fluorine-free bisamides, *d (AFM)* and *d (XRD)* are equal. With respect to the fluorine-containing bisamides from series 3 and 4, values of *d (AFM)* appear to be somewhat smaller than the ones of *d (XRD)*. This phenomenon, which is more pronounced when longer or more fluorocarbon chains are involved, is not fully understood to date.

Combining the platelet thickness *D* with the average layer thickness *d* determined in section 3.4., the number of layers per platelet can be calculated as *D*/*d*. Thereto, *d (XRD)* is used where available, as it is thought to be more precise and reliable than *d (AFM)*. Moreover, the

platelets feature more internal layer surfaces than exposed ones, which are better probed by XRD as discussed above. The resulting numbers for all seven bisamides are also given in Table 6. As here the effects of thicker layers and thinner platelets come into play together, increasing fluorocarbon chain length exerts a strong effect on the number of layers per platelet: For the asymmetric bisamides, a reduction from 34 layers with C_3F_7 to only 15 layers with C_7F_{15} is found. For 3A, these 15 layers equal a reduction of layer number about more than 85% compared to its analogue 2, which features two *tert*-butyl substituents. For the symmetric bisamides in series 4, even a reduction from 446 to 76 layers is observed between the molecules with shortest and longest fluorocarbon chains. Compared to their asymmetric analogues of series 3, these bisamides feature an at least fivefold increase in layer numbers. This is explained by the poor interaction of fluorocarbon chains and the non-fluorinated solvent *o*-DCB used for self-assembly, as this poor interaction yields an interface with high energy, which fosters thickness growth of the platelets. Nevertheless, when discussing the layer number of 4C, one should keep in mind, that this value is based on *d (AFM)* due to the lack of a value for *d (XRD)*. This limits its comparability to layer number values of other bisamides, which are all based on *d (XRD)*.

Summarizing, it was shown that the concept of asymmetrical substitution for reduced platelet thickness *D* works well, although the assembly pattern was different from the one initially expected. Moreover, an elongation of fluorocarbon chains further decreases *D* effectively.

Table 6: Comparison of averages of layer thickness *d* as determined via AFM, *d* values taken from crystal structures with platelet thickness *D* measured by AFM. In addition, average numbers of layers are given, which are calculated as *D*/*d*. For this calculation, *d (XRD)* is used, except for 4C, where *d (XRD)* is not available.

Compound	d (AFM) [nm]	d (XRD) [nm]	D [nm]	number of layers
2	1.2	1.23	142	115
3A	1.5 - 1.8	1.54	53	34
3B	1.6	1.86	36	19
3C	1.9	2.07	32	15
4A	1.3	1.60	713	446
4B	2.0	2.11	253	120
4C	1.7 – 2.1	---	130	61 - 77

3.6. Wetting behavior of 2D-structures formed by benzene bisamides with water

In the previous section, benzene bisamides featuring fluorocarbon substituents have successfully been shown to assemble into platelets. The platelet's upper and lower surfaces consist of fluorocarbon or mixtures of fluorocarbon and hydrocarbon substituents, based on the respective benzene bisamide applied. Consequently, the fluorophilic character of the surfaces can easily be tuned. Thus, a short section on surface properties is included in the following. As representative model compounds for this the bisamides 3A and 4A, featuring one and two fluorocarbon substituents, were chosen and their wetting behavior, by means of contact angle measurements with water was investigated. A common method to easily determine the contact angle is the sessile drop method using water as test liquid. For the sessile drop method, water drops are carefully cast onto the tested surface through a syringe. These drops are recorded via a camera system and contact angles of each drop are measured, as exemplarily depicted in Figure 43. To get reliable results about a compound's surface, it is crucial to generate a layer with as less defects as possible for measurement. To achieve this, a straightforward sample preparation was chosen: Both compounds were found to be suitable for physical vapor deposition in high vacuum. Prior to the evaporation step, glass platelets were silanized to offer a more hydrophobic substrate, which fits the surface of the fluorophilic bisamides. The respective benzene bisamide was vapor deposited on the surface in high vacuum resulting in a thin homogeneous film on the glass substrate. Via crazing incidence X-ray experiments it was proven by Kasper van der Zwan (Inorganic Chemistry III of the University of Bayreuth) that the crystal surface forming the top of the bisamide film correlates with the crystal structure of bisamides' substituents. This finding demonstrates that the film was deposited on the substrate in a manner comparable to a flat platelet.

The measured contact angles are presented in Table 7. The asymmetrically substituted bisamide 3A features a contact angle of approx. 105°, whereas the symmetrically substituted bisamide 4A yields a contact angle of approx. 118° with water. This tendency is explained by the molecular design of 3A featuring a mixed fluorocarbon/hydrocarbon surface in the crystal, while the surface of layers of 4A consists only of fluorocarbons. Most remarkably, these values are in the range of the 112 to 114° reported for static contact angles of water on smooth PTFE surfaces.[105] Taking into account the high fluorocarbon character of PTFE, the contact angles of both benzene bisamides appear quite high. Possible explanations for

such high values are textured or rough surfaces, as they are well-known under the term “lotus-effect”. In the case of bisamides, this roughness can either origin in the texture of the platelets surfaces on the nano-scale (see space-filling models in Figure 25 and Figure 26) or, in thickness variations within the bisamide film.

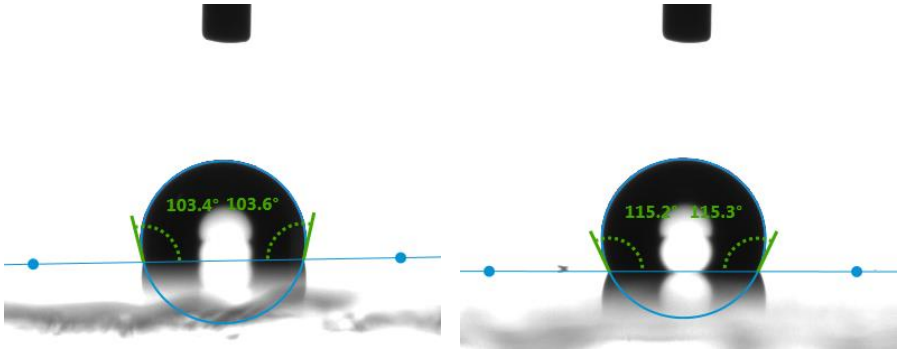

Figure 43: Water drops on thin vapor deposited films of 3A (left) and 4A (right). The dark object at each image’s top is the tip of the syringe applied for casting each drop. Blue baselines were adjusted manually. The measured contact angles are given in green.

Table 7: Contact angles with standard deviations for different surfaces. Non-treated and silanized glass are included as references.

Surface	Contact angle
3A	104.6 ± 1.4°
4A	118.0 ± 1.8°
glass	16.9 ± 2.5
silanized glass	90.8 ± 5.1°

Thus, the principal applicability of benzene bisamides substituted with fluorocarbon substituents for a highly hydrophobic modification of surfaces was successfully demonstrated in this section. The comparison of compounds 3A and 4A showed that resulting contact angles can be tuned by molecular design of the bisamides. For possible further applications, the supramolecular nature of the bisamide film is of particular interest. This is due to the fact, that it in principle allows dissolution and recycling of the bisamides applying suitable solvents.

3.7. Conclusions

The major subject of this chapter deals with the self-assembly of 1,4-benzene- and 1,4-cyclohexanebisamides into 2D-nanoobjects and the identification of a facile route to produce nano-platelets with low thickness.

The molecular design of the supramolecular building blocks comprises 1,4-bisamides with different fluorocarbon or *tert*-butyl substituents yielding compounds with a symmetrical or asymmetrical substitution pattern. Within each substitution pattern, the length of the fluorocarbons was varied from C_3F_7 over C_5F_{11} to C_7F_{15} yielding six compounds in total. A symmetric 1,4-bisamide with *tert*-butyl groups was used as reference. Most of the compounds were obtained in good yield and their molecular structure was clearly identified by common characterization methods. Thermal characterization proved the thermal stability of all compounds to be sufficient for all subsequent self-assembly experiments.

An important aspect was the structural elucidation by single crystal or powder X-ray diffraction, revealing the H bonding pattern, which may also reflect the shape of nano-objects on the mesoscale. Crystal structures were solved as part of a cooperation project at the department of Inorganic Chemistry III for the compounds. Remarkably, it was found that the presence of *tert*-butyl groups exerts decisive influence on the crystal packing pattern. All bisamides featuring *tert*-butyl substituents form layers with rows consisting of tilted molecules, whereby the tilt direction alternates between the rows. In these structures, each molecule is connected to four neighboring ones via H-bonds. On the contrary, molecules lacking *tert*-butyl groups assemble into layers with all molecules parallel. Here, each molecule forms H-bonds to only two of its neighbors. For all crystal structure solutions, the layer thicknesses extracted from them could successfully be proven by AFM measurements.

Based on these findings, 1,4-cyclohexanebisamide with *tert*-butyl substituents 1 was used as a model compound to evaluate different self-assembly processes and to tune self-assembly conditions to obtain thinner nano-platelets. 1 is known to feature a similar crystallographic structure and to assemble into platelets with a layer thickness of 1.2 nm. A bottom-up approach based on the self-assembly from hot solutions was ultimately selected as process due to its good reproducibility of the formed platelets and the control of the parameters. A parameter mapping for this process was conducted to gain deeper insight into the self-assembly process and to prepare platelets as thin as possible. This included the solvent, cooling rate and concentration in the solution. It was found that a high residual solubility of

the bisamide in the respective solvent at ambient temperature is unfavorable, as it led to unwanted self-assembly upon drying of the samples for further analysis. Promisingly, the self-assembly process with *o*-DCB as solvent resulted in platelets with a very regular shape and low thickness. Moreover, the cooling rate, which was tested between 20 and 8000 K/min, also showed a huge impact on self-assembly. A moderate increase of cooling rates up to 330 K/min yields smaller and thinner platelets, as expected. Surprisingly, extreme cooling cates of several thousands of K/min led to thick platelets with a poorly defined appearance. Under the selected conditions, cooling with an ice bath yielded a cooling rate around 140 K/min and supramolecular nano-platelets with an average thickness of 48 nm. Thus, it was selected as a facile method for further experiments. The influence of the concentration was investigated in the range from 50 to 1000 ppm. It was found that lower concentrations yield smaller platelets, which is attributed to a higher ratio of nucleation density during cooling and material available for object growth.

Using the identified straightforward method to nano-platelets, the findings were transferred to investigate the seven symmetric and asymmetric 1,4-benzene bisamides. All of them were successfully assembled into platelets upon cooling from hot solutions in *o*-DCB. It was found that the asymmetric bisamides yielded the thinnest platelets. This is attributed to weaker interactions between their mixed fluorocarbon/hydrocarbon surfaces, which is a key point of the initial concept for the design of the investigated bisamides. Also within each series, fluorocarbon substituents with increasing length decrease the platelet thickness. For example, 3C, featuring a C_7F_{15} group and a *tert*-butyl group, assembles into platelets with an average thickness of 32 nm, which equals as few as 15 layers. Its symmetrical analogues bearing two C_7F_{15} or *tert*-butyl substituents form thicker platelets with 130 nm (around 62 to 77 layers) or 142 nm (115 layers) on the average. These results demonstrate the successful application of the concept of asymmetric substitution of bisamides for reduced platelet thickness.

In view of potential applications, contact angles of selected vapor deposited symmetrical (4A) or asymmetrical (3A) bisamides with C_3F_7 substituents were performed. Crazing incidence X-ray experiments revealed that the fluorophilic side groups form the interface to air. Both compounds showed superhydrophobic behavior with contact angles of 105° for 3A and 118° for 4A, which varied depending on the substitution pattern of the applied bis-amide, rendering these compounds suitable as highly hydrophobic supramolecular coatings.

4. Length control of supramolecular 1D-objects via ultrasound

4.1. Dimensional control of submicron- and nano-sized objects

Benzene trisamide derivatives (BTAs) have attracted great research interest in recent years. This is mainly due to their well-known capability to form supramolecular columnar stacks, which build up further submicron fibers and nanofibers.[30,37,66,106] By controlling the conditions for self-assembly, Weiß *et al.* were able to influence the average diameter of such supramolecular fibers, yet all formed fibers were extremely long.[66] Length control of supramolecular BTA fibers has not been achieved yet.

In general, for self-assembled fibers, two general ways of controlling the length are known: 1) The desired fiber length is already achieved within the self-assembly step by carefully selecting the conditions like e.g. cooling rate or concentration (bottom-up approach). 2) Self-assembled fibers may cut to the desired length in a subsequent step (top-down approach). In literature, various bottom-up methods for length control of supramolecular assemblies are present[107], while top-down methods are rare: For example, the length of supramolecular 1D-assemblies can be varied to some extent by control of the building block concentration in the solution. Alternatively, fiber length can be regulated by end-capping, i.e. the addition of a second species of building blocks, which feature just one binding site and thus terminate the assembled structure when joining the assembly.[108,109] Another way of length control are vernier assemblies: Two molecules, featuring different numbers (*m* and *n*) of complementary supramolecular binding sites, are combined. In the examples published by Hunter and Tomas and Kelly *et al.*, *m* and *n* were equal to 3 and 2. If two of these molecules combine, one binding site remains unsaturated; this leads to addition of further building blocks. At an assembly length of *m*n*, the numbers of binding sites are counterbalanced and the assembly's growth is terminated.[110,111] This approach allows synthesis of monodisperse assemblies, but suffers from low assembly stability, since the weakest supramolecular link determines the stability of the whole assembly.[107] Another way towards monodisperse 1D-assemblies was presented by Bull *et al.*: They assembled peptide amphiphile building blocks around a dumbbell-shaped template made of oligo(phenylene ethynylene). The template efficiently limited the assembly's length, the same way as it works at the tobacco mosaic virus in nature, where coat proteins assemble around a single viral RNA strand.[112] Several groups have also presented a *seeded growth* approach for length control of 1D-nanoobjects

at the example of block copolymer micelles. This approach is based on the use of very short micelles, produced via a top-down approach by sonication of larger ones, as seeds. When these seeds are added to an oversaturated building block solution, the molecularly dissolved building blocks crystallize onto the seeds in a bottom-up step and form monodisperse objects. Furthermore, this so-called living supramolecular polymerization can form block co-assemblies, when different materials are used for seeds and dissolved building blocks.[20,113]

With respect to top-down approaches, ultrasound is a tool frequently used. A broad variety of 1D-structures featuring diameters in the range of nano- or micrometers has been shortened by ultrasound, such as e-spun polymer fibers[114], carbon nanotubes[115,116,117] silver nanowires[117,118], SiO_2-nanowires[119], molecular bottlebrushes[120], protein fibrils[117], block copolymer micelles[20,113] and cellulose nanofibrils[121].

Cutting by ultrasound is due to mechanical drag forces caused by imploding cavities, as Rooze *et al.* showed at the example of a coordination polymer.[122] To elucidate the fragmentation mechanism, Zeiger and Suslick investigated the sonofragmentation of acetyl-salicylic acid crystals. By variation of the sonication setup, they excluded breaking of the crystals by collisions with the setup. They also tested different crystal mass loadings and found no correlation between sonofragmentation and mass loading. This indicates that particle-particle collisions play no major role in sonofragmentation, since then a linear dependency of mass loading and fragmentation speed would have been observed. Having excluded all these factors, they consequently concluded, that direct interaction of crystals with imploding cavities is the dominant mechanism behind sonofragmentation.[123] Investigating the ultrasonic cutting of carbon nanotubes, Lucas *et al.* found a linear correlation between average fiber fragment length and delivered ultrasonic energy, regardless the power amplitude, at which sonication was done. This means, that the total energy determines the cutting process. This finding further supports the theory of cutting by collapsing cavities, since ultrasonic energy correlates with the number of cavities, at least, if the acoustic pressure exceeds the cavitation threshold.[116] Hennrich *et al.* established a model for the cavitation-induced scission of 1D-nanoobjects at the example of carbon nano-tubes (CNTs): Assuming a radial orientation of the 1D-nanoobjects towards the collapsing bubble, they found the strain field caused by the solvent displacement upon bubble collapse to exert a force *F* on the object. F can be expressed as a function of the object's length *L*, the solvent's viscosity μ and the strain rate $d\varepsilon/dt$, as expressed in equation 3.[115]

$$F = \frac{\pi \mu L^2}{2}\left(\frac{d\epsilon}{dt}\right) \tag{3}$$

This dependency on the object length *L* also explains the decrease of cutting speed with shorter objects and the existence of a terminal object length, which is approached after long sonication times, both observed by different researchers.[114,115,116,120] The shorter the objects become, the lower is the drag force *F*. If *F* becomes smaller than the force needed for rupture, the object cannot be shortened any further, which means, that the terminal object length is reached.[115]

This in turn means that from a given terminal length the minimum force needed for rupture can be calculated. If the fiber's diameter is known, the tensile strength of the 1D-nanoobject can be derived from this force. Following this approach, Huang *et al.* were able to measure values for tensile strengths of carbon nanotubes, silver nanowires and protein fibrils, which were in agreement with literature values.[117] Later, Saito *et al.* successfully adopted this method for tensile strength measurements of cellulose nanofibrils.[121] By simulation of nanofibers in proximity to collapsing cavities, Pagani *et al.* found the theory described above to hold only for short fibers. For longer fibers, a tangential orientation towards the collapsing cavity is more likely than the radial one, on which the model discussed above is based. This tangential fiber orientation results in cutting via buckling. This makes the cutting speed scale with the fourth power of the length, L^4, as Figure 44 schematically shows at the example of carbon nanotubes (CNTs). For shorter fibers, the cutting speed scales with L^2, as these orient radially and are ruptured.[124]

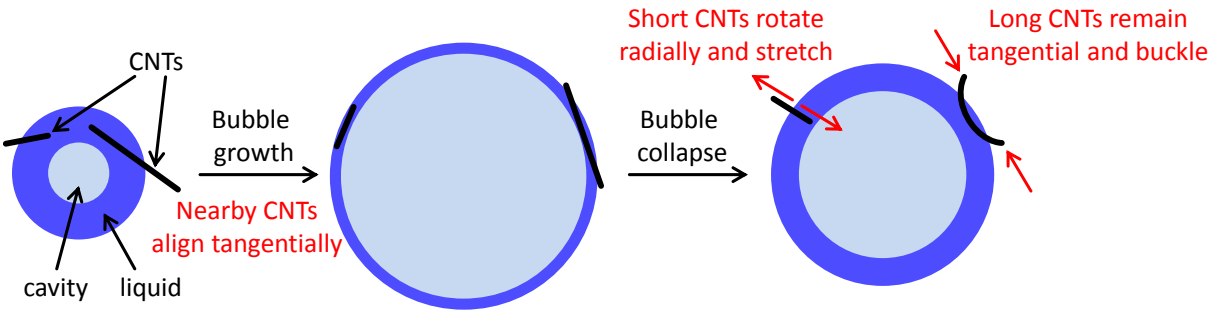

Figure 44: Schematic representation of the orientation of carbon nanotubes (CNTs) relative to a growing and collapsing cavity (light blue) and the influence on their failure mechanism. CNTs (black) are oriented by the incompressible liquid layer (dark blue) surrounding the cavity. Upon bubble collapse, short fibers are stretched, resulting in the scission rate to scale with L^2. Longer fibers remain tangential and buckle, resulting in the scission rate to scale with L^4. *Adapted with permission from ref.(Pagani et al. 2012)*[124]*. © (2012) National Academy of Sciences of the United States of America*

Sawawi *et al.* investigated the behavior of electro spun polymer fibers made of poly(styrene) (PS), poly(methyl methacrylate) (PMMA), poly(acryl nitrile) (PAN) and poly (L-lactide acid) (PLLA) when treated with ultrasound. They found that the fibers made of the brittle polymers PS and PMMA were easily cut, while the ones made of the more ductile polymers PAN and PLLA remained intact. Only after rendering the latter ones brittle by an UV-ozone treatment, they were cut by ultrasound. This shows that ultrasonic fiber cutting is sensitive to the fibers' material properties. Moreover, in the investigated temperature range from 30 to 90 °C, the temperature did not have any impact on the sonication of PS fibers. Despite the high local temperatures generated in sonicated liquids, no melting of any polymer fibers was observed in this study.[114]

So far, most of the works on ultrasonic comminution of dispersed solids used water as dispersion medium, and typically surfactants had to be added to gain stable dispersions. Despite that, in principle, variation of sonication media is an interesting field of research, since solvent parameters like viscosity, surface tension and vapor pressure are known to affect sonication results.[125] For example, Cheng *et al.* investigated the dispersion of CNTs in twelve different organic solvents. They found a strong correlation between vapor pressure and viscosity of the media and the dispersing efficiency of ultrasound in these media: Dispersion of CNTs was worsened by higher vapor pressures, which was attributed to cushioning effects by solvent vapor filling cavities prior to their collapse. Contrary, increasing viscosity enhanced dispersion of CNTs. This was explained by the higher amount of energy

being released by cavity collapse in more viscous media. This also matches the models described above, where the drag force F is proportional to the solvent viscosity μ (see equation 3).[126]

The aim of this work was to systematically and comprehensively investigate ultrasonic cutting of supramolecular fibers, which has to the best of my knowledge not been done hitherto. As a material forming supramolecular fibers via self-assembly, benzene trisamides (BTAs) were used. Fibers of these compounds may feature the ability to splice into thinner nanofibers, because they are composed of smaller columnar stacks, as discussed in the introduction (chapter 1.3). The possibility of ultrasound induced splicing, which has not been reported yet, is to be investigated in this chapter, alongside with cutting into shorter fibers. As mentioned above, in most reports of ultrasonic comminution of submicron- and nano-sized objects water was used as dispersion medium, while knowledge on organic media is rare. Therefore, this study focuses on organic dispersion media and their applicability in ultrasonic treatment of BTAs is tested.

The results in this chapter are divided into three sections: The first section deals with the production of defined supramolecular fibers made of BTA 5 as raw material for later sonication experiments. Thereby, upscaling of the self-assembly process applied is important to obtain sufficient amounts of fibers for several series of ultrasonication experiments. In the second section, the produced supramolecular BTA fibers are dispersed in different media and treated with ultrasound. Based on the results obtained, BTA 5 is combined with several suitable media to obtain model systems for more detailed sonication studies. In addition, sonication parameters suited for subsequent experiments are identified. Finally, in the third section, the sonication of the selected BTA is investigated more in detail. To this purpose, sonication conditions, i.e. sonication time, dispersion medium, cooling bath temperature and concentration of supramolecular fibers in the slurry, are varied systematically. The effect of these variations on the dimensions of the particles obtained after sonication is evaluated to establish correlations between sonication conditions and dimensions of resulting nanofibers. Understanding these correlations is crucial to enable future production of BTA nanofibers with controlled dimensions. Parts of the results in this chapter have been published in *Macromolecular Materials and Engineering*.[127]

4.2. Materials and preparation of supramolecular fibers

4.2.1. Materials

Preliminary experiments showed that BTA 5 is well-suited for sonication experiments, as distinct supramolecular fibers can be easily obtained as starting material for sonication. Moreover, being a commercially available material, which was received from BASF SE, access to amounts sufficient for all experiments is granted. The molecular structure of BTA 5 is shown in Figure 45.

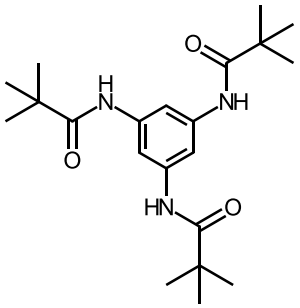

5

Figure 45: Molecular structure of BTA 5.

4.2.2. Preparation of supramolecular fibers

Preparation of dispersions

Prior to sonication experiments, supramolecular fibers with defined dimensions were prepared. These fibers were processed via self-assembly of BTA 5 upon cooling of 250 °C hot solutions in the high-boiling hydrocarbons Marlotherm and paraffin. To this, the respective amount of BTA was dispersed in Marlotherm or paraffin. Amounts of BTA 5 and the respective medium were chosen in a manner, so that a dispersion mass of 1500 g in the case of Marlotherm and 1300 g in the case of paraffin was reached. For example, 0.3 g of BTA 5 was added to 1499.7 g of Marlotherm to yield a dispersion comprising 200 ppm of BTA 5.

Dissolution- and self-assembly behavior

Each of the dispersions was heated to 250 °C under stirring with a mechanical stirrer at 300 rpm. To determine the self-assembly temperature of the BTA, the liquid was allowed to cool under continued stirring. The temperature, when the solution distinctly turned turbid,

was denoted as self-assembly temperature. Subsequently, the dispersion was once again heated to 250 °C and the temperature, when the liquid turned clear and exhibited no more optically visible laser scattering, was denoted as dissolution temperature (see Figure 47A). Concentration dependent solubility curves, as they are shown in Figure 46, were recorded for different BTA contents. Using Marlotherm as medium, dissolution and self-assembly temperatures were obtained over a wide range of concentrations from 40 to 500 ppm. At 40 ppm the BTA was dissolved upon heating around 120 °C, while self-assembly took place slightly below 60 °C upon cooling. At 500 ppm, which is the highest concentration investigated, the dissolution temperature was around 180 °C and the self-assembly temperature was around 155 °C. By contrast, the solubility in paraffin is much lower, with 50 ppm of 5 dissolving only at 180 °C and self-assembly occurring already at temperatures around 150 °C. Due to the low solubility in paraffin, 200 ppm was the highest concentration of 5 investigated in paraffin. At this concentration, dissolution took place above 200 °C and self-assembly was observed at 170 °C. Since this temperature is already close to 175 °C, which in the following preparation step is the temperature for the application of the cooling bath, no higher concentrations were applied. Higher concentrations are expected to feature self-assembly temperatures above 175 °C, where a cooling bath was planned to be applied during the preparation of supramolecular fibers (see below). As a start of self-assembly during application of the cooling bath would probably make the process more complicated and less reproducible, no higher concentrations were tested.

Due to the ice bath, cooling rates in the fiber preparation process explained below are much higher than the ones applied here. Hence, self-assembly is likely to occur at slightly lower temperatures than the ones reported here during fiber preparation.

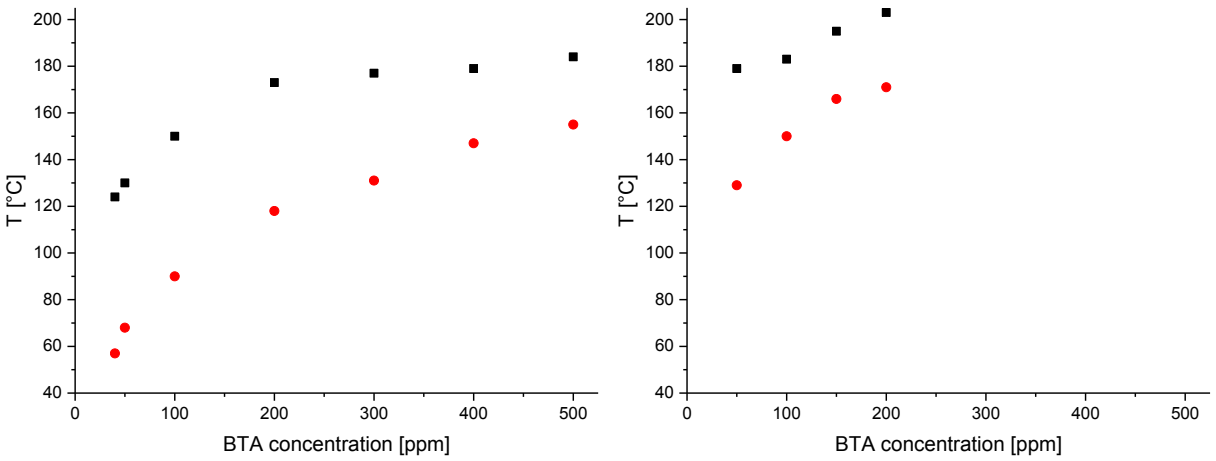

Figure 46: Concentration dependent dissolution and self-assembly temperatures of BTA 5 in Marlotherm (left) and paraffin (right). The temperature, at which the respective dispersion turned optically clear upon heating, was denoted as dissolution temperature (black), while the temperature, at which visible turbidity was observed upon cooling, was denoted as self-assembly temperature (red).

Self-assembly into supramolecular fibers

Finally, to prepare supramolecular fibers, each dispersion was heated to 250 °C (Figure 47A). Then, the heating mantle was removed and the solution was allowed to cool to 175 °C at ambient temperature (Figure 47B). Above 175 °C, no cooling bath was applied in order not to risk rupture of the flask by temperature-induced stress within the glass wall. Then, an ice bath was applied to cool the solution more rapidly from 175 to 20 °C (Figure 47C). During the whole procedure, the liquid was continuously stirred at 300 rpm.

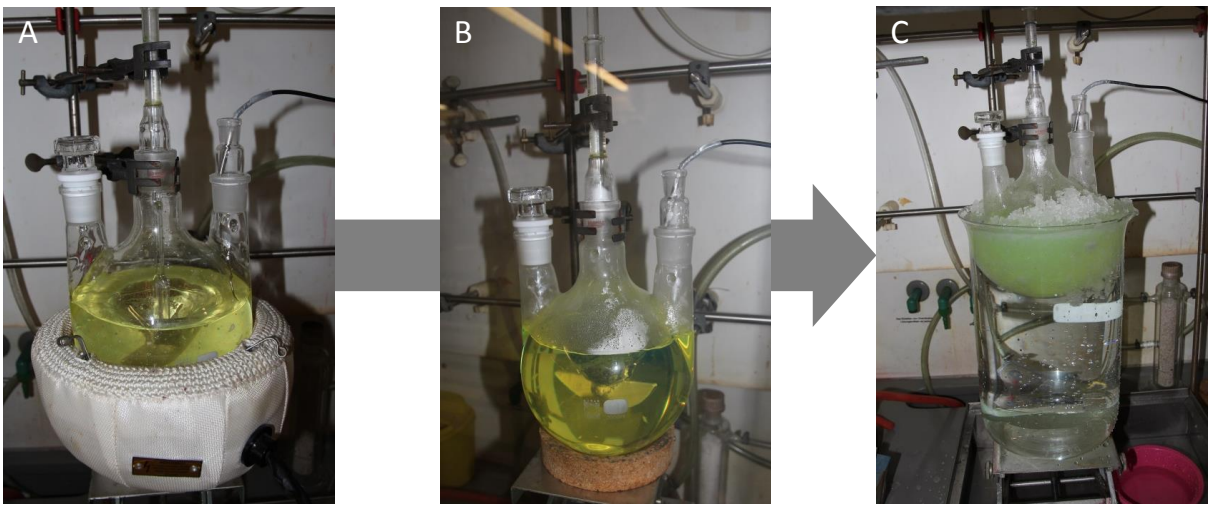

Figure 47: Preparation of supramolecular nanofibers from marlotherm: A: Heating under stirring, until a clear solution is reached. B: Subsequent cooling to 175 °C at ambient conditions. C: Further cooling with an ice bath from 175 to 20 °C. All three steps are done under continued stirring.

Using a thermocouple, temperature profiles of the cooling process were monitored. Figure 48 exemplarily shows such temperature profiles for Marlotherm and paraffin. From 250 °C to 175 °C, the solution was allowed to cool at ambient conditions, which is reflected by the relatively low cooling rate. At 175 °C, an ice bath was added to raise cooling rates. As Figure 48 shows, high cooling rates were achieved in doing so. The average cooling rate between 170 and 140 °C is 32 K/min for Marlotherm and 34 K/min for paraffin. Upon further cooling, the temperature difference to the ice bath is decreased, which lowers cooling rates to 22 K/min and 21 K/min between 125 and 120 °C. Between 105 and 100 °C, both solutions feature a cooling rate of only 17 K/min. This cooling process is highly reproducible and therefore well suited for homogeneous self-assembly of supramolecular BTA fibers, as it has already been shown.[66]

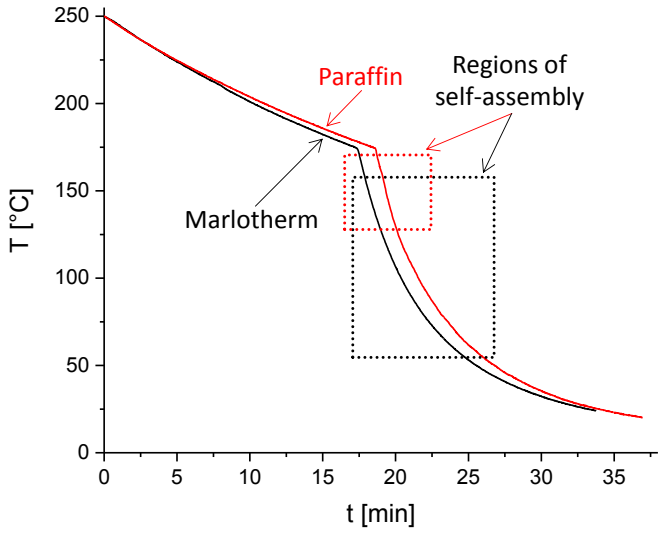

Figure 48: Cooling curves of 250 °C hot solutions of BTA 5 in Marlotherm and paraffin during the fiber production process. Cooling from 250 to 175 °C is at ambient conditions, while from 175 to 20 °C an ice bath is applied for cooling. Both liquids are stirred during the whole cooling process. The self-assembly regimes for the selected BTA concentrations of 40 to 500 ppm (Marlotherm) and 50 to 200 ppm (paraffin) are marked.

At the end of the self-assembly process, when the liquid had reached room temperature, the fibers were filtered off using a filter paper, washed with hexane twice and dried.

Morphology of supramolecular fibers

To prepare SEM samples of the fibers, SEM stubs were equipped with a conductive tab and carefully put onto the fiber mat, so that some of the supramolecular fibers were glued to the tab's sticky surface. Using these samples, the morphology of fibers formed by self-assembly at different concentrations in both media was investigated. Corresponding SEM micrographs are shown in Figure 49. To cover a broad concentration range, SEM images of one low and one high concentration per medium are presented. Supramolecular fibers from all four compositions show similar morphology. Supramolecular fibers from small concentrations of BTA in the solvent, i.e. 50 ppm in Marlotherm or paraffin, appear thinner and more bent than the ones from 400 ppm of BTA in Marlotherm or 150 ppm in paraffin.

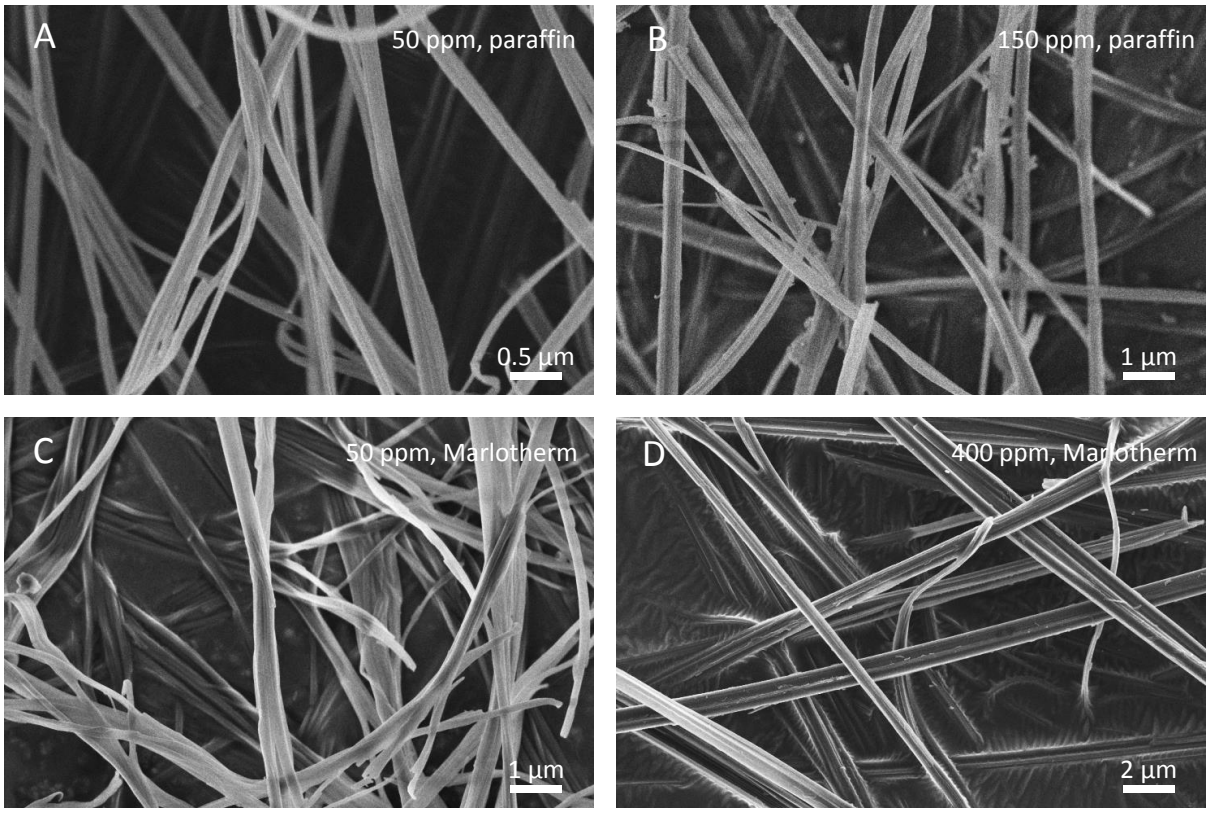

Figure 49: SEM images of nanofibers of BTA 5 self-assembled from non-polar media. Concentrations of BTA in paraffin shown are 50 ppm (A) and 150 ppm (B). Concentrations in Marlotherm shown are 50 ppm (C) and 400 ppm (D).

To quantitatively evaluate these concentration dependent fiber diameters, they were measured for all prepared samples. Figure 50 shows the mean fiber diameters with corresponding standard deviations. All average fiber diameters are between 0.17 and

0.60 µm. Fibers assembled from solutions comprising less than 200 ppm of BTA tend towards smaller diameters with decreasing BTA concentration. For fibers prepared in Marlotherm, the lowest average diameter of 0.17 µm is reached at 50 ppm. Using paraffin as medium, only BTA concentrations up to 200 ppm were investigated, since at 200 ppm the self-assembly temperature already raised to around 170 °C, which is too high for the applied self-assembly process, as discussed above. Significantly lower diameters than for the corresponding samples assembled in Marlotherm are reached at 100 and 200 ppm of BTA in paraffin. For example, at 200 ppm average diameters are 0.30 µm in paraffin and 0.49 µm in Marlotherm. All compositions feature broad fiber diameter distributions, which is attributed to temperature inhomogeneities. They may be present due to the huge solution volume during the self-assembly process of the supramolecular fibers despite stirring. As it has been shown above, assembly of fibers occurs at lower temperatures, when the fiber concentration is decreased. At the same time, the cooling rate is decreased at lower temperatures (see Figure 48), which means, that fibers are assembled with lower cooling rates, when the BTA concentration is decreased. It has been shown in literature that lower cooling rates result in thicker fibers.[66] It is a most interesting finding, that this effect here is overbalanced by the influence of lower concentration, which causes thinner fibers.

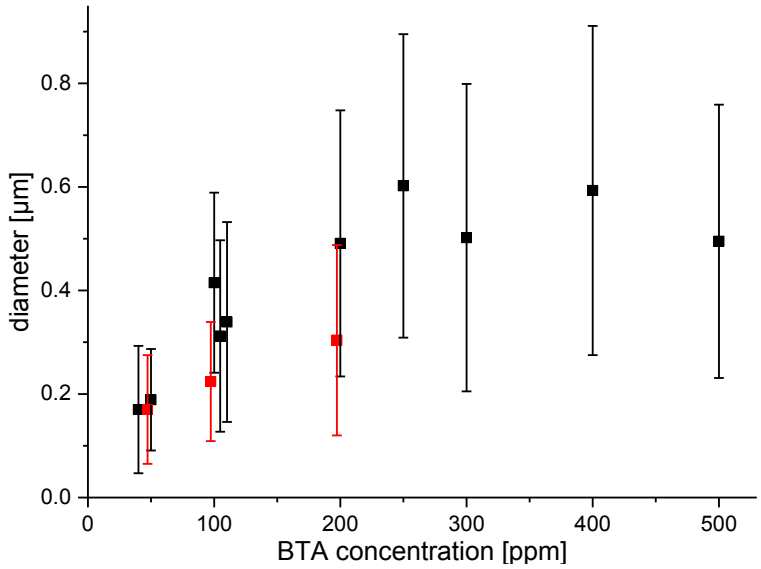

Figure 50: Concentration dependent diameters of fibers of BTA 5 assembled from Marlotherm (black) or paraffin (red). Averages and standard deviations (error bars) are based on at least 150 measured fibers each. Symbols at 100 ppm and red symbols are slightly shifted for the sake of clarity.

Summarizing, it was found, that self-assembly of BTA 5 from the non-polar media Marlotherm and paraffin is possible. The developed procedure allows production of large quantities of fibers (up to 0.75 g) in one batch. Depending on the BTA concentration used, average fiber diameters between 0.17 und 0.6 µm were realized.

To also determine the fiber length for BTA 5, the dried supramolecular fibers were dispersed in anisole and a drop of the dispersion was dried on a Si-wafer piece, yielding some spatially separated fibers, whose length could be measured via SEM. This procedure was exemplarily conducted for supramolecular fibers self-assembled from a 400 ppm solution in Marlotherm. Corresponding SEM images are shown in Figure 51, alongside with length and diameter histograms. The average fiber length was found to be around 150 µm, while the average fiber diameter is 0.6 µm, as discussed above. Hence, an aspect ratio around 250 is found.

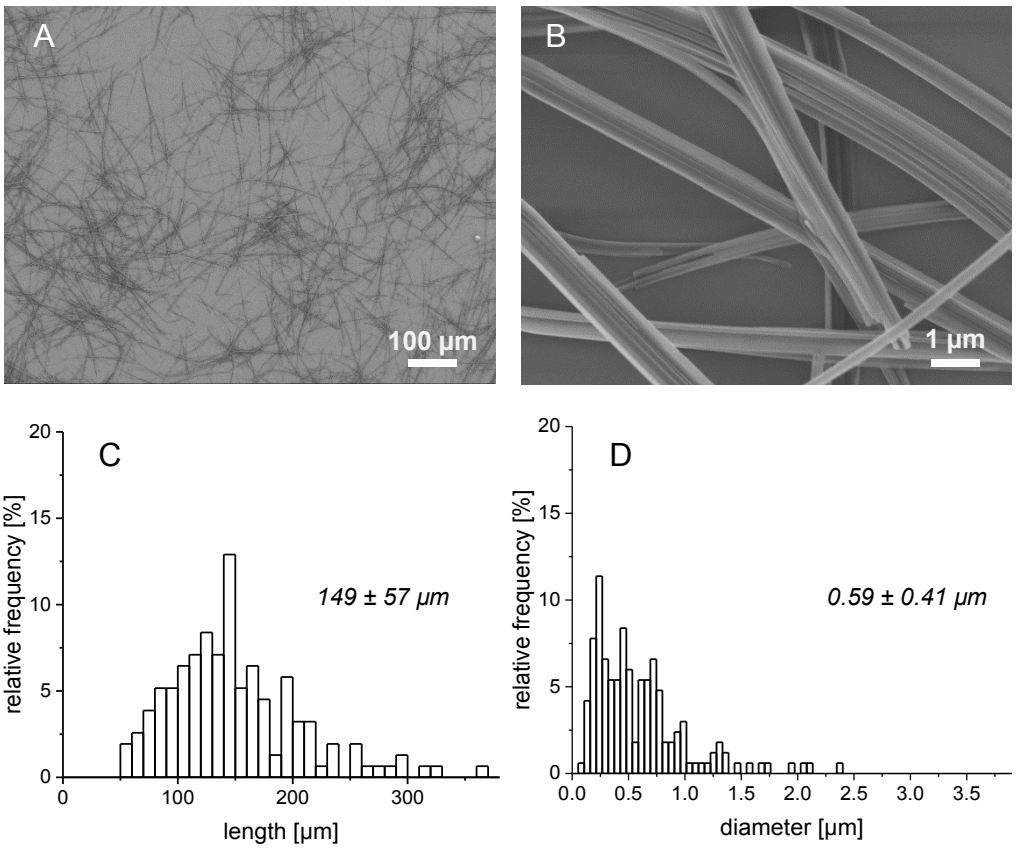

Figure 51: Supramolecular fibers of BTA 5, assembled upon cooling of a 400 ppm solution in Marlotherm. Histograms are based on at least 150 measured fibers each. *Adopted with permission from ref. (Steinlein et al. 2019)[127]. © (2019) John Wiley and Sons*

4.3. Setup for ultrasonic treatment and selection of media

4.3.1. Setup for ultrasonic treatment

Ultrasonication was done using a Branson 450 sonifier with a tapped step horn (101-147-037; Branson) at 20 kHz. The ultrasonic horn (tip diameter: 12.7 mm) was immersed to a depth of 2.4 cm in 25 mL of the respective supramolecular fiber dispersion contained in a 40 mL welded glass. To make sure that the rate, at which ultrasonic energy is delivered into the dispersion, is the same for all experiments, this immersion depth was maintained in all sonication experiments. To control the setup's temperature, the glass vial containing the dispersion was cooled by a surrounding ethanol/dry ice bath. Cooling bath temperature and dispersion temperature were monitored by thermocouples (type K). To adjust the cooling bath temperature, dry ice was added until the desired temperature was reached.[127] The described setup is schematically displayed in Figure 52.

To estimate the ultrasonic power absorbed by the liquid in the applied setup, calorimetric experiments using 25 mL of water as model substance were conducted, similar to procedures described in literature.[128] Here, the water was exposed to continuous sonication with defined power amplitudes (30, 50 or 70%) in the setup described above, but without any cooling bath. The temperature increase of the water upon ultrasonic treatment was monitored. Using the specific heat capacity of water and considering the warming of the glass vial as well, the energy absorbed by the liquid was calculated. Here, for a power amplitude of 30% a power of 13 W, at 50% of 23 W and at 70% of 32 W was obtained.

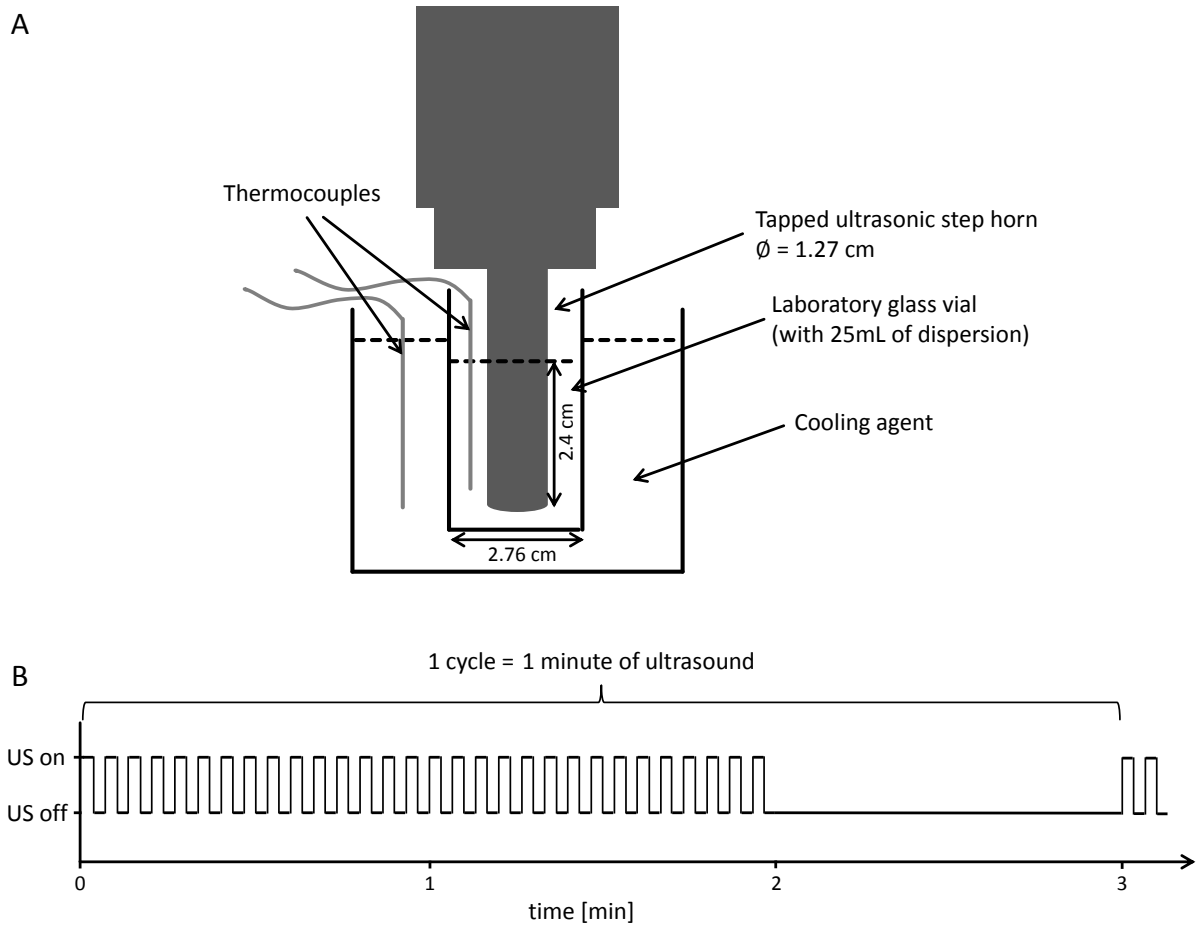

Figure 52: Ultrasonication setup. A: The ultrasonic horn is immersed in the sample dispersion contained in a glass vial. The vial is cooled by a surrounding CO_2/EtOH bath. Using thermocouples, the temperatures of dispersion and cooling bath are monitored. B: Schematic representation of one sonication cycle, which equals one minute of sonication. One cycle lasts 180 s in total and includes 30 segments of sonication taking 2 s each. *Adopted with permission from ref. (Steinlein et al. 2019)[127]. © (2019) John Wiley and Sons*

4.3.2. Investigation of BTA fiber/dispersion media systems for ultrasonic treatment

Before starting investigations concerning dimensional control of supramolecular trisamide fibers via ultrasound, suitable dispersion media for supramolecular fibers of BTA 5 had to be identified. These media have to meet several selection criteria: 1) Preparation of homogeneous dispersions must be achieved. This is crucial, as big agglomerates of BTA might influence sonication results. In addition, non-dispersed BTA fibers floating at the liquid's surface in case of poor dispersion are expected not to be exposed to ultrasonic energy the same way as within the medium. 2) The respective medium's melting point should be low, at best below -15 °C to allow sonication at low dispersion temperatures. 3) The medium in question may not solve significant amounts of BTA (at least at low

temperatures), to avoid effects associated with partial dissolutions such as Ostwald ripening of formed objects, i.e. growth of larger objects at the expense of smaller ones. Preliminary experiments with isopropanol/water mixtures as media, in which BTA 5 exhibits a certain solubility, emphasize the importance of this requirement: Mixtures containing larger amounts of isopropanol, which solve larger amounts of BTA 5 resulted in larger fibers and a poor reproducibility of sonication experiments. To avoid this problem, media, which feature a lower solubility of BTA 5, had to be found to investigate the behavior of this BTA in ultrasound experiments. Hence, the solubility and dispersibility of BTA 5 was tested in several solvents and their respective melting points were considered. From that, *n*-hexane, toluene, methyl cyclohexane (MCH) and anisole were selected.

Ultrasonic experiments were conducted at a cooling bath temperature of -15 °C, dispersion concentration of 1000 ppm and an ultrasonic power amplitude of 50% using the pulse program shown in Figure 52 to avoid excessive heating of the samples. To prepare samples for SEM characterization, one drop of each sonicated supramolecular fiber dispersion was drop-cast on a clean silicon wafer piece of approx. 1 cm^2. Supernatant liquid was removed from the wafer using a piece of filter paper. Subsequently, the sample was allowed to dry, before it was glued onto a SEM stub with a conductive tab. All samples were coated with 2.0 nm of platinum prior to SEM investigation.

Figure 53 shows nanofibers formed by ultrasonic treatment of supramolecular fibers of BTA 5 for 15 min in the four media *n*-hexane, toluene, methyl cyclohexane and anisole. In all four media, nanofibers of BTA 5 were formed successfully by ultrasonic treatment. Nanofibers obtained from *n*-hexane seem thinner and longer than those from the other media used. Nanofibers from toluene and anisole give a quite similar impression. It is noteworthy, that fibers from both of these media show rough surfaces where the initial fiber was ruptured. This is an indication that no significant dissolution occurs during sonication of these systems, as otherwise the fractured surfaces would be smoother due to surface minimization by Ostwald ripening. As results in toluene and anisole are comparable, toluene was not used as medium for further experiments any more to reduce the number of experiments. Consequently, to elucidate effects of the used medium, three different media, *n*-hexane, MCH and anisole, were selected for further use.

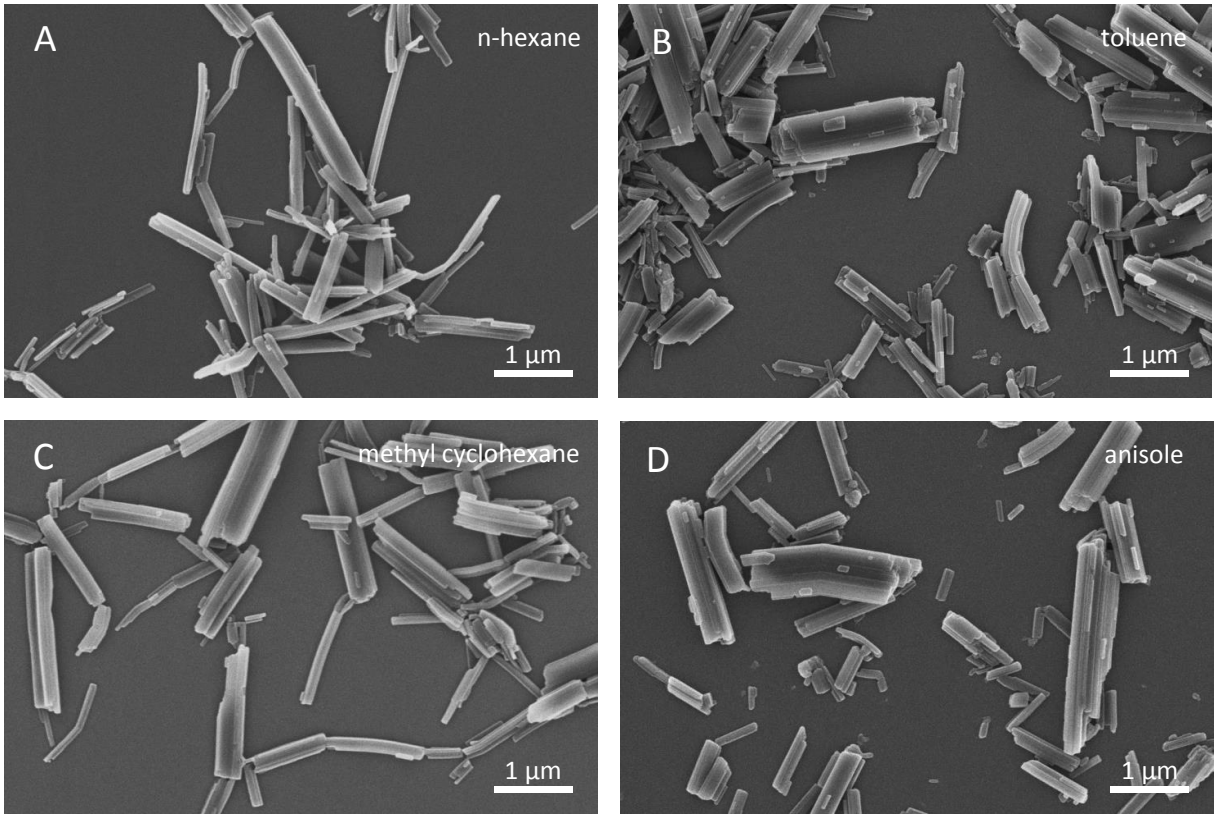

Figure 53: SEM images of nanofibers of BTA 5 after 15 min of sonication in A: *n*-hexane, B: toluene, C: methyl cyclohexane and D: anisole.

4.3.3. Ultrasonic power amplitude

In the applied sonication setup, the ultrasonic power amplitude, i.e. the rate, at which ultrasonic energy is delivered into the dispersion, can be adjusted. In principle, the cutting speed could either just depend on the total absorbed sonication energy or it could (additionally) depend on the applied power amplitude. To find proper starting conditions for the correlation of selected process parameters with resulting nanofibers, this possible dependency on power amplitude was investigated. Hence, three different power amplitudes, namely 30, 50 and 70%, which equal absorbed powers of 13 W, 23 W and 32 W, were applied with the pulse program shown in Figure 52. SEM samples from the treated dispersions were prepared as described above. Fiber dimensions after treatment with these different power amplitudes for different sonication times were measured and plotted as a function of ultrasonic power absorbed by the corresponding samples in Figure 54.

It is clearly visible, that all results form a single curve quite well, despite they origin from experiments with different power amplitudes. Yet, average fiber lengths show some

deviations at short sonication times, which is attributed to fluctuations in the measurements, as it is also implied by the huge standard deviations observed in this region. The existence of the single curve found indicates that the total absorbed ultrasonic energy is the factor governing the cutting of the supramolecular fibers, while the power amplitude plays no significant role, at least for the power amplitudes tested. This finding is in agreement with reports by Lucas *et al.*, where the supplied ultrasonic energy, but not the power amplitude, determines the scission of carbon nanotubes.[116] Also the phenomenon of the fiber dimensions approaching a terminal value when treated with sufficient ultrasonic energy agrees with results reported for other systems, e.g. carbon nanotubes[115,116] or electrospun polymer fibers[114].

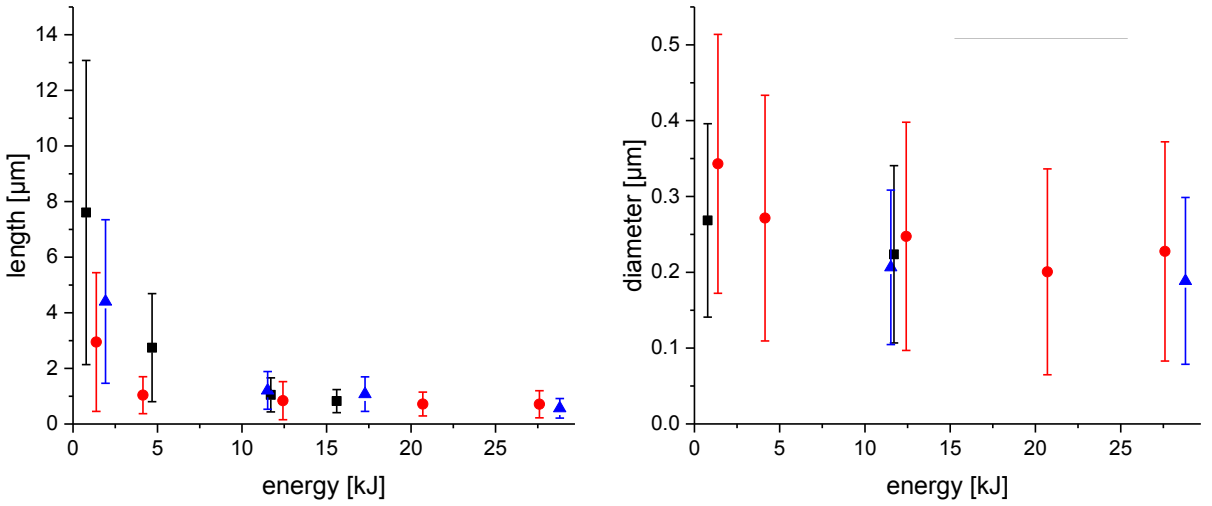

Figure 54: Evolution of length (left) and diameter (right) of nanofibers with increasing absorbed sonication energy. Sonication energy is supplied with ultrasonic power amplitudes of 30% (■), 50% (●) or 70% (▲). Sonication medium is anisole, BTA concentration is 1000 ppm and cooling bath temperature is -15 °C. Averages and standard deviations (error bars) are based on at least 150 measured fibers each.

As it has been shown, the power amplitude, adversely to the total applied ultrasonic energy, does not affect the resulting fibers' dimensions, a medium power amplitude of 50% was chosen and maintained for all further sonication experiments. The intention for this choice was to avoid the rapid heating of the samples caused by high power amplitudes. At the same time, a sufficiently high power amplitude was chosen to shorten the experiments' duration.

4.4. Influence of sonication process parameters on the dimensions of nanofibers

Control of the resulting fibers' dimensions is crucial to successfully utilize ultrasound for the production of nanofibers. This control can only be achieved, when the impact of all relevant process conditions is known. Therefore, those parameters, i.e. sonication time, sonication medium, BTA concentration in the dispersion and temperature are systematically varied in this chapter. The dimensions of resulting submicron fibers are determined via SEM and correlated with sonication conditions. The initial set of parameters was adopted from the previous section: Ultrasonic power amplitude is 50%, BTA concentration is 1000 ppm and cooling bath temperature is -15 °C. The BTA used is BTA 5 and anisole is used as medium, where not stated otherwise.

To prepare dispersions for later ultrasonic treatment, 1000 (50, 2000) ppm of supramolecular fibers of BTA 5 were dispersed in 25 mL of 4 °C cold *n*-hexane, MCH or anisole by mixing with a vortex shaker (Merck Eurolab). Next, the vial containing the cold liquid was attached to the ultrasonic horn as described above (section 4.3.1.). Sonication was done using the pulse program shown in Figure 52 B (section 4.3.1.): 2 s of sonication were followed by 2 s without sonication. This sequence was repeated 30 times, so that the total sonication time within the 2-minute-program was 1 min. This pulse program was followed by 1 min resting time without any sonication, before the next pulse program was applied, until the total sonication time for the sample was reached. To monitor the temporal evolution of fiber dimensions, the resting time was used to draw samples of about 0.1 mL. This was typically done after 1, 3, 6, 9, 12, 15 and 20 min of sonication. All breaks integrated in the described sonication procedure are meant to give the sonicated dispersion time to thermally equilibrate with the cooling bath. After sonication, all samples were stored at 4 °C prior SEM samples preparation. To measure the dimensions of resulting fibers, SEM images from at least three different areas of each sample were taken into account. Using Image Tool 3.00 (The University of Texas Health Science Center in San Antonio) at least 150 fibers per sample were analyzed. All dimensions presented in the following were measured this way to obtain comparable results.

4.4.1. Sonication time

In order to study the influence of sonication time, a dispersion of supramolecular fibers in anisole was treated with the pulse sonication program described in the previous section for 90 min. Samples were taken from this dispersion after different sonication times to monitor the temporal evolution of fiber dimensions. Figure 55 shows SEM micrographs and corresponding fiber length and diameter histograms for samples up to 90 min of sonication taken in the same single experiment.

Within only 1 min of sonication, the initial fibers featuring lengths of around 150 µm have been cut into shorter supramolecular fibers with an average length of 2.76 µm and an average diameter of 0.24 µm (Figure 55 A). After 6 min of sonication, supramolecular nanofibers with an average length of 0.92 µm are found. Among them are only very few ones with lengths between 2 and 4 µm and none with a length above 4 µm (Figure 55 C). As shown in the image, long fibers exist besides very small ones, which also are significantly thinner. After 30 min of sonication, the longest fibers have been comminuted to the benefit of small fibers featuring lengths below 0.5 µm (Figure 55 H). Finally, after 90 min of sonication, the fiber length distribution is further narrowed: After this sonication time, very few fibers longer than 1.0 µm are left. At this stage, fibers feature an average thickness of 0.14 µm and no fibers thicker than 0.6 µm are present anymore (Figure 55 L).

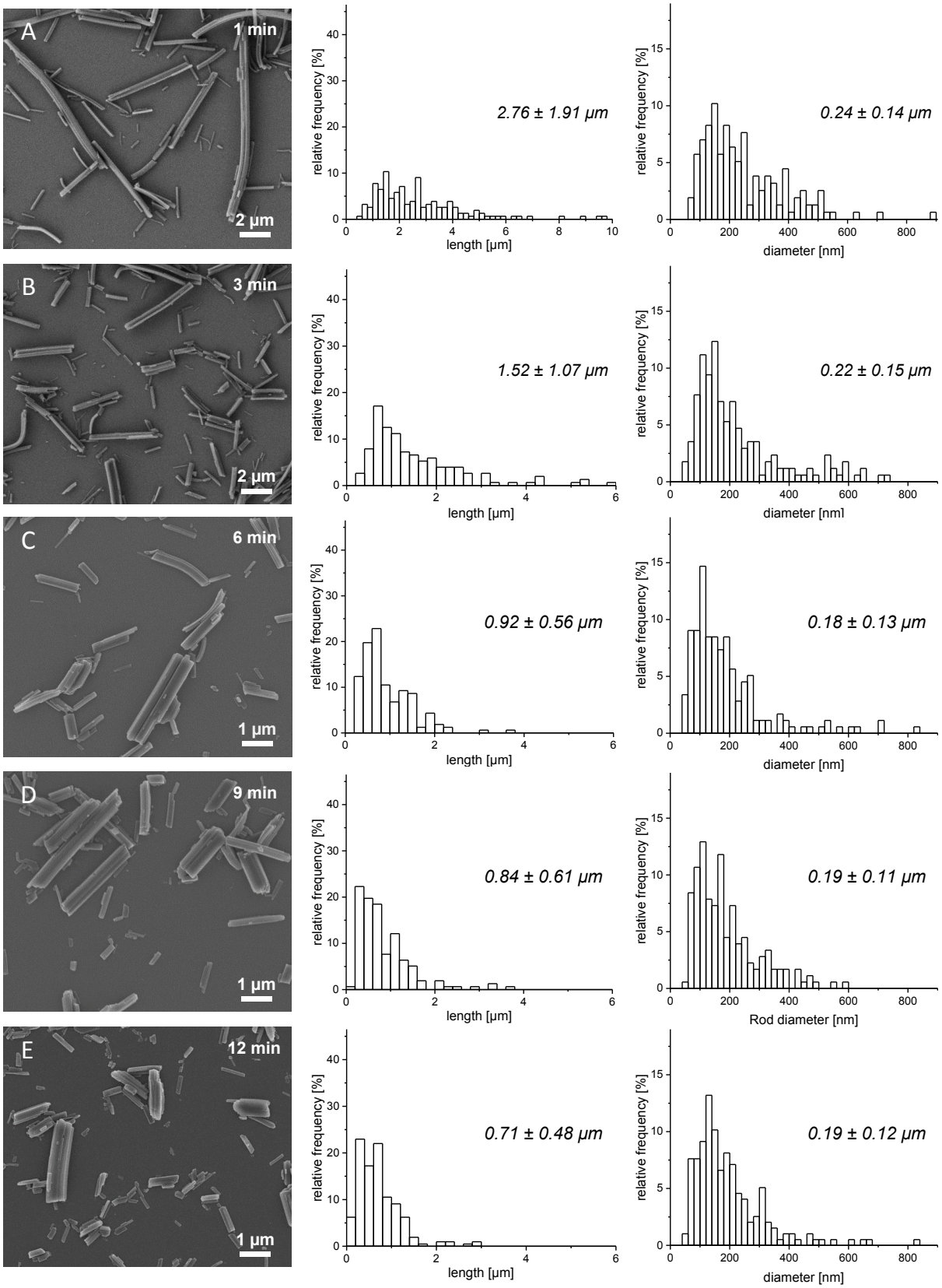
A
1 min
2 µm
2.76 ± 1.91 µm
0.24 ± 0.14 µm
B
3 min
2 µm
1.52 ± 1.07 µm
0.22 ± 0.15 µm
C
6 min
1 µm
0.92 ± 0.56 µm
0.18 ± 0.13 µm
D
9 min
1 µm
0.84 ± 0.61 µm
0.19 ± 0.11 µm
E
12 min
1 µm
0.71 ± 0.48 µm
0.19 ± 0.12 µm
relative frequency [%]
length [µm]
diameter [nm]
Rod diameter [nm]

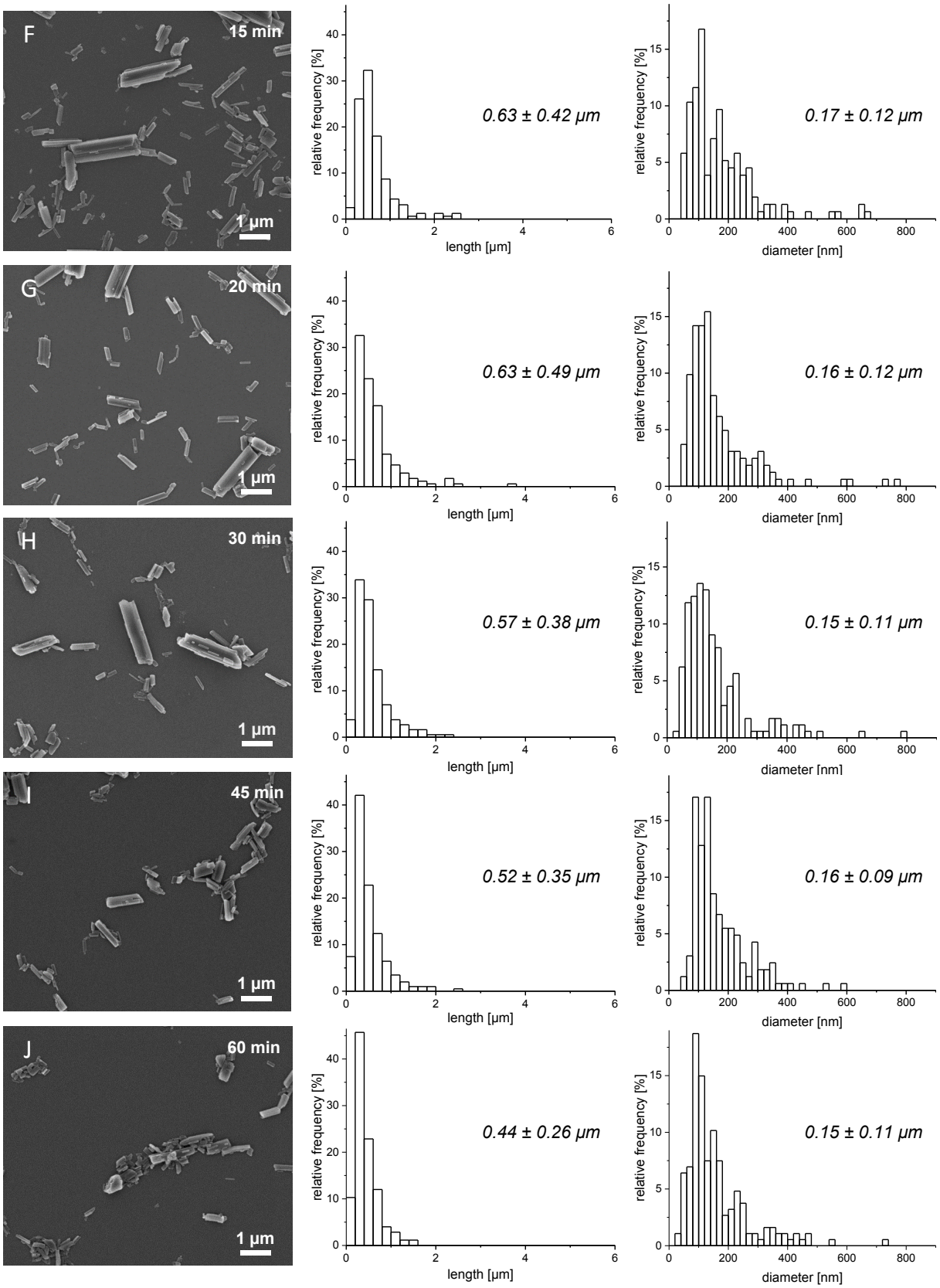
F
15 min
1 µm
0.63 ± 0.42 µm
0.17 ± 0.12 µm
G
20 min
1 µm
0.63 ± 0.49 µm
0.16 ± 0.12 µm
H
30 min
1 µm
0.57 ± 0.38 µm
0.15 ± 0.11 µm
I
45 min
1 µm
0.52 ± 0.35 µm
0.16 ± 0.09 µm
J
60 min
1 µm
0.44 ± 0.26 µm
0.15 ± 0.11 µm
relative frequency [%]
length [µm]
diameter [nm]

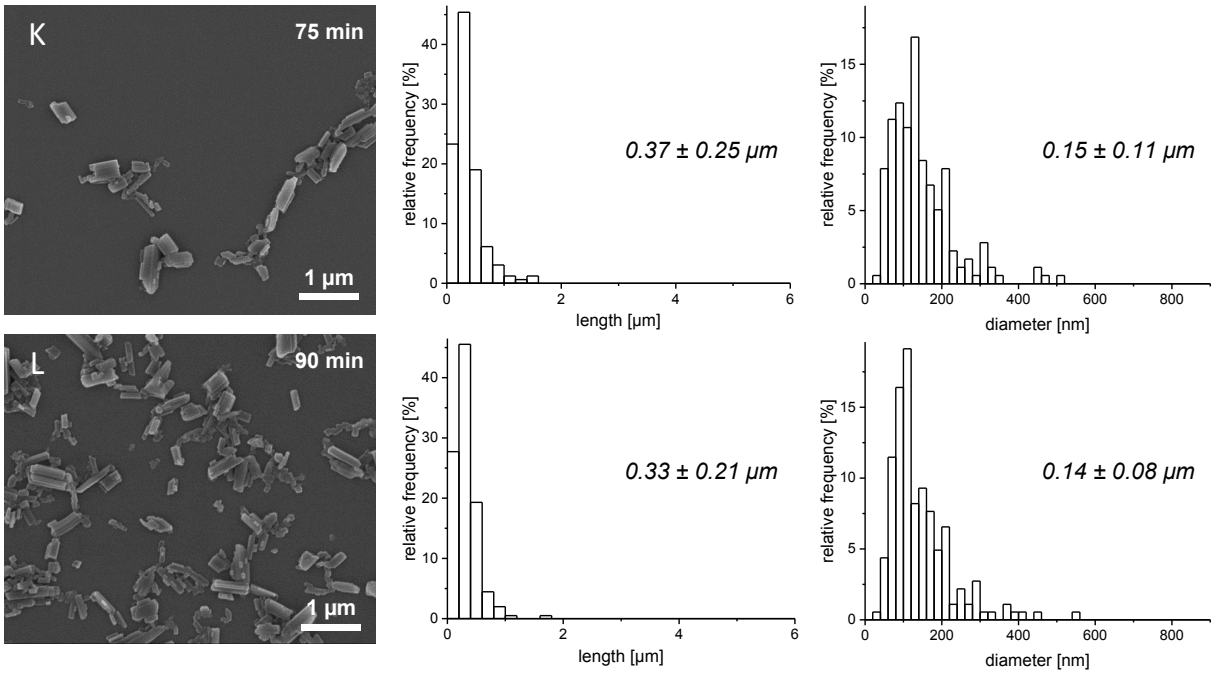

Figure 55: SEM images of nanofibers of BTA 5 after sonication in anisole for 1 min (A) to 90 min (L). BTA concentration was 1000 ppm and cooling bath temperature was -15 °C. Histograms are based on at least 150 measured fibers each. *Adopted with perm. from ref. (Steinlein et al. 2019)[127]. © (2019) John Wiley and Sons*

To quantitatively analyze temporal evolution of the lengths and diameters of the nanofibers after sonication, averages and standard deviations of all samples are displayed in Figure 56. Even after only one minute of sonication, the average fiber length has already been reduced from an initial value of 148.93 µm to 2.76 µm by a factor of 54. Upon continued sonication, this value is further reduced. For example, after 20 min the average fiber length is 0.63 µm, after 60 min it is 0.44 and after 90 min it is as low as 0.33 µm. The latter value equals a length reduction by a factor of 455 compared to the non-sonicated sample. The shorter the nanofibers become, the slower is the cutting speed, which leads to the asymptotic curve shape visible in Figure 56. This curve shape also implies a terminal value, after which no significant further cutting occurs any more. Yet, this terminal value appears not to have fully been achieved after 90 min. This means that fiber dimensions may be further reduced to some extent by increasing the sonication time. Looking at fibers' average diameters, a less pronounced reduction is observed: Within the first minute of sonication, the diameter is more than halved from 0.59 µm to 0.24 µm. By continued sonication, this value is reduced to 0.16 µm after 20 min and to 0.15 µm after 60 min. After 90 min, an average fiber diameter of 0.14 µm is reached, which represents a 4.3 times lower diameter than that of the initial

self-assembled fibers. Summarizing, both fiber dimensions are reduced drastically by sonication, whereas this effect is much more pronounced with respect to fiber length.

As shown, most of the cutting of the fibers occurs within the first 20 min of sonication. Therefore, to focus on this most interesting part of the cutting process, all further experiments were only run up to total sonication times of 20 min.

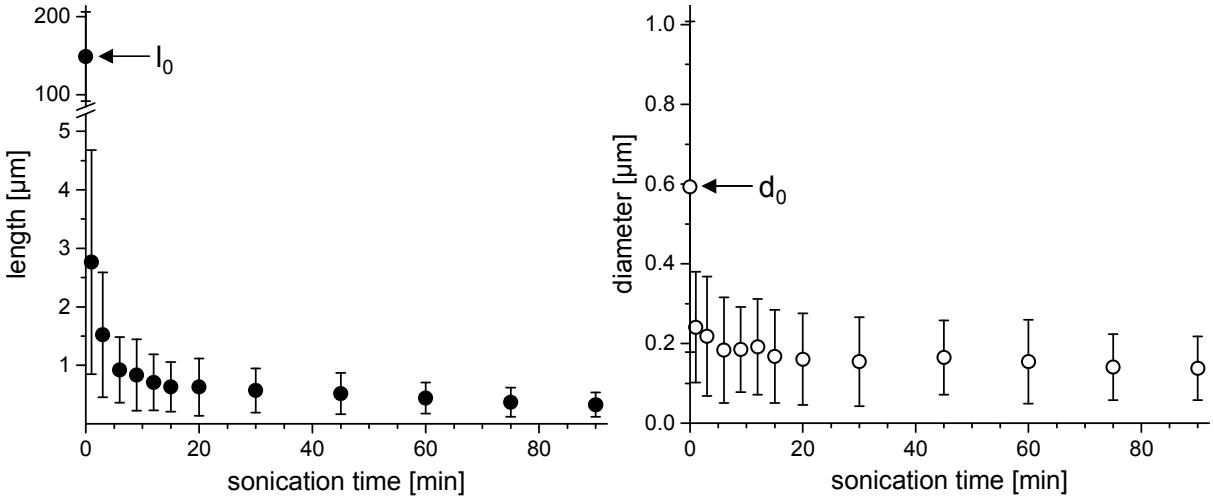

Figure 56: Temporal evolution of length (left) and diameter (right) of nanofibers during sonication. Sonication medium is anisole, BTA concentration is 1000 ppm and cooling bath temperature is -15 °C. Initial fiber dimensions l_0 and d_0 are marked. Averages and standard deviations (error bars) are based on at least 150 measured fibers each. *Reprinted with permission from ref. (Steinlein et al. 2019)[127]. © (2019) John Wiley and Sons.*

Reproducibility of these fiber dimensions is crucial to draw valid conclusions from fiber dimensions after sonication. To investigate this, one sonication experiment was run up to 20 min three times independently and samples were drawn after defined sonication times. Figure 57 gives a comparison of the resulting fiber dimensions. The plots show slight differences between fiber dimensions. For example, in the first run, the fiber length after 1 min of sonication is approx. 1.0 µm, whereas it is approx. 1.5 µm after the same time in the second run. Yet, such differences are still in an acceptable dimension, when taking the broad standard deviation of the 150 measured fiber dimensions for each data point into account. This argument is further supported by no run showing consistently lower or higher values than the others. For instance, the mentioned average fiber length after 3 min is lower in the first than in the second run. By contrast, the fiber length after 6 min is higher in the first run. Concluding, slight deviations in fiber dimensions exist, which are attributed to statistical fluctuations caused by the broad distributions of fiber dimensions. To further improve the data

basis for the following results, each experiment was conducted three times and the resulting data were merged to get a data basis of at least 450 measured fibers per data point.

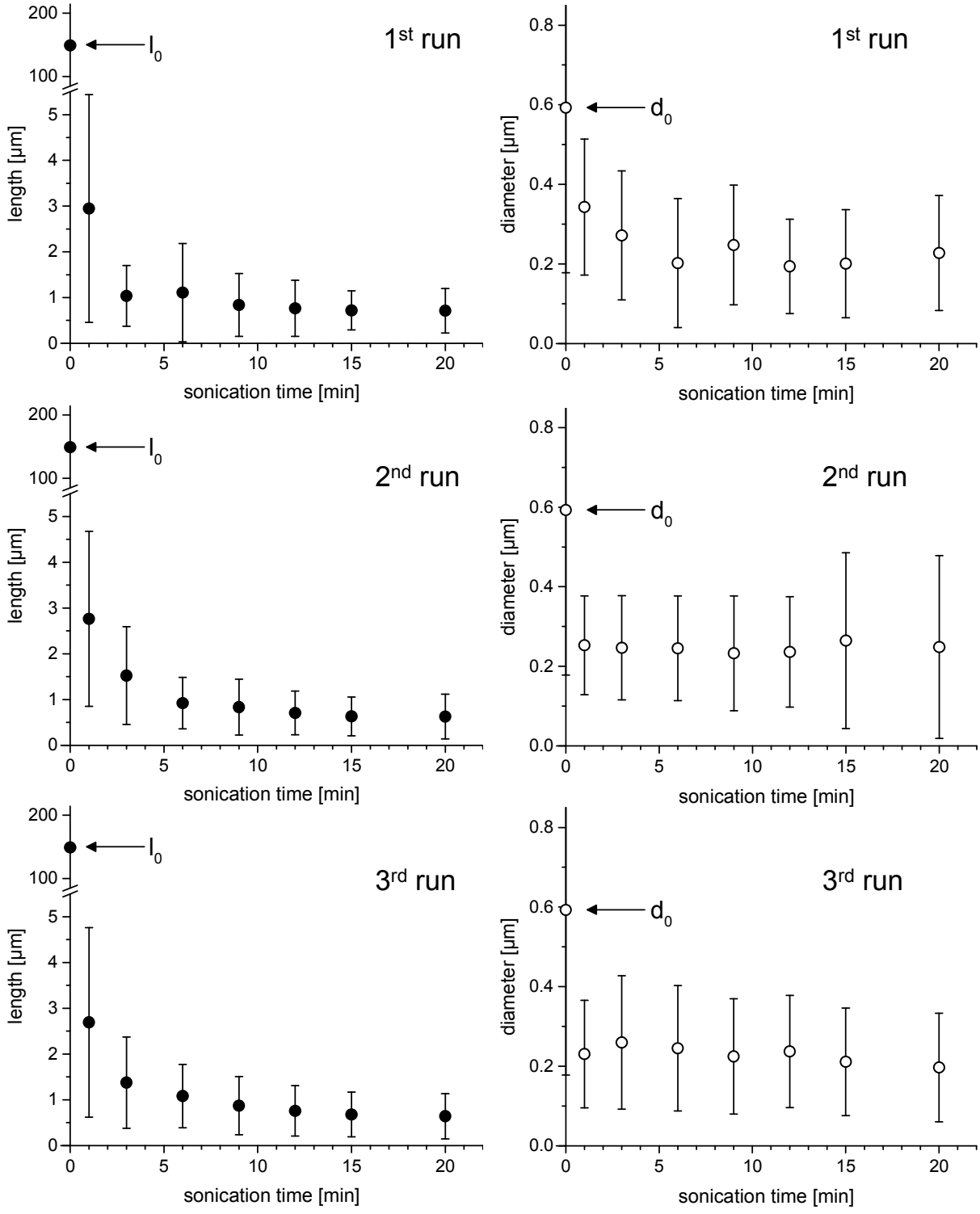

Figure 57: Temporal evolution of length (left) and diameter (right) of nanofibers during sonication during three independent runs. The sonication medium is anisole, BTA concentration is 1000 ppm and the cooling bath temperature is -15 °C. Initial fiber dimensions l_0 and d_0 are marked. Averages and standard deviations (error bars) are based on at least 150 measured fibers each. *Reprinted with permission from ref. (Steinlein et al. 2019)[127]. © (2019) John Wiley and Sons*

4.4.2. Sonication medium

Results from the previous section already indicated an influence of sonication media on fiber cutting speed. Hence, variation of sonication media was evaluated next. Based on the experiments described in the previous section, *n*-hexane, MCH and anisole were chosen as sonication media. All three media feature no significant solubility of BTA 5 at ambient temperature. Figure 58 shows a comparison of the temporal evolution of nanofiber dimensions after ultrasonic treatment for up to 20 min in all three selected solvents.

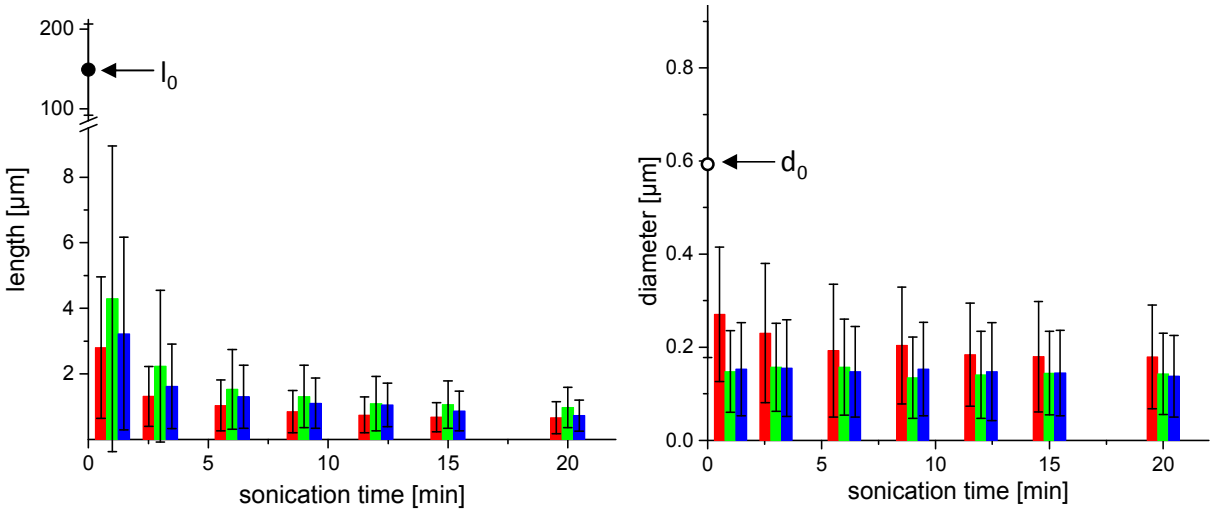

Figure 58: Temporal evolution of length (left) and diameter (right) of nanofibers during sonication in dispersions in anisole (■), MCH (■) and n-hexane (■). The dispersion concentration is 1000 ppm, the ultrasonic power amplitude is set to 50% and the cooling bath temperature is -15 °C. Averages and standard deviations (error bars) are based on at least 450 measurements per medium each.

Looking at the length of the nanofibers, clear differences between results from the three media are observed: After one minute of sonication, 4.29 µm are reached in *n*-hexane, 3.23 µm are reached in MCH and 2.80 µm are reached in anisole. This means that nanofibers from *n*-hexane are 53% longer and the ones from MCH are 15% longer than those sonicated in anisole. This huge difference decreases with further sonication. With respect to the diameter of supramolecular nanofibers, the opposite phenomenon is visible: Highest values for the diameter are achieved by use of anisole. After one minute of sonication, the average diameter is 0.27 µm using anisole and 0.15 µm using MCH or *n*-hexane. By contrast, diameters from MCH and *n*-hexane appear to be comparable throughout all sonication times investigated. From the dependency of fiber dimensions on the sonication media used arise differences in the aspect ratio. The aspect ratio of the fibers is defined as fiber length divided

by fiber diameter (*l*/*d*). After one minute, *l*/*d* equals 10.3 with anisole, 21.1 with MCH and even 29.0 with *n*-hexane. Further sonication up to a total duration of 20 min reduces aspect ratios to 3.7 for anisole, 5.3 for MCH and 6.8 for *n*-hexane. Table 8 lists selected data gained from the sonication medium variation experiments for comparison.

Concluding from all these results, average dimensions of nanofibers after sonication are dependent on the medium used during sonication. This opens a facile way to control dimensions and aspect ratios of the nanofibers: By picking the matching dispersion medium and sonication time for each aspect ratio desired, aspect ratios ought to be adjustable at least between 4 and 29. The reason for the differences between the media will be discussed later on.

Table 8: Length (*l*), diameter (*d*) and aspect ratio (*l*/*d*) of nanofibers after sonication for 1, 6 and 20 min in anisole, *n*-hexane and MCH. For each dispersion, BTA concentration is 1000 ppm, cooling bath temperature is -15 °C and the ultrasonic power amplitude is set to 50%. Averages and standard deviations (error bars) are based on three independent experiments per medium each.[127]

Sonication time [min]	**Anisole**			***n*-Hexane**			**Methylcyclohexane**		
	l [µm]	**d** [µm]	**l/d**	**l** [µm]	**d** [µm]	**l/d**	**l** [µm]	**d** [µm]	**l/d**
1	2.80	0.27	**10.3**	4.29	0.15	**29.0**	3.23	0.15	**21.1**
6	1.04	0.19	**5.4**	1.53	0.15	**9.7**	1.30	0.15	**8.8**
20	0.66	0.18	**3.7**	0.98	0.14	**6.8**	0.73	0.14	**5.3**

4.4.3. Temperature

The temperature of the dispersion during sonication is another factor known to possibly affect results achieved by ultrasonic treatment of dispersions.[114] To examine this factor's impact on the ultrasonic cutting of BTA fibers, a 1000 ppm dispersion of BTA 5 in anisole was sonicated at a power amplitude of 50% applying cooling bath temperatures of -30, -15 and 20 °C. For each temperature, temporal evolution of fiber dimensions is shown in Figure 59.

At a cooling bath temperature of 20 °C, slightly longer nanofibers were formed, compared to nanofibers from both other temperatures. For instance, after one minute of sonication the average fiber length was 2.97 µm at 20 °C, 2.80 µm at -15 °C and 2.36 µm at -30 °C. After prolonged sonication, the differences between the curves were reduced. All three curves exhibit a similar shape and the cutting speed was reduced with increasing sonication time

for all cooling bath temperatures. As far as the fiber diameter is concerned, sonication at 20 °C also tended to result in higher values. Cutting at -15 °C appears to have been slightly slower than at -30 °C, but this small effect is superimposed by the standard deviations of the length averages from three independent runs of the same experiment, respectively. All in all, there appears to be a slight decrease of cutting speed with increasing temperature. In literature, this effect is attributed to lower energy release upon collapse of cavities, which had been formed by ultrasound beforehand, in warmer media.[114]

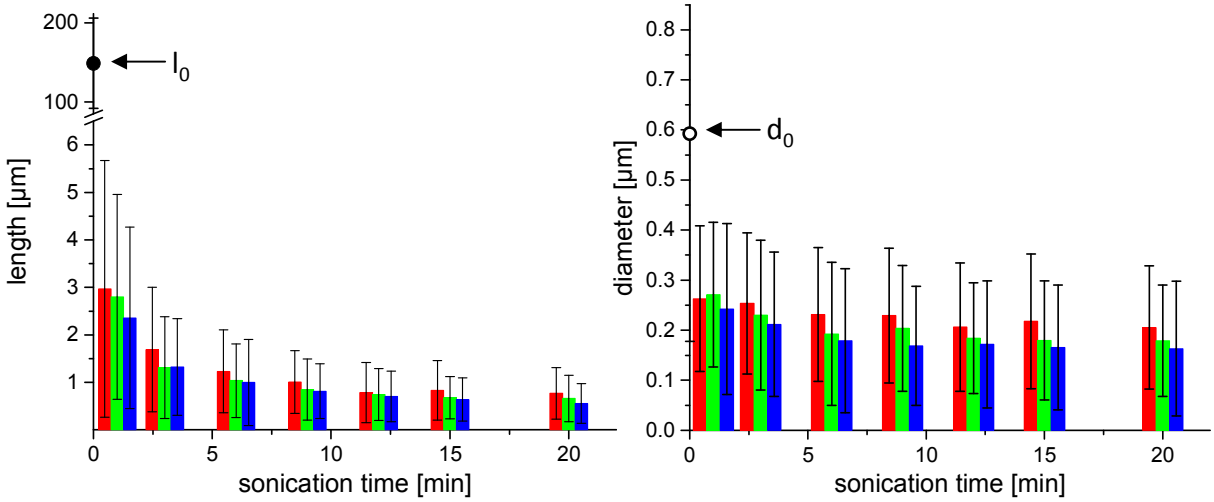

Figure 59: Temporal evolution of length (left) and diameter (right) of nanofibers during sonication in anisole at cooling bath temperatures of 20 °C (■), -15 °C (■) and -30 °C (■). BTA concentration is 1000 ppm and the ultrasonic power amplitude is set to 50%. Averages and standard deviations (error bars) are based on at least 450 measured fibers per temperature each.

Summarizing, it can be stated that the temperature of the medium cooling the sonicated dispersion plays a minor role in the ultrasonic cutting of BTA 5, at least in the temperature window investigated. At higher temperatures, additional effects due to partial dissolution of the BTA would expectantly have to be taken into account.

4.4.4. Concentration of BTA fibers

The concentration of BTA fibers in the sonicated dispersion is the last processing parameter investigated. Variation of this parameter yields information on the cutting mechanism of supramolecular fibers: In principle, cutting can either occur upon interaction of fiber and

imploding ultrasound-induced cavity or upon collision of two fibers, which are accelerated by implosions of cavities. In the first case, the cutting speed is independent of the fiber concentration, whereas in the second case it depends on the number of fiber-fiber collisions, which rises by the squared fiber concentration.[123] For this investigation, eligible concentrations were limited: BTA 5 was found to be insoluble in anisole at ambient temperature. Nevertheless, at high temperatures, as they can locally be generated by ultrasound, it is likely to be soluble to some small extent. Using high concentrations, this effect can be neglected, but at very low dispersion concentrations it might become significant. Therefore, the lowest concentration chosen was 50 ppm. On the other hand, at high concentrations, the initial long fibers render the viscosity of the dispersion very high, which is attributed to entanglements of the fibers. This effect could also influence the fiber cutting results and therefore was avoided by choosing 2000 ppm of BTA 5 as the highest concentration. As a third concentration, 1000 ppm were chosen, which is the standard concentration used for all sonication experiments described so far. Figure 60 shows the temporal evolution of nanofiber dimensions upon sonication of dispersions comprising 2000, 1000 and 50 ppm of supramolecular fibers in anisole. The cooling bath temperature in the experiments shown is -15 °C and the ultrasonic power amplitude is 50%.

There is no significant difference visible between experiments with 1000 or 2000 ppm of BTA 5, with respect to both, length and diameter. By contrast, fibers from sonication of 50 ppm dispersions are significantly larger in both dimensions. For example, an average length of 1.31 µm is achieved after 3 min of sonication with 1000 ppm, while it takes twice as long, i.e. 6 min, to achieve a comparable average length of 1.34 µm with 50 ppm. This means that the cutting speed is approximately halved in this region for the 50 ppm sample. As described by Zeiger and Suslick, a linear correlation between concentration and particle size would be expected, if particle breakage was exclusively caused by fiber-fiber collisions and the decrease of the cutting rate with smaller fiber size was neglected.[123] Comparing the samples with 50 and 1000 ppm of BTA 5, this would mean a 20 times higher cutting speed for the 1000 ppm sample. Even if the decrease of the cutting speed with smaller fibers is considered, a much higher difference than the observed factor of two (or less, if comparing other data points) would be expected for exclusive cutting by collision of fibers. This means, that such collisions are not the predominant cutting mechanism. Yet, they may play a minor role and thus cause the differences found for different BTA concentrations. These findings

are in good agreement with those by Zeiger and Suslick. Investigating the fragmentation of three-dimensional crystals of acetylsalicylic acid, they reported direct interactions between cavities and the particles to be the dominating fragmentation mechanism. At the same time, they found the cutting speed to slowly increase with higher particle concentrations, the same way as it is demonstrated here.[123]

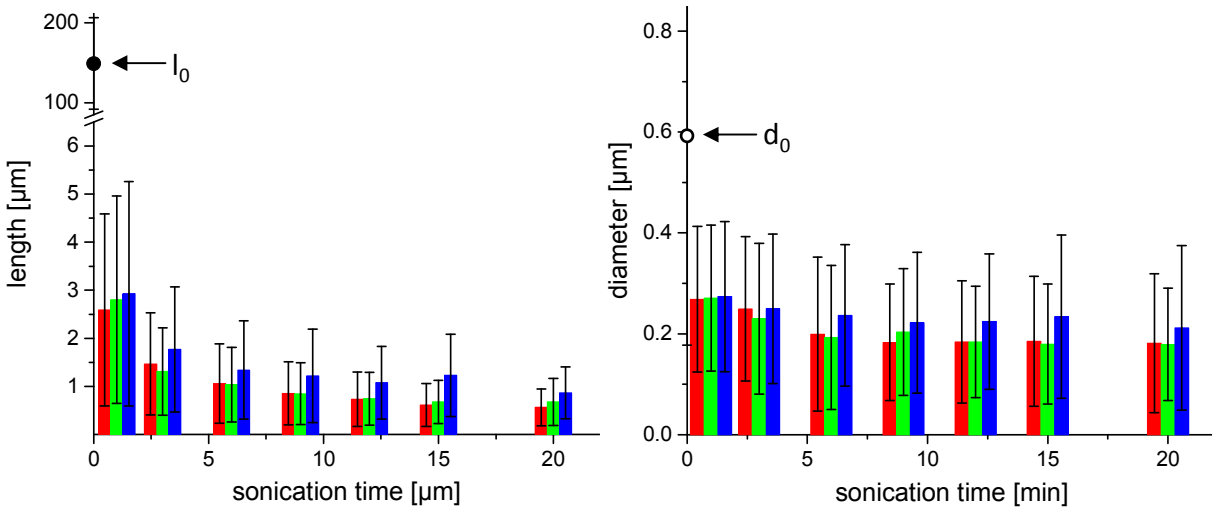

Figure 60: Temporal evolution of length (left) and diameter (right) of submicron objects upon sonication in anisole at supramolecular BTA fiber concentrations of 2000 ppm (■), 1000 ppm (■) and 50 ppm (■). Cooling bath temperature is -15 °C and the ultrasonic power amplitude is set to 50%. Averages and standard deviations (error bars) are based on at least 450 measurements per concentration each.

All in all, it was found that the impact of the BTA concentration is small, with lower concentrations resulting in slightly larger fibers. Since this affects fiber length as well as fiber diameter, the aspect ratio cannot be altered by this parameter. From the comparison of cutting speeds at different concentrations it can be concluded that fiber-fiber collisions are not the predominant cutting mechanism.

4.4.5. Underlying factors determining ultrasonic fiber cutting

As described above, an influence of the chemical nature of the medium as well as an influence of the cooling bath temperature on the dimensions of nanofibers was found. Since both parameters alter characteristics like e.g. viscosity of the media, both effects might be traced back to such a solvent property. There are three main parameters in question to

cause the size differences of nanofibers upon ultrasonic treatment: 1) Surface energy of the medium. The surface energy difference between BTA and medium governs the free energy at this surface, which in turn influences the ultrasound-induced formation of cavities at this surface. 2) Vapor pressure of the medium. When a cavity is formed, the vapor pressure of the medium governs its filling with solvent vapor due to medium evaporating at the surface of the cavity. The higher the vapor pressure, the more gaseous medium will enter the cavity, building up an internal pressure. When the cavity finally collapses, a higher internal pressure will decrease the energy released by that collapse.[129] 3) Viscosity of the medium. Energy from the collapse of a cavity is transported to the dispersed solid fibers by the flow induced by solvent filling the imploding cavity. This flow is governed by viscosity.[116,117] To identify the dominant factor behind supramolecular fiber cutting, possible correlations of all three parameters with the average fiber length were investigated. The applied average fiber lengths were taken after sonication of a dispersion of 1000 ppm of supramolecular fibers of BTA 5 with an ultrasonic power amplitude of 50% for 20 min. To achieve a variation of solvent parameters, data from medium and temperature variation experiments described above were applied together and the respective solvent properties were determined from literature data. For the viscosity, a very strong correlation was found, which is displayed by the plot in Figure 61. The graph shows a plot of fiber length versus viscosity of the medium. Viscosities for anisole were extrapolated using various literature data[130,131,132] while for *n*-hexane and MCH they were calculated using an equation from literature[103]. For the viscosity of the medium, a very strong linear correlation, at least in the viscosity range displayed, is observed.

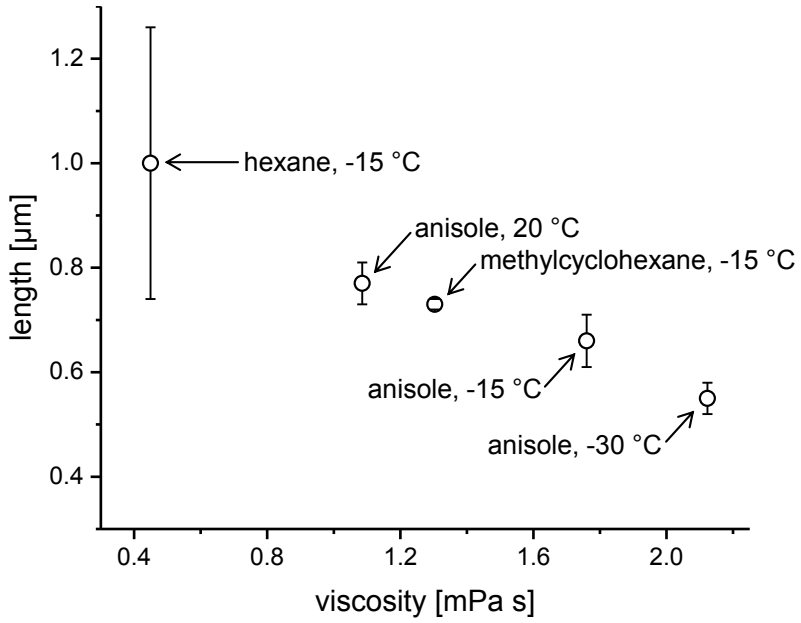

Figure 61: Plots of average fiber lengths after 20 minutes of sonication versus viscosity of dispersion media. Media are anisole, MCH and *n*-Hexane. Besides the standard cooling bath temperature of -15 °C, for anisole also data with cooling bath temperatures of 20 °C and -30 °C are presented. Dispersion concentration was 1000 ppm and the ultrasonic power amplitude was set to 50%. Averages and standard deviations shown are based on three independent experiments each. *Adapted with permission from ref. (Steinlein et al. 2019)[127]. © (2019) John Wiley and Sons* [127]

Secondly, possible correlations with the medium's surface energy were examined. Surface energies used in this were calculated using data provided by Yaws.[133] The plot of fiber length after 20 min of sonication versus surface energy showed a certain correlation of both parameters, with a higher surface energy yielding shorter nanofibers. Nevertheless, this correlation was much weaker than the one found between viscosity and fiber length.

Thirdly, vapor pressures of media and average fiber length were correlated. Here, a positive correlation of medium's vapor pressure and average fiber length after sonication was observed. This correlation is stronger than the one for the surface energy, as it was expected concluding from considerations described in literature.[114,129] Nevertheless, it is still significantly weaker than the correlation with viscosity. All values for vapor pressures were calculated using literature data.[103,133,134,]

Based on the comparison of these three solvent properties, the viscosity of the medium was identified as the factor having the strongest impact on the length of nanofibers after sonication. Hence, it is exclusively plotted in this thesis. Nevertheless, both other parameters also show relatively good correlation strengths and therefore are supposed to exert at least

some influence on the fiber length. A clearer analysis of these three factors is hindered by the difficulty of varying single factors independently: Media with high surface energy typically feature lower vapor pressure and higher viscosity and vice versa. Hence, it is hard to clearly discriminate the individual contributions of these three solvent properties to fiber length after sonication.

The massive influence of the sonication medium's viscosity on the cutting of fibers has also been described in literature by Huang *et al*.: They used a formula indicating a negative correlation of viscosity with the square of the terminal length approached by fibers upon extensive sonication.[117] By contrast, the correlation found in this work appears linear, at least in the investigated viscosity range. A possible explanation for these divergent results is that, the fiber lengths applied here are taken after only 20 min of sonication. Hence, they do not represent final lengths approached after long sonication, as can be seen from Figure 56, where even after 90 min of sonication further fiber length decrease is visible. This means that in this work a length slightly different from the terminal fiber length used by Huang *et al.* is correlated to the medium's viscosity.

4.5. Conclusions

The major subject of this chapter deals with the dimensional control of supramolecular submicron fibers of 1,3,5-benzene¬trisamides via a top-down approach. In particular, the length control as well as the aspect ratio of such fibers was addressed via ultrasound.

In a first step, the preparation of supramolecular fibers based on a BTA with *tert*-butyl substituents (BTA 5) in large amounts by self-assembly upon cooling was successfully conducted. Self-assembly was performed using hydrocarbons as media in a batch process with a solution mass of up to 1.5 kg, yielding up to 0.75 g of supramolecular BTA fibers per batch. The obtained supramolecular fibers feature average diameters in the range of a few hundred nanometers and an average length around 150 µm.

In a second step, suitable conditions for sonication experiments were identified. Thus, a setup for reproducible sonication experiments was established. It consists of an ultrasonic horn immersed into the sample dispersion. A sonication program including sufficient breaks and a cooling bath were applied to avoid excessive heating of the sample during sonication. With a water bath, the ultrasonic power exerted by this setup was determined to be 13, 23 and 32 W when setting the amplitude of the sonication device to 30, 50 or 70%, respectively. Anisole, *n*-hexane, toluene and methyl cyclohexane were identified as media suited for dispersion of BTA 5 and subsequent sonication, as they yielded well-defined nanofibers upon sonication. In addition, the dependency of the fiber cutting speed on the ultrasonic power amplitude was tested. It was found, that the overall applied ultrasonic energy, i.e. the product of applied ultrasonic power amplitude and sonication time, plays a major role. By contrast, the ultrasonic power amplitude itself had no major impact. Hence, for all further experiments, the power amplitude was fixed and the sonication time, correlating with the ultrasonic energy, was altered. As a result of these experiments, a standard set of parameters, i.e. anisole as medium, a dispersion concentration of 1000 ppm and a cooling bath temperature of -15 °C was established.

In the third section, BTA 5 was used as a model BTA for a detailed study of the impact of sonication process parameters on the dimensions of the obtained fibers. Based on the results from the second section, the parameters sonication time, sonication medium, cooling bath temperature during sonication and supramolecular BTA fiber concentration in the sonicated dispersion were tested. It was found that the fiber length was reduced from 148.93 µm to 2.76 µm, i.e. by a factor of 54, within only one minute of sonication.

Furthermore, with decreasing fiber length the cutting speed decreased, indicating, that it will approach zero after sufficient sonication time. Hence, terminal nanofiber dimensions which than cannot be reduced any more, should be reached then. Yet, this state has not been reached even after 90 min of sonication for the applied system. After 90 min, which was the longest sonication time applied in this work, averages for nanofiber length and diameter were 0.33 µm and 0.14 µm. Variation of the concentration of BTA in the sonicated dispersion (50, 1000 and 2000 ppm) and of the cooling bath temperature (-30, -15 and 20 °C) only shows minor impact on the fiber dimensions after sonication. Thereby, increased concentration and decreased temperature yield smaller fibers after sonication, respectively. By contrast, the dispersion medium reproducibly exhibited significant impact on the nanofibers' length and diameter. For example, sonication for 20 min in *n*-hexane yielded nanofibers with an average length of 0.98 µm and an aspect ratio of 6.8, while sonication in anisole under the same conditions yielded an average fiber length of only 0.66 µm and a much lower aspect ratio of 3.7. This finding allows control of length and aspect ratio of BTA nanofibers in the future by choosing appropriate sonication media and total sonication energies. Finally, the viscosity of the sonication medium was found to explain as well the influence of temperature as the one of sonication medium on fiber length after sonication. Therefore, it is thought to be the other decisive parameter for the cutting speed of BTA supramolecular fibers by ultrasound, besides the ultrasonic energy applied.

To conclude, it was shown that ultrasonication is a straightforward top-down method to produce supramolecular submicron short fibers with controlled fiber lengths and aspect ratios. These findings may pave the way to use the submicron short fibers as seeds for the production of long BTA nanofibers with small size dispersity via a seeded growth process. Moreover, these submicron short fibers may be suitable to be homogeneously dispersed into polymer matrix materials feasibly, where these objects can act as nucleating sites for the foam cell nucleation or the crystal nucleation.

5. Supramolecular cell nucleating agents for foam extrusion of *i*-PP

5.1. Polymer foams

5.1.1. Polymer foam fundamentals

Generally, foams are referred to as a discontinuous gaseous phase dispersed in a continuous liquid or solid phase.[135] For polymer foams, the continuous phase consists of a polymer. Due to this morphology, polymer foams provide several outstanding properties, which bring their wide use in different applications. Perhaps the most prominent property of polymer foams is their low thermal conductivity, which renders them interesting for thermal insulation applications.[136] Good energy absorption, i.e. shock absorption, is another property of polymer foams: Energy is absorbed by buckling of the foam's cell walls. With an elastomeric polymer phase, this buckling is mostly elastic. After deformation, the energy is again released.[136] This is used in applications like e.g. sports shoes. If a rigid polymer phase is applied, cells are irreversible deformed due to brittle failure of cell walls, as it is the case e.g. for PS foams. Nevertheless, these materials are good in absorbing the first impact, as it is important in packaging applications, for instance.[136] In this context, it is also of importance, that polymer foams generally feature low densities compared to compact solids. Moreover, depending on the cell sizes, polymer foams can feature much better specific mechanical properties, i.e. a much better property per weight ratio. This makes them important for lightweight construction applications, particularly in the transportation sector.[135]

Polymer foams are typically classified along their structural properties like density, cell size, cell density and open cell content.[136] The foam density is an intuitive parameter widely used for the description of polymer foams. Usually, it is determined by the buoyancy method (Archimedes method). There are several numbers associated with the foam density ρ_F: The expansion ratio Φ equals ρ_F divided by the density of the compact polymer ρ_P. Φ is connected to relative density ρ_{rel} and void fraction υ_F via equation 4:[137]

$$\Phi = \frac{\rho_F}{\rho_P} = \frac{1}{\rho_{rel}} = \frac{1}{1 - \upsilon_F} \tag{4}$$

Using the expansion ratio, foams are classified into high-density ($\Phi \leq 4$), medium-density ($4 < \Phi < 10$) and low-density ($\Phi \geq 10$) foams.[138] Another important property of foams is the cell size. Typically, it is measured by means of SEM at cut or cryo-fractured surfaces of foam

samples. Apparent cell areas are taken from SEM micrographs. For each apparent cell area, a circle featuring the same area is calculated and the circle's diameter is taken as cell diameter, as it is depicted in Figure 62.

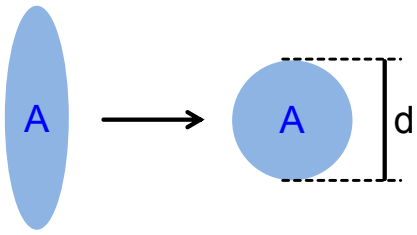

Figure 62: Procedure for the determination of cell diameters. Left: The area A of the cell is determined. Right: A circle of area A equivalent to the one of the cell section is calculated and its diameter d is taken as cell diameter.

Yet it is commonly applied, results generated via this procedure should be taken with care: When a foam with randomly placed cells is cut by a plane, the cells are mostly not cut at the plane showing their average (or largest) intersectional area. This causes a broad distribution of cell diameters measured, even if the foam solely contained monodisperse spherical cells, as shown in Figure 63.[139]

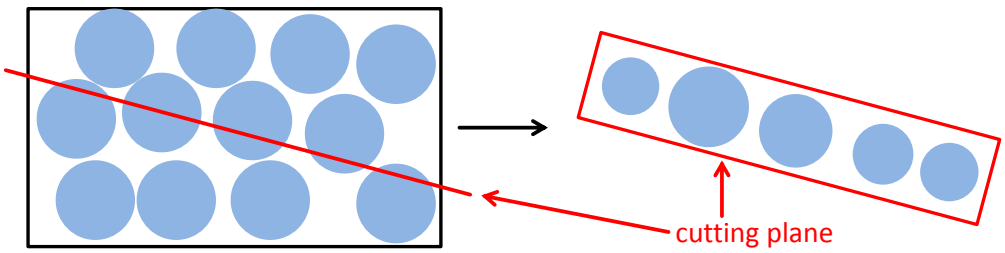

Figure 63: Left: Two-dimensional representation of a section (red) through a foam comprising ideal monodisperse spherical cells. Here, the cutting plane is seen from the side. Right: View onto the cutting plane. Most cell diameters appear smaller here, as they originate from cells not cut in the middle. The left side of this figure is adapted from Park (Park 2017)[139].

Despite these limitations, the cell size is very popular in describing foams. Based on this number, a classification into conventional, fine-celled, microcellular and nanocellular foams is made.[67] As the cell size does not allow conclusions on the number of cells in a foam, a third common number for foam characterization, the cell density, i.e. the number of cells

within a certain foam volume, typically within one cubic centimeter, is necessary. For cell density determination, similar SEM micrographs as for the cell diameter are used. The number of cells n on each micrograph is counted (also considering cells only partly on the image) and the area of the sample A_S depicted on the image is calculated. Using equation 5, this 2D-information is expanded into the final cell density in 3D-space.

$$cell\ density = (\frac{n}{A})^{1,5} \quad (5)$$

The respective cell size and cell density limits for the classification into conventional, fine-celled, micro-cellular and nanocellular foams are listed in Table 9.

Table 9: Classification of foams based on cell size and cell density.[67]

Foam type	**Cell size [µm]**	**Cell density [1/cm^3]**
Conventional	> 300	< 10^6
Fine-celled	10 – 300	10^6 – 10^9
Microcellular	0.1 – 10	10^9 – 10^{15}
Nanocellular	< 0.1	> 10^{15}

Small cell diameters and high cell densities are typically beneficial for foam properties like thermal insulation and impact strength. The next section provides a closer look at the foaming process with a focus on the improvement of these two properties.

5.1.2. Foaming process

The foaming process can be divided into polymer/gas homogenization, foam cell nucleation, foam expansion and foam stabilization, as they are schematically depicted in Figure 64.[139,140,141] These four steps are used as a guideline in this chapter to lead through the process of polymer foam generation from thermoplastic polymers. In addition, a short discussion of means to reduce cell size and enhance cell density in each step is given.

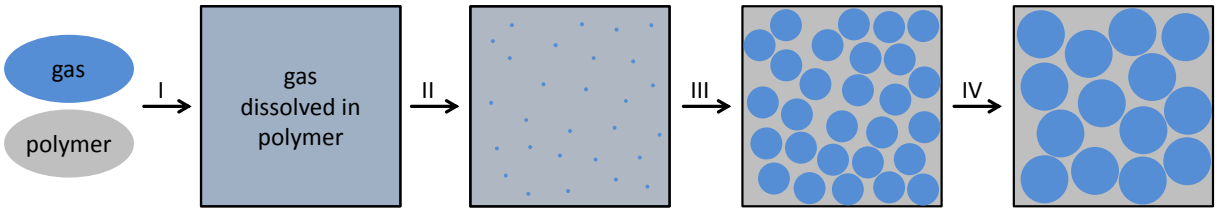

Figure 64: Schematic representation of the single steps in the foaming process: I) Homogenization. II) Foam cell nucleation. III) Foam expansion. IV) Foam stabilization.

The first step for the preparation of polymer foams is the homogenization of gas and polymer melt. Gas used in this process may either stem from a physical blowing agent (e.g. CO_2 or N_2) or be formed during the homogenization step by release from a chemical blowing agent. In this step, the gas is dissolved in the liquid polymer and the gas concentration is equilibrated in the whole material by diffusion. To obtain homogeneous foam in the end, complete dissolution of the gas in this first step is of particular importance.

The second step is the nucleation of the foam cells. To induce nucleation, normally the pressure is released, so that the polymer/gas phase becomes supersaturated. For homogeneous small cells, a nucleation density N_N as high as possible is needed. The nucleation density N_N here is understood as the number of supercritical nuclei formed in a given volume of polymer/gas phase. Assuming that all nuclei have grown into foam cells, it can be estimated from cell density and expansion ratio Φ of the final foam according to equation 6:[142,143]

$$N_N = cell\ density \times \Phi \tag{6}$$

In practice, the actual nucleation density will most likely be higher than the one calculated using equation 6, as not every nucleus grows into a cell and several cells can unite to form one larger one. There are several methods to enhance nucleation density: A common way is intentional heterogeneous nucleation at the surface of added nucleating agents. Offering sufficient nucleation sites this way, more cells are nucleated.[143] Besides, nucleation can be facilitated by increasing the supersaturation of the melt, i.e. dissolving more gas, which may require higher pressure.[143] Finally, the pressure drop rate plays a key role: As the third step, cell growth, and nucleation in practice occur parallel to each other, they compete for dissolved gas. Hence, the pressure should drop as quickly as possible to induce at best

instantaneous nucleation in the entire polymer melt.[143,144] Furthermore, simultaneous nucleation reduces Ostwald ripening, i.e. further growth of larger cells on the expense of smaller nuclei.

The third step is foam expansion due to growth of foam cells. Here, supercritical nuclei start to grow into foam cells. This process is driven by gas diffusion from the supersaturated melt into the foam cells. As a result, the melt is depleted of gas around each growing foam cell, which hinders further nucleation in direct vicinity of the cell.[144] When a cell expands, the polymer layer at its surface is prone to biaxial stretching. If the melt strength of the polymer is insufficient, this layer forming the cell wall between two cells may rupture, which results in cell coalescence, i.e. both cells unite into a larger one. To suppress this process decreasing cell density, the melt strength of the polymer must be enhanced. This can be achieved by reducing the melt temperature. Unfortunately, the melt viscosity also raises upon cooling, rendering the melt too viscous for foam processing at a certain temperature.[145] From these two limitations, i.e. too low melt strength at high temperatures and too high viscosity at low temperatures, the so-called foaming window arises. It describes the temperature window, where the material can be foamed.[146] Amorphous polymers generally feature a slow decrease of viscosity in the foaming temperature region and hence provide a wide foaming window, which allows easy processing. By contrast, the beginning crystallization of semi-crystalline polymers causes a rapid increase of viscosity in the critical temperature region, rendering the foaming window much narrower.[145] For example, linear *i*-PP exhibits a foaming window of only up to 4 °C[145], which is hard to realize in an industry-scale process. To overcome this problem, long-chain branched polymers are frequently applied, because they provide increased melt strength at elevated temperature, thus widening the foaming window.[137,146,147] Generally, determination of the melt strength under realistic conditions is hard, as this includes biaxial stretching under high pressure to allow investigation of gas-loaded polymer melts. Commonly, at least relative values can be obtained by extensional rheology (Rheotens experiment).[137] In this experiment, the polymer melt without any blowing agent is extruded through a die and the strand is hauled off. During the measurement, the haul-off speed is increased to enhance the extensional strain exerted on the melt strand. Hereby, the melt strength is understood as the maximum stress the strand is able to bear prior to rupture.

The fourth and final step of the foaming process is foam stabilization. Stabilization is caused by decreasing foam temperature, which enhances the viscosity of the polymer. This increased viscosity raises the force necessary for further cell expansion and, consequently, stops foam expansions. This is supported by the melt being depleted of gas, which ceases the plasticizing effect of the gas. During the foam stabilization step, expansion ratio and shape of the final foam can be adjusted to some extent: Fast freezing of the foam prevents excessive loss of gas to the surrounding air by diffusion through the outer foam skin or cell wall rupture. Hence, it increases the expansion ratio of the foam, which is of particular importance for small foamed parts with a high surface to volume ratio.[148] To accelerate freezing of the foam, e.g. a water bath or a cooled mold, depending on the processing method chosen, can be applied. Besides that, the foam can also be shaped, e.g. by a thickness calibration unit in the case of foam extrusion.[148] At the end of this step, solid polymeric foam is obtained.

5.1.3. Thermoplastic foam processing

The foaming process described in the previous section can be realized in different ways. For thermoplastic polymers, which are exclusively treated here, foam extrusion, batch foaming, foam injection molding and particle foam processes are widely used. All these techniques are shortly introduced here, whereby the main focus is on foam extrusion, as it is the foam processing technique applied in this work. Moreover, a short introduction to chemical and physical blowing agents (CBAs and PBAs), which can be used in these processing techniques, is given.

Foam extrusion is perhaps the most straightforward processing technique presented here. During foam extrusion, only the first step described above, homogenization, takes place in the extruder, while all subsequent steps are located outside of it. In the extruder, first the raw polymer is plasticized. Next, the blowing agent is injected (PBAs) or gas is released by the elevated temperature (CBAs). This gas subsequently has to be dispersed in the polymer to accelerate dissolution. As the gas typically acts as a plasticizing agent, the melt temperature must normally be lowered towards the extrusion die to approach the foaming window, while the pressure simultaneously is increased. Finally, the die should cause a high pressure drop rate to reduce cell size.[144] Extrusion into a water bath or calibration allows

control of the cooling profile and the shape of the final foam to some extent. In principle, the whole extrusion process can be realized using a simple single-screw extruder. In case additives must be dispersed, a twin-screw extruder typically yields better results.[135] To facilitate control of the temperature profile within the process, a tandem extrusion line is applied frequently.[137] Here, the gas is injected (or released) at the end of the first extruder, where the highest melt temperature of the process is found. The second extruder is applied to solve the gas and to cool the gas-loaded melt. Therefore, it has to build up pressure towards the foaming die. This particular setup including a tandem extrusion line is applied in this work and hence is described more in detail at the practical example in chapter 5.4.

Foam injection molding is another industrial relevant foam processing technology. It is very similar to foam extrusion with respect to the first foam processing step: Homogenization of polymer and gas takes place in the barrel of the injection unit. The difference here is that the gas-loaded melt is not extruded continuously, but is held back by a valve in the nozzle to form a cushion between nozzle and screw. All other foaming steps occur when the gas-loaded melt is injected into the mold. In the simplest case of a standard mold, nucleation and foam expansion immediately start upon injecting, due to the ambient pressure in the mold. The stabilization of the foam is induced by the mold's cold walls. Typically, the melt volume injected is lower than the volume of the cavity to allow foam expansion ("short-shot"). A problem associated with this simple method is the low control of foaming. During expansion, the foam fills the mold beginning at the end adjacent to the nozzle. This leads to cells being elongated along the direction of expansion, which causes anisotropic foam properties. In addition, the foam density within the molded part usually is lowered with increasing distance from the nozzle. To suppress this effect, a counter-pressure can be applied to the cavity.[148,149] Another option for better control of the foaming is the so-called breathing mold technology: Here the cavity is completely filled with melt, which at first prevents foaming. Then, the cavity's volume is abruptly increased, which instantly induces foaming.[150] In injection molding, foams typically feature a comparably thick non-foamed skin layer, which is caused by the cold mold surface freezing the outer melt layer before foaming of this region can occur. This layer formation can be governed by tempering the mold prior to injection. Over all, foam injection molding offers good control of molded foam parts in terms of shape and foam density, the latter being precisely adjusted by the filling grade of the cavity. A major drawback is the formation of foams being inhomogeneous in their

properties, which can only be reduced by elaborated machinery and process conditions, as described above.

In research, where mostly small material amounts are required, batch foaming often is the processing technique of choice. Two methods of thermoplastic batch foaming can be distinguished based on whether foaming is induced by a pressure drop or raising temperature. Pressure-induced batch foaming is somewhat similar to the previously presented industrial techniques: A compact polymer sample, which is typically disc-shaped, is heated to foaming temperature in an autoclave and saturated with gas at high pressure. Since there is no mechanical mixing associated with this process, saturation of the molten polymer sample may take up to several hours, depending on the sample's dimensions. When saturation is reached, the pressure is rapidly released to induce foaming. By contrast, in temperature-induced batch foaming the sample is saturated with gas below the foaming temperature. Thus, no foaming is induced by the subsequent pressure release. Foaming only starts when the sample is subsequently immersed in a liquid bath at foaming temperature,.[137,138] Temperature-induced batch foaming does not work well with semi-crystalline polymers, as gas saturation happens below the polymer's melting temperature. Hence, crystalline regions are present, into which no or almost no gas diffuses, resulting in inhomogeneous foams. In addition, crystalline regions act as a barrier for the gas and hence drastically slow the saturation of the polymer's amorphous regions. Advantages of batch-foaming are low equipment costs and small sample size. Furthermore, processing conditions can easily be varied and adjusted. Its major drawback is the discontinuous process and the limited sample thickness due to saturation occurring only by diffusion. Both result in a very limited throughput, rendering this process interesting rather for research than for production.

Particle foaming is the last foam processing technology presented here. It typically includes three independent steps: At first, the polymer particles (normally beads) are formed. Secondly, the particles are loaded with a physical blowing agent and pre-foamed. Finally, the pre-foamed particles are filled into the mold and further foamed and fused together at elevated temperature using steam, obtaining the final foamed part.[139,148] Advantages of this procedure are the access to various shapes of the foamed parts and good control of foaming conditions due to the separation of the process into independent steps.

Foaming or blowing agents for foam processing of thermoplastic polymers are subdivided into physical (PBAs) and chemical blowing agents (CBAs) by the way they provide the gas needed for foaming. PBAs are inert (supercritical) liquids or gases, which diffuse into the sample or are injected into the polymer melt during foam processing. They dissolve in the polymer without any chemical reactions. PBAs must meet various requirements like e.g. inertness, safety, sufficient solubility in the polymer melt under pressure, low solubility in the polymer at ambient pressure, a boiling point adequate to the process chosen and low price.[135] Examples of typical PBAs are hydrocarbons, e.g. *n*-pentane, supercritical carbon dioxide and nitrogen.[137] In contrast, CBAs are solid or liquid substances which decompose under foam processing conditions releasing the gas needed for foaming. They have to meet requirements such as sufficient and controllable gas liberation within a narrow temperature window, formation of inert decomposition products, a decomposition temperature matching the respective foaming process and good dispersibility in the polymer prior to decomposition.[137] Common CBAs are azo compounds like azodicarbonamide, hydrazine derivatives like *p*-toluene sulfonyl hydrazide or bicarbonate/acid combinations like sodium bicarbonate/citric acid.[136,137] CBAs are mainly used for the production of high- or medium-density foams due to their high price compared to PBAs.[136] Over time, PBAs or the gases released by CBAs normally diffuse out of the foamed parts and are replaced by the ambient gas, typically air.[148]

5.1.4. Cell nucleating agents

Within the last two decades, there was an increase in world energy consumption about approx. 50% from 2000 to 2016, with a further increase about more than 30% until 2040 being forecast.[151] Since this growing demand cannot be met with renewable energies alone, an increase about 34% in energy-related emissions of the greenhouse gas CO_2 from 2012 to 2040 is expected.[152] To limit these emissions, energy saving by improving energy efficiency is of paramount importance. Rigid thermoplastic foams can support this mainly in the important fields of thermal insulation and of lightweight construction, the latter particularly in the transportation sector. Rigid thermoplastic polymer foams are mainly made of PE, PS and PP. Yet, PE and PS suffer from low service temperatures, being not applicable beyond

100 °C.[67] Moreover, PP offers, among other advantageous properties, low materials cost, chemical resistance and, compared to PS, better impact properties.[67]

To enhance thermal insulation properties and to improve mechanical properties, cell sizes of foams have to be decreased towards microcellular (cell size ≤ 10 µm) or, at best, nanocellular (cell size ≤ 1 µm) foams.[138] As the cell diameter reaches the region of the mean free path length of cell gas molecules, the so-called Knutsen effect comes into play, which drastically lowers thermal conduction through the cell gas.[138,153] However, also foams not reaching cell sizes prerequisite for the Knutsen effect benefit from smaller cells via a reduction of the thermal conductivity of the solid phase. This is attributed to increasing solid phase tortuosity with decreasing cell sizes.[153] At the same time, foam density plays a major role, with low density foams (≥ 90% void) featuring best insulation properties, while medium density foams (50 - 90% void) offer a higher specific strength, defined as the ratio of tensile strength over density, which is highly advantageous in construction and packaging applications.[154]

To achieve foams with small cells and low foam density, two steps are crucial: First, during foam cell nucleation, the largest number of cell nuclei possible has to be formed.[155] Secondly, as many of these nuclei as possible must grow into foam cells during the subsequent growth of the foam cells.[142,156]

The latter is achieved by suppressing cell coalescence via increasing the melt strength of the polymer. This is of paramount importance in the case of PP, since normal linear PP suffers from low melt strength.[67,138,157,158,159] There are several ways to address this problem by modification of the polymer: 1) Use of long chain branched PP[146,149,156,160,161], 2) crosslinking of the PP[162] and 3) blending with a polymer featuring higher melt strength such as PE[163,164],PS[165], PTFE[166] or an ethylene-octene copolymer[141].

To address the other leverage point, i.e. the foam cell nucleation step, heterogeneous nucleation is utilized. Heterogeneous nucleation happens at interfaces, in contrast to homogeneous nucleation, which spontaneously occurs in the supersaturated melt. Heterogeneous nucleation is advantageous, as the number of formed nuclei can be increased by the surface present, which depends on the amount of nucleating agent applied. According to McClurg *et al.*, ideal nucleating agents must feature nucleation sites, at which nucleation is energetically favored compared to homogeneous nucleation. Furthermore, size, shape and surface properties of the nucleating agent should be uniform, to guarantee

simultaneous nucleation at all nucleation sites or at least to prevent premature nucleation at few sites. Also, an ideal nucleating agent should be present in excess in the polymer, to nucleate as many foam cells as possible, and it must be easily dispersed homogeneously, to achieve constant foam morphologies in the whole material.[167] Concerning the nucleating agents' surface geometry, Leung *et al.* showed that a surface comprising many crevices featuring small opening angles as nucleation sites is highly beneficial.[168] There are different approaches to generate such nucleating surfaces: Firstly, a second polymer like e.g. PS can be used. In this case, cells are nucleated at the interface between PP and the second polymer.[165] Secondly, nanostructures, typically nanoparticles, can be applied.

Most frequently, insoluble inorganic nanoparticles made of Talc[146,169,170,171,172,173], montmorillonite[159,174,175,176], cloisit[157,158,177], nanosilica[178,179], titanium dioxide[171], graphite[170] or carbon nanotubes[180] are applied as nucleating agents. The use of organic insoluble cellulose nanofibers has also been reported.[175] All of these nanoobjects work as cell nucleation agents, yet they tend to agglomerate during processing. Since this would deteriorate foam morphology, agglomeration has to be suppressed by use of compatibilizers as dispersing agents.[179] Moreover, Lee *et al.* showed at the example of nanosilica that the nanoparticle dispersion quality is also highly sensitive to extrusion conditions.[178] Yet, Zhai *et al.* were able to achieve cell densities up to 10^9 cells/cm^3 by extrusion of linear PP using up to 1% of nanosilica.[179]

To overcome aggregation problems associated with insoluble nucleating agents, soluble ones can be used. For the crystal nucleation of *i*-PP, soluble additives based on sorbitol derivatives or 1,3,5-benzene trisamides are well established.[181] In general, such soluble additives are solved in the polymer melt in a first step at high temperature, yielding a homogeneous solution. In a second step, when the melt is cooled to foaming temperature, these additives form nanoobjects. The objects formed this way are well dispersed in the entire melt volume and later nucleate foam cells in the foaming step. There are some reports on the use of soluble nucleating agents for foaming of PP in literature: Wang *et al.* used the sorbitol derivative 1,3:2,4-bis(*p*-methylbenzylidene) sorbitol (S20) for pressure induced batch foaming experiments with linear *i*-PP. Applying only 0.7% of S20 in *i*-PP, they achieved a cell density of $5.5*10^7$ 1/cm^3. This is a more than 3-fold improvement relative to neat *i*-PP, which yielded a cell density of $1.5*10^7$ 1/cm^3, when processed under the same conditions.[182] Saniei *et al.* also used pressure induced batch foaming to process *i*-PP com-

prising 1,2,3-tridesoxy-4,6:5,7-bis-*o*-[(4-propylphenyl)methylene]nonitol sorbitol (NX8000). Applying 0.5% of NX8000 they obtained a nanoporous medium featuring open cells with an average cell size of around 70 nm and a cell density in the order of 10^{15} 1/cm^3. The thermal conductivity of this foamed material was found to be almost eight times lower than the one of the compact material.[183] Another sorbitol derivative, 1,3:2,4-bis-O-(4-methylbenzylidene)-D-sorbitol (Gel-all MD) was applied in a foam injection molding process by Miyamoto *et al.*. They also reported high open cell contents (> 9%) using 0.5 or 1.0% of Gel-all MD. They achieved cell diameters below 5 µm and cell densities higher than 10^9 1/cm^3. However, the expansion ratio of the foams obtained was limited to a maximum of only five by the applied injection molding process.[184] 1,3,5-trisamide derivatives have also been used as cell nucleating agents: Stumpf *et al.* used 1,3,5-tris(2,2-dimethylpropionylamino)-benzene (BTA 5) and *N,N',N''*-tris(3-methylbutyl)-1,3,5-benzenetricarboxamide (BTA 6) to improve the foaming behavior of *i*-PP in a foam injection molding process employing a breathing mold. They found the cell size to be reduced from 120 µm for the neat *i*-PP to 20 µm by addition of only 0.02% of BTAs, while reaching cell densities higher than 10^9 1/cm^3. However, the foam expansion ratio in this study was only two, which means, that very dense foams have been produced.[150]

Apart from this morphological foam characterization, mechanical foam characterization is crucial for rigid thermoplastic foams, since the foam's mechanical properties determine its applicability e.g. for lightweight construction applications. There exist many test methods for this purpose, e.g. compression testing (yields compressive modulus and compressive strength)[137], tensile testing (yields, among others, tensile strength)[185], flexural testing (yields flexural strength)[137,150], impact testing (yields impact toughness)[185] and dynamic shock cushioning[137]. Nevertheless, compression is the most popular testing mode for polymer foams.[137] Bureau *et al.* showed at the example of PS that compression properties like modulus and compression strength depend on the foam morphology: They found, that both, modulus and strength, drastically increased with foam density. Next, they defined a 'microstructural parameter' as foam density divided by average cell diameter. Also for that parameter, they found a positive correlation with mechanical properties. This implies, that foam mechanics can be maintained while reducing foam density by reduction of the cell size.[186] For PE containing PTFE fibrils, Zhao *et al* reported an improvement of compressive strength with increased foam density and reduced cell diameters.[187] This improvement

associated with smaller cells was confirmed by Gong *et al.*, who also found a narrower cell diameter distribution to be beneficial for mechanical properties of PP foams.[185] Concerning the improvement of foam mechanics, particularly compressive properties, by using additives, Chen *et al.* were able to improve modulus and collapse strength of PMMA foams by addition of carbon nanotubes to a great extent. Furthermore, an increase in nanotube length further enhanced this phenomenon, which indicates a reinforcing effect of the nanotubes.[188] For PS, Ogunsona *et al.* achieved a more than doubled compression modulus by reinforcement with montmorillonite. This tremendous increase could not be related to cell size or foam density and was attributed to a reinforcing effect of the additive montmorillonite.[189] Shen *et al.* reported an increase of specific compression moduli about up to around 45% by addition of up to 5% of carbon nanofibers to PS, which they also attributed to reinforcing effects of the nanofibers. Furthermore, they showed the extent of this reinforcement to be highly dependent on the foaming process applied.[190]

In this thesis, the effect of the use of 1,3,5-benzenetrisamides (BTAs) as soluble additives on morphology and mechanical properties of extruded *i*-PP foams is investigated. The aim was to use low-cost, linear *i*-PP as polymer to meet industry demands. Avoiding the much more expensive long chain branched *i*-PP, which provides higher melt strength and is by far easier to foam [146], special care had to be taken when selecting a proper *i*-PP grade. The characterization of the selected *i*-PP grade later used for foaming is presented in the first part of this chapter. Next, suitable BTAs for the foaming experiments had to be chosen. Therefore, based on data already present[32], BTAs were pre-selected and thoroughly characterized. This is presented in the second section of this chapter. As processing technique, foam extrusion was chosen. This is due to its higher industrial relevance compared to batch foaming. A main focus of this work was to test a novel concept for using BTAs as foam cell nucleating agents in foam extrusion. This concept, along with machine configurations resulting from it, is presented in Figure 65.

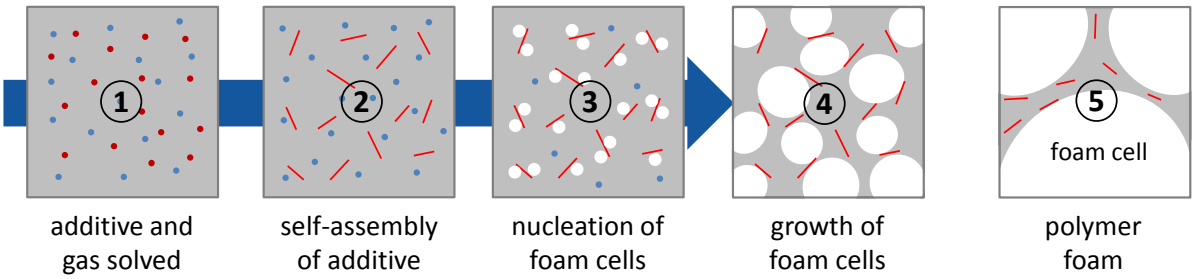

Figure 65: Concept of foam cell nucleation with the aid of supramolecular additives. From left to right, the system's temperature decreases. (1) At first, physical blowing agent (PBA) and additives are dissolved in the polymer melt under pressure. (2) Upon cooling, the additive self-assembles into supramolecular nanostructures, while the PBA remains dissolved. (3) When the pressure is beginning to be released, foam cells are nucleated at the interfaces between supramolecular nanostructures and polymer melt. (4) While the pressure further decreases, the cell nuclei simultaneously grow into foam cells. (5) When the polymer melt becomes sufficiently viscous due to further cooling, stable polymer foam with fine cells is obtained. *Adapted with permission from ref. (Mörl et al. 2019)*[191]*. © (2017) The authors.*

To characterize the resulting foams, their foam morphology, i.e. foam density, cell diameter distribution and cell density, was investigated. Finally, foam mechanics were characterized at the example of the compressive modulus, which is a method to show possible reinforcing effects of additives on foams well-established in literature, as discussed above. The BTAs were pre-selected in such a way that a wide range of BTA contents can be adjusted. The study of the impact of both parameters, nature and content of BTA, on the compressive properties of the foams is a main goal of this chapter.

The project presented in this chapter was done in cooperation with Dr. Michaela Mörl from the department of Polymer Engineering at the University of Bayreuth. Most of the results presented here have also been published in the *Journal of Cellular Plastics*.[191]

The following results in this chapter are structured into four sections. The first section shows the characterization of the applied *i*-PP-grade with respect to its usability in later foaming experiments. The second section also includes compact, i.e. non-foamed materials. It presents properties of different compounds of four BTAs with the selected *i*-PP-grade. The third section focusses on the foaming process and the morphology of resulting foams. Finally, the fourth section demonstrates a drastic improvement of the compression modulus of foams by application of BTAs and aims to shed light on the mechanism of this improvement.

5.2. Characterization of *i*-PP for foaming experiments

Foaming of linear *i*-PP is typically difficult due to its low melt strength and the small foaming window resulting from this. Nevertheless, a linear *i*-PP grade is applied in this work, as linear *i*-PP is significantly less expensive than long-chain branched *i*-PP tailored for foaming. Firstly, an *i*-PP grade supposed suitable for foaming was preselected. This linear *i*-PP (Moplen HF400G) was kindly supplied by LyondellBasell. The material was a reactor grade without any further additives. In the following, its properties are characterized with respect to its foaming behavior. In addition, first foam extrusion experiments are presented to prove the formation of appropriate foams.

At first, the *i*-PP was characterized with regard to its thermal behavior, i.e. phase transitions, which were detected by means of DSC. For these measurements, the *i*-PP was compounded with stabilizers. Figure 66 depicts DSC results. Upon heating, the material shows a distinct melting peak at 161 °C. Upon cooling, a crystallization peak maximum at 115 °C is observed.

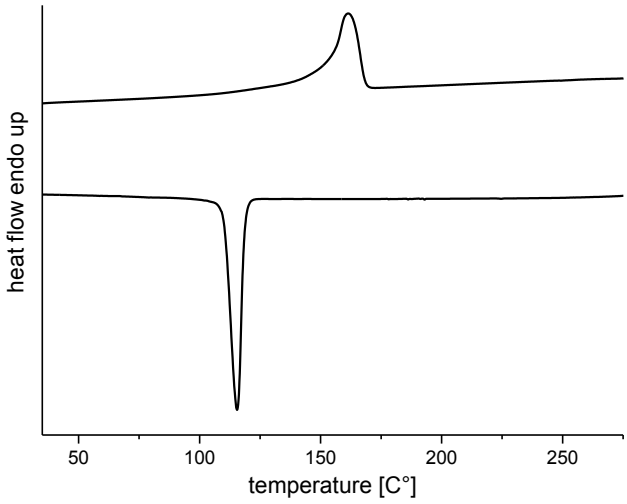

Figure 66: DSC second heating (top) and cooling (bottom) scans of stabilized *i*-PP. Curves were measured between 30 and 280 °C with a heating/cooling rate of 10 K/min under N_2 flow.

To determine the molecular weight distribution of the *i*-PP, SEC was kindly measured with hot 1,3,5-trichlorobenzene as eluent by Dr. W. Kretschmer at the department of Inorganic Chemistry II at the University of Bayreuth. Results are shown in Figure 67. As the SEC has been calibrated with a PS standard, the absolute molecular weight value for *i*-PP has to be

taken with care and might be shifted. The curve maximum is at 157 kg/mol and the weight average molecular weight (M_w) is 218 kg/mol. The polydispersity (PD) is 2.9.

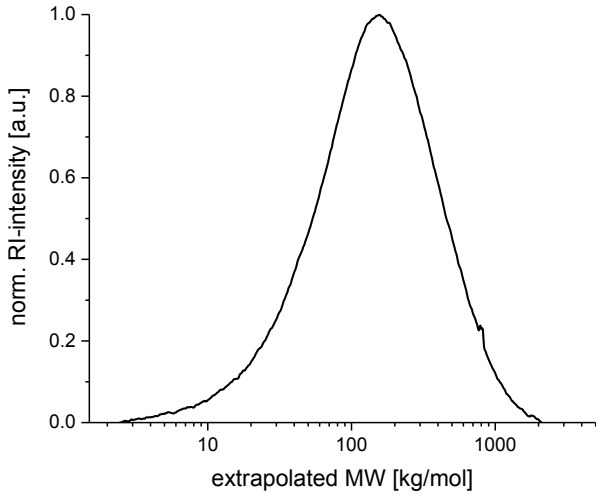

Figure 67: Molecular weight distribution of the applied *i*-PP. Curves were measured by SEC in 1,3,5-trichlorobenzene at 160 °C using a polystyrene calibration.

For foam extrusion, the temperatures of die and melt can only be varied in a very narrow range. Too low temperatures make the polymer freeze in the extruder, whereas too high temperatures cause too low melt strength, resulting in collapse of the foam. Hence, the melt viscosity can only be adjusted in a narrow range by temperature variation. Therefore, a material with a suitable viscosity has to be selected for foam extrusion beforehand. The behavior of the polymer upon pressing through a die is well simulated by the facile standard characterization method of melt flow index (MFI) determination, where polymer melt is pressed through a die with defined pressure and temperature and the mass of polymer pressed out in a given time is measured. The MFI of a neat and a stabilized sample of the *i*-PP was measured to learn about the influence of stabilization. Stabilization was done by compounding *i*-PP with 0.05 wt% of Irganox 1010 and 0.1 wt% of Irgafos 168. MFI values were determined at 235°C with a weight of 2.15 kg following ISO 1133. Neat, i.e. non-stabilized, *i*-PP features an MFI of 34.2 g/10 min, which is supposed much too high for foam extrusion. With stabilizers, the MFI is reduced about more than 93% to 2.5 g/10 min. This tremendous difference indicates a significant degradation of non-stabilized material under test conditions (235 °C in air). Hence, the use of stabilizers for the foam extrusion is

obligatory in order to avoid degradation of *i*-PP, which could not only worsen the foaming performance, but also make the experiments less reproducible.

For the foaming of *i*-PP, the melt strength of the material is of vital importance. Melt strength describes the resistance of the melt against rupture. Hence, a high melt strength during foaming prevents the cell walls from tearing apart, which would otherwise cause collapse of the foam. Melt strength measurements of the stabilized *i*-PP and, for comparison, of neat *i*-PP are presented in Figure 68. They were done by means of Rheotens at the department of Polymer Engineering at the University of Bayreuth. Both curves do not reach a flat plateau of drawing force F with sufficient drawing speed, but show a wave-like pattern. This is attributed to the high molecular weight of the investigated materials. As Rheotens measurements depend on various factors, it is hard to reproduce reliable absolute values. Nevertheless, if measurements are done in a row by the same operator, as it is the case here, they allow good conclusions about the relative melt strength of the investigated materials. Here, the non-stabilized *i*-PP, which was measured for comparison, features a lower slope in the beginning and finally reaches drawing forces much lower than the one reached for the stabilized material. This is in good accordance with the findings of MFI measurements, where the non-stabilized *i*-PP featured much lower viscosity, which correlates to a lower melt strength compared to the stabilized material. Concluding, also from the point of melt strength, stabilization of *i*-PP for foam extrusion is crucial for later foam extrusion.

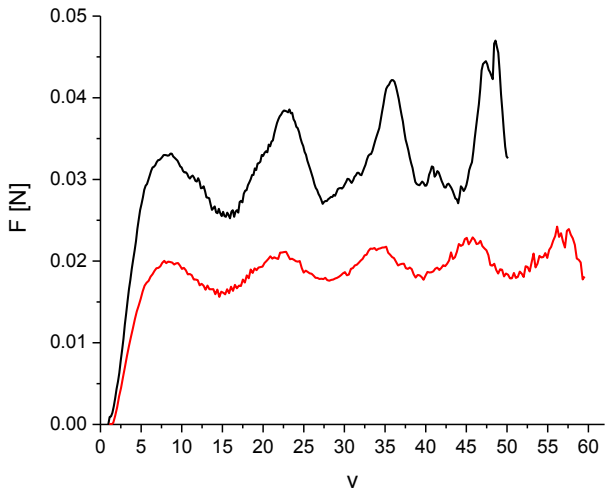

Figure 68: Melt strength of stabilized (black) and non-stabilized (red) *i*-PP. Shown curves are averages of at least five measurements each.

To finally prove the foaming performance of the stabilized material, preliminary foam extrusion tests were performed. The applied foam extrusion process is discussed in detail in chapter 5.4. All relevant foam extrusion parameters applied are given in the experimental section (6.4.). Figure 69 exemplarily shows an obtained foam strand. The shown foam strand clearly features a high expansion ratio and a relatively homogeneous shape. Hence, the applied stabilized *i*-PP is well-suited for foam extrusion and consequently is used for all further experiments in this chapter, i.e. additive characterization, foaming and foam investigation.

Figure 69: Extruded foam strand of stabilized *i*-PP. The strand's diameter is between 5 and 7 mm. Foam extrusion was done with 6 wt% of CO_2.

5.3. Selection of additives for cell nucleation in compact i-PP

In this chapter, the next step towards foam extrusion, i.e. the selection of promising BTA/*i*-PP systems, is taken. Therefore, four different BTAs were compounded in the *i*-PP in various concentrations and the resulting compounds were characterized thoroughly. The analysis of solubilities of BTAs in the polymer melt, *i*-PP crystallization temperatures, share of β-modification of *i*-PP, haze and clarity and melt strength of the compounds, is presented in the following chapter.

At first, different BTAs for the characterization in *i*-PP had to be preselected. To this purpose, BTAs already studied in other *i*-PP grades were employed. A key criterion for the BTA selection was the possibility of a scale-up to amounts exceeding 100 grams. This means, that the educts had to be relatively inexpensive and available in sufficient amounts, and, that synthesis and purification protocols, which tolerate large amounts of material, are available. The secondary selection criterion applied was the solubility in the *i*-PP melt. Based on their known solubility in other *i*-PP grades as a guideline, BTAs covering a broad solubility range, were to be selected in order to discover possible correlations between BTA solubility (and therefore applicable BTA concentration) and cell nucleation performance. The four BTAs selected according to these criteria are shown in Figure 70, sorted from left to right by increasing solubility in the *i*-PP melt as reported by Blomenhofer *et al.*[32].

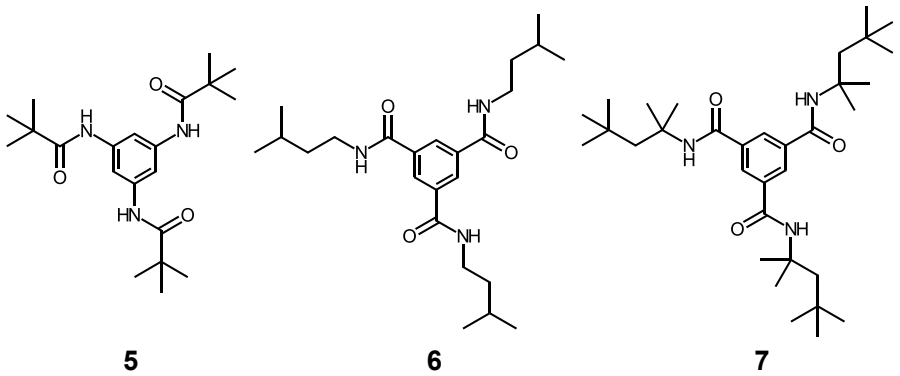

Figure 70: Molecular structures of BTAs investigated as cell nucleating agents for *i*-PP.

BTA 5, commercially available as Irgaclear XT 386, is an α-nucleating agent which features a very low solubility of less than 500 ppm at 240 °C in *i*-PP. BTA 6 is another α-nucleating agent. It features a much higher solubility of more than 3000 ppm at 240 °C in the *i*-PP melt.

BTA 7 is reported to both nucleate α- and β-modification (k-value: 0.40). For this BTA no solubility data in *i*-PP were available in literature.[32]

BTAs self-assemble into supramolecular nanofibers in the polymer melt upon cooling and these nanofibers are supposed to nucleate foam cells. Therefore, the morphology of formed nanofibers is of vital importance for the foaming performance. Since *i*-PP is chemically much more stable than BTAs, the *i*-PP matrix can't be etched away to directly see the nano-structures formed by the BTAs in the *i*-PP compounds. At best, marks, which are left by the BTA structures etched away, remain and allow indirect conclusions about the BTA structures.[53]

Hence, 2,2,4,4,6,8,8-heptamethylnonane (HMN), a solvent featuring a molecular structure related to the one of *i*-PP, was applied as a model system for *i*-PP: BTA and HMN were mixed in the desired relation and the dispersion was boiled under reflux at 240 °C for one hour. After cooling at ambient conditions, the homogeneous dispersion was filled into a dropping point cell. There, after anew heating to 240 °C, the cooling could be conducted with very controlled speed (e.g. 20 K/min) to yield self-assembled nanofibers. Subsequently, HMN was removed by means of high vacuum, leaving the self-assembled BTA structures for SEM investigations. Figure 71 shows SEM micrographs of self-assembled structures of the three BTAs prepared that way. All three BTAs form fibers with diameters far below 1 µm, which therefore are denoted as nanofibers in the following. BTAs 5 and 7 form comparably thick nanofibers with diameters partly thicker than 100 nm. These fibers appear stiff (BTA 5) and brittle (note breaking points in fibers of BTA 7). On the contrary, nanofibers of BTAs 6 exhibit significantly smaller diameters and appear softer. Concluding, all three BTAs can be used for further experiments, since they self-assemble into the desired nanofibers in HMN, which is a model system for *i*-PP.

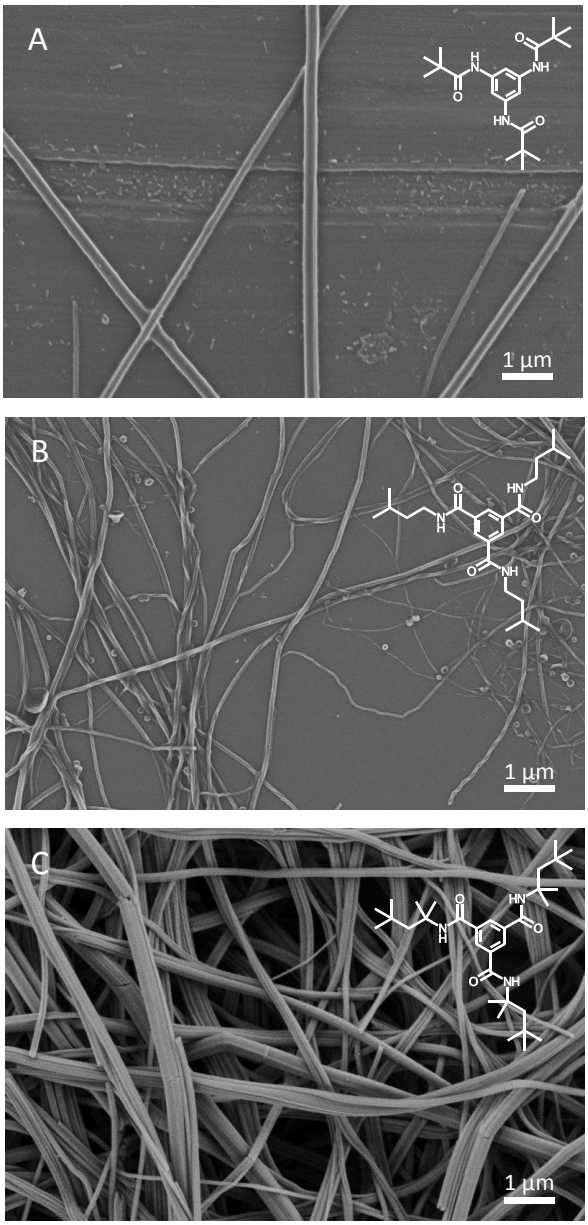

Figure 71: SEM micrographs of fibers of BTAs 5 (A), 6 (B) and 7 (C). Fibers were prepared by cooling hot solutions of 200 ppm of BTA in HMN at a rate of 20 K/min.

To produce samples with a defined BTA content in *i*-PP for the following characterization experiments, stabilized *i*-PP powder and BTA powder were mixed in a tumble mixer, compounded in a twin-screw mini compounder under nitrogen and subsequently injection molded into disc-shaped specimens with a diameter of 25 mm and a thickness of 1.1 mm. Since the effect of BTA additives is highly concentration dependent, samples with different BTA contents were investigated. Therefore, a concentration series for each BTA was done by diluting the aforementioned powder-powder mixture with additional stabilized *i*-PP powder prior to compounding.

As the next step, dissolution and self-assembly temperatures for each BTA concentration were measured by means of polarized light microscopy (PolMic). Samples for PolMic were prepared by melting a grain of the respective BTA/*i*-PP compound between two glass slides, obtaining a thin film after cooling to ambient temperature. Film and glass slides were placed in a hot-stage to precisely control the temperature. Each sample was heated from 150 to 260 °C, or, where necessary, to 270 °C. The temperature, where the last visible birefringence caused by BTA objects disappeared, was denoted as dissolution temperature of the BTA. Of course, one should keep in mind that even above this temperature BTA objects, yet too small to be detected by PolMic, may exist. So, in this context, dissolution does not necessarily mean the formation of a molecular solution of BTA in *i*-PP. After heating, the samples were again cooled to 100 °C. The temperature where the first birefringence caused by BTA objects appeared was denoted as self-assembly temperature. In Figure 72, this dissolution/self-assembly process is displayed at the example of 8000 ppm of BTA 6 in *i*-PP. Figure 72 A shows BTA objects present in the *i*-PP melt during the heating step. In Figure 72 B, the dissolution temperature is reached and an optically isotropic melt is formed. In Figure 72 C, which is taken during the subsequent cooling process, few BTA objects have formed, causing visible birefringence. This picture is taken little below the self-assembly temperature. Upon further cooling, more BTA self-assembles, forming additional objects and growing the existing ones (Figure 72 D). The BTA structures formed during this process are much larger than the ones formed beforehand in the injection molding or film pressing process (Figure 72 A). This size difference is attributed to the much slower cooling in the PolMic (10 K/min) compared to the other processes, where the hot material is cooled by a metal surface at ambient temperature.

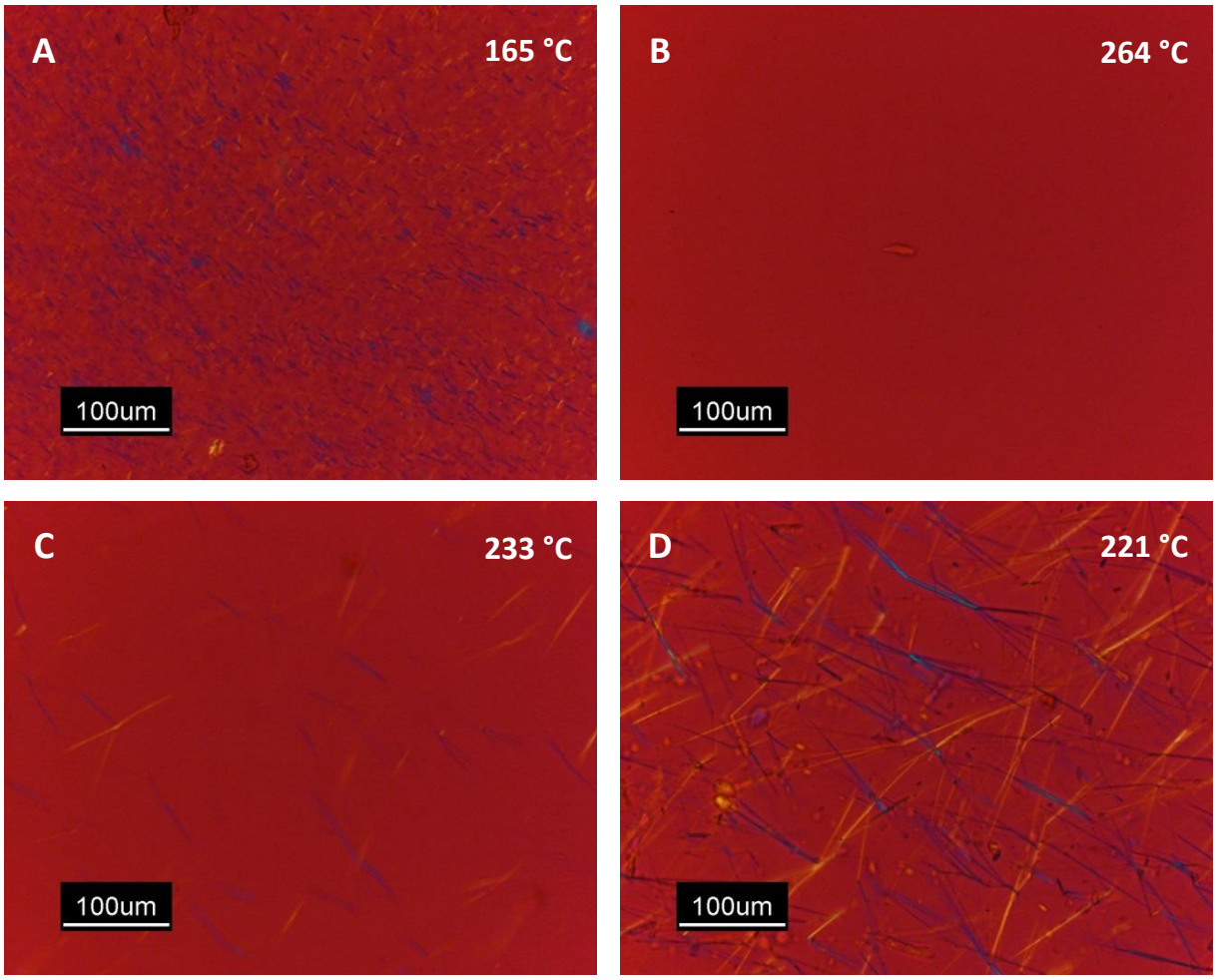

Figure 72: Dissolution and self-assembly of a BTA in molten *i*-PP. BTA objects (blue and yellow) (A) are dissolved upon heating with 10 K/min (B). Subsequent cooling with 10 K/min results in self-assembly into fibers (C and D). Images show 8000 ppm of BTA 6 in *i*-PP observed through an optical microscope equipped with crossed polarizers and a λ platelet.

Dissolution and self-assembly temperatures of different concentrations of a BTA in *i*-PP melt determined this way are then plotted versus BTA concentration. This is exemplarily shown for BTA 6 in Figure 73. The presented data originate from two heating/cooling cycles applied directly after each other. All curves show a steep slope at low concentrations. At higher concentrations the slope flattens with exception of the first dissolution curve, which shows a steeper slope above 6000 ppm. In the second cycle, dissolution temperatures could be measured down to lower concentrations than in the first cycle. This is due to the fact that BTA objects are larger after the first cycle than before: The bigger aggregates can be detected even at lower concentrations, which is necessary for dissolution temperature determination, while the smaller ones are invisible at low concentrations. In principle, at high concentrations, some very big BTA objects are not totally dissolved during the com-

pounding step and remain in the compound, being the third species of BTA objects which can be detected from Figure 73. Upon heating with a constant heating rate, objects with more volume are generally dissolved slower than those with less volume. This phenomenon can be used to distinguish the three described species of nanofibers from the dissolution temperature data: Medium sized fibers are only present in the second heating curve. In the first heating curve, either smaller fibers (in the case of complete dissolution during compounding) or bigger fiber fragments (from incomplete dissolution during compounding) occur. Smaller objects dissolve faster, which means that the dissolution temperature for the small species is below the one of medium sized objects from second heating. Vice versa, it is above for the big undissolved species. In Figure 73, the transition from small to big fibers is in the area around 6000 ppm of BTA, which means that BTA concentrations above this level have not been completely dissolved during compounding. At 6000 ppm, the BTA dissolves at around 245 °C during second heating in the PolMic. Since 240 °C was the melt temperature during compounding, this indicates that dissolution temperatures during compounding and in the PolMic match to some extent.

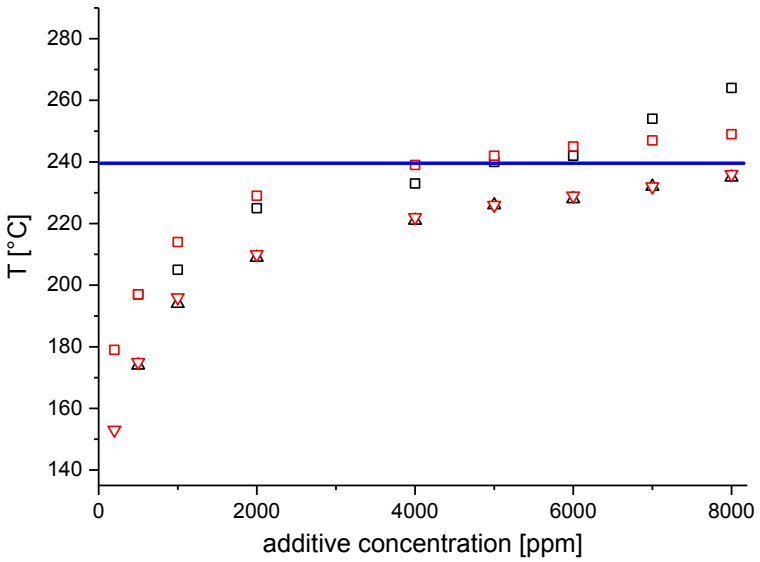

Figure 73: Concentration dependent dissolution and self-assembly behavior of a BTA in molten *i*-PP at the example of BTA 6. Data from first (black) and second (red) heating/cooling cycles are shown. Dissolution temperatures (□ and □) indicate the disappearance of birefringence caused by BTA objects, while the self-assembly temperatures (△ and ▽) mark the reappearance of the birefringence. Heating and cooling rate was 10 K/min. The blue line marks the melt temperature during the previous compounding of the samples. *Parts of the data presented here have already been published (Mörl et al. 2018)*[191], also see Figure 74.

Data from the second heating/cooling cycle are less sensitive to compounding parameters and can easily be reproduced in additional heating/cooling cycles. Therefore, they were exclusively used and are displayed in the following. Figure 74 gives concentration dependent dissolution and self-assembly temperatures in the *i*-PP melt for all three BTAs. BTA 5 exhibits low solubility: 300 ppm are soluble at 240 °C, while 400 ppm are already insoluble. For BTA 6, up to 4000 ppm are soluble at this temperature. This more than 10-fold increased solubility compared to BTA 5 is attributed to the switching of amide groups and the longer and more flexible substituents. BTA 7 shows an even higher solubility of 8000 ppm at 240 °C. All results presented here are in good accordance with literature values measured using different *i*-PP grades, as far as those are available.[32]

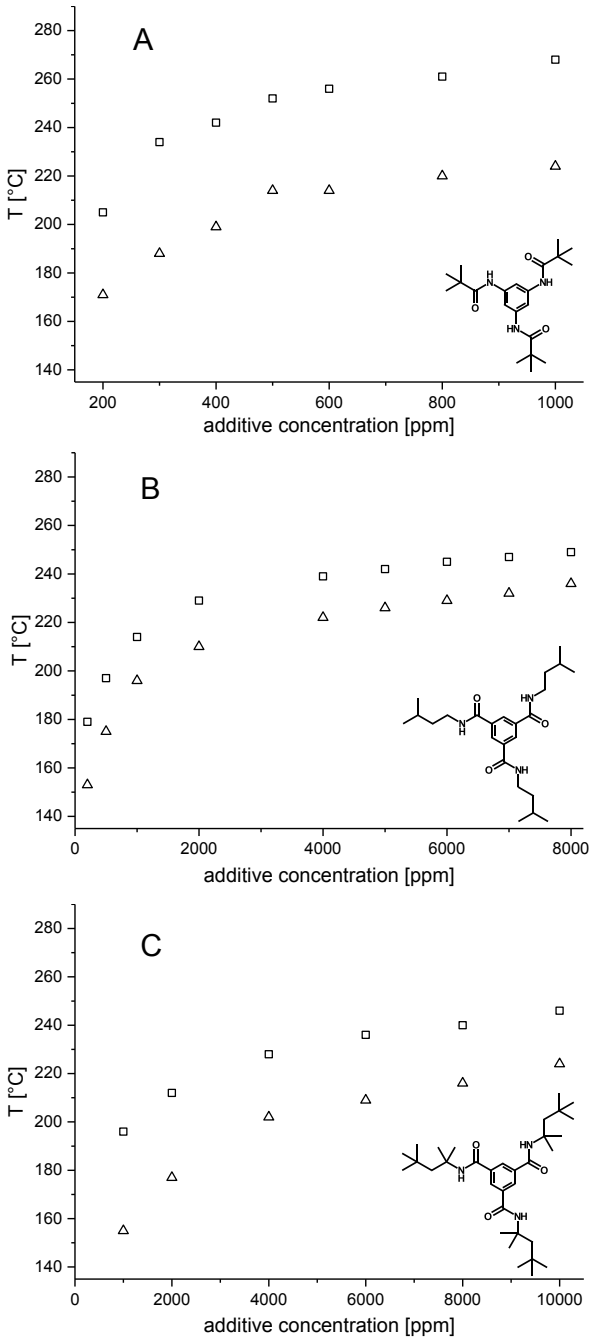

Figure 74: Concentration dependent dissolution and self-assembly behavior of BTAs 5 (A), 6 (B) and 7 (C) and in molten *i*-PP. Dissolution temperatures (□) indicate the disappearance of birefringence caused by BTA objects, while the self-assembly temperatures (△) mark the reappearance of birefringence. Data from second heating/cooling cycles are shown. Heating and cooling rate was 10 K/min. *Adapted with permission from ref. (Mörl et al. 2019)[191]. © (2017) The authors.*

Next, crystallization temperatures of *i*-PP in all compounds were determined as a measure of the nucleating efficiency of the three BTAs. These data are necessary to identify possible correlations of foam properties with the nucleation of *i*-PP by BTAs later. All *i*-PP crystallization temperatures presented in Figure 75 were determined by DSC with a cooling

rate of 10 K/min. Shown data are averages of crystallization temperatures (maxima of exothermic peaks) from first and second cooling cycles.

Under these conditions, the neat stabilized *i*-PP crystallizes at 114 °C. Already at a concentration of only 100 ppm, BTA 6 raises this temperature to 121 °C, reaching a maximum of 122 °C at 500 ppm. BTA 7 is an even more efficient nucleating agent, shifting the *i*-PP crystallization temperature up to 126 °C at a BTA concentration of 1000 ppm, which is 12 °C above the value of neat *i*-PP. BTA 5 shows a more complex behavior: It promotes a local crystallization temperature maximum of 125 °C at only 100 ppm of BTA. Increasing the concentration, the value fluctuates around a lower level, until a new maximum of 127 °C is reached around 1000 ppm. This behavior is attributed to the poor solubility of BTA 5: After the first maximum, partly non-dissolved BTA acts as a nucleus for the self-assembly of the BTA, removing the BTA from the surrounding area. Thus, in this area no further BTA objects are formed, which in consequence reduces the BTA object concentration and, via that, the *i*-PP crystallization temperature. By addition of more BTA, the concentration of non-dissolved BTA aggregates finally reaches a level which again provides sufficient BTA object surface for efficient nucleation of *i*-PP, causing the the second *i*-PP crystallization temperature maximum.

To sum it up, all three BTAs nucleate *i*-PP. BTA 6 is the worst nucleating agent reaching an *i*-PP crystallization temperature of only 122 °C and therefore. BTA 7 is, at least in the soluble range, the best nucleating agent, reaching an *i*-PP crystallization temperature of 126 °C.

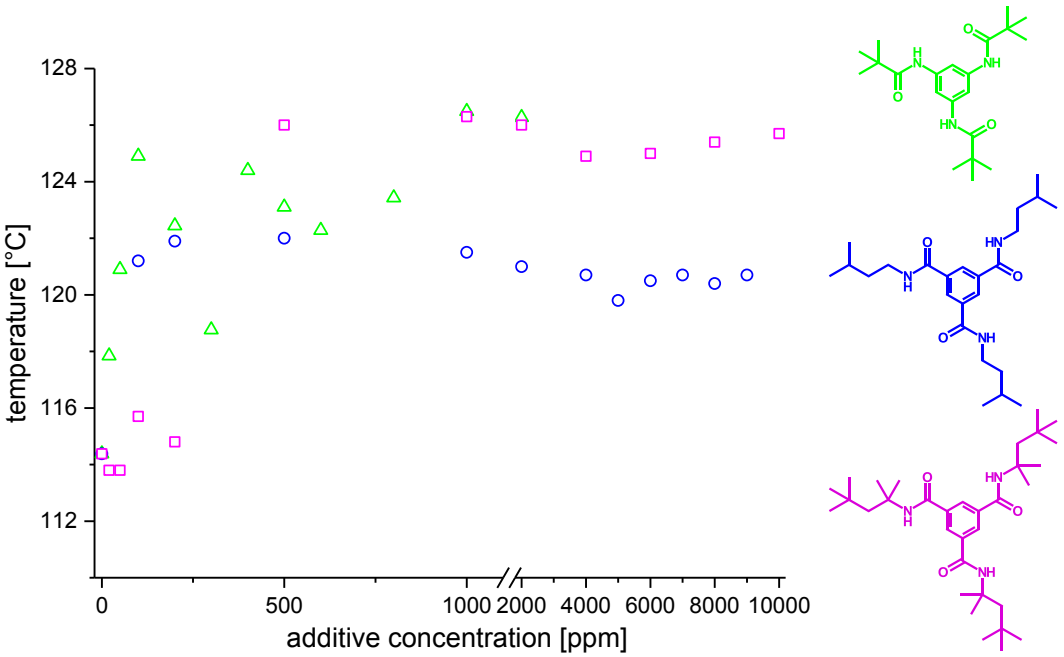

Figure 75: Crystallization temperatures of *i*-PP containing various concentrations of BTAs 5 (△), 6 (○) and 7 (□). Data represent peaks of crystallization enthalpies measured by DSC. Heating and cooling rate was 10 K/min.

As a final characterization for compact *i*-PP/BTA compounds, melt strength was measured. It describes the resistance of the melt against rupture. Hence, a high melt strength during foaming prevents the cell walls from tearing apart, which otherwise would cause collapse of the foam. Therefore, to achieve foams with fine cells, a melt strength as high as possible is desirable. To detect possible effects of the BTAs on melt strength, the highest concentration of each of the three BTAs, which was still in the soluble regime, was selected. As a state-of-the-art reference material, talc with a median size of 0.7 µm was applied. Talc is a hydrated magnesium silicate of the formula $Mg_3Si_4O_{10}(OH)_2$, which is insoluble in polymer melts. It is often used as a cell nucleating agent for foaming of polymers.

The selected compounds alongside with neat stabilized *i*-PP were expressed through a die and the resulting strand was abstracted with a Rheotens machine. The force needed for abstraction was measured while increasing the abstraction speed, which is proportional to the shear rate applied. Resulting plots of force vs. speed are shown in Figure 76.

As it was the case for neat *i*-PP samples, the curves show strong oscillation in the plateau area. All curves show similar slopes at low drawing speeds. Neat *i*-PP and all samples containing BTAs reach the same plateau level, while values for *i*-PP containing 5000 ppm of

talc are slightly higher. These findings indicate that the investigated BTAs do not significantly influence melt strength within the investigated concentration range.

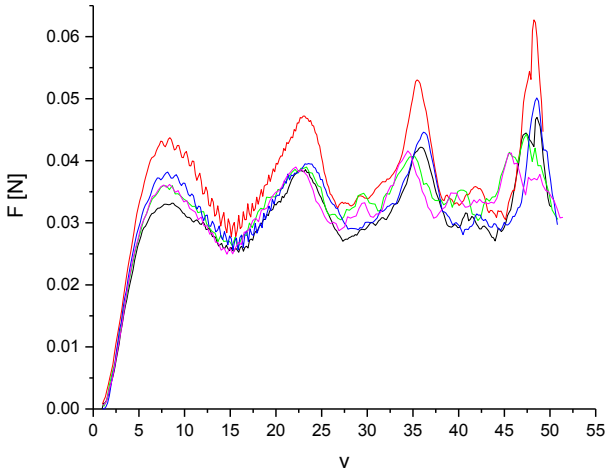

Figure 76: Melt strength of stabilized *i*-PP (black), stabilized *i*-PP comprising 5000 ppm of talc (red) and BTAs. The maximum concentration of each BTA for later foaming is displayed, i.e. 300 ppm of BTA 5 (green), 5000 ppm of BTA 6 (blue) and 4000 ppm of BTA 7 (magenta). Shown curves are averages of at least five measurements each.

5.4. Foam extrusion of i-PP with additives for cell nucleation

For foam extrusion, thirteen selected materials were compounded in amounts of 10 kg each: neat stabilized *i*-PP, stabilized *i*-PP with 200 or 300 ppm of BTA 5, 500, 1000, 2000, 3000 or 5000 ppm of BTA 6, 2000, 3000 or 4000 ppm of BTA 7 and 1000 or 5000 ppm of talc. The compound comprising 5000 ppm of BTA 6 is included as a reference material, since this concentration of this BTA does not dissolve in the foam extrusion process, as it was shown in the previous section. This reference is meant to prove that BTA dissolution during foam extrusion is necessary to obtain good foams.

The setup for foam extrusion of these materials followed our concept for foam extrusion with supramolecular additives. Setup and concept are schematically shown and explained in Figure 77.

Following this concept, it is of particular importance that the chosen BTA in the respective concentration is completely dissolved at 240 °C at the end of the first extruder (A-extruder), to avoid big undissolved BTA objects, which otherwise would worsen foam properties. In the second extruder (B-extruder), the BTA must self-assemble into supramolecular nano-objects before reaching the die to ensure the presence of sufficient nucleating sites in the subsequent foaming step. When the pressure is released, CO_2 becomes insoluble and the foaming starts, yielding a thin foam strand.

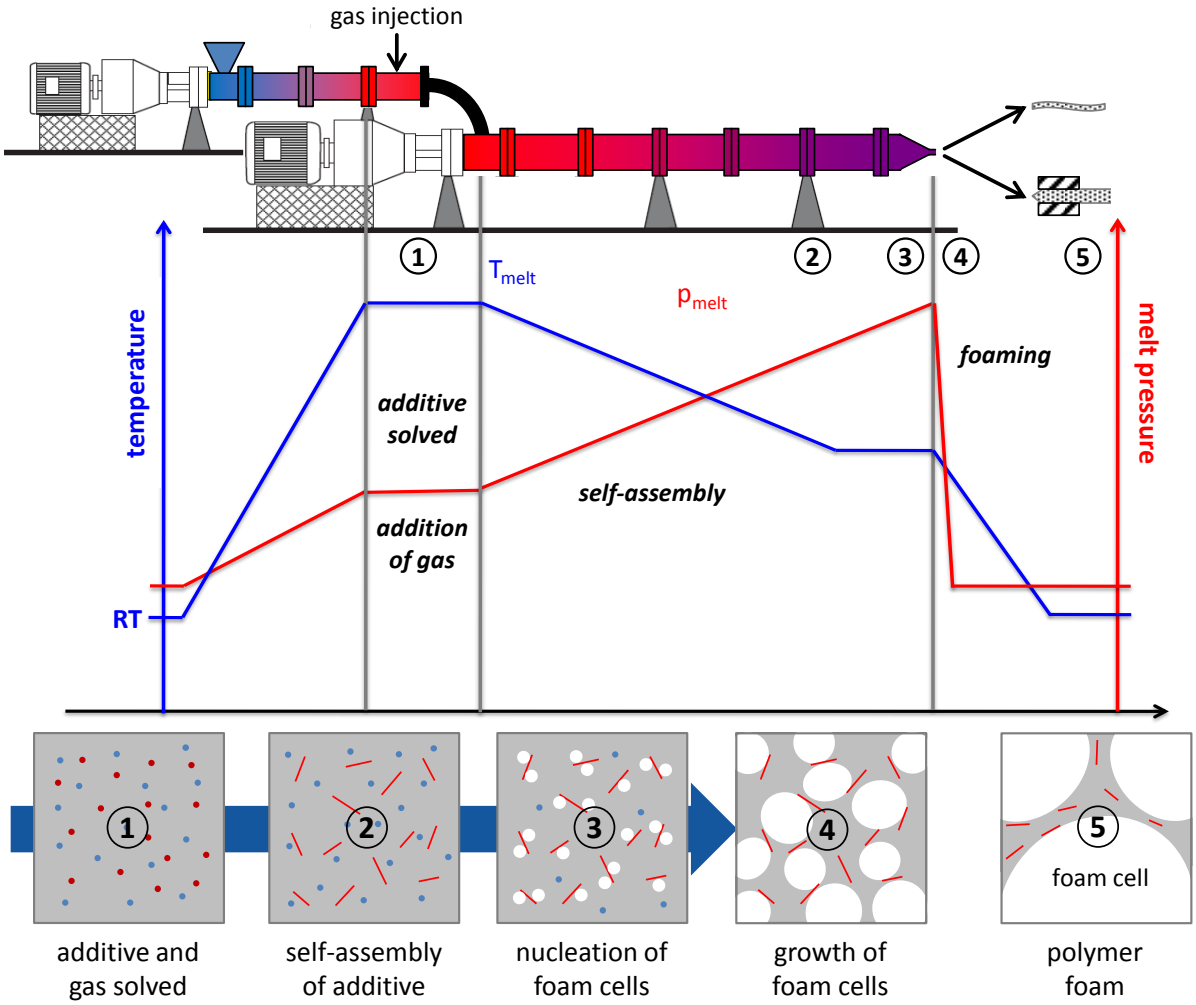

Figure 77: Schematic representation of the foam extrusion process (top) and of the concept of foam cell nucleation with supramolecular additives (bottom). In the first extruder the polymer-additive mixture is heated to 240°C and the physical blowing agent CO_2 is added. At the end of the first extruder additive and CO_2 are both dissolved in the polymer melt (1). In the second extruder the melt is cooled to the foaming temperature, which is around 160 °C. Here, the additives self-assemble into supramolecular nano-objects (2). At the same time, the melt is compressed to the foaming pressure towards the die. At the die the pressure is abruptly released and foam cells are nucleated at the nano-objects' surfaces (3). Subsequently, the nuclei grow into larger foam cells (4) to yield the final foam after cooling to room temperature (5). *Adapted with permission from ref. (Mörl et al. 2019)*[191]*. © (2017) The authors.*

To produce larger samples, which are suitable for mechanical investigations, a calibration unit can optionally be added to the setup. This unit features two parallel water-cooled plates at a distance of 18 mm. They retard the movement of the hot foam and thus accumulate it into a thicker, oval shape, as it is exemplarily shown in Figure 78.

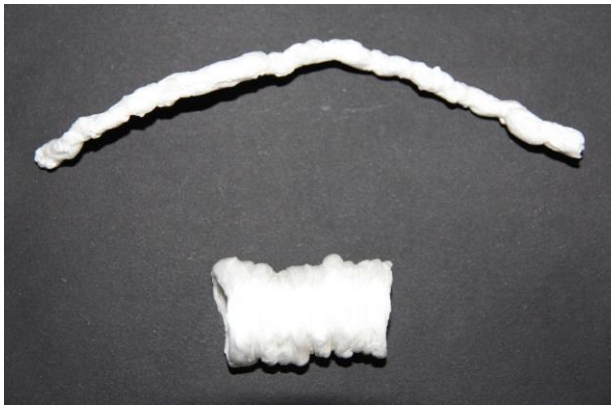

Figure 78: Extruded strand (top) and calibrated sample (bottom) of *i*-PP with 200 ppm of BTA 5.

To achieve a foam extrusion according to the concept explained above, process parameters have to be slightly adjusted for each material processed. In Table 10, a set of the most important parameters is given at the example of stabilized *i*-PP containing 200 ppm of BTA 5. The shown parameters are optimized for the material with respect to foam morphology.

Table 10: Selected processing parameters for the foam extrusion of stabilized *i*-PP with 200 ppm of BTA 5.

material	through-put	T_{melt} @ end of A-extruder	T_{set} @ end of B-extruder	T_{melt} @ end of B-extruder	T_{die}	p_{melt} @ die
i-PP + 200 ppm 5	4.3 kg/h	240 °C	155 °C	161 °C	150 °C	100 bar

The foam extrusion parameters found for this compound were slightly adapted for subsequent foam extrusion of all thirteen compounded materials, including neat *i*-PP, *i*-PP with talc and *i*-PP with BTAs, as described above. The different materials to some extent varied actual throughput and pressure before the die. Yet, these differences were not significant. Process data from foam extrusion experiments, which were done at the Department of Polymer Engineering at the University of Bayreuth, are listed in in the experimental section (see 6.4) for each individual material.

5.5. Morphology of extruded i-PP foam strands

In this section, the morphology of the foams, which were produced as described in the previous chapter, is presented. Here, extruded foam strands are characterized with regard to foam density, cell diameter, foam appearance and cell density. The next section (5.6), covers calibrated foams: There, foam density and cell diameter will give an overview of morphological differences introduced by calibration. A further focus is set on BTA objects and crystal modification of *i*-PP in the foams.

Average densities of foam strands of the extruded compounds are shown in Figure 79 alongside with standard deviations based on at least three samples each. Density measurements were conducted at the department of Polymer Engineering at the University of Bayreuth using the buoyancy method.

The neat stabilized *i*-PP features a density of 0.15 g/cm^3. Both compounds comprising BTA 5 show significantly reduced densities below 0.12 g/cm^3. With increasing amounts of BTA 6, foam density raises to a maximum of 0.18 g/cm^3 at 3000 ppm of BTA 6. The reference material *i*-PP with 5000 ppm of BTA 6 does not fit into that trend, which is attributed to the fact that BTA 6 does not completely dissolve during foam extrusion at this concentration. For BTA 7, no trend is observed, as all three compositions yielding densities between 0.10 and 0.16 g/cm^3. Foam densities for compounds with talc are among the lowest measured, with a minimum of 0.08 g/cm^3 at 5000 ppm of talc. Summarizing, all compounds show good foam densities in the range from 0.08 to 0.18 g/cm^3. Compounds comprising talc yielded slightly lower densities than the other compounds.

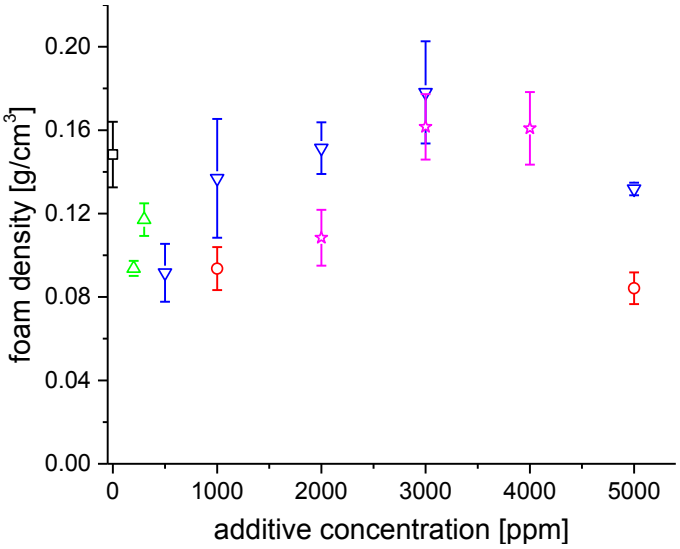

Figure 79: Foam densities of extruded foam strands of neat *i*-PP (black), *i*-PP containing talc (red) and *i*-PP containing BTAs 5 (green), 6 (blue) and 7 (magenta). Symbols represent averages and error bars represent standard deviations of three measurements each.

Next, cell diameters of all foam strands were determined using SEM images. The area of the cross section of at least 100 cells per material was measured. The diameter of a circle of the same area was calculated and is taken as the cell diameter. This SEM based method tends to underestimate the cell diameters since not all cells are cut in half, which results in smaller cross-sections and thus too small determined cell radii, as already discussed in Figure 63. Cell diameters determined by this method are presented in Figure 80. The neat stabilized *i*-PP features an average cell size of 52 µm. Addition of BTA 5 results in much finer cells with a minimum diameter of 29 µm at 300 ppm, which equals a cell size reduction of 44% compared to the neat sample. Cell diameters of samples comprising BTA 6 show strong fluctuation, but a weak tendency towards smaller cells with increasing BTA content can be deduced. At a concentration of 5000 ppm, where the BTA is insoluble, best results with a cell diameter of 27 µm were found. Yet, considering the large standard deviations, this is comparable to the best result in the soluble region, which is 30 µm at 1000 ppm. Increasing the content of BTA 7, also a slight tendency towards smaller cells can be observed, finally reaching an average cell diameter of 27 µm at 4000 ppm of BTA 7. This equals an improvement about 49% compared to neat *i*-PP. Using talc, the addition of 1000 ppm even deteriorates the cell size to 61 µm. This is attributed to a too low nucleation density due to the insufficient concentration of dispersed talc objects in the melt. This is in accordance with the finding that a good value of 30 µm is reached with 5000 ppm of talc.

Concluding, it has been shown that the concept of foam cell nucleation with BTAs works in foam extrusion, halving cell diameters at best. BTAs perform as well as the established cell nucleating agent talc while requiring much lower additive concentrations.

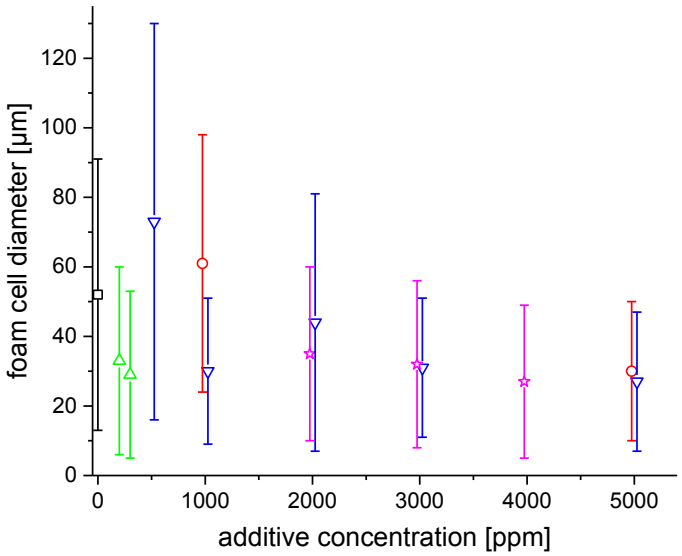

Figure 80: Average foam cell diameters of extruded foam strands of neat *i*-PP (black), *i*-PP containing talc (red) and *i*-PP containing BTAs 5 (green), 6 (blue) and 7 (magenta). Averages and standard deviations (error bars) are based on at least 100 measured foam cells each. Overlapping symbols are slightly shifted for the sake of clarity.

To further investigate these results, SEM images and cell diameter histograms of the respective concentration of each additive, which yielded finest cells, are compared to the neat stabilized *i*-PP in Figure 81. Neat stabilized *i*-PP exhibits many small cells along with few huge ones in the SEM image, which is also distinct in the diameter histogram: Though most of the cells feature diameters below 50 µm, many cells with diameters up to 100 µm are also found. Addition of 5000 ppm of talc causes a pronounced shift towards smaller cell diameters. However, some cells larger than 50 µm are still found. Application of 300 ppm of BTA 5 results in an even higher content of very small cells, but parallel also in an increase of the amount of cells larger than 50 µm. This might indicate insufficient nucleation density in that compound, as big cells are supposed to grow in areas where no nucleating BTA objects are available. The compound comprising 3000 ppm of BTA 6 shows a very homogeneous cell size distribution with all cells being smaller than approx. 120 µm. Use of 4000 ppm of BTA 7 yields the highest amount of very small cells, but also some large cells. Summarizing, all shown samples comprising cell nucleating agents feature a unimodal cell diameter distribution with a maximum at low values below 25 µm and a tail towards higher values.

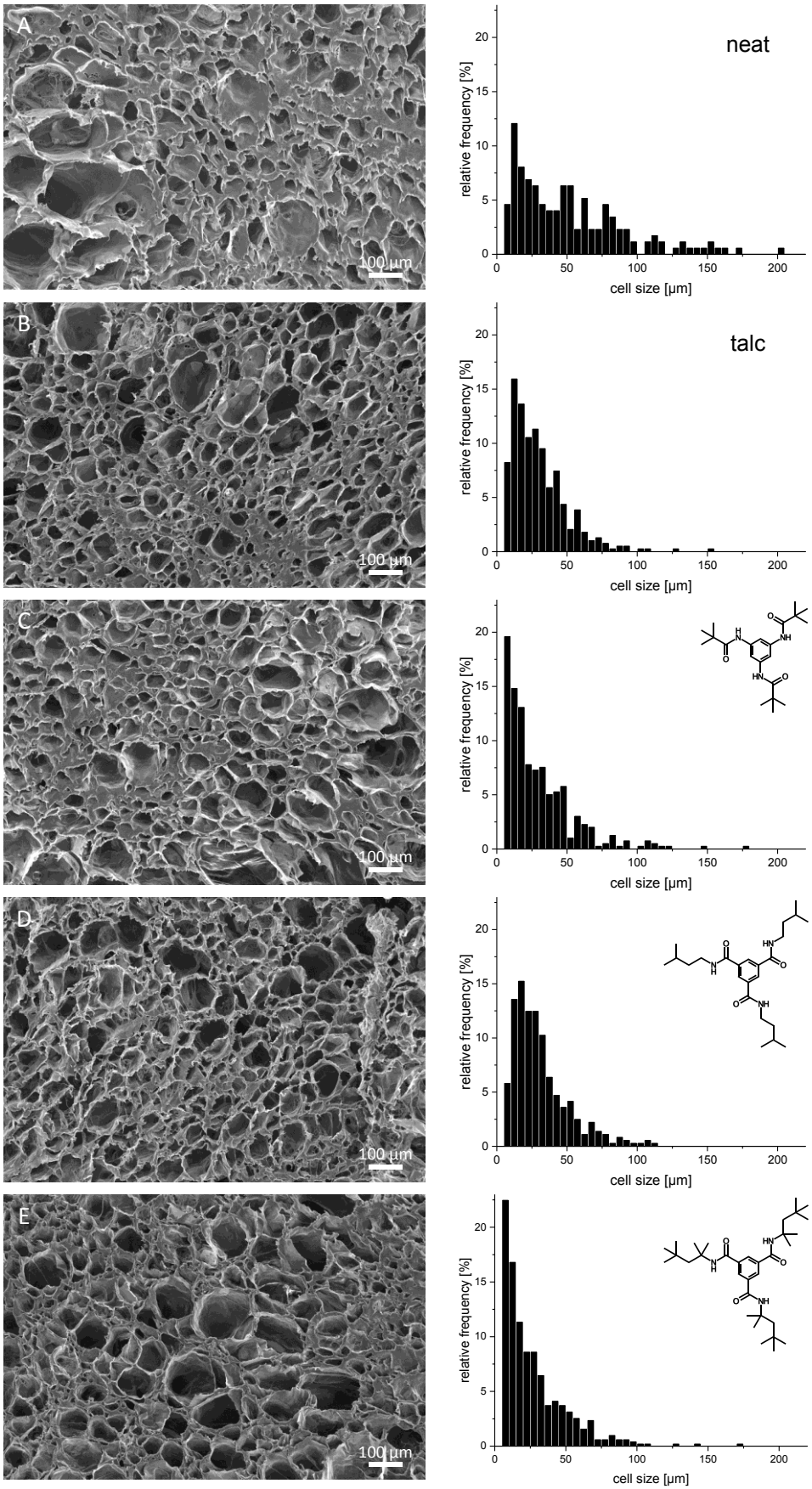

Figure 81: SEM micrographs of extruded foam strands and corresponding cell diameter histograms. Materials are neat *i*-PP (A) and *i*-PP with 5000 ppm of talc (B), 300 ppm of BTA 5 (C), 3000 ppm of BTA 6 (D) and 4000 ppm of BTA 7 (E). Histograms are based on at least 100 measured cells each.

The second property critical for macroscopic foam properties like thermal conductivity found on a microscopic scale is the cell density. It is determined by counting the number of cells on an SEM image of known area and potentiating it by 1.5 to obtain the cell density in 3D-space. Figure 82 presents cell densities of extruded foam strands determined this way and plotted on a logarithmic scale.

Strands of neat stabilized *i*-PP exhibit a cell density of $1.1*10^7$ cm^{-3}. Addition of 1000 ppm talc improves this value almost 4-fold to $4.0*10^7$ cm^{-3}, while a concentration of 5000 ppm does not alter the neat value. By the use of BTA 5 cell density is slightly increased to $1.2*10^7$ cm^{-3} at 200 ppm and more than halved to $4.3*10^6$ cm^{-3} at 300 ppm. For all concentrations of BTA 6 soluble in the extruder, no big changes in foam density are observed, whereas the not completely soluble concentration of 5000 ppm reduces cell density to $6.4*10^6$ cm^{-3}. With BTA 7 cell density is not altered significantly at all tested concentrations compared to the neat stabilized *i*-PP reference material.

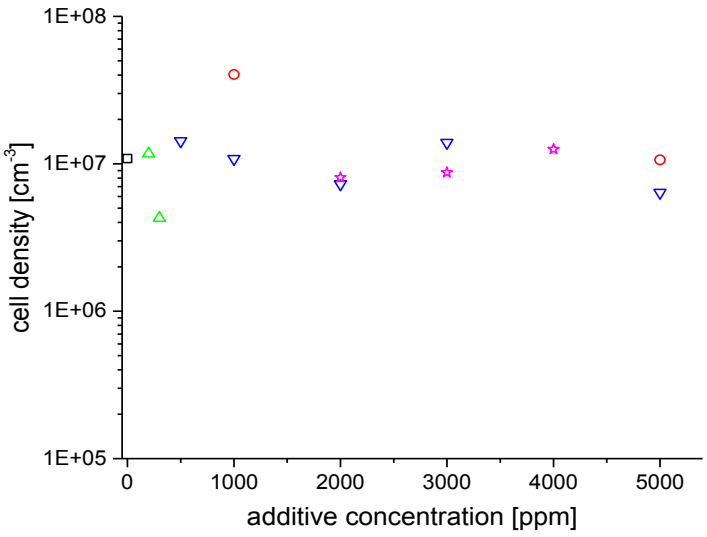

Figure 82: Cell densities of extruded foam strands of neat *i*-PP (black), *i*-PP containing talc (red) and *i*-PP containing BTAs 5 (green), 6 (blue) and 7 (magenta).

All in all, the cell density values determined are in the same order of magnitude, with 1000 ppm of talc giving a slight improvement, while all samples comprising BTAs show no significantly enhanced cell densities. The well-established method for cell density determination used is likely to cause a certain scattering of values since all foams investigated are

inhomogeneous to some extent (see Figure 63). Hence, small changes in cell density are not considered relevant.

However, following the concept of foam cell nucleation by supramolecular additives, one would expect drastically increased foam cell densities by the use of BTAs. As a reason for the low cell densities found, insufficient nucleation density can be excluded, since the applied BTAs form a dense network of fine fibers (see Figure 71). In addition, BTAs are known to feature high nucleation densities from *i*-PP crystal nucleation studies in literature.[32] So, if a great number of cells is nucleated during foaming, the problem must be associated with the growth of nucleated cells into their final shape. In this step, a loss of cells typically occurs by cell coagulation, which is the fusion of cells upon rupture of the cell wall separating them. This indicates a lack of melt strength, which otherwise would prevent cell wall rupture. Low melt strength and cell coagulation resulting from this is a well-known issue with linear *i*-PP. Thus, the low cell densities found are attributed to cell coagulation, which prevents reliable conclusions about nucleation densities during foaming.

5.6. Morphology of calibrated foams

The thin foam strands treated above are too small for mechanical measurements. Hence, a calibration unit was applied to obtain calibrated foams, which enable preparation of larger test specimens. In this section the morphology of these calibrated foam samples is discussed and compared to the morphology of the foam strands.

Figure 83 depicts densities of all calibrated foams investigated, which were measured at the department of Polymer Engineering at the University of Bayreuth using the buoyancy method. Densities of all calibrated foams are in the range between 0.24 and 0.33 g/cm^3. This means a drastic density enhancement caused by the compression of the hot foam during calibration compared to densities of foam strands without calibration, which are between 0.08 and 0.18 g/cm^3. Neat stabilized *i*-PP without any cell nucleating agents features a density of 0.33 g/cm^3 after foam calibration, which is the highest of all calibrated foams. All samples comprising cell nucleating agents feature lower densities. For these samples, correlations with foam density after calibration are observed neither for the chemical structure nor the concentration of additive. Concluding, by calibration of foams, large samples for mechanical testing were successfully produced, which feature densities in a narrow range. The comparability of foam densities after calibration is highly beneficial for later mechanical testing, as it prevents variation of mechanical properties due to density differences.

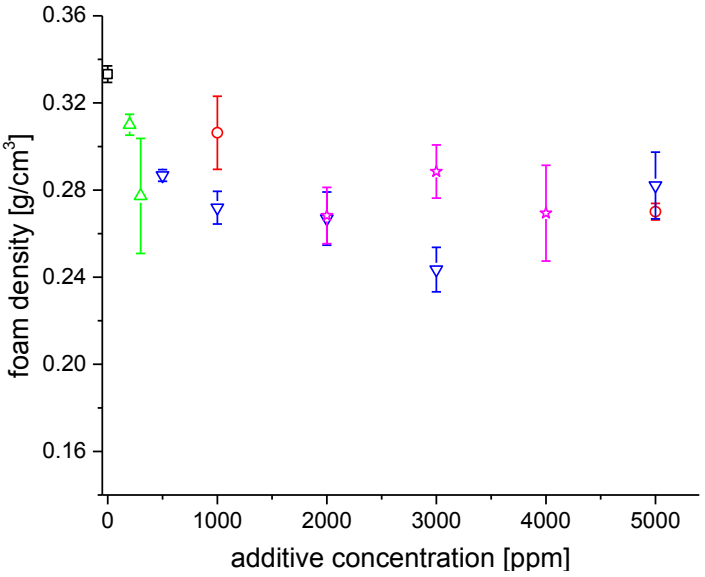

Figure 83: Foam densities of calibrated foams of neat *i*-PP (black), *i*-PP containing talc (red) and *i*-PP containing BTAs 5 (green), 6 (blue) and 7 (magenta). Symbols represent averages and error bars represent standard deviations of three measurements each. *Adapted with permission from ref. (Mörl et al. 2019)[191]. © (2017) The authors.*

Next, the microscopic morphology in the bulk of calibrated samples was investigated, being another property which could alter mechanical properties. Figure 84 shows SEM images of selected examples of calibrated foams. The images show that the cellular structure is still intact after calibration. In contrast to the foam strands discussed above, cells of calibrated foams feature clear shape anisotropy, i.e. they have been deformed during calibration.

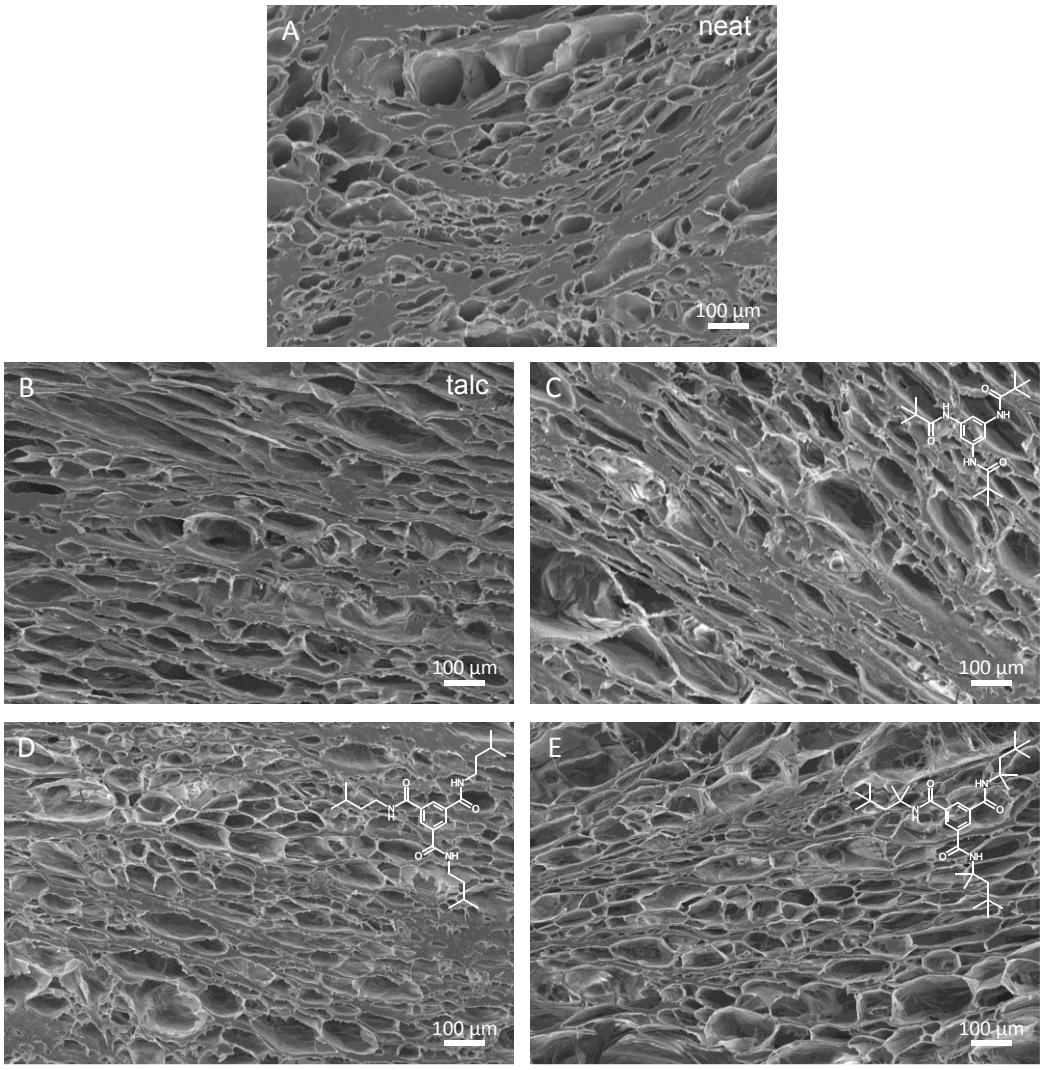

Figure 84: SEM micrographs of calibrated foams. Materials are neat *i*-PP (A) and *i*-PP with 5000 ppm of talc (B), 300 ppm of BTA 5 (C), 3000 ppm of BTA 6 (D) and 4000 ppm of BTA 7 (E).

Foam cell size was taken as a quantitative measure for the bulk morphology. Figure 85 shows average cell diameters of calibrated foams measured from SEM images at the department of Polymer Engineering at the University of Bayreuth. After calibration, foam cell diameters are in the range between 27 and 68 µm. This is quite the same as for non-

calibrated foams, which featured diameters in the range of 27 to 73 µm. Moreover, after calibration no correlation between cell diameter and cell nucleating agent is observed anymore. By contrast, a tendency towards smaller cells with increasing additive content was visible for foam strands (see Figure 80). Besides, standard deviations have increased, meaning that foam cell sizes are less homogeneous after calibration. This is attributed to the mechanical deformation of the foam during the calibration process. Summarizing, average cell sizes after calibration are comparable to the ones prior to calibration, which indicates that the calibration process does not alter the inner foam structure to a great extent.

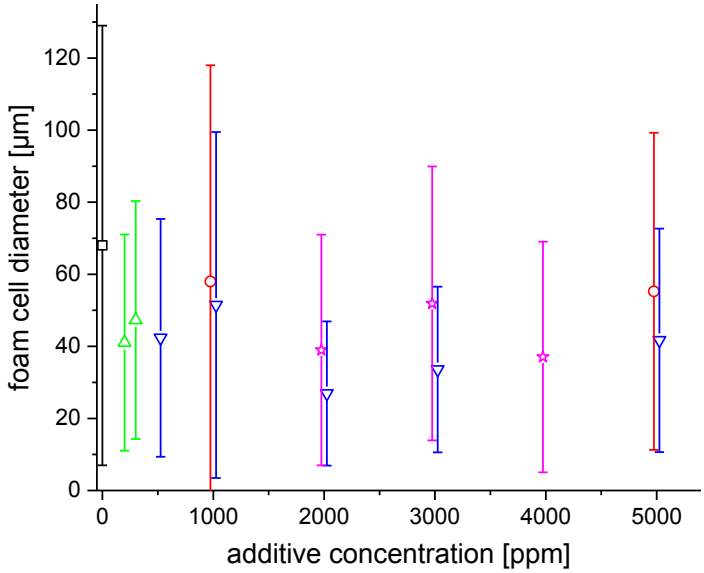

Figure 85: Average foam cell diameters of calibrated foams of neat *i*-PP (black), *i*-PP containing talc (red) and *i*-PP containing BTAs 5 (green), 6 (blue) and 7 (magenta). Symbols represent averages and error bars represent standard deviations of at least 100 measured foam cells each. Overlapping symbols are slightly shifted for the sake of clarity. *Data have already been published in ref. (Mörl et al. 2019)[191]. © (2017) The authors.*

Up to now, all compounds of stabilized *i*-PP and cell nucleating agents have been treated as macroscopically homogeneous materials. To obtain information about the single nano-objects present in the materials, calibrated foam samples were searched for additive objects at the SEM. In doing so, foams without further treatment as well as etched foams were investigated. For the latter, etching was done in an aqueous solution of $KMnO_4$, H_2SO_4 and H_3PO_4 for 1 h. SEM images of etched and non-etched foams after sputtering with Pt are shown in Figure 86. To increase the chance of finding objects, only foams comprising the maximum concentration applied in foaming of each additive were investigated this way.

Neat stabilized *i*-PP (1A) exhibits a rough surface texture with spikes prior to etching. This surface texture is removed by etching (1B), resulting in a smoother surface. The rough surface may stem from polymer crystallization processes at the gas/polymer interface. At the sample comprising 5000 ppm of talc, nano-platelets covered by a thin *i*-PP layer were observed without etching (2A). After etching, similar platelets lying at the surface without any cover layer were apparent (2B). These structures are identified as talc nano-platelets. For all three samples comprising BTAs, nanofibers were present in the non-etched samples (3A-5A). These fibers all seem to be partly covered by the *i*-PP matrix, while other parts pierce closer to the surface and can therefore be observed. In most cases it cannot be decided from SEM images whether visible fiber segments are still covered with a thin *i*-PP film or are in direct contact with cell gas. Nevertheless, at least for the right fiber in image 5A, a direct contact with air is visible for the fiber's end. This direct contact is required for the applied cell nucleation concept: It is based on cell nucleation at the interface between *i*-PP and the nano-object. When a cell nucleated this way grows, the nucleation site is supposed to stay uncovered at the foam cell surface. Yet, reliable conclusions on the occurrence of the proposed cell nucleation mechanism from these pictures are not possible.

After etching, all samples comprising BTAs show structures which are understood as impressions from the above mentioned nanofibers (Figure 86 3B-5B). Since BTA fibers are completely removed from the surface in the etching process, these impressions are supposed to be relicts of these fibers. The impressions only feature a small length reflecting the formerly uncovered area of the former fibers, which could exclusively be removed by the etching solution. In image 3B at the top end of the impression, a brighter area indicates that the fiber was longer than the imprint. Of course, fibers which are totally buried deep in the *i*-PP matrix cannot be displayed by this method. Also, due to the curved morphology of the foam surface, only a very small area of each cell could be investigated with the SEM, which is nevertheless assumed representative for the whole cell.

Concluding, it is possible to detect BTA fibers at the surface of foam cells. The use of non-etched samples is preferable to etched ones, as those allow direct observation of fibers, whereas after etching only a negative impression remains. Moreover, etching removes some *i*-PP from the cell surface and so prevents observation of fiber structures at the cell surface, which are the most interesting ones for drawing conclusions on the nucleation process.

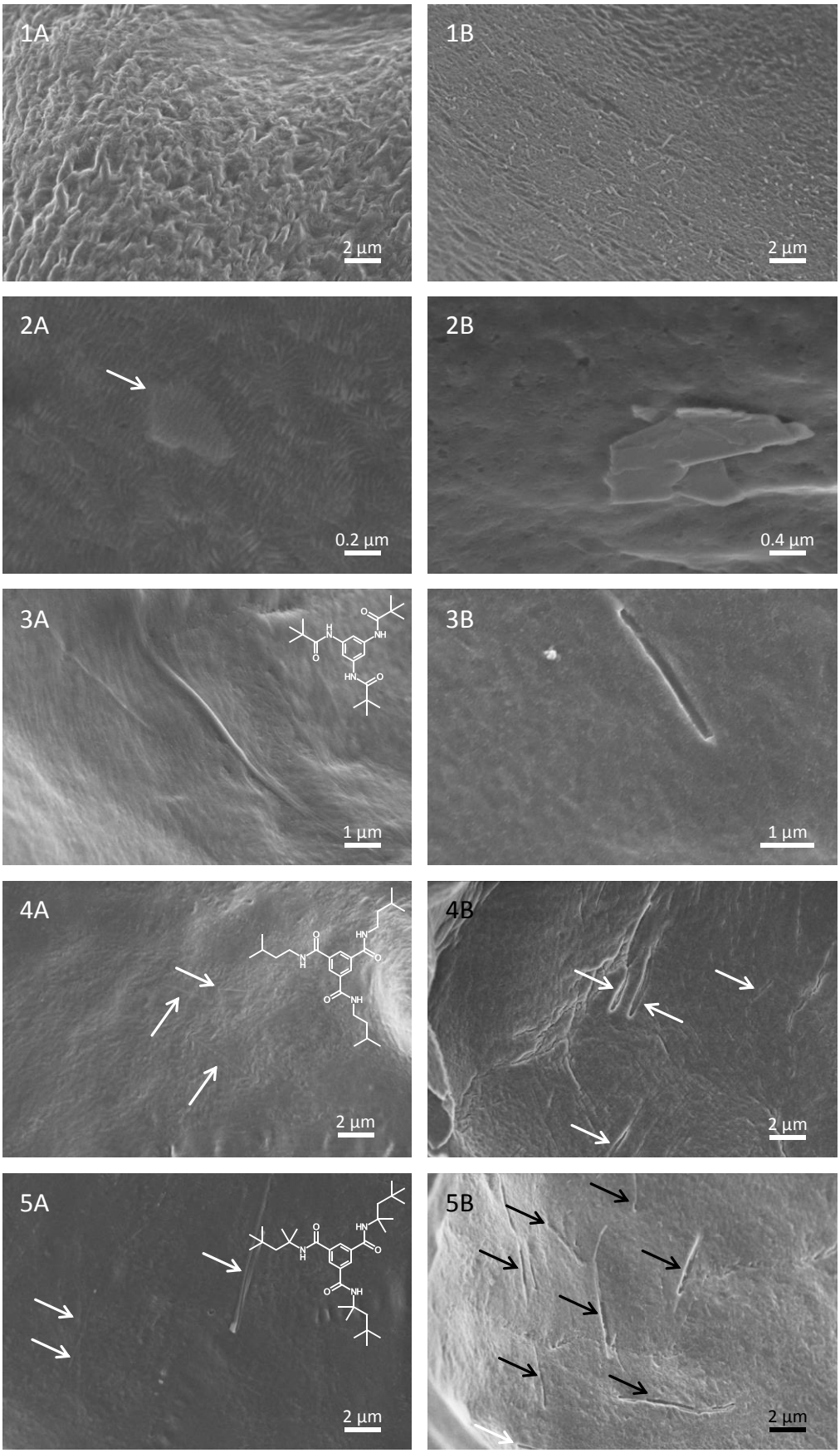

Figure 86: SEM micrographs of calibrated foams prior to (A) and after (B) etching. Materials are neat *i*-PP (1) and *i*-PP with 5000 ppm of talc (2), 300 ppm of BTA 5 (3), 3000 ppm of BTA 6 (4) and 4000 ppm of BTA 7 (5). Poorly visible nanostructures are marked with arrows.

5.7. Compression modulus of calibrated i-PP foams

In this section, mechanical properties of the calibrated foams and possible correlations of these properties with foam morphology are investigated. From all modes of load possible for solid matter, compression was selected, as it is the most used one for foams, as discussed in chapter 5.1.4. To exclude the effect of the more compact skin layer on foam mechanics, it was cut off the cylinders punched out of the calibrated foams. Thus, cylindrical specimens with a height and a diameter of 8 mm were obtained. All specimens were tested in compression using a universal testing machine at the department of polymer engineering at the University of Bayreuth.

Figure 87 exemplarily shows stress-strain-curves of neat *i*-PP, *i*-PP containing talc as reference and *i*-PP containing BTA. *i*-PP and *i*-PP with 5000 ppm talc exhibit a similar behavior up to a compression of around 7%. By contrast the sample comprising BTA exhibits higher stress values than both others up to around 8% of compression. However, at higher compressions, the sample comprising 4000 ppm of BTA 7 shows a much smaller slope, reaching a maximum compressive stress of almost 5 MPa at 50% strain. Its slope at high compressions is even flatter than that of the sample with talc, which reaches between 5 and 6 MPa at 50% compression. Neat *i*-PP reaches more than 8 MPa at 50% compression.

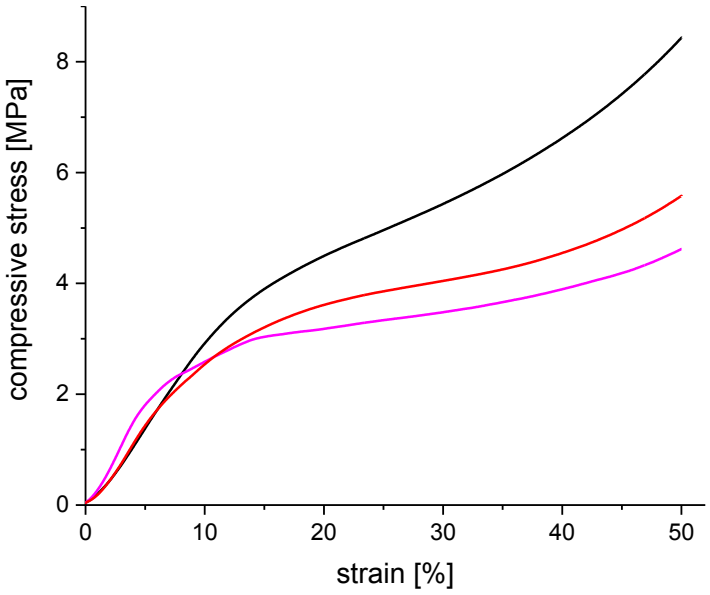

Figure 87: Stress-strain curves of foamed samples of neat *i*-PP (black), *i*-PP containing 5000 ppm of talc (red) and *i*-PP containing 4000 ppm of BTA 7 (magenta). *Data have already been published in ref. (Mörl et al. 2019)[191]. © (2017) The authors.*

The specific compressive modulus is a property well-suited to compare the compression behavior of different foams. It is derived from the slope of the curve in the linear region, i.e. at low compressions. Thus, the compression modulus describes reversible small deformations, as they are supposed to be predominant for construction materials.

Specific compression moduli of all calibrated foams are given in Figure 88. The neat stabilized *i*-PP features a specific compression modulus of around 100 MPa*cm^3/g. Addition of only 200 ppm of BTA 5 more than doubles this value to 210 MPa*cm^3/g. This is the highest value measured. Compounds comprising BTA 6 show a slow increase of compression modulus with increasing additive content in the concentration regime, where the BTA is soluble under compounding conditions. Finally, a maximum modulus of 185 MPa*cm^3/g is reached at 3000 ppm. By contrast, the sample comprising 5000 ppm of BTA 6 features a lower modulus. This is attributed to big BTA objects, which remained undissolved during compounding. Also for BTA 7, improved moduli are observed with increased BTA content, reaching a maximum of 194 MPa at 4000 ppm of BTA 7. Similarly, talc improves the compression modulus at both concentrations. Yet, with talc only the level of the worst performing compound comprising BTA in a soluble concentration is reached. Thus, BTA additives must feature an additional effect, which enables such drastic modulus improvements. As shown above, the densities of all calibrated foams are in the same region and thus cannot be the reason for the superior performance of the foams containing BTAs.

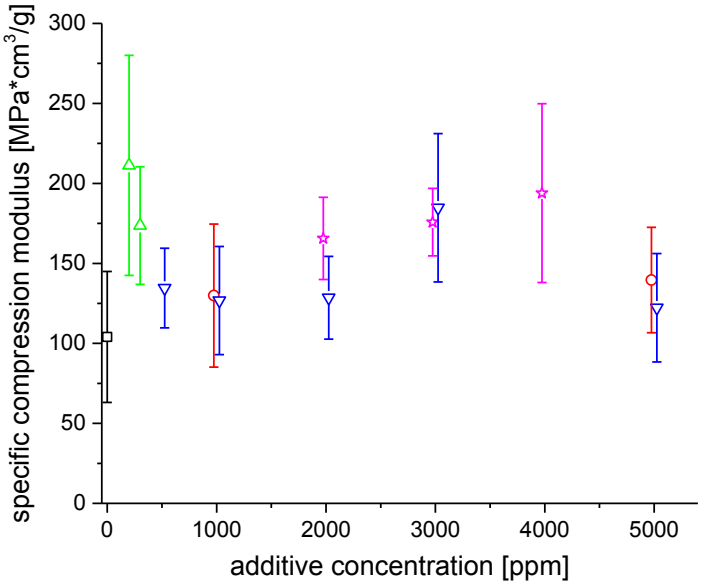

Figure 88: Specific compression moduli of calibrated foams of neat *i*-PP (black), *i*-PP containing talc (red) and *i*-PP containing BTAs 5 (green), 6 (blue) and 7 (magenta). Averages and standard deviations (error bars) are based on at least eight measured samples each. Overlapping symbols are slightly shifted for the sake of clarity. *Data have already been published in ref. (Mörl et al. 2019)[191]. © (2017) The authors.*

To shed light on the cause of this partly tremendous modulus improvement, factors which could influence mechanical properties of foams are excluded systematically. Therefore, compression moduli were plotted versus degree of crystallinity of *i*-PP, polymer crystallization temperature and foam cell size.

The degree of crystallinity of *i*-PP was taken into account as it is well-known that a higher degree of crystallinity renders polymers more brittle[192]. The degree of crystallinity was calculated from melting enthalpies as measured by means of DSC at the department of Polymer Engineering at the University of Bayreuth. No correlation between degree of crystallinity of *i*-PP and compression modulus of the foam was found. Moreover, the compound comprising 5000 ppm of talc, which does not perform better than any BTA, even yielded the highest degree of crystallinity.

Even if the overall degree of crystallinity of a sample is not changed, still the size and size of crystals might be. It is known that crystal nucleating BTAs reduce the crystal size of *i*-PP while enhancing the number of crystals[32]. In addition, heterogeneous crystal nucleation will take place on the surface of the nanofibers, while homogeneous nucleation occurs in the bulk *i*-PP material. In the first case, rod-like crystals are formed, while the second case yields spherulites. This crystal shape is also likely to have an impact on foam mechanics. Since the

applied BTAs feature dissimilar efficiencies in crystal nucleation, which results in different *i*-PP crystallization temperatures, these temperatures are used to track possible mechanics improvements by crystal shape: It is assumed that the worst nucleating agents yield a higher content of homogeneously nucleated *i*-PP. Hence, these samples should perform differently from the ones comprising better nucleating agents in terms of compression modulus, if there was a correlation between crystal shape and compression modulus. For the investigated samples, no clear correlation was observed. For the well nucleating BTAs 5 and 6, high compression moduli are found, which could indicate a weak correlation.

The cellular morphology is a third possible reason for drastically enhanced compression moduli using BTAs. Therefore, the already discussed cell sizes of calibrated foams were plotted versus compression moduli. No apparent correlation between both properties was observed. Thus, the compression modulus variations also cannot be attributed to differences in the foam morphology.

Having excluded all these possible reasons for enhancement of compression moduli of foams containing BTAs, another hypothesis remains: The BTA nanofibers present in the foams could reinforce the *i*-PP matrix, thus prevent bending of the cell walls and consequently raise the modulus.[191] Unfortunately, this hypothesis is hard to test, particularly, since the 3D-structure of BTA fibers in the cell walls cannot be accessed by etching due to the high chemical stability of *i*-PP.

For further investigation of the increase of compression modulus upon use of BTAs, which is beyond the scope of this thesis, it should be tested, whether this phenomenon is also present under other load types like shear or tensile stress. In addition, transfer of the concept to different polymers, which can be hydrolyzed, should allow studying the 3D-structure of the BTA formed. This will answer the question, whether isolated single fibers or a fiber network, which could bear load more easily, are present. Finally, a combination of two or more BTAs, which have to assemble independently, could be applied. This combination should not alter the single BTA's solubility, so that a much greater amount of BTAs can be solved overall. This is expected to yield more nanofibers and a further increased compression modulus, if the enhancement of the compression modulus is in fact due to the nanofibers,.

5.8. Conclusions

A major topic of this chapter was the improvement of extruded thermoplastic foams by supramolecular cell nucleating agents at the example of *i*-PP and BTAs. To overcome inhomogeneous dispersion, which is a possible negative feature of established non-soluble nucleating agents, a concept for foam extrusion including a step at which the BTA is dissolved, was applied. Following this concept, BTA and physical blowing agent are solved at high temperature and pressure in the first stage, providing good distribution of the BTA due to diffusion. Secondly, the temperature is lowered towards the foaming temperature to have the BTA self-assemble. In the third stage, the pressure is released rapidly to render the blowing agent insoluble. Here, the self-assembled structures from the second stage are intended to act as nucleation sites, reducing the foam cell diameter and hence improving final foam properties.

In the first part of this chapter, the applied linear *i*-PP was characterized thoroughly. The applied *i*-PP grade was investigated with and without stabilizers. The stabilized material was found to be well-suited for foam extrusion, while the non-stabilized *i*-PP suffered from degradation.

In the second section, three different preselected BTAs, which cover a broad range in terms of concentration, were self-assembled from 2,2,4,4,6,8,8-heptamethylnonane (HMN) to simulate later self-assembly in *i*-PP. All three BTAs yielded well-defined nanofibers. Next, different concentrations of each BTA were compounded into stabilized *i*-PP. The obtained compounds were characterized with respect to their dissolution and self-assembly temperatures to be able to select concentrations with a behavior matching the intended concept for the foaming process. In addition, the melt strength of the compounds was proven not to be significantly altered by the presence of the BTAs.

In the third section, ten compounds were produced in amounts of 10 kg each, comprising amounts from 200 to 4000 ppm of the three BTAs, selected on basis of the dissolution and self-assembly temperatures determined in the second section of this chapter. For comparison, also one compound without any cell nucleating agents, one BTA concentration being not entirely soluble in the foaming process and two compounds containing the insoluble reference material talc were produced. Using supercritical CO_2 as physical blowing agent, all materials were successfully processed with a tandem foam extrusion line, obtaining foams with densities in the range from 0.08 to 0.18 g/cm^3. Foam morphology

studies revealed that all additives reduced cell diameters, when applied in suitable concentrations. Average cell diameters down to around 27 µm were realized with talc as well as with a BTA bearing *tert*-octyl substituents. This shows that the initial concept, comprising dissolution and self-assembly of BTAs, followed by cell-nucleation at the self-assembled structures, works at least as well as the application of non-soluble standard nucleating agents such as talc, while making dispersing easier due to the dissolution step. In anticipation of the sample treatment for mechanical testing, the morphology of calibrated foams was compared to the one of foam strands discussed above. As expected, the foam density was drastically enhanced to the range from 0.24 to 0.33 g/cm^3 by calibration. By contrast, cell diameters still were in the same range as in the foam strands. Yet, they showed broader distributions after calibration, which is taken as a sign of shear-induced deformation and, to some degree, coagulation of cells. In addition, BTA fibers were visualized in foams, to the best of my knowledge for the first time. As well, talc platelets were found in the respective compounds. This was performed by SEM without any etching of the foams. Samples, which had been etched for comparison, just showed impressions in the *i*-PP matrix. These were caused by BTA fibers, which had been removed by the previous etching. The detected structures prove that the self-assembly prerequisite for the presented cell nucleation concept yields nanoobjects even under real foam processing conditions.

The fourth section reports results of compression modulus measurements of calibrated samples of the foams, which were conducted at the department of Polymer Engineering. Addition of up to 5000 ppm of talc improves the specific compression modulus just to 140 MPa*cm^3/g from 104 MPa*cm^3/g for neat *i*-PP. By contrast, only 200 ppm of the best performing BTA raise the neat value by more than 100% to 211 MPa*cm^3/g. Having excluded several possible other factors, a reinforcing effect of BTA nanofibers is thought to be responsible for this drastic improvement. Furthermore, foam mechanics were shown to be highly dependent on the respective BTA's chemical nature, which opens further optimization possibilities by investigation of other BTAs. The results presented also have partly been published in the *Journal of Cellular Plastics*.[191]

6. Experimental Section

6.1. Materials

Solvents and isotactic polypropylene

Marlotherm (Marlotherm SH; Julabo Labortechnik GmbH) and paraffin (Grüssing GmbH) were destilled prior to use. Anisole (Sigma Aldrich; 99%), methyl cyclohexane (MCH; Sigma Aldrich; 99%), 1-Heptanol (ABCR; 99%) and *n*-hexane (Acros; 96%) were used as received. All other solvents were destilled prior to use.

The investigated linear *i*-PP (Moplen HF400G) was kindly supplied by LyondellBasell. The material was a reactor grade without any further additives.

Chemicals

BTA 5 (trade name XT386) was kindly provided by Ciba Specialty Chemicals. BTAs 6 and 7 where synthesized as described in literature[193,194,195]. Detailed synthetical procedures and product characterizations are given in the respective compound sheets.

Talc for cell nucleation (Jetfine 3 C A) with a median particle size of 0.7 µm was retrieved from Imerys Talc. The stabilizers Irganox 1010 and Irgafos 168 were supplied by BASF SE. All *i*-PP samples were stabilized with 0.05 wt% of Irganox 1010 and 0.1 wt% of Irgafos 168, if not stated otherwise.

6.2. Analytical methods

Nuclear magnetic resonance (NMR)

^{1}H-NMR experiments were performed using a Bruker Ultrashield 300 NMR spectrometer. The corresponding resonance frequency was 300 MHz. Data evaluation was performed with SpinWorks 4 (University of Manitoba). As internal reference, peaks of the respective solvent were utilized.

Mass spectroscopy (MS)

Mass spectroscopy was performed on a Finnigan MAT 8500 mass spectrometer using electron ionization.

Thermogravimetric analysis (TGA)

TGA measurements were done using a Mettler Toledo TGA/DTA-system (TGA/SDTA851e). Typically, for analysis 8 to 12 mg of the substance were heated from ambient temperature to 700 °C with a rate of 10 K/min under a nitrogen flow of 50 mL/min.

Differential scanning calorimetry (DSC)

DSC measurements were done using a Mettler Toledo DSC 2 with a nitrogen flow of 50 mL/min.

For the investigation of pure bis- and trisamides, a high pressure steel pan was completely filled with sample material and closed. Next, the pan containing the sample was heated from 50 °C to the respective maximum temperature with a heating rate of 10 K/min and held at this temperature for five minutes. Subsequently, it was cooled to 50 °C again with a cooling rate of 10 K/min. This heating/cooling cycle was repeated once. Typically, second heating and cooling scans are given. For compounds prone to decomposition, first heating and cooling scans are given instead.

Compounded *i*-PP samples were molten into the aluminium DSC pans prior to the measurements to improve the heat transfer between samples and pans. For the BTA screening, compounded samples of BTAs in *i*-PP were heated from 50 to 240 °C, kept at 240 °C for 5 min and subsequently cooled to 50 °C again. Heating and cooling rate was 10 K/min. This thermal profile was repeated at least once and the polymer crystallization temperature of

each composition was determined as the average of the crystallization peaks of first and second heating/cooling cycle. For the determination of the *i*-PP crystallization temperatures of the compounds for foam extrusion a higher top temperature was necessary to erase orientation effects originating in the harsher compounding conditions applied: Here, DSC samples were heated to 280 °C instead of 240 °C. Besides that, the rest of the temperature program was unchanged and corresponds the BTA screening measurements reported above.

Crystal structure determination

Powder X-ray diffraction was done with a STOE StadiP diffractometer using Cu $K\alpha_1$-radiation (λ = 1.5418 Å). The ground powder was filled into capillary tubes with a diameter of 0.5 mm. Measurements were done in Debye–Scherrer geometry with a step size of 0.015° in an angular range (2Θ) from 3 to 50°. For the bisamides 1 and 2, a DFT optimization was conducted using Accelrys MS Modeling. For the other bisamides, the program Castep 6 was utilized in this step. The geometry was optimized by means of the Tkatchenko-Scheffler method. For Rietveld refinement, the program Topas 5 was applied.

Single crystal diffraction was done using a STOE IPD II diffractometer equipped with a Ge(111) monochromator at 173 K with Mo Kα radiation (λ = 0.71073 Å). The software STOE X-Area was applied for data acquisition, space group determination and construction of reciprocal space planes. Structure solution and refinement was done using ShellX. Refinement was done with isotropic displacement parameters for H-atoms and with anisotropic displacement parameters for non-H-atoms. All protons were added geometrically. These crystal structure determinations were conducted at the department of Inorganic Chemistry III at the University of Bayreuth.

To visualize the structures, the resulting files (*.cif) were used to display the molecular structures with viewing directions along the crystallographic axes with Diamond (version 3.0). For the sake of clarity, H-Atoms not involved in any hydrogen bonds were omitted for the ball-and-stick-models.

Solid-state NMR spectroscopy

Solid-state NMR experiments were performed using a Bruker Avance III HD 600 spectrometer. The frequency for magic angle spinning (MAS) was 10 kHz, if not stated otherwise, and the magnetic field strength B_0 was 14.10 T. At this field strength the

resonance frequencies were 600.15 MHz for ^{1}H, 150.92 MHz for ^{13}C and 564.65 MHz for ^{19}F., ^{1}H ^{13}C cross polarization was done for ^{13}C spectra. Therefore, ^{1}H was excited with a 90°-pulse for 2.7 µs, before a contact time of 3 ms was allowed. During this time, a linear ramp from 50 to 100% intensity was applied. During data acquisition, protons were decoupled with the spinal 64 sequence.

Fourier-transform infrared spectroscopy (FTIR)

FTIR was done by means of a Spectrum 100 FTIR spectrometer (Perkin Elmer) in attenuated total reflection (ATR) mode. The respective sample powder was placed on the ATR window and fixed with a stamp. Four scans from 650 to 4000 cm^{-1} with a step size of 4 cm^{-1} were performed for each sample.

Surface energy measurement

The test substance was pressed into flat circular specimens with a diameter of 1.2 mm. Therefore, 80 to 140 mg of the substance was placed between two circular capton foils and compacted with a pressure of 10 bars for 5 min by a manually operated pump. For six test liquids (water, formamide, glycerol, ethylene glycol, diiodo-methane and aniline), contact angles on the the specimens' flat surfaces were determined by the sessile drop method using a Krüss DSA25S drop shape analyzer. The average contact angle of at least five measurements was determined for each liquid. Using the polar and disperse contribution to the surface energy of each liquid, as they are listed in Table 11, the surface energy of the sample was calculated with a analysis software (DSA4; Krüss GmbH, 2004) using the OWRK method[99].

Table 11: Disperse and polar contributions and the total surface tension for all six test liquids according to the analysis software (DSA4; Krüss GmbH) used for surface energy determination.[99]

Liquid	disperse	polar	total
Water	26.4	46.4	72.8
Formamide	39.5	18.7	57.0
Glycerol	37.0	26.4	63.4
Ethylene glycol	26.4	21.3	47.7
Diiodo-methane	50.8	0.0	50.8
Aniline	33.1	10.3	43.4

Micro differential scanning calorimetry (µ-DSC)

µ-DSC measurements were done using a Setaram Micro DSC III. A dispersion of 500 ppm of bisamide 1 in *o*-DCB was heated to 120 °C and a homogeneous dispersion of nano-platelets was formed by shaking the hot vial in an ice bath. This is described in detailed at the self-assembly methods. 909 mg of the dispersion were filled into the sample cell of the µ-DSC. The reference cell was filled with 911 mg of pure *o*-DCB. The sample was heated from 20 to 115 °C and subsequently cooled to 20 °C. After an isothermal step lasting 2 h, this heating/cooling cycle was repeated once. This experiment was conducted with three different heating/cooling rates (1, 0.5 and 0.1 K/min) using the same sample.

Atomic force microscopy (AFM)

AFM measurements were done using a Veeco dimension 3100 atomic force microscope equipped with a NanoScope IV controller. Bruker OTESPA-R3 silicon cantilevers were used in tapping mode. Squared AFM height images were recorded with 512 lines and 512 points per line. Images were evaluated using Bruker NanoScope Analysis software (version 1.40). Prior to further analysis, the images were flattened (1^{st} order).

To analyze layer thicknesses, small sections from crystals' top surfaces were used. A step analysis, which considers many parallel lines to reduce noise in z direction, gave a profile of the steps along the x axis. From this profile, tilts were removed using the evaluation software. Next, parallel lines were fitted to the different step levels and the lines' distance was measured to obtain the step heights.

Total heights of platelets were determined fom cross sections. The z distance between wafer level and top of the individual platelet was measured from each cross section. Average and standard deviation of the height were calculated from a minimum of 12 platelets from at least three areas of each sample. Agglomerated platelets were excluded in this analysis, since these at least partly overlapping specimens did not give reliable data.

Scanning electron microscopy (SEM)

For the preparation of SEM samples from dispersions, one drop of the respective dispersion was cast on a clean silicon wafer. The supernatant solvent was removed with a filter paper from the rim of the wafer piece. Then, the sample was dried at ambient conditions or in high vacuum and fixed on a SEM stub using a conductive tab. Subsequently, the sample was

sputtered with a typically 1.3 nm thick platinum layer using a Cressington 208HR sputter coater.

Foam samples were prepared by cutting up to 2 mm thick slices out of the foams with a scalpel and gluing them onto a SEM stub using a conductive tab. Foam samples were etched in a freshly prepared solution consisting of 3 wt% of $KMnO_4$, 64.7 wt% of H_2SO_4 (95%) and 32.3 wt% of H_3PO_4 (85%). Etching took 1 h in the stirred solution. Afterwards, the samples were rinsed with H_2O_2, water and acetone. Foam samples were sputtered with a 1.3 nm thick platinum layer or with gold.

SEM was done with a field emission scanning electron microscope (Zeiss LEO 1530) using an accelerating voltage of 3 kV.

Size exclusion chromatography (SEC)

SEC was done at 160 °C using 1,3,5-trichlorobenzene as solvent. Samples of *i*-PP in 1,3,5-trichlorobenzene with a concentration of 2.30 mg/mL were prepared by stirring at 160 °C overnight. 200 µL of each sample were injected on the SEC column. Signal detection was done with a refractive index detector. For the data evaluation a calibration curve based on a polystyrene standard was used. Therefore, measured values of *i*-PP allow a good relative comparison, but should not be taken as absolute values.

Melt flow index (MFI)

MFI measurements were done using a Meltflixer MT (SWO Polymertechnik GmbH) at 235 °C with a weight of 2.16 kg following ISO 1133.

Melt strength determination

Melt strength determination was done using a Rheograph 6000 capillary rheometer (Göttfert) with a Rheotens 71.97 (Göttfert). Measurement temperature was 210 °C. Piston speed was 0.208 mm/s and a die with a length of 30 mm and a diameter of 2 mm was used. The strand length was 95 mm and the shear speed was 30 s^{-1}. Five measurements were conducted for each material and average curves were plotted.

Additive solubility determination

Concentration dependent dissolution and self-assembly temperatures of the additives were recorded using a Diaphot 300 light microscope (Nikon) equipped with crossed polarizers, while the samples were heated with a FP82TM hot-stage (Mettler). Films of about 10 mg of the injection molded materials were heated from 100 to 260 °C at a heating rate of 10 K/min. The temperature at which the last visible birefringent additive structures vanished was denoted as dissolution temperature. Then, the film was cooled to 100 °C again with 10 K/min. When the first birefringent additive structures were observed, the corresponding temperature was denoted as self-assembly temperature. This heating/cooling procedure was repeated once.

Wide angle X-ray scattering (WAXS)

WAXS of the injection molded samples was done using a D8 advance X-ray diffractometer (Bruker). Measurements were done using Cu K-α radiation in transmission geometry in an angular range (2Θ) from 8 to 30° with a step size of 0.05° and an acquisition time of 10 s per step. Peak heights were evaluated with the software X'Pert High Score Plus (PANalytical).

Optical properties of injection molded samples

Haze and clarity of the injection molded samples were measured with a hazemeter Haze Gard plus (BYK Gardener). Three samples of each composition were measured to determine average values and standard deviations.

Foam density measurements

Foam densities were determined according to ISO 1183 using the buoyancy method in a water bath. At least three samples per material were investigated to determine average values and standard deviations. Pieces of the foam strand or cylinders (8 mm diameter and height) drilled out of the calibrated foams were used as samples. From the cylinders the skin layer was cut from bottom and top prior to measurements.

Characterization of foam morphology

To characterize foam morphologies, cell densities and diameters were investigated using SEM images of the foams (see above). To enhance the image contrast for automated

evaluation, the cell walls were manually traced onto a transparent foil, covered with a white paper and scanned. The resulting black and white image was evaluated with ImageJ (National Institute of Mental Health). Cell radii were calculated from circles featuring the same area as the cell sections on the SEM images. Cell densities were determined from representative rectangular sections of the SEM images. The cell density was calculated from the section's area A and the number of cells within the section n via equation 7:

$$cell\ density = (\frac{n}{A})^{1,5} \quad (7)$$

For all cell density determinations, n was calculated taking all cells, even those only partly within the section, into account.

Determination of the compression modulus

Compression moduli were measured in compression mode following DIN 53421 with a Z 2,5 universal testing machine (Zwick). Cylinders (8 mm diameter and height) drilled out of the calibrated foam were measured. Prior to the measurement, the samples were pre-loaded with 2 N. For modulus determination, the test speed was 1.0 mm/min. At higher compressions, the test speed was reduced to 0.8 mm/min. Measurements were stopped at 50% compression strain. Each compression modulus was calculated from the linear region of the stress-strain curve. At least eight samples per material were measured to determine averages and standard deviations.

6.3. Synthesis and properties of compounds

6.3.1. Symmetrically substituted 1,4-bisamides with tert-butyl-substituents

Bisamide based on *trans*-1,4-diaminocyclohexane with *tert*-butyl-substituents

Identifier: **1** (in this thesis)

N,N'-(Cyclohexane-*trans*-1,4-diyl)bis(2,2-dimethylpropanamide)

Synthesis:

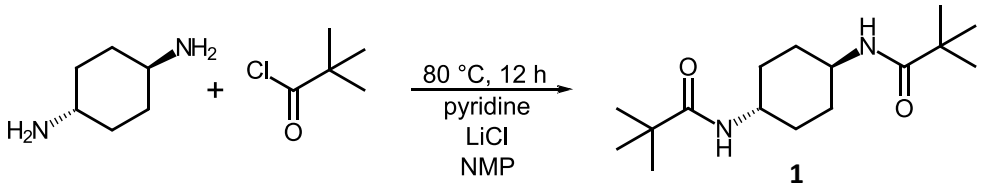

1

7.3 g of pivalic acid chloride (61 mmol) were slowly added to a mixture of 3.0 g of *trans*-1,4-diaminocyclo-hexane (26 mmol), 10 mL of pyridine, 0.05 g of LiCl and 180 mL of *N*-methyl-2-pyrrolidone (NMP) at 0 °C under nitrogen atmosphere. The reaction mixture was heated to 80 °C and stirred overnight. The mixture was precipitated in cold water and the white solid was filtered off, dried under vacuum for 2 h (70 °C, 100 mbar) and crystallized from methanol. Yield: 4.5 g (62%) of 1 were obtained as white crystals.

Characterization

^{1}H-NMR (300 MHz, $CDCl_3/CF_3COOD$): δ (ppm) = 3.89 (2 H,m), 2.00 (4 H, m), 1.44 (4 H, m), 1.27 (18 H, s)

MS (m/z, %): 282 (M^+, 3.3), 197 (10.4), 181 (74.5), 127 (5.7), 102 (100), 85 (9.4), 80 (6.6), 57 (3.8)

Thermogravimetric analysis (TGA)

- mass loss of 5% at 267 °C.

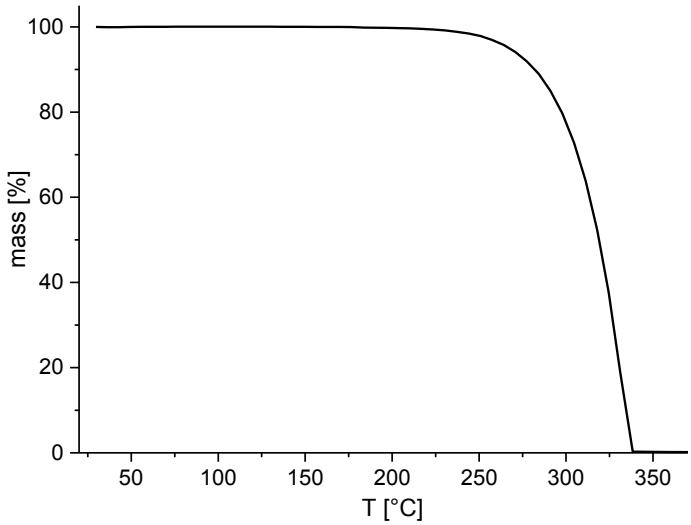

Figure 89: TGA curve of compound **1**. The Measurement was done with a heating rate of 10 K/min under N_2.

Differential scanning calorimetry (DSC)

- 2nd heating curve: Phase transition at 272 °C (6.4 kJ/mol)
- 2nd cooling curve: Phase transition between 130 °C and 190 °C (9.2 kJ/mol)

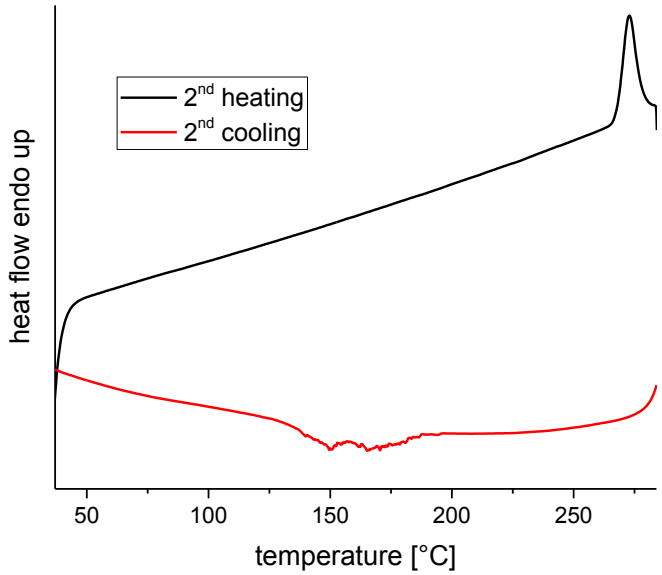

Figure 90: DSC second heating and cooling scans of compound **1**. Measurements were performed with a heating/cooling rate of 10 K/min in a sealed high-pressure steel pan.

Bisamide based on 1,4- phenylendiamine with *tert*-butyl-substituents

Identifier: **2** (in this thesis)

N,N'-(phenyl-1,4-diyl)bis(2,2-dimethylpropanamide)

Synthesis:

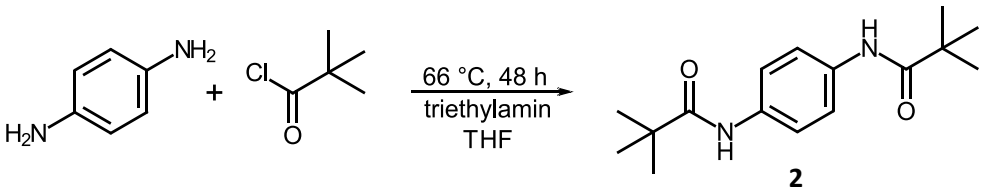

2

8.6 g of pivalic acid chloride (71 mmol) were slowly added to a mixture of 3.5 g 1,4-phenylenediamine (32 mmol), 40 mL of triethylamine and 250 mL of tetrahydrofuran (THF) at 0 °C under argon atmosphere. The reaction mixture was refluxed and stirred for two days. After evaporation of solvents, the solid residue was dispersed in water and filtered off. Recrystallization from methanol yielded 6.8 g (77%) of the product as white crystals.

Characterization

^{1}H-NMR (300 MHz, DMSO): δ (ppm) = 9.12 (2 H, s), 7.52 (4 H, s), 1.21 (18 H, s)

MS (m/z, %): 276 (M^{+}, 81.0), 233 (4.7), 192 (48.3), 108 (17.4), 85 (7.2), 58 (100), 42 (15.9)

Thermogravimetric analysis (TGA)

- mass loss of 5% at 295 °C.

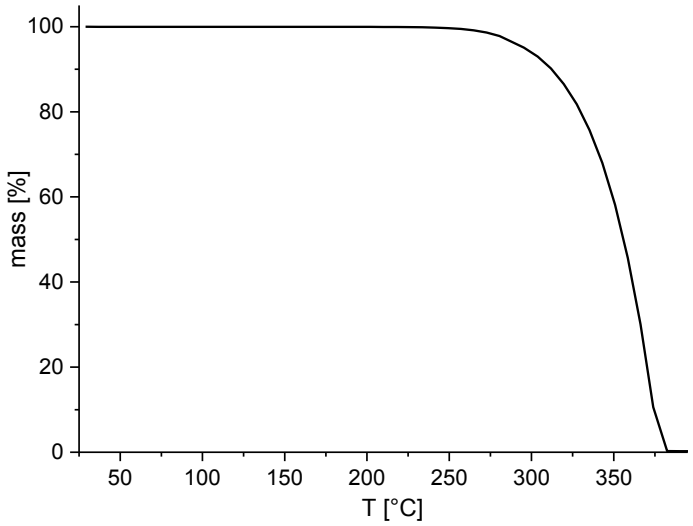

Figure 91: TGA curve of compound **2**.The measurement was done with a heating rate of 10 K/min under N_2.

Differential scanning calorimetry (DSC)

- 2nd heating curve: Phase transitions at 263 °C (0.6 kJ/mol) and 281 °C (36.0 kJ/mol)
- 2nd cooling curve: Phase transitions at 237 °C (0.7 kJ/mol) and 268 °C (37.1 kJ/mol).

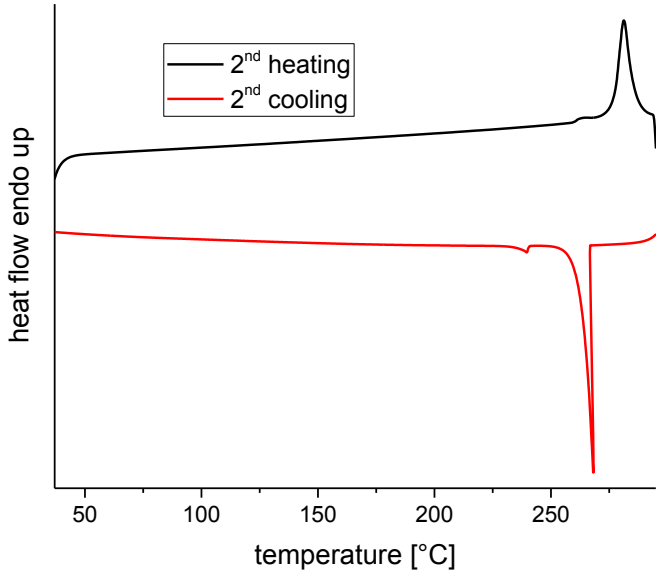

Figure 92: DSC second heating and cooling scans of compound **2**. Measurements were performed with a heating/cooling rate of 10 K/min in a sealed high-pressure steel pan.

6.3.2. Asymmetrically substituted 1,4-bisamides

Synthesis of the *mono*-substituted intermediate

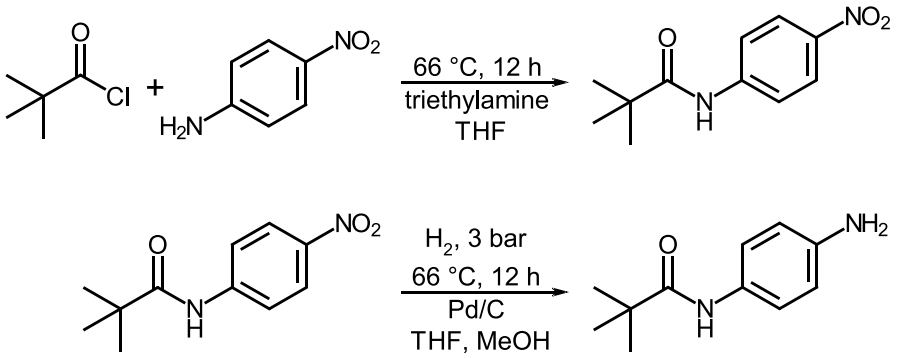

2.9 g of pivaloyl chloride (24 mmol) was dropped to a mixture of 3.0 g 4-nitroaniline (22 mmol), 20 mL of trimethylamine and 150 mL of anhydrous tetrahydrofuran (THF) at 0 °C under argon atmosphere. The reaction mixture was refluxed and stirred overnight. After removal of solvents, the solid residue was washed with water and recrystallized from hexane, yielding 4.3 g (89%) of *N*-(4-nitrophenyl)-2,2-dimethylpropionamide.

Subsequently, 250 mL of THF and 50 mL of MeOH were added to the product together with palladium on activated charcoal (10% Pd, 0.4 g). Hydrogenation with H_2 (3 bar) at 35 °C was performed overnight. The catalyst was removed by filtration over Alox N and the solvents were evaporated. The product *N*-(4-aminophenyl) -2,2-dimethylpropanamide was obtained as white powder in a quantitative yield (3.7 g).

Bisamide based on 1,4-phenylenediamine with *tert*-butyl- and *n*-perfluoropropane substituents

Identifier: **3A** (in this thesis)

2,2,3,3,4,4,4-Heptafluoro-1-(*p*-pivaloylaminophenylamino)-1-butanone

Synthesis:

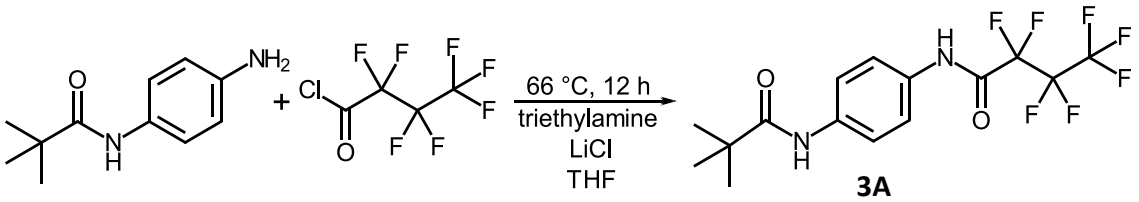

3.1 g of *n*-perfluorobutanoyl chloride (14 mmol) were slowly added to a mixture of 2.0 g of *N*-(4-aminophenyl)-2,2-dimethylpropanamide (11 mmol), 10 mL of triethylamine and 100 mL of anhydrous THF at 0 °C under argon atmosphere. The reaction mixture was kept at 0 °C and stirred for one hour. Subsequently, it was refluxed and stirred overnight. After evaporation of solvents, the solid residue was dispersed in water and filtered off. Crystallization from methanol yielded 2.6 g (64%) of the product as white crystals.

Characterization

^{1}H-NMR (300 MHz, DMSO): δ (ppm) = 11.23 (1 H, s), 9.30 (1 H, s), 7.62 (4 H, m), 1.22 (9 H, s)

MS (m/z, %): 388 (M^{+}, 72.1), 369 (6.7), 354 (4.5), 304 (29.3), 133 (2.1), 107 (17.1), 85 (14.8), 69 (4.2), 57 (100), 41 (12.0)

Thermogravimetric analysis (TGA)

- mass loss of 5% at 221 °C

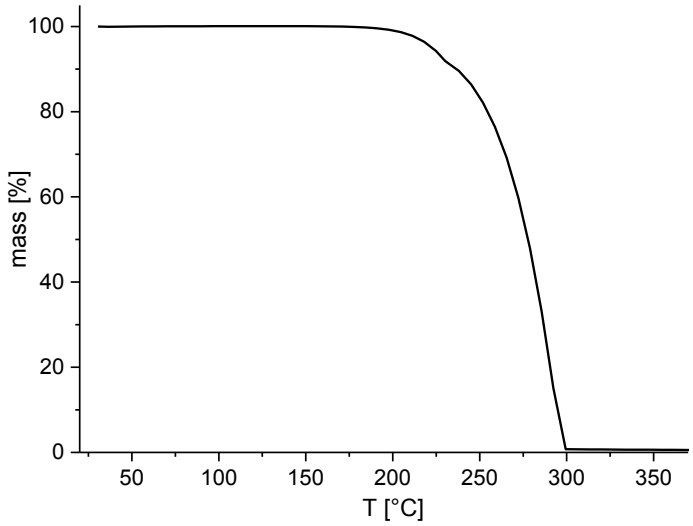

Figure 93: TGA curve of compound **3A**. The measurement was done with a heating rate of 10 K/min under N_2.

Differential scanning calorimetry (DSC)

- 2nd heating curve: Phase transition at 226 °C (3.7 kJ/mol)
- 2nd cooling curve: Phase transition at 213 °C (3.6 kJ/mol)

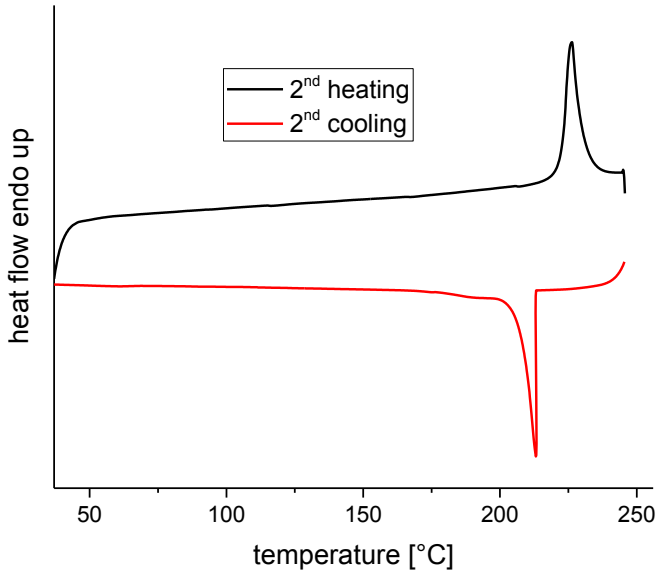

Figure 94: DSC second heating and cooling scans of compound **3A**. Measurements were performed with a heating/cooling rate of 10 K/min in a sealed high-pressure steel pan.

Bisamide based on 1,4-phenylenediamine with *tert*-butyl- and *n*-perfluoropentane substituents

Identifier: **3B** (in this thesis)

2,2,3,3,4,4,5,5,6,6,6-Undecafluoro-1-(*p*-pivaloylaminophenylamino)-1-hexanone

Synthesis:

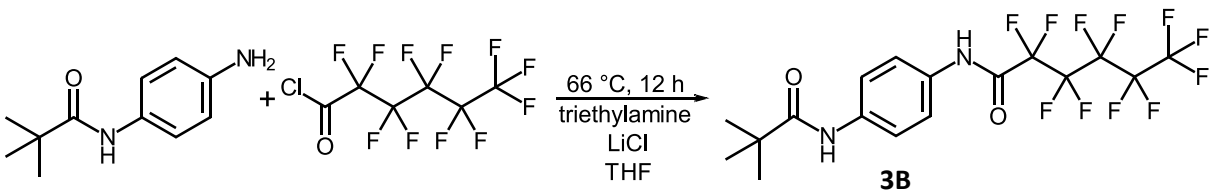

3B

Perfluorohexanoyl chloride (4.5 g, 14 mmol) was slowly added to a mixture of 2.0 g of *N*-(4-aminophenyl)-2,2-dimethylpropanamide (10 mmol), 10 mL of triethylamine and 100 mL of anhydrous THF at 0 °C under argon atmosphere. The reaction mixture was refluxed and stirred overnight. After evaporation of solvents, the solid residue was dispersed in water and filtered off. Crystallization from methanol yielded 1.0 g (20%) of the product as white crystals.

Characterization

^{1}H-NMR (300 MHz, DMSO): δ (ppm) = 11.23 (1 H, s), 9.30 (1 H, s), 7.62 (4 H, m), 1.22 (9 H, s)

MS (m/z, %): 488 (M^{+}, 77.0), 469 (13.9), 445 (4.77), 404 (30.9), 107 (13.9), 85 (15.4), 57 (100), 41 (10.8)

Thermogravimetric analysis (TGA)

- mass loss of 5% at 221 °C

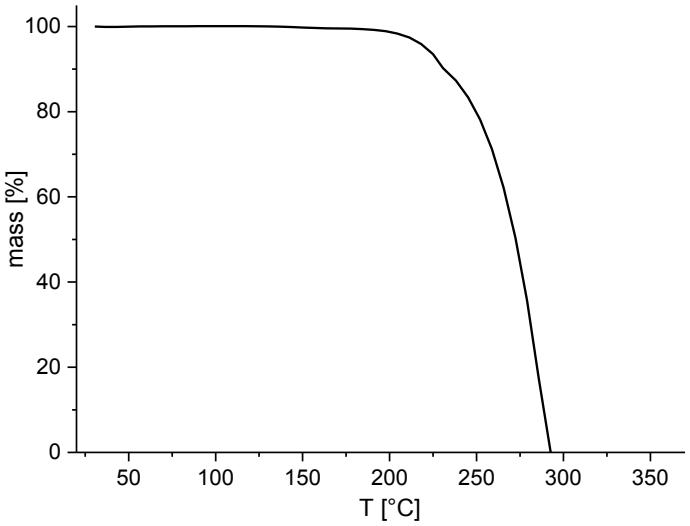

Figure 95: TGA curve of compound **3B**. The measurement was done with a heating rate of 10 K/min under N_2.

Differential scanning calorimetry (DSC)

- 2nd heating curve: Phase transition at 226 °C (9.8 kJ/mol)
- 2nd cooling curve: Phase transition at 195 °C (10.5 kJ/mol)

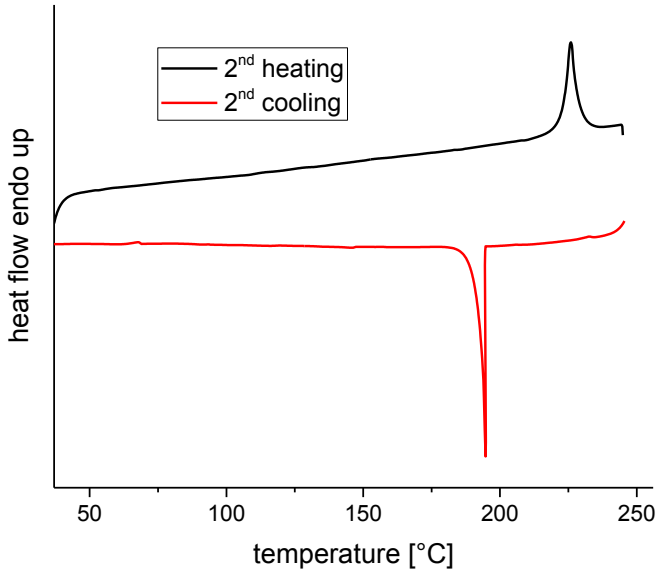

Figure 96: DSC second heating and cooling scans of compound **3B**. Measurements were performed with a heating/cooling rate of 10 K/min in a sealed high-pressure steel pan.

Bisamide based on 1,4-phenylenediamine with *tert*-butyl- and *n*-perfluoroheptane substituents

Identifier: **3C** (in this thesis)

2,2,3,3,4,4,5,5,6,6,7,7,8,8,8-Pentadecafluoro-1-(*p*-pivaloylaminophenylamino)-1-octanone

Synthesis:

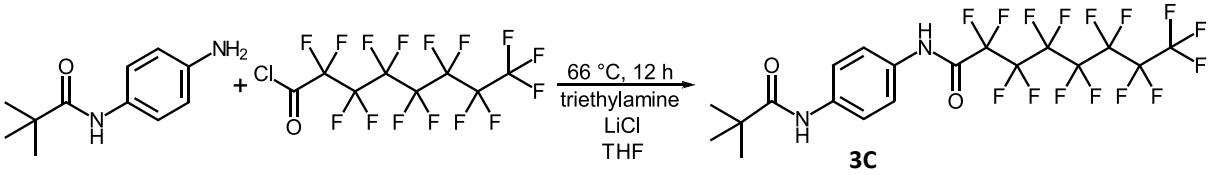

3C

4.4 g of perfluorooctanoyl chloride (10 mmol) were slowly added to a mixture of 1.5 g of *N*-(4-aminophenyl)-2,2-dimethylpropanamide (7.8 mmol), 10 mL of triethylamine and 100 mL of anhydrous THF at 0 °C under argon atmosphere. The reaction mixture was refluxed and stirred overnight. After evaporation of solvents, the solid residue was dispersed in water and filtered off. Crystallization from ethyl acetate yielded 3.85 g (84%) of the product as white crystals.

Characterization

^{1}H-NMR (300 MHz, DMSO): δ (ppm) = 11.21 (1 H, s), 9.30 (1 H, s), 7.61 (4 H, m), 1.22 (9 H, s)

MS (m/z, %): 588 (M^{+}, 26.9), 569 (7.5), 504 (14.0), 107 (10.7), 85 (15.1), 57 (100)

Thermogravimetric analysis (TGA)

- mass loss of 5% at 221 °C

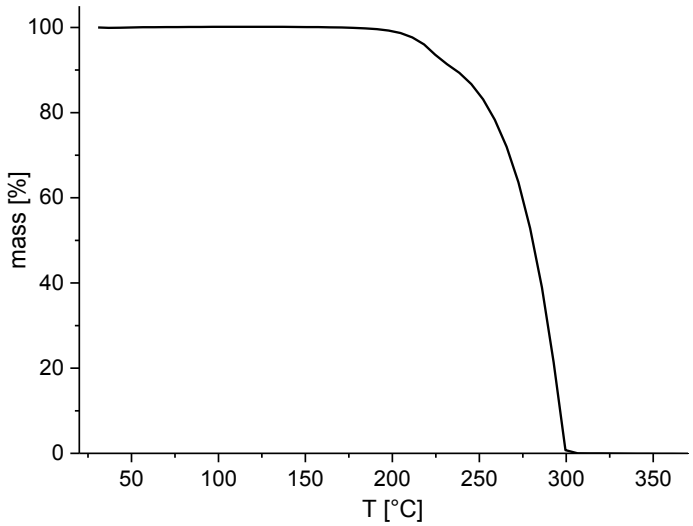

Figure 97: TGA curve of compound **3C**. The measurement was done with a heating rate of 10 K/min under N_2.

Differential scanning calorimetry (DSC)

- 2nd heating curve: Phase transition at 221 °C (11.0 kJ/mol)
- 2nd cooling curve: Phase transition at 203 °C (11.7 kJ/mol)

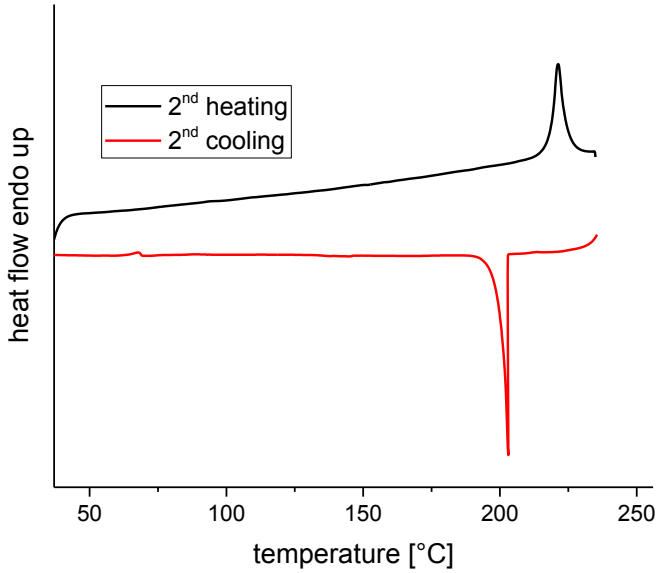

Figure 98: DSC second heating and cooling scans of compound **3C**. Measurements were performed with a heating/cooling rate of 10 K/min in a sealed high-pressure steel pan.

6.3.3. Symmetrically substituted 1,4-bisamides with fluorocarbon substituents

Bisamide based on 1,4-phenylendiamine with *n*-perfluoropropane substituents

Identifier: **4A** (in this thesis)

N,N'-1,4-phenylenebis(2,2,3,3,4,4,4-heptafluorobutanamide)

Synthesis:

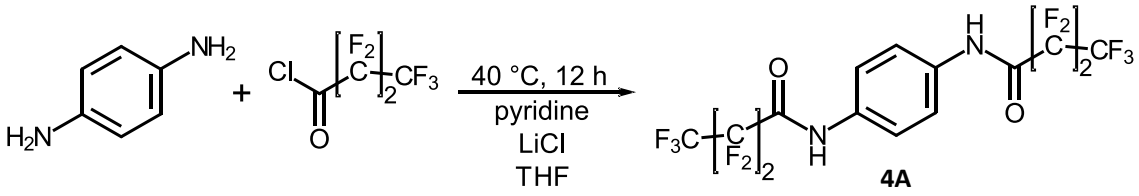

4.73 g of perfluorobutanoyl chloride (20.3 mmol) were dropped to a mixture of 1.00 g of 1,4-phenylene diamine (9.2 mmol), 3 mL of pyridine, LiCl and 100 mL of anhydrous tetrahydrofuran (THF) at 0 °C under argon atmosphere. The reaction mixture was heated to 40 °C and stirred overnight. After evaporation of solvents, the solid residue was dispersed in water and filtered off. Crystallization from methanol yielded 4.35 g (94%) of the product as white crystals.

Characterization

^{1}H-NMR (300 MHz, DMSO): δ (ppm) = 11.40 (2 H, s), 7.71 (4 H, s)

MS (m/z, %): 500 (M^{+}, 100), 481 (31.3), 331 (15.1), 303 (98.3), 169 (11.5), 133 (10.9), 108 (65.2), 81 (14.8), 69 (22.9)

Thermogravimetric analysis (TGA

- mass loss of 5% at 212 °C

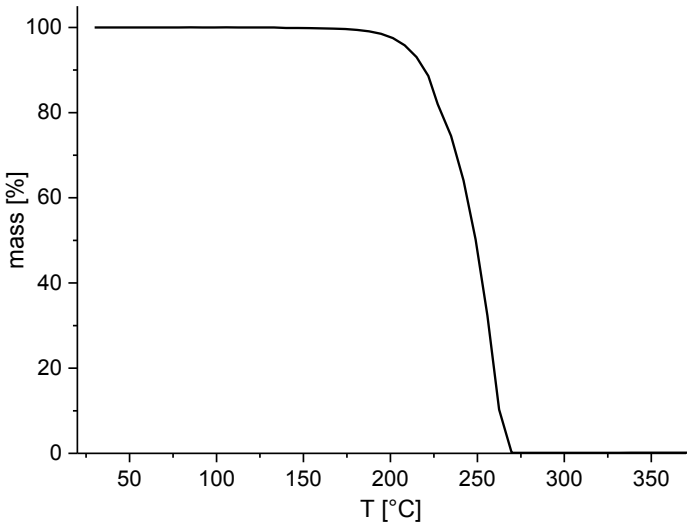

Figure 99: TGA curve of compound **4A**. The measurement was done with a heating rate of 10 K/min under N_2.

Differential scanning calorimetry (DSC)

- 2nd heating curve: Phase transition at 225 °C (38.9 kJ/mol)
- 2nd cooling curve: Phase transition at 219 °C (57.4 kJ/mol)

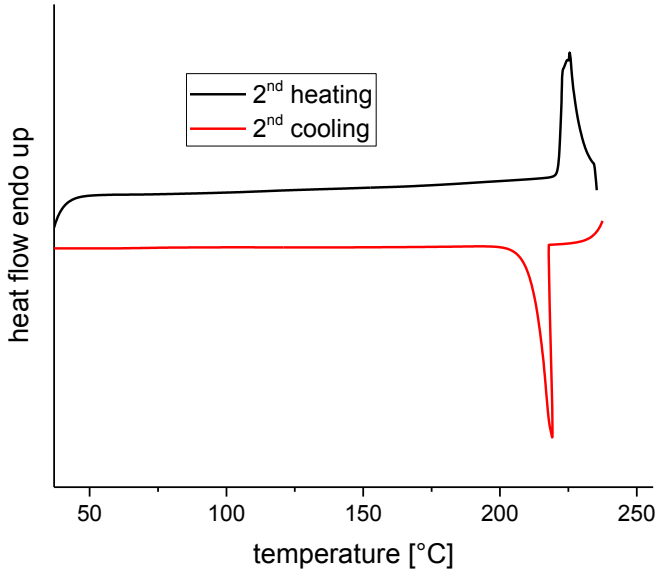

Figure 100: DSC second heating and cooling scans of compound **4A**. Measurements were performed with a heating/cooling rate of 10 K/min in a sealed high-pressure steel pan.

Bisamide based on 1,4-phenylenediamine with *n*-perfluoropentane substituents

Identifier: **4B** (in this thesis)

N,N'-1,4-phenylenebis(2,2,3,3,4,4,5,5,6,6,6-undecafluorohexanamide)

Synthesis:

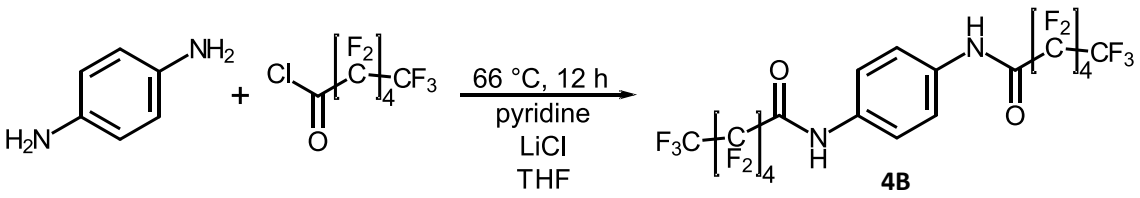

5.28 g of perfluorohexanoyl chloride (15.9 mmol) were slowly added to a mixture of 0.66 g of 1,4-phenylene diamine (6.10 mmol), 3 mL of pyridine, LiCl and 100 mL of anhydrous tetrahydrofuran (THF) at 0 °C under argon atmosphere. The reaction mixture was refluxed and stirred overnight. After evaporation of solvents, the solid residue was dispersed in water and filtered off. Crystallization from methanol yielded 1.83 g (43%) of the product as white solid.

Characterization

^{1}H-NMR (300 MHz, DMSO): δ (ppm) = 11.39 (2 H, s), 7.69 (4 H, s)

MS (m/z, %): 700 (M^{+}, 100), 681 (9.9), 431 (13.0), 303 (95.2), 133 (11.5), 119 (5.1), 108 (37.6), 81 (7.7), 69 (10.8)

Thermogravimetric analysis (TGA)

- mass loss of 5% at 216 °C

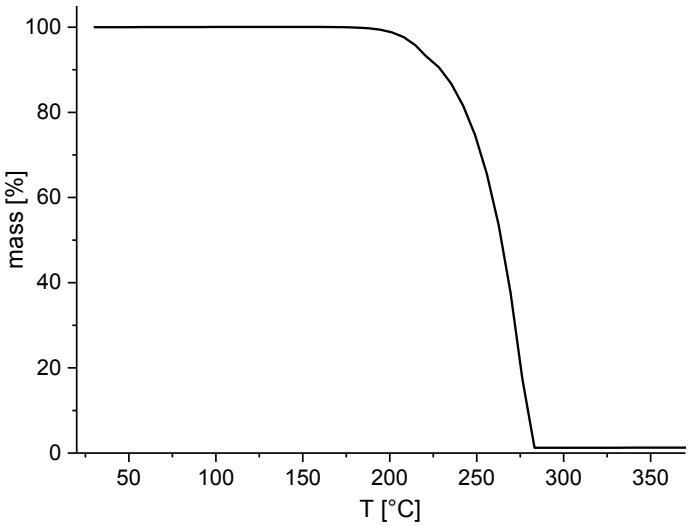

Figure 101: TGA curve of compound **4B**. The measurement was done with a heating rate of 10 K/min under N_2.

Differential scanning calorimetry (DSC)

- 2nd heating curve: Phase transition at 215 °C (58.7 kJ/mol)
- 2nd cooling curve: Phase transition at 206 °C (65.0 kJ/mol)

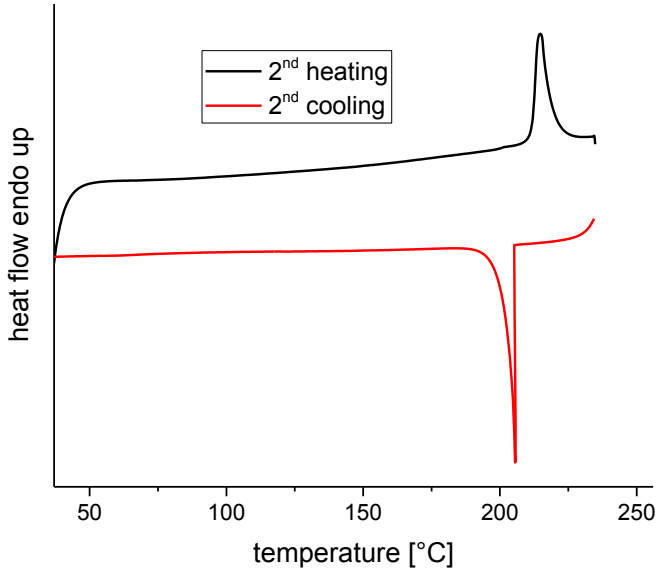

Figure 102: DSC second heating and cooling scans of compound **4B**. Measurements were performed with a heating/cooling rate of 10 K/min in a sealed high-pressure steel pan.

Bisamide based on 1,4-phenylenediamine with *n*-perfluoroheptane substituents

Identifier: **4C** (in this thesis)

N,N'-1,4-phenylenebis(2,2,3,3,4,4,5,5,6,6,7,7,8,8,8-pentadecafluorooctan-amide)

Synthesis:

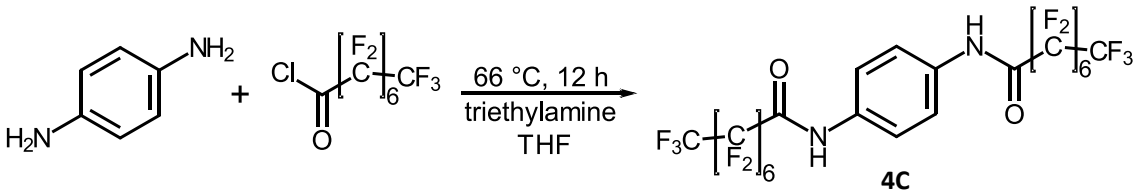

4C

6.62 g of perfluorooctanoyl chloride (15.3 mmol) were slowly added to a mixture of 0.75 g of 1,4-phenylene diamine (6.96 mmol), 5 mL of triethylamine and 200 mL of anhydrous tetrahydrofuran (THF) at 0 °C under argon atmosphere. The reaction mixture was refluxed and stirred overnight. After evaporation of solvents, the solid residue was dispersed in water and filtered off. Crystallization from *N,N*-dimethylformamide yielded 5.07 g (81%) of the product as white solid.

Characterization

^{1}H-NMR (300 MHz, DMF): δ (ppm) = 11.68 (2 H, s), 8.20 (4 H, s)

MS (m/z, %): 900 (M^{+}, 100), 881 (46.9), 531 (6.2), 503 (54.6), 169 (4.9), 133 (6.3), 119 (5.7), 108 (28.2), 81 (5.1), 69 (10.7)

Thermogravimetric analysis (TGA)

- mass loss of 5% at 235 °C

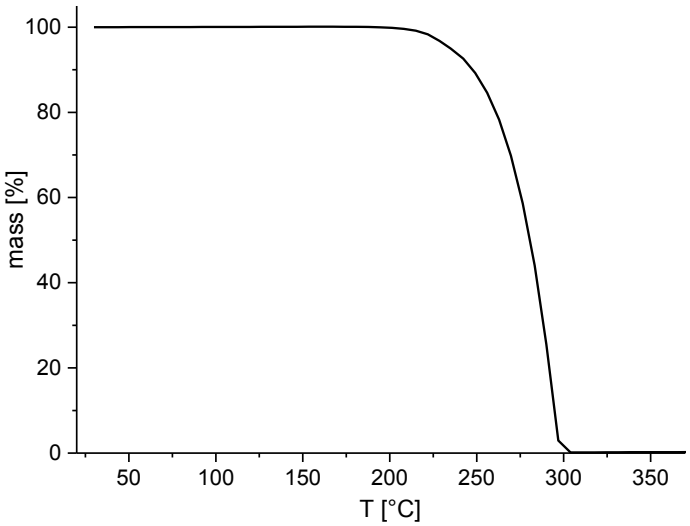

Figure 103: TGA curve of compound **4C**. The measurement was done with a heating rate of 10 K/min under N_2.

Differential scanning calorimetry (DSC)

- 2nd heating curve: Phase transitions at 213 °C (5.7 kJ/mol) and 228 °C (61.6 kJ/mol)
- 2nd cooling curve: Phase transition at 219 °C (75.6 kJ/mol)

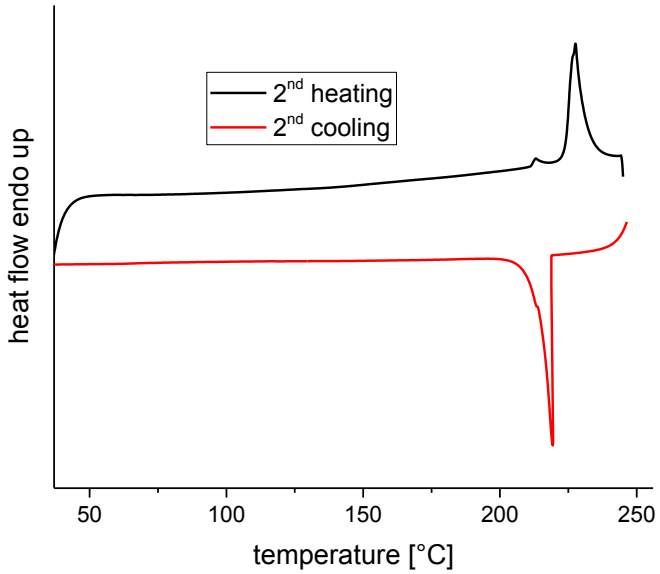

Figure 104: DSC second heating and cooling scans of compound **4C**. Measurements were performed with a heating/cooling rate of 10 K/min in a sealed high-pressure steel pan.

6.3.4. 1,3,5-cyclohexane- and 1,3,5-benzene-based trisamides

Trisamide based on 1,3,5-cyclohexanetricarboxylic acid with isopentyl substituents

Identifier: **6** (in this thesis)

N,N',N''-tris-isopentyl-1,3,5-cyclohexane-tricarboxamide

Synthesis:

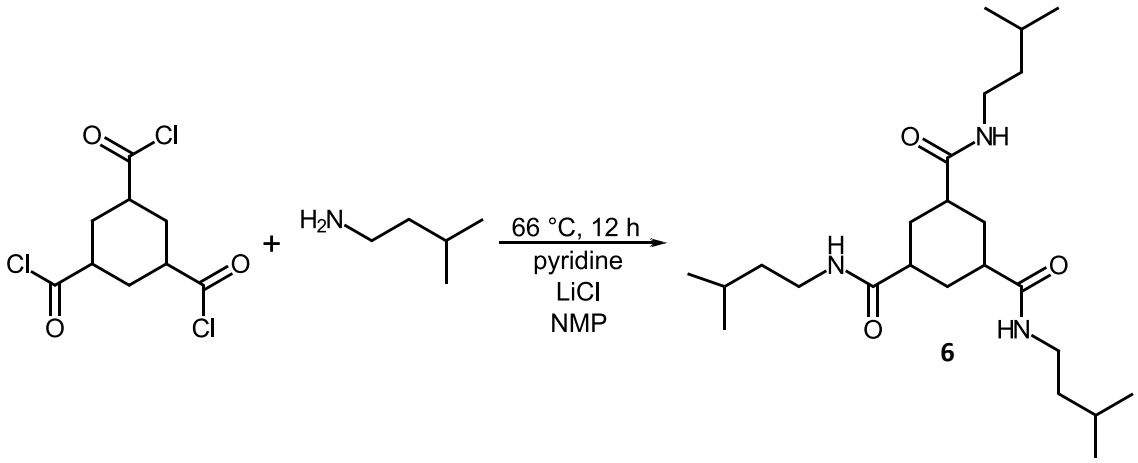

5.1 g of isopentylamine (58 mmol) was slowly added to a mixture of 4.8 g of 1,3,5-cyclohexanetricarbonyl chloride (18 mmol), 30 mL of pyridine, 2 spatula tips of lithium chloride and 150 mL of *n*-methyl-2-pyrrolidone (NMP) at 0 °C under argon atmosphere. The reaction mixture was stirred at 60 °C overnight. Afterwards, it was quenched with ice water and the resulting white solid was filtered off. Crystallization from methanol yielded 5.5 g (67%) of the product as white solid.

Characterization

^{1}H-NMR (300 MHz, $CDCl_3/CF_3COOD$): δ (ppm) = 3.71 (6 H, m), 3.05 (3 H, m), 2.48 (3 H, m), 2.20 (3 H, m), 1.94 (3 H, m), 1.81 (6 H, m), 1.27 (18 H, d)

MS (m/z, %): 423 (M^+, 63.8), 408 (9.5), 380 (19.2), 367 (17.4), 337 (78.3), 321 (12.8), 309 (100), 282 (14.4), 267 (20.8), 253 (26.9), 222 (5.4), 195 (25.2), 169 (25.8), 142 (16.0), 109 (29.8), 88 (51.4), 81 (54.8), 71 (38.4), 55 (10.5), 43 (61.6)

Thermogravimetric analysis (TGA)

- mass loss of 5% at 356 °C

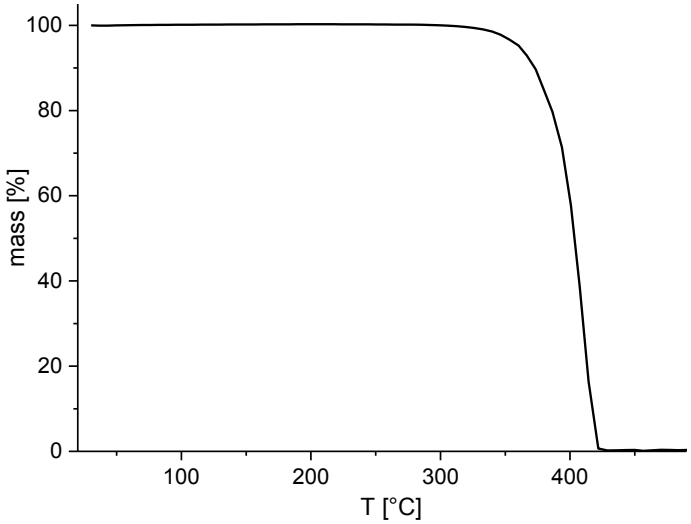

Figure 105: TGA curve of compound **6**. The measurement was done with a heating rate of 10 K/min under N_2.

Differential scanning calorimetry (DSC)

- 1st heating curve: Phase transitions around 172 °C (broad), 216 °C (7.2 kJ/mol) and 358 °C (50.8 kJ/mol)
- 1st cooling curve: Phase transition at 258 °C (6.1 kJ/mol)

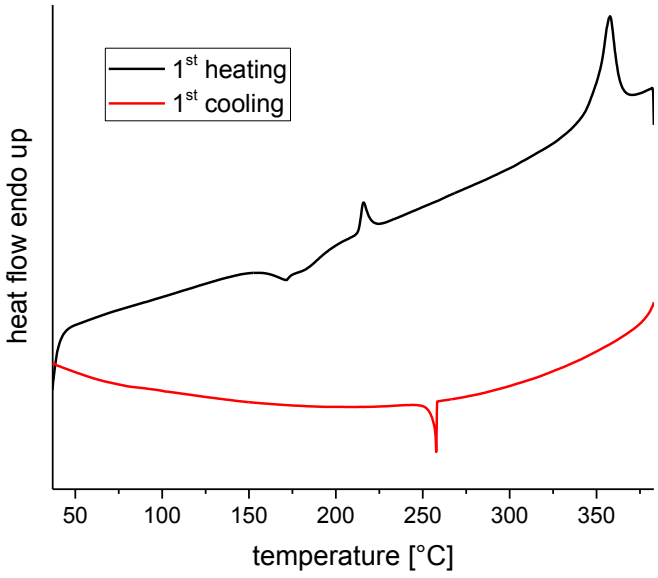

Figure 106: DSC heating and cooling scans of compound **6**. Measurements were performed with a heating/cooling rate of 10 K/min in a sealed high-pressure steel pan.

Trisamide based on trimesic acid with *tert*-octyl substituents

Identifier: **7** (in this thesis)

1,3,5-Benzenetricarboxylic acid tris(*tert*-octylamide)

Synthesis:

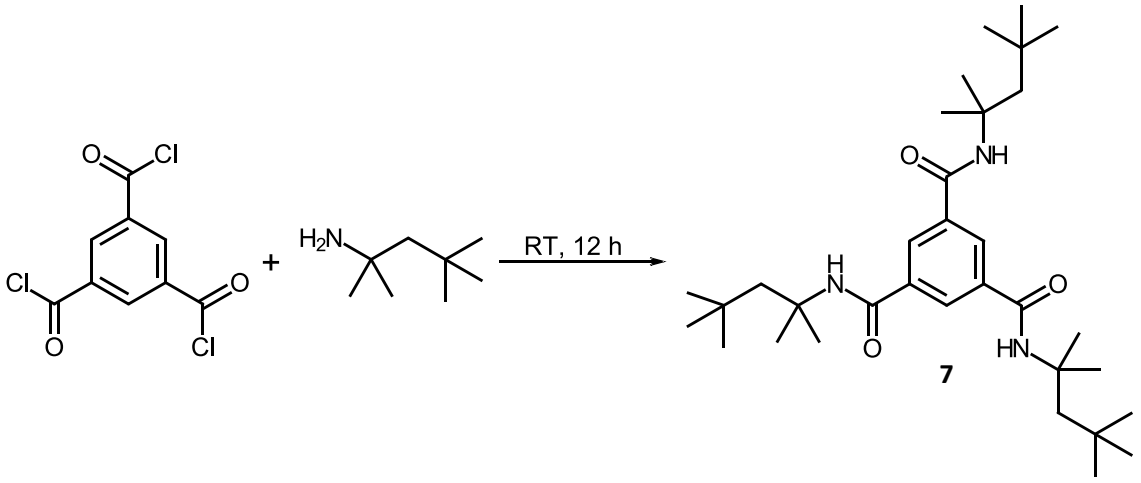

To 1000 g (7.73 mol) of degassed *tert*-octylamine 100 g (0.376 mol) of 1,3,5-benzenetricarbonyl trichloride were slowly added at 0 °C under inert gas and stirring. Subsequently, the mixture was allowed to warm to ambient temperature and it was stirred overnight. The solid product was precipitated by addition of 0.5 L of water and some spatulas of potassium carbonate and filtered off. Crystallization from 4 L of *N,N*-dimethylformamide yielded 180.9 g (88%) of the product as white solid.

Characterization

^{1}H-NMR (300 MHz, $CDCl_3/CF_3COOD$): δ (ppm) = 8.52 (3 H, s), 1.96 (6 H, s), 1.60 (18 H, s), 1.04 (27 H, s)

MS (m/z, %): 543 (M^+, 4.3), 528 (17.1), 486 (16.9), 472 (100), 433 (48.4), 415 (93.1), 360 (22.8), 320 (15.1), 303 (19.2), 259 (4.6), 248 (13.8), 231 (4.7), 208 (18.0), 191 (118.8), 163 (7.2), 146 (4.1), 97 (8.4), 57 (15.8)

Thermogravimetric analysis (TGA)

- mass loss of 5% at 324 °C

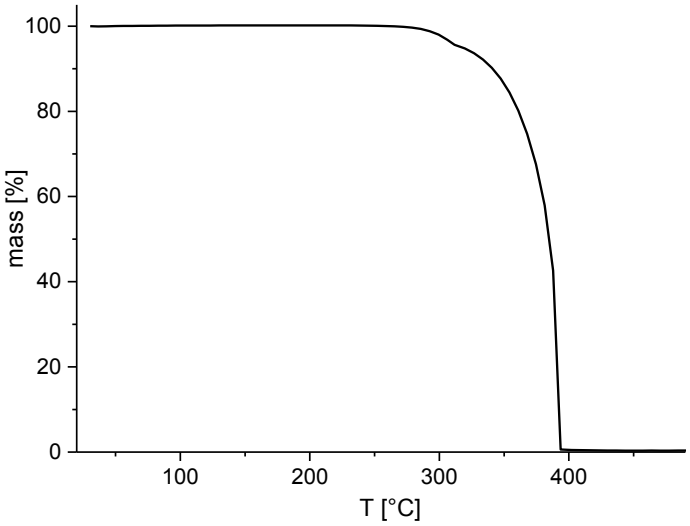

Figure 107: TGA curve of compound **7**. The measurement was done with a heating rate of 10 K/min under N_2.

Differential scanning calorimetry (DSC)

- 1st heating curve: Phase transitions around 280 °C, 291 °C and 308 °C (67.6 kJ/mol)
- 1st cooling curve: Phase transition at 306 °C (43.5 kJ/mol)

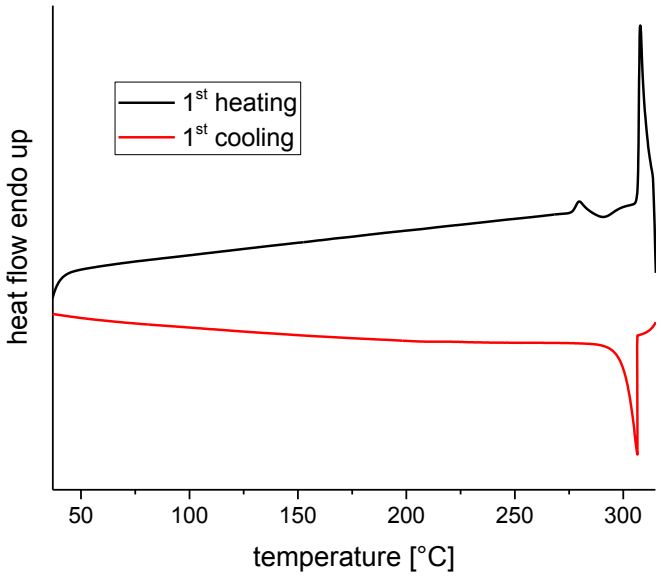

Figure 108: DSC heating and cooling scans of compound **7**. Measurements were performed with a heating/cooling rate of 10 K/min in an argon-flushed sealed high-pressure steel pan.

6.4. Sample preparation procedures

Preparation of bisamides solutions for self-assembly experiments

The respective bisamide was placed in a 4 mL glass vial. The amount of bisamide was chosen in a manner that subsequent filling with a solvent resulted in approx. 2.5 mL of dispersion of the desired concentration (e.g. 1.65 mg of bisamide 1 and 3.298 g of *o*-DCB gave 2.5 mL of a 500 ppm dispersion). Next, the vial was sealed using a PTFE septum and a screw cap. The sample was placed in a custom-made laboratory shaker. The metal block of the laboratory shaker carrying the vial with the sample was heated under shaking. The target temperatures for the solvents were chosen with respect to each solvent's boiling point and the durability of the screw caps, which allow gas proof tightening up to 120 °C. Maximum temperatures used for the applied solvents are listed in Table 12. The samples were kept at this temperature at least for 2 h to dissolve the solid and gain optically clear solutions.

Table 12: Temperatures, at which disassembly in the respective solvents was done, for all solvents applied in bisamide self-assembly studies.

Solvent	Selected maximum temperature for bisamide dissolution [°C]
Toluene	110
Anisole	110
Acetonitrile	80
Butanone	75
Cyclohexanone	120
1,4-Dioxane	95
THF	60
Benzyl alcohol	120
Ethanol	75
1-Heptanol	120
1-Pentanol	120
Chloroform	55
Chlorobenzene	120
o-Dichlorbenzene	120
1,2,4-Trichlorobenzene	120

Self-assembly in 2,2,4,4,6,8,8-heptamethylnonane (HMN)

A solution of 200 ppm (BTAs 5 and 6) or 500 ppm (BTA 7) of BTA in 10 g HMN was prepared by boiling under reflux while stirring for 1 h in a round bottom flask. Subsequently, each solution was cooled to room temperature and some drops of the homogeneous dispersion were filled into the sample chamber of a FP83HT dropping point cell (Mettler Toledo). After closing the sample chamber, it was inserted into the dropping point cell, heated to 240 °C and held at 240 °C for 5 min. Next, the sample was cooled down to 30 °C at a cooling rate of 20 K/min. Afterwards, one drop of the resulting dispersion was dropped onto a silicon wafer piece and dried at high vacuum overnight.

Compounding of i-PP

To prepare compounds for additive screening stabilizer powder (0.05 wt% Irganox 1010 and 0.1 wt% Irgafos 168) was placed in a laboratory glass bottle together with *i*-PP powder. Subsequently, the powders were mixed in a tumble mixer overnight at 45 rpm. Next, additive powder was added to the *i*-PP/stabilizer mixture the same way. In the following step, the powder mixture was compounded at a melt temperature of 240 °C in a Xplore co-rotating twin-screw extruder (DSM) at 50 rpm under nitrogen atmosphere for 5 min. The temperature at all three heating zones of the compounder was set to 250 °C during that. Then, the melt was collected in a heated transfer barrel and injection molded using an Xplore 12 mL (DSM) micro injection molding machine. For injection molding, an injection pressure of 6 bars, an injection time of 5 s and a back pressure time of 15 s was applied. The mold was kept at ambient temperature. Three circular sample platelets of each composition with a thickness of 1.1 mm were injection-molded (see Figure 109). To vary the additive concentration, the highest concentration was processed first and the remaining dead volume in the compounder was diluted with neat stabilized *i*-PP.

Figure 109: Injection molded sample platelet

Compounding of selected compositions for foam extrusion in amounts of 10 kg was done by Lifocolor Farben GmbH & Co. KG using a twin-screw extruder at a temperature of 240 °C. Subsequently, the compounds were granulated.

Foam extrusion

Foam extrusion was performed at the department of Polymer Engineering at the University of Bayreuth. It was done using a tandem extrusion line (Dr. Collin), combining a twin-screw extruder A (25 mm screws, L/D 42) and a single screw extruder B (45 mm screw, L/D 30). The second extruder was equipped with a 3 mm round die. The throughput was around 4.5 kg/h. At the end of extruder A 6 wt% of CO_2 were injected as physical blowing agent. The melt temperature was around 240 °C at the end of extruder A and around 160 °C at the foaming die. An optional additional calibration unit with a gap distance of 18 mm between the water-cooled plates was used directly after the die to produce calibrated foams. The processing scheme is displayed in Figure 77. All *i*-PP samples were stabilized with 0.05 wt% of Irganox 1010 and 0.1 wt% of Irgafos 168. The materials were kindly compounded by Dr. Markus Blomenhofer (Lifocolor Farben GmbH & Co. KG). Process parameters used for foam extrusion of the compounds are given in Table 13.

Table 13: Selected processing parameters from the foam extrusion of *i*-PP. Each compound contained the same basic stabilization package.

material	**throughput** [kg/h]	**T** [°C]				**p** [bar]
		melt @ end of A-extruder	as set @ end of B-extruder	melt @ end of B-extruder	@ die	melt @ die
Neat *i*-PP	4.5	240	151	157	150	79
i-PP + 1000 ppm talc	4.3	239	155	162	150	94
i-PP + 5000 ppm talc	4.0	239	155	161	150	97
i-PP + 200 ppm 5	4.3	240	155	161	150	100
i-PP + 300 ppm 5	4.3	240	155	159	150	99
i-PP + 2000 ppm 7	4.2	241	155	160	150	100
i-PP + 3000 ppm 7	4.3	239	155	160	150	116
i-PP + 4000 ppm 7	4.3	241	155	160	150	99
i-PP + 500 ppm 6	3.8	240	155	160	150	88
i-PP + 1000 ppm 6	3.9	239	155	160	150	99
i-PP + 2000 ppm 6	3.9	240	155	160	150	95
i-PP + 3000 ppm 6	4.3	240	155	161	150	95
i-PP + 5000 ppm 6	4.2	240	155	160	150	106

6.5 Supplementary information to crystal structure solutions

NMR-Crystallography

NMR crystallography is - besides XRD - a second way to obtain information about molecular crystals. Here, it is mainly applied to check the similarity of crystal packing patterns in series 3 suggested by XRD. In case the packing pattern varies between several compounds, the distance of carbon atoms in each molecule to other atoms and thus their electronic structure is altered. This consequently would reflect in ^{13}C NMR spectra of the solids, as they are presented in Figure 110. The signals of bisamide 3A are assigned to the carbon atoms in the molecular structure representatively for the whole series. In this spectrum, the signals for both CF_2 groups overlap. It is clearly visible, that all signals except for the ones of the CF_2 groups, which are altered by the variation of fluorocarbon chain length, are exactly the same for all three asymmetric bisamides. This is a further indication for the crystal packing of these compounds to be the same. Consequently, all conclusions from the packing pattern of 3A are valid for all three bisamides of series 3.

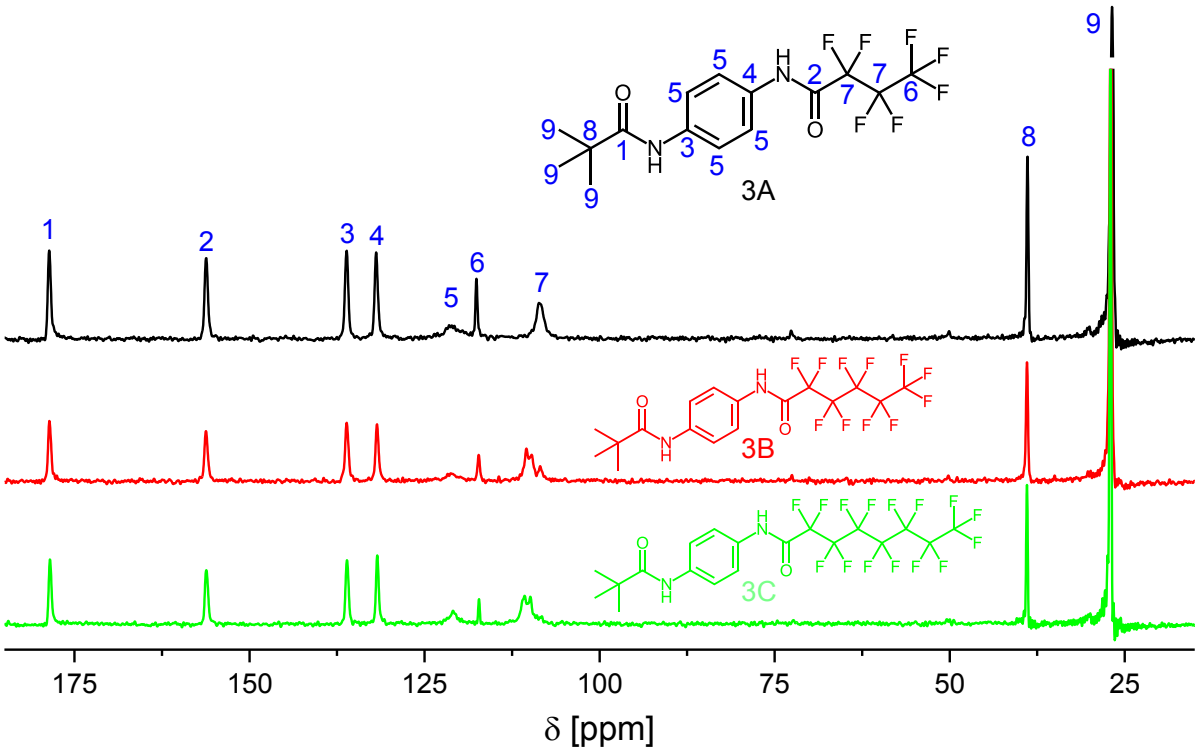

Figure 110: Solid state ^{13}C NMR spectra of asymmetric bisamides 3A (black), 3B (red) and 3C (green). Spectra were recorded using ^{1}H ^{13}C CP under MAS condition (ν_{rot} = 16 kHz). Signals of 3A are assigned exemplarily.

A similar investigation is done here for the compounds of series 4. NMR spectra of all three bisamides of series 4 in solid state, which are displayed in Figure 111, are furthermore used to gain information about the crystal packing 4C. All signals are assigned to the C-atoms in the molecular structure at the example of compound 4A. For 4A and 4B, chemical shift and shape of most signals are similar. Yet, signals of the CF_2-groups are slightly shifted at 4B, which is attributed to its increased fluorocarbon chain length. Moreover, 4B and 4C lack any signal of the CF_3-groups. This is attributed to the fact that these groups do not feature any protons in their vicinity, which could transfer polarization to C-atoms. Hence, these C-atoms lack sufficient polarization for visible signals in the spectra. Interestingly, for 4C signals 1 – 3, which belong to the aromatic core and the carbonyl group, are split into duplets (1 and 2) or into a duplet and a singlet (3). This finding indicates at least two distinct positions for these atoms in the crystal, i.e. the crystal structure of this compound is expected to be different from the ones of 4A and 4B.

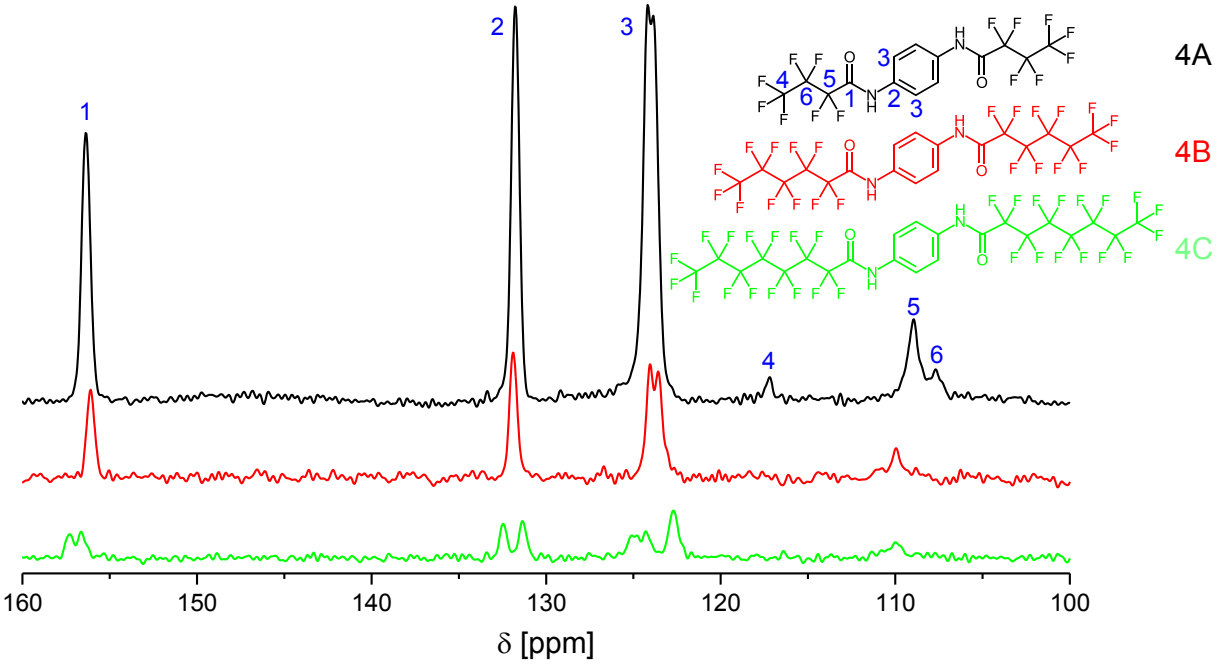

Figure 111: Solid state ^{13}C NMR spectra of symmetric bisamides 4A (black), 4B (red) and 4C (green). Spectra were recorded using ^{1}H ^{13}C CP under MAS condition (ν_{rot} = 16 kHz). Signals of 4A are assigned exemplarily. Please note the splitting of signals 1 to 3 for 4C.

Crystallographic data of bisamides

Table 14 gives an overview of selected crystallographic data from structure solutions of bisamides. Literature data of bisamide 1 are included for comparison.[63] In addition, Table 14 provides values for the layer thickness d of all seven compounds with their crystal structure solved. These values were calculated from cell parameters using trigonometric functions. Since all bisamides investigated assemble with their molecules almost upright within their respective layers, d is highly dependent on the length of the molecules. For example, 2, featuring two relatively short *tert*-butyl groups, gives a crystallographic monolayer thickness of only 1.2 nm, whereas 4, bearing two C_7F_{15}-chains, yields 2.1 nm for d, which is the highest value determined. For 4C, no layer thickness can be derived, as no structure solution for crystals of this compound has been performed successfully yet.

Table 14: Selected crystallographic data of the six crystal structures of 1,4-benzene bisamides yet solved. In addition, available information for 4C, where data allow indexing of space groups, yet no structure solution, is given. For comparison, data for 1 are taken from the published crystal structure solution.[63] Values for the layer thickness d calculated from the crystallographic data are also provided.

	1	**2**	**3A**	**3B**	**3C**	**4A**	**4B**	**4C**
crystal system	mono-clinic	mono-clinic	mono-clinic	mono-clinic	mono-clinic	triclinic	triclinic	mono-clinic
space group	$P2_1/c$	$P2_1/c$	$P2_1$	$P2_1$	$P2_1$	$P\bar{1}$	$P\bar{1}$	$P2$
d [Å]	14.18	12.25	15.36	18.56	20.68	16.02	21.10	---
a [Å]	14.183(3)	12.166(4)	9.2124(2)	9.2340	21.2891	5.1278	5.1161	10.4482
b [Å]	6.159(1)	7.677(3)	5.8994(1)	5.8718	6.0489	5.2125	5.2824	27.0334
c [Å]	9.889(2)	9.243(3)	30.732(6)	18.787(4)	8.9188	16.090(3)	21.1583	5.4466
α [°]	90	90	91.57(3)	90	90	95.27(3)	93.97	90
β [°]	98.383(1)	96.61(1)	90.57(3)	98.87(3)	103.78	90.74(3)	88.83	85.66
γ [°]	90	90	90	90	90	91.74(3)	89.26	90
V [Å^3]	854.6(8)	857.54	1669.58	1006.45	1115.48	428.00	570.25	1533.99
Z	2	2	4	2	2	1	1	2
ρ [g/cm^3]	1.097(1)	1.070	1.545	1.611	1.751	1.941	2.153	1.949

7. References

[1] National Nanotechnology Initiative. About the NNI. http://nano.gov/about-nni (accessed February 20, 2018).

[2] European commision. Nanotechnologies. https://ec.europa.eu/programmes/horizon2020/en/h2020-section/nanotechnologies (accessed February 20, 2018).

[3] Commission Recommendation of 18 October 2011 on the definition of nanomaterial. Official Journal of the European Union 2011, L 275, 38–40.

[4] ISO. Nanotechnologies — Vocabulary — Part 2: Nano-objects (ISO/TS 80004-2:2015(en)). https://www.iso.org/obp/ui/ (accessed January 2, 2018).

[5] Amendola, V.; Pilot, R.; Frasconi, M.; Maragò, O. M.; Iatì, M. A. Surface plasmon resonance in gold nanoparticles: A review. J. Phys. Condens. Matter.2017, 29, 203002.

[6] Krutyakov, Y. A.; Kudrinskiy, A. A.; Olenin, A. Y.; Lisichkin, G. V. Synthesis and properties of silver nanoparticles: Advances and prospects. Russ. Chem. Rev. 2008, 77, 233–257.

[7] Weir, A.; Westerhoff, P.; Fabricius, L.; Hristovski, K.; Goetz, N. von. Titanium dioxide nanoparticles in food and personal care products. Environ. Sci. Technol. 2012, 46, 2242–2250.

[8] Joo, J.; Yu, T.; Kim, Y. W.; Park, H. M.; Wu, F.; Zhang, J. Z.; Hyeon, T. Multigram scale synthesis and characterization of monodisperse tetragonal zirconia nanocrystals. J. Am. Chem. Soc. 2003, 125, 6553–6557.

[9] Slowing, I. I.; Trewyn, B. G.; Giri, S.; Lin, V. S.-Y. Mesoporous Silica Nanoparticles for Drug Delivery and Biosensing Applications. Adv. Funct. Mater. 2007, 17, 1225–1236.

[10] Sun, Y.; Yin, Y.; Mayers, B. T.; Herricks, T.; Xia, Y. Uniform Silver Nanowires Synthesis by Reducing $AgNO_3$ with Ethylene Glycol in the Presence of Seeds and Poly(Vinyl Pyrrolidone). Chem. Mater. 2002, 14, 4736–4745.

[11] Ajayan, P. M.; Ebbesen, T. W. Nanometre-size tubes of carbon. Rep. Prog. Phys. 1997, 60, 1025.

[12] Hou, H.; Jun, Z.; Reuning, A.; Schaper, A.; Wendorff, J. H.; Greiner, A. Poly(*p*-xylylene) Nanotubes by Coating and Removal of Ultrathin Polymer Template Fibers. Macromolecules 2002, 35, 2429–2431.

[13] Coleman, J. N.; Lotya, M.; O'Neill, A.; Bergin, S. D.; King, P. J.; Khan, U.; Young, K.; Gaucher, A.; De, S.; Smith, R. J.; Shvets, I. V.; Arora, S. K.; Stanton, G.; Kim, H.-Y.; Lee, K.; Kim, G. T.; Duesberg, G. S.; Hallam, T.; Boland, J. J.; Wang, J. J.; Donegan, J. F.; Grunlan, J. C.; Moriarty, G.; Shmeliov, A.; Nicholls, R. J.; Perkins, J.M.; Grieveson, E. M.; Theuwissen, K.; McComb, D. W.; Nellist, P. D.; Nicolosi, V. Two-dimensional

nanosheets produced by liquid exfoliation of layered materials. Science 2011, 331, 568–571.

[14] Stöter, M.; Kunz, D. A.; Schmidt, M.; Hirsemann, D.; Kalo, H.; Putz, B.; Senker, J.; Breu, J. Nanoplatelets of sodium hectorite showing aspect ratios of ≈20,000 and superior purity. Langmuir 2013, 29, 1280–1285.

[15] Nicolosi, V.; Chhowalla, M.; Kanatzidis, M. G.; Strano, M. S.; Coleman, J. N. Liquid Exfoliation of Layered Materials. Science 2013, 340, 1226419.

[16] Lotya, M.; Hernandez, Y.; King, P. J.; Smith, R. J.; Nicolosi, V.; Karlsson, L. S.; Blighe, F. M.; De, S.; Wang, Z.; McGovern, I. T.; Duesberg, G. S.; Coleman, J. N. Liquid phase production of graphene by exfoliation of graphite in surfactant/water solutions. J. Am. Chem. Soc. 2009, 131, 3611–3620.

[17] Boverhof, D. R.; Bramante, C. M.; Butala, J. H.; Clancy, S. F.; Lafranconi, M.; West, J.; Gordon, S. C. Comparative assessment of nanomaterial definitions and safety evaluation considerations. Regul. Toxicol. Pharmacol. 2015, 73, 137–150.

[18] Gaffet, E. Nanomaterials : a review of the definitions, applications, health effects.: How to implement secure development. C. R. Phys. 2011, 12, 648-658 (english translation).

[19] Vance, M. E.; Kuiken, T.; Vejerano, E. P.; McGinnis, S. P.; Hochella, M. F.; Rejeski, D.; Hull, M. S. Nanotechnology in the real world: Redeveloping the nanomaterial consumer products inventory. Beilstein J. Nanotechnol. 2015, 6, 1769–1780.

[20] Nazemi, A.; Boott, C. E.; Lunn, D. J.; Gwyther, J.; Hayward, D. W.; Richardson, R. M.; Winnik, M. A.; Manners, I. Monodisperse Cylindrical Micelles and Block Comicelles of Controlled Length in Aqueous Media. J. Am. Chem. Soc. 2016, 138, 4484–4493.

[21] Zhang, C.; Yan, Y.; Sheng Zhao, Y.; Yao, J. Synthesis and applications of organic nanorods, nanowires and nanotubes. Annu. Rep. Prog. Chem., Sect. C: Phys. Chem. 2013, 109, 211-239.

[22] Osada, M.; Sasaki, T. Two-dimensional dielectric nanosheets: Novel nanoelectronics from nanocrystal building blocks. Adv. Mater. 2012, 24, 210–228.

[23] Lehn, J.-M. Supramolecular Chemistry – Scope and Perspectives Molecules, Supermolecules, and Molecular Devices (Nobel Lecture). Angew. Chem. Int. Ed. Engl. 1988, 27, 89–112.

[24] Steed, J. W.; Atwood, J. L. Supramolecular chemistry, 2nd ed.; Wiley & Sons: Chichester, UK, 2009.

[25] Adams, M. J.; Adkins, S.; Bragard, C.; Gilmer, D.; Li, D.; MacFarlane, S. A.; Wong, S.-M.; Melcher, U.; Ratti, C.; Ryu, K. H. and ICTV report commision. ICTV Virus Taxonomy Profile: Virgaviridae. J. Gen. Virol. 2017, 98, 1999–2000.

[26] Khalily, M. A.; Bakan, G.; Kucukoz, B.; Topal, A. E.; Karatay, A.; Yaglioglu, H. G.; Dana, A.; Guler, M. O. Fabrication of Supramolecular n/p-Nanowires via Coassembly of

Oppositely Charged Peptide-Chromophore Systems in Aqueous Media. ACS nano 2017, 11, 6881–6892.

[27] Howe, E. J.; Okesola, B. O.; Smith, D. K. Self-assembled sorbitol-derived supramolecular hydrogels for the controlled encapsulation and release of active pharmaceutical ingredients. Chem. Commun. 2015, 51, 7451–7454.

[28] Curtius, T. Hydrazide und Azide organischer Säuren. Journal für praktische Chemie 1915, 91, 39–100.

[29] Cantekin, S.; Greef, T. F. A. de; Palmans, A. R. A. Benzene-1,3,5-tricarboxamide: A versatile ordering moiety for supramolecular chemistry. Chem. Soc. Rev. 2012, 41, 6125–6137.

[30] Albuquerque, R. Q.; Timme, A.; Kress, R.; Senker, J.; Schmidt, H.-W. Theoretical investigation of macrodipoles in supramolecular columnar stackings. Chem. Eur. J. 2013, 19, 1647–1657.

[31] Abraham, F.; Ganzleben, S.; Hanft, D.; Smith, P.; Schmidt, H.-W. Synthesis and Structure-Efficiency Relations of 1,3,5-Benzenetrisamides as Nucleating Agents and Clarifiers for Isotactic Poly(propylene). Macromol. Chem. Phys. 2010, 211, 171–181.

[32] Blomenhofer, M.; Ganzleben, S.; Hanft, D.; Schmidt, H.-W.; Kristiansen, M.; Smith, P.; Stoll, K.; Mäder, D.; Hoffmann, K. “Designer” Nucleating Agents for Polypropylene. Macromolecules 2005, 38, 3688–3695.

[33] Kristiansen, M.; Smith, P.; Chanzy, H.; Baerlocher, C.; Gramlich, V.; McCusker, L.; Weber, T.; Pattison, P.; Blomenhofer, M.; Schmidt, H.-W. Structural Aspects of 1,3,5-Benzenetrisamides−A New Family of Nucleating Agents. Crystal Growth & Design 2009, 9, 2556–2558.

[34] Abraham, F.; Kress, R.; Smith, P.; Schmidt, H.-W. A New Class of Ultra-Efficient Supramolecular Nucleating Agents for Isotactic Polypropylene. Macromol. Chem. Phys. 2013, 214, 17–24.

[35] van Gorp, J. J.; Vekemans, J. A. J. M.; Meijer, E. W. C3-symmetrical supramolecular architectures: fibers and organic gels from discotic trisamides and trisureas. J. Am. Chem. Soc. 2002, 124, 14759–14769.

[36] Palmans, A. R. A.; Vekemans, J. A. J. M.; Havinga, E. E.; Meijer, E. W. Sergeants-and-Soldiers Principle in Chiral Columnar Stacks of Disc-Shaped Molecules with C_3 Symmetry. Angew. Chem. Int. Ed. Engl. 1997, 36, 2648–2651.

[37] Lightfoot, M. P.; Mair, F. S.; Pritchard, R. G.; Warren, J. E. New supramolecular packing motifs: p-stacked rods encased in triply-helical hydrogen bonded amide strands. Chem. Commun. 1999, 1945–1946.

[38] Zehe, C. S.; Hill, J. A.; Funnell, N. P.; Kreger, K.; van der Zwan, K. P.; Goodwin, A. L.; Schmidt, H.-W.; Senker, J. Mesoscale Polarization by Geometric Frustration in Columnar Supramolecular Crystals. Angew. Chem. Int. Ed. Engl. 2017, 56, 4432–4437.

[39] Schmidt, M.; Wittmann, J. J.; Kress, R.; Schneider, D.; Steuernagel, S.; Schmidt, H.-W.; Senker, J. Crystal Structure of a Highly Efficient Clarifying Agent for Isotactic Polypropylene. Crystal Growth & Design 2012, 12, 2543–2551.

[40] Hou, X.; Schober, M.; Chu, Q. A Chiral Nanosheet Connected by Amide Hydrogen Bonds. Crystal Growth & Design 2012, 12, 5159–5163.

[41] Neumann, L. N.; Baker, M. B.; Leenders, C. M. A.; Voets, I. K.; Lafleur, R. P. M.; Palmans, A. R. A.; Meijer, E. W. Supramolecular polymers for organocatalysis in water. Org. Biomol. Chem. 2015, 13, 7711–7719.

[42] Kluge, D.; Abraham, F.; Schmidt, S.; Schmidt, H.-W.; Fery, A. Nanomechanical properties of supramolecular self-assembled whiskers determined by AFM force mapping. Langmuir 2010, 26, 3020–3023.

[43] Kluge, D.; Singer, J. C.; Neubauer, J. W.; Abraham, F.; Schmidt, H.-W.; Fery, A. Influence of the molecular structure and morphology of self-assembled 1,3,5-benzenetrisamide nanofibers on their mechanical properties. Small 2012, 8, 2563–2570.

[44] Misslitz, H.; Kreger, K.; Schmidt, H.-W. Supramolecular nanofiber webs in nonwoven scaffolds as potential filter media. Small 2013, 9, 2053-8, 2053-2058.

[45] Weiss, D.; Skrybeck, D.; Misslitz, H.; Nardini, D.; Kern, A.; Kreger, K.; Schmidt, H.-W. Tailoring Supramolecular Nanofibers for Air Filtration Applications. ACS Appl. Mater. Interfaces 2016, 8, 14885–14892.

[46] Loos, M. de; van Esch, J. H.; Kellogg, R. M.; Feringa, B. L. C3-Symmetric, amino acid based organogelators and thickeners: A systematic study of structure – property relations. Tetrahedron 2007, 63, 7285–7301.

[47] Shi, N. E.; Dong, H.; Yin, G.; Xu, Z.; Li, S. H. A Smart Supramolecular Hydrogel Exhibiting pH-Modulated Viscoelastic Properties. Adv. Funct. Mater. 2007, 17, 1837–1843.

[48] Friggeri, A.; van der Pol, C.; van Bommel, K. J. C.; Heeres, A.; Stuart, M. C. A.; Feringa, B. L.; van Esch, J. Cyclohexane-based low molecular weight hydrogelators: A chirality investigation. Chem. Eur. J. 2005, 11, 5353–5361.

[49] Albertazzi, L.; van der Veeken, N.; Baker, M. B.; Palmans, A. R. A.; Meijer, E. W. Supramolecular copolymers with stimuli-responsive sequence control. Chem. Commun. 2015, 51, 16166–16168.

[50] Abraham, F.; Schmidt, H.-W. 1,3,5-Benzenetrisamide based nucleating agents for poly(vinylidene fluoride). Polymer 2010, 51, 913–921.

[51] Richter, F.; Schmidt, H.-W. Supramolecular Nucleating Agents for Poly(butylene terephthalate) Based on 1,3,5-Benzenetrisamides. Macromol. Mater. Eng. 2013, 298, 190–200.

[52] Kersch, M.; Pischke, L.; Schmidt, H.-W.; Altstädt, V. Influence of trisamide-based additives on the morphological and mechanical properties of isotactic polypropylene. Polymer 2014, 55, 3227–3233.

[53] Kersch, M.; Schmidt, H.-W.; Altstädt, V. Influence of different beta-nucleating agents on the morphology of isotactic polypropylene and their toughening effectiveness. Polymer 2016, 98, 320–326.

[54] Mohmeyer, N.; Behrendt, N.; Zhang, X.; Smith, P.; Altstädt, V.; Sessler, G. M.; Schmidt, H.-W. Additives to improve the electret properties of isotactic polypropylene. Polymer 2007, 48, 1612–1619.

[55] Nam, K. T.; Shelby, S. A.; Choi, P. H.; Marciel, A. B.; Chen, R.; Tan, L.; Chu, T. K.; Mesch, R. A.; Lee, B.-C.; Connolly, M. D.; Kisielowski, C.; Zuckermann, R. N. Free-floating ultrathin two-dimensional crystals from sequence-specific peptoid polymers. Nat. Mater. 2010, 9, 454–460.

[56] Wu, D.; Liu, R.; Pisula, W.; Feng, X.; Müllen, K. Two-dimensional nanostructures from positively charged polycyclic aromatic hydrocarbons. Angew. Chem. Int. Ed. Engl. 2011, 50, 2791–2794.

[57] Kim, J.-U.; Kim, K.-H.; Haberkorn, N.; Roth, P. J.; Lee, J.-C.; Theato, P.; Zentel, R. Two-dimensional self-assembly of disulfide functionalized bis-acylurea: A nanosheet template for gold nanoparticle arrays. Chem. Commun. 2010, 46, 5343–5345.

[58] Davis, R.; Berger, R.; Zentel, R. Two-Dimensional Aggregation of Organogelators Induced by Biaxial Hydrogen-Bonding Gives Supramolecular Nanosheets. Adv. Mater. 2007, 19, 3878–3881.

[59] Mohmeyer, N.; Schmidt, H.-W.; Kristiansen, P. M.; Altstädt, V. Influence of Chemical Structure and Solubility of Bisamide Additives on the Nucleation of Isotactic Polypropylene and the Improvement of Its Charge Storage Properties. Macromolecules 2006, 39, 5760–5767.

[60] Mohmeyer, N.; Schmidt, H.-W. Synthesis and structure-property relationships of amphiphilic organogelators. Chem. Eur. J. 2007, 13, 4499–4509.

[61] Mohmeyer, N.; Schmidt, H.-W. A new class of low-molecular-weight amphiphilic gelators. Chem. Eur. J. 2005, 11, 863–872.

[62] Ikeda, N.; Yoshimura, M.; Mizoguchi, K.; Kitagawa, H.; Kawashima, Y.; Sadamitsu, K.; Kawahara, Y. Crystalline polypropylene resin composition and amide compounds. EP 0692489 B1

[63] Schmidt, M.; Zehe, C. S.; Siegel, R.; Heigl, J. U.; Steinlein, C.; Schmidt, H.-W.; Senker, J. NMR-crystallographic study of two-dimensionally self-assembled cyclohexane-based low-molecular-mass organic compounds. CrystEngComm 2013, 15, 8784-8796.

[64] Guo, H.-Z.; Yin, G.-D.; She, N.-F.; Wu, A.-X. N -[4-(2,2-Dimethylpropionylamino)phenyl]-2,2-dimethylpropionamide. Acta Cryst. E 2005, 61, o4062-o4063.

[65] Jones, P. G.; Ossowski, J.; Kus, P. Crystal Structures of Seven Terephthaldiamide Derivatives. Z. Naturforsch. B 2002, 57, 914–921.

[66] Weiss, D.; Kreger, K.; Schmidt, H.-W. Self-Assembly of Alkoxy-Substituted 1,3,5-Benzenetrisamides Under Controlled Conditions. Macromol. Mater. Eng. 2017, 302, 1600390.

[67] Mohebbi, A.; Mighri, F.; Ajji, A.; Rodrigue, D. Current Issues and Challenges in Polypropylene Foaming: A Review. Cell. Polym. 2015, 34, 299-338.

[68] Ishijima, Y.; Okaniwa, M.; Oaki, Y.; Imai, H. Two exfoliation approaches for organic layered compounds: Hydrophilic and hydrophobic polydiacetylene nanosheets. Chem. Sci. 2017, 8, 647–653.

[69] Butler, S. Z.; Hollen, S. M.; Cao, L.; Cui, Y.; Gupta, J. A.; Gutiérrez, H. R.; Heinz, T. F.; Hong, S. S.; Huang, J.; Ismach, A. F.; Johnston-Halperin, E.; Kuno, M.; Plashnitsa, V.; Robinson, R. D.; Ruoff, R. S.; Salahudin, S.; Shan, J.; Shi, L.; Spencer, M. G.; Terrones, M.; Windl, W.; Goldberger, J. E. Progress, challenges, and opportunities in two-dimensional materials beyond graphene. ACS nano 2013, 7, 2898–2926.

[70] Wang, J.-Y.; Peng, H.-D.; Yang, J.-M.; Yan, J.-H.; Pan, G.-B. Large-size nanosheets of 9,10-bis(phenylethynyl)anthracene with high photoresponse and light emission anisotropy. Phys. Chem. Chem. Phys. 2016, 18, 10836–10839.

[71] Kunz, D. A.; Schmid, J.; Feicht, P.; Erath, J.; Fery, A.; Breu, J. Clay-based nanocomposite coating for flexible optoelectronics applying commercial polymers. ACS nano 2013, 7, 4275–4280.

[72] Hausner, J.; Fischer, B.; Stöter, M.; Edenharter, A.; Schmid, J.; Kunz, R.; Rosenfeldt, S.; Altstädt, V.; Breu, J. Increasing time of ignition for PS-clay nanocomposites filled with $[Fe(bpy)_3]^{2+}$-modified hectorite. Polym. Degrad. Stab. 2016, 128, 141–148.

[73] Govindaraju, T.; Avinash, M. B. Two-dimensional nanoarchitectonics: Organic and hybrid materials. Nanoscale 2012, 4, 6102–6117.

[74] Bonaccorso, F.; Lombardo, A.; Hasan, T.; Sun, Z.; Colombo, L.; Ferrari, A. C. Production and processing of graphene and 2d crystals. Materials Today 2012, 15, 564–589.

[75] Coleman, J. N.; Khan, U. Atomically thin crystals and films and process for making same. WO 2014/001519 A1.

[76] Wang, S.; Zhang, Y.; Abidi, N.; Cabrales, L. Wettability and surface free energy of graphene films. Langmuir 2009, 25, 11078–11081.

[77] Hernandez, Y.; Nicolosi, V.; Lotya, M.; Blighe, F. M.; Sun, Z.; De, S.; McGovern, I. T.; Holland, B.; Byrne, M.; Gun'Ko, Y. K.; Boland, J. J.; Niraj, P.; Duesberg, G.; Krishnamurthy, S.; Goodheu, R.; Hutchison, J.; Scardaci, V.; Ferrari, A. C.; Coleman, J. N. High-yield production of graphene by liquid-phase exfoliation of graphite. Nat. Nanotechnol. 2008, 3, 563–568.

[78] Miró, P.; Audiffred, M.; Heine, T. An atlas of two-dimensional materials. Chem. Soc. Rev. 2014, 43, 6537–6554.

[79] Stöter, M.; Rosenfeldt, S.; Breu, J. Tunable Exfoliation of Synthetic Clays. Annu. Rev. Mater. Res. 2015, 45, 129–151.

[80] Möller, M. W.; Handge, U. A.; Kunz, D. A.; Lunkenbein, T.; Altstädt, V.; Breu, J. Tailoring shear-stiff, mica-like nanoplatelets. ACS nano 2010, 4, 717–724.

[81] Govindaraju, T.; Pandeeswar, M.; Jayaramulu, K.; Jaipuria, G.; Atreya, H. S. Spontaneous self-assembly of designed cyclic dipeptide (Phg-Phg) into two-dimensional nano- and mesosheets. Supramolecular Chemistry 2011, 23, 487–492.

[82] Avinash, M. B.; Swathi, K.; Narayan, K. S.; Govindaraju, T. Molecular Architectonics of Naphthalenediimides for Efficient Structure-Property Correlation. ACS Appl. Mater. Interfaces 2016, 8, 8678–8685.

[83] Narayanaswamy, N.; Avinash, M. B.; Govindaraju, T. Exploring hydrogen bonding and weak aromatic interactions induced assembly of adenine and thymine functionalised naphthalenediimides. New J. Chem. 2013, 37, 1302.

[84] Wang, F.-X.; Liu, Y.-Q.; Qiu, S.; Pan, G.-B. Solvent effect on hierarchical assembly of 2-aminooctane-functionalized naphthalenediimide. RSC Adv. 2014, 4, 6009-6013.

[85] Yang, C.; Wu, D.; Zhao, W.; Ye, W.; Xu, Z.; Zhang, F.; Feng, X. Anion-induced self-assembly of positively charged polycyclic aromatic hydrocarbons towards nanostructures with controllable two-dimensional morphologies. CrystEngComm 2016, 18, 877–880.

[86] Lai, Y.; Li, H.; Pan, J.; Guo, J.; Kang, L.; Cao, Z. Synthesis of Ultrathin Nanosheets of Perylene. Crystal Growth & Design 2015, 15, 1011–1016.

[87] Kim, J.-U.; Davis, R.; Zentel, R. Two dimensional self-assembly of bis-acylureas having various functional end groups. J. Colloid Interface Sci. 2011, 359, 428–435.

[88] Kim, J.-U.; Zentel, R. Organic nanosheets with charged surface: Two dimensional self-assembly of a non-symmetric bis-acylurea with pyridyl end group. Soft Matter 2011, 7, 2019–2024.

[89] Ray, S.; Hegde, R. P.; Das, A. K.; Shamala, N.; Banerjee, A. Nanostaircase formation in the solid state from self-assembling synthetic terephthalamides with a common molecular scaffold. Tetrahedron 2006, 62, 9603–9609.

[90] Aminuzzaman, M.; Mitsuishi, M.; Miyashita, T. Fabrication of fluorinated polymer nanosheets using the Langmuir-Blodgett technique: Characterization of their surface properties and applications. Polym. Int. 2010, 59, 583-596.

[91] Krafft, M. P.; Riess, J. G. Chemistry, physical chemistry, and uses of molecular fluorocarbon – hydrocarbon diblocks, triblocks, and related compounds – unique "apolar" components for self-assembled colloid and interface engineering. Chem. Rev. 2009, 109, 1714–1792.

[92] Yamada, S.; Iwama, S.; Kinoshita, K.; Yamazaki, T.; Kubota, T.; Yajima, T. Facile synthetic protocols for perfluoroalkyl-substituted diazapentaphenes. Tetrahedron 2014, 70, 6749–6756.

[93] Tretyakov, K. V.; Todua, N. G.; Borisov, R. S.; Zaikin, V. G.; Stein, S. E.; Mikaia, A. I. Unique para-effect in electron ionization mass spectra of bis(perfluoroacyl) derivatives of bifunctional aminobenzenes. Rapid Commun. Mass Spectrom. 2010, 24, 2529–2532.

[94] Widder, R.; Distler, H.; Fuchs, F. Neue organische Fluorverbindungen und ihre Verwendung als Oleophobiermittel. DE 1901710.

[95] Gilbert, E. E.; Herz, J. L.; Murray, J. J.; Price, A. K.; Sweeney, R. F. Substrate Treated with a Fluorine-containing Aromatic Compound. US 3595689.

[96] Kabalnov, A.; Wennerström, H. Macroemulsion Stability: The Oriented Wedge Theory Revisited. Langmuir 1995, 276–292.

[97] Hesse, M.; Meier, H.; Zeeh, B. Spektroskopische Methoden in der organischen Chemie: 102 Tabellen, 7., überarb. Aufl.; Thieme electronic book library; Thieme: Stuttgart, 2005.

[98] Timme, A.; Kress, R.; Albuquerque, R. Q.; Schmidt, H.-W. Phase behavior and mesophase structures of 1,3,5-benzene- and 1,3,5-cyclohexanetricarboxamides: Towards an understanding of the losing order at the transition into the isotropic phase. Chem. Eur. J. 2012, 18, 8329–8339.

[99] Krüss GmbH. DSA4: Software zur Tropfenkonturanalyse - Benutzerhandbuch; Hamburg, 2004.

[100] Yaws, C. L. Thermophysical properties of chemicals and hydrocarbons, 2. ed.; Elsevier: Amsterdam, 2014.

[101] Beck, U.; Löser, E. Chlorinated Benzenes and Other Nucleus-Chlorinated Aromatic Hydrocarbons. In Ullmann's Encyclopedia of Industrial Chemistry (Ed.).doi: 10.1002/14356007.o06_o03, 2011.

[102] Lidle, D. R., Ed. CRC Handbook of Chemistry and Physics: Internet Version, CRC Press,Boca Raton, Fl., 2005.

[103] VDI e.V. VDI-Wärmeatlas, 11th ed.; Springer Berlin Heidelberg: Berlin, Heidelberg, 2013.

[104] Mullin, J. W. Crystallization, 2. ed.; Butterworth: London, 1972.

[105] Bernett, M. K.; Zisman, W. A. Relation of Wettability by Aqueous Solutions to the Surface Constitution of Low-energy Solids. J. Phys. Chem. 1959, 63, 1241–1246.

[106] Stals, P. J. M.; Smulders, M. M. J.; Martín-Rapún, R.; Palmans, A. R. A.; Meijer, E. W. Asymmetrically substituted benzene-1,3,5-tricarboxamides: Self-assembly and odd-

even effects in the solid state and in dilute solution. Chem. Eur. J. 2009, 15, 2071–2080.

[107] Palmer, L. C.; Stupp, S. I. Molecular self-assembly into one-dimensional nanostructures. Acc. Chem. Res. 2008, 41, 1674–1684.

[108] Stupp, S. I.; Palmer, L. C. Supramolecular Chemistry and Self-Assembly in Organic Materials Design. Chem. Mater. 2014, 26, 507–518.

[109] Lehn, J.-M. Supramolecular polymer chemistry – Scope and perspectives. Polym. Int. 2002, 51, 825–839.

[110] Hunter, C. A.; Tomas, S. Accurate length control of supramolecular oligomerization: Vernier assemblies. J. Am. Chem. Soc. 2006, 128, 8975–8979.

[111] Kelly, T. R.; Xie, R. L.; Weinreb, C. K.; Bregant, T. A Molecular Vernier. Tetrahedron Letters 1998, 39, 3675–3678.

[112] Bull, S. R.; Palmer, L. C.; Fry, N. J.; Greenfield, M. A.; Messmore, B. W.; Meade, T. J.; Stupp, S. I. A templating approach for monodisperse self-assembled organic nanostructures. J. Am. Chem. Soc. 2008, 130, 2742–2743.

[113] Schmelz, J.; Schedl, A. E.; Steinlein, C.; Manners, I.; Schmalz, H. Length control and block-type architectures in worm-like micelles with polyethylene cores. J. Am. Chem. Soc. 2012, 134, 14217–14225.

[114] Sawawi, M.; Wang, T. Y.; Nisbet, D. R.; Simon, G. P. Scission of electrospun polymer fibres by ultrasonication. Polymer 2013, 54, 4237–4252.

[115] Hennrich, F.; Krupke, R.; Arnold, K.; Rojas Stütz, J. A.; Lebedkin, S.; Koch, T.; Schimmel, T.; Kappes, M. M. The Mechanism of Cavitation-Induced Scission of Single-Walled Carbon Nanotubes. J. Phys. Chem. B 2007, 111, 1932–1937.

[116] Lucas, A.; Zakri, C.; Maugey, M.; Pasquali, M.; van der Schoot, P.; Poulin, P. Kinetics of Nanotube and Microfiber Scission under Sonication. J. Phys. Chem. C 2009, 113, 20599–20605.

[117] Huang, Y. Y.; Knowles, T. P. J.; Terentjev, E. M. Strength of Nanotubes, Filaments, and Nanowires From Sonication-Induced Scission. Adv. Mater. 2009, 21, 3945–3948.

[118] Park, M.; Sohn, Y.; Shin, W. G.; Lee, J.; Ko, S. H. Ultrasonication assisted production of silver nanowires with low aspect ratio and their optical properties. Ultrasonics sonochemistry 2015, 22, 35–40.

[119] Zhang, L.; Belova, V.; Wang, H.; Dong, W.; Möhwald, H. Controlled Cavitation at Nano/Microparticle Surfaces. Chem. Mater. 2014, 26, 2244–2248.

[120] Li, Y.; Niu, Z.; Burdyńska, J.; Nese, A.; Zhou, Y.; Kean, Z. S.; Dobrynin, A. V.; Matyjaszewski, K.; Craig, S. L.; Sheiko, S. S. Sonication-induced scission of molecular bottlebrushes: Implications of the “hairy” architecture. Polymer 2016, 84, 178–184.

[121] Saito, T.; Kuramae, R.; Wohlert, J.; Berglund, L. A.; Isogai, A. An Ultrastrong Nanofibrillar Biomaterial: The Strength of Single Cellulose Nanofibrils Revealed via Sonication-Induced Fragmentation. Biomacromolecules 2013, 14, 248–253.

[122] Rooze, J.; Groote, R.; Jakobs, R. T. M.; Sijbesma, R. P.; van Iersel, M. M.; Rebrov, E. V.; Schouten, J. C.; Keurentjes, J. T. F. Mechanism of ultrasound scission of a silver-carbene coordination polymer. J. Phys. Chem. B 2011, 115, 11038–11043.

[123] Zeiger, B. W.; Suslick, K. S. Sonofragmentation of molecular crystals. J. Am. Chem. Soc. 2011, 133, 14530–14533.

[124] Pagani, G.; Green, M. J.; Poulin, P.; Pasquali, M. Competing mechanisms and scaling laws for carbon nanotube scission by ultrasonication. Proc. Natl. Acad. Sci. U. S. A. 2012, 109, 11599–11604.

[125] Lorimer, J. P.; Mason, T. J. Sonochemistry. Part 1 – The physical aspects. Chem. Soc. Rev. 1987, 16, 239–274.

[126] Cheng, Q.; Debnath, S.; Gregan, E.; Byrne, H. J. Ultrasound-Assisted SWNTs Dispersion: Effects of Sonication Parameters and Solvent Properties. J. Phys. Chem. C 2010, 114, 8821–8827.

[127] Steinlein, C.; Kreger, K.; Schmidt, H.-W. Controlling the Aspect Ratio of Supramolecular Fibers by Ultrasonication. Macromol. Mater. Eng. 2019, 304, 1900258.

[128] Ratoarinoro F. C.; Wilhelm, A. M.; Berlan, J.; Delmas, H. Power measurement in sonochemistry. Ultrasonics sonochemistry 1995, 2, S43-S47.

[129] Vijayalakshmi, S.; Madras, G.; Effect of temperature on the ultrasonic degradation of polyacrylamide and poly(ethylene oxide). Polym. Degrad. Stab. 2004, 84, 341–344.

[130] Lide, D. R., Ed. CRC Handbook of Chemistry and Physics, Internet Version 2005; Boca Raton, FL, 2005.

[131] Bao, Z.; Zhang, W.; Chen, Y.; Xu, J.; Cui, X. Densities, viscosities and volumetric properties of BF3·anisole and BF3·phenetole complexes at T=(283.15 to 303.15)K. J. Mol. Liq. 2014, 198, 187–192.

[132] Rathnam, M. V.; Ambavadekar, D. R.; Nandini, M. Studies on Excess Volume, Viscosity, and Speed of Sound of Binary Mixtures of Methyl Benzoate in Ethers at T=(303.15,308.15, and 313.15) K. Journal of Thermodynamics 2013, 2013, 1–8.

[133] Yaws, C. L. Thermophysical properties of chemicals and hydrocarbons, 2. ed.; Elsevier: Amsterdam, 2014.

[134] Mackay, D. Handbook of physical-chemical properties and environmental fate for organic chemicals, 2nd ed.; CRC/Taylor & Francis: Boca Raton, FL, 2006.

[135] Lee, S.-T., Ed. Foam extrusion: Principles and practice; Technomic Publishing: Lancaster, Pa., 2000.

[136] Eaves, D., Ed. Handbook of polymer foams; Rapra Technology: Shawbury, Shrewsbury, Shropshire, U.K, 2004.

[137] Gendron, R., Ed. Thermoplastic foam processing: Principles and development; Polymeric foams series; CRC Press: Boca Raton, Fla, 2005.

[138] Okolieocha, C.; Raps, D.; Subramaniam, K.; Altstädt, V. Microcellular to nanocellular polymer foams: Progress (2004–2015) and future directions – A review. European Polymer Journal 2015, 73, 500–519.

[139] Park, C. B. Foaming Technology: Fundamentals and Foaming Technologies; Bayreuth, 2017.

[140] Naguib, H. E.; Park, C. B.; Reichelt, N. Fundamental foaming mechanisms governing the volume expansion of extruded polypropylene foams. J. Appl. Polym. Sci. 2004, 91, 2661–2668.

[141] Gunkel, F.; Spörrer, A. N. J.; Lim, G. T.; Bangarusampath, D. S.; Altstädt, V. Understanding Melt Rheology and Foamability of Polypropylene-based TPO Blends. J. Cell. Plast. 2008, 44, 307–325.

[142] Park, C. B.; Cheung, L. K. A study of cell nucleation in the extrusion of polypropylene foams. Polym Eng Sci 1997, 37, 1–10.

[143] Xu, X.; Park, C. B.; Xu, D.; Pop-Iliev, R. Effects of die geometry on cell nucleation of PS foams blown with CO_2. Polym. Eng. Sci. 2003, 43, 1378–1390.

[144] Park, C. B.; Baldwin, D. F.; Suh, N. P. Effect of the pressure drop rate on cell nucleation in continuous processing of microcellular polymers. Polym. Eng. Sci. 1995, 35, 432–440.

[145] Burt, J. G. The Elements of Expansion of Thermoplastics: Part II. j cell plast 1978, 14, 341–345.

[146] Spitael, P.; Macosko, C. W. Strain hardening in polypropylenes and its role in extrusion foaming. Polym Eng Sci 2004, 44, 2090–2100.

[147] Reichelt, N.; Stadlbauer, M.; Folland, R.; Park, C. B.; Wang, J. PP-Blends with Tailored Foamability and Mechanical Properties. Cell. Polym. 2003, 22, 315-327.

[148] Lee, S.-T.; Park, C. B.; Ramesh, N. S. Polymeric foams: Science and technology; CRC/Taylor & Francis: Boca Raton, 2007.

[149] Guo, M.-C.; Heuzey, M.-C.; Carreau, P. J. Cell structure and dynamic properties of injection molded polypropylene foams. Polym. Eng. Sci. 2007, 47, 1070–1081.

[150] Stumpf, M.; Spörrer, A.; Schmidt, H.-W.; Altstadt, V. Influence of supramolecular additives on foam morphology of injection-molded i-PP. J. Cell. Plast. 2011, 47, 519–534.

[151] EIA. IEO2016 World energy demand and economic outlook. 2016.

[152] EIA. IEO2016 Energy-related CO2 emissions. 2016.

[153] Notario, B.; Pinto, J.; Solorzano, E.; Saja, J. A. de; Dumon, M.; Rodríguez-Pérez, M. A. Experimental validation of the Knudsen effect in nanocellular polymeric foams. Polymer 2015, 56, 57–67.

[154] Dey, S. K.; Natarajan, P.; Xanthos, M.; Braathen, M. D. Use of inert gases in extruded medium density polypropylene foams. J. Vinyl Addit. Technol. 1996, 2, 339–344.

[155] Kim, Y.; Park, C. B.; Chen, P.; Thompson, R. B. Towards maximal cell density predictions for polymeric foams. Polymer 2011, 52, 5622–5629.

[156] Liao, R.; Yu, W.; Zhou, C. Rheological control in foaming polymeric materials: II. Semi-crystalline polymers. Polymer 2010, 51, 6334–6345.

[157] Zheng, W. G.; Lee, Y. H.; Park, C. B. Use of nanoparticles for improving the foaming behaviors of linear PP. J. Appl. Polym. Sci. 2010, 117, 2972-2979.

[158] Nofar, M.; Majithiya, K.; Kuboki, T.; Park, C. B. The foamability of low-melt-strength linear polypropylene with nanoclay and coupling agent. J. Cell. Plast. 2012, 48, 271–287.

[159] Nam, P. H.; Maiti, P.; Okamoto, M.; Kotaka, T.; Usuki, A.; Hasegawa, N.; Okamoto, H. Foam processing and cellular structure of polypropylene/clay nanocomposites. Polym. Eng. Sci. 2002, 42, 1907–1918.

[160] Naguib, H. E.; Park, C. B.; Panzer, U.; Reichelt, N. Strategies for achieving ultra low-density polypropylene foams. Polym. Eng. Sci. 2002, 42, 1481–1492.

[161] Nam, G. J.; Yoo, J. H.; Lee, J. W. Effect of long-chain branches of polypropylene on rheological properties and foam-extrusion performances. J. Appl. Polym. Sci. 2005, 96, 1793–1800.

[162] Zhai, W.; Wang, H.; Yu, J.; Dong, J.; He, J. Cell coalescence suppressed by crosslinking structure in polypropylene microcellular foaming. Polym. Eng. Sci. 2008, 48, 1312–1321.

[163] Zhang, P.; Zhou, N. Q.; Wu, Q. F.; Wang, M. Y.; Peng, X. F. Microcellular foaming of PE/PP blends. J. Appl. Polym. Sci. 2007, 104, 4149–4159.

[164] Rachtanapun, P.; Selke, S. E. M.; Matuana, L. M. Relationship between cell morphology and impact strength of microcellular foamed high-density polyethylene/polypropylene blends. Polym. Eng. Sci. 2004, 44, 1551–1560.

[165] Zhai, W.; Wang, H.; Yu, J.; Dong, J.; He, J. Foaming behavior of polypropylene/polystyrene blends enhanced by improved interfacial compatibility. J. Polym. Sci. B Polym. Phys. 2008, 46, 1641–1651.

[166] Rizvi, A.; Tabatabaei, A.; Barzegari, M. R.; Mahmood, S. H.; Park, C. B. In situ fibrillation of CO2-philic polymers: Sustainable route to polymer foams in a continuous process. Polymer 2013, 54, 4645–4652.

[167] McClurg, R. B. Design criteria for ideal foam nucleating agents. Chem. Eng. Sci. 2004, 59, 5779–5786.

[168] Leung, S. N.; Wong, A.; Park, C. B.; Zong, J. H. Ideal surface geometries of nucleating agents to enhance cell nucleation in polymeric foaming processes. J. Appl. Polym. Sci. 2008, 108, 3997–4003.

[169] Lee, J. W.S.; Park, C. B.; Kim, S. G. Reducing Material Costs with Microcellular/Fine-celled Foaming. J. Cell. Plast. 2007, 43, 297–312.

[170] Fasihi, M.; Targhi, A. A.; Bayat, H. The simultaneous effect of nucleating and blowing agents on the cellular structure of polypropylene foamed via the extrusion process. e-Polymers 2016, 16, 235-241.

[171] Chen, L.; Blizard, K.; Straff, R.; Wang, X. Effect of Filler Size on Cell Nucleation During Foaming Process. J. Cell. Plast. 2002, 38, 139–148.

[172] Leung, S. N.; Wong, A.; Wang, L. C.; Park, C. B. Mechanism of extensional stress-induced cell formation in polymeric foaming processes with the presence of nucleating agents. J. Supercrit. Fluids 2012, 63, 187–198.

[173] Naguib, H. E.; Park, C. B.; Lee, P. C. Effect of Talc Content on theVolume Expansion Ratio of Extruded PP Foams. J. Cell. Plast. 2003, 499–511.

[174] Hu, D.; Chen, J.; Sun, S.; Liu, T.; Zhao, L. Solubility and Diffusivity of CO_2 in Isotactic Polypropylene/Nanomontmorillonite Composites in Melt and Solid States. Ind. Eng. Chem. Res. 2014, 53, 2673–2683.

[175] Velasco, J. I.; Antunes, M.; Realinho, V.; Ardanuy, M. Characterization of rigid polypropylene-based microcellular foams produced by batch foaming processes. Polym. Eng. Sci. 2011, 51, 2120–2128.

[176] Zhai, W.; Kuboki, T.; Wang, L.; Park, C. B.; Lee, E. K.; Naguib, H. E. Cell Structure Evolution and the Crystallization Behavior of Polypropylene/Clay Nanocomposites Foams Blown in Continuous Extrusion. Ind. Eng. Chem. Res. 2010, 49, 9834–9845.

[177] Wang, C.; Leung, S. N.; Bussmann, M.; Zhai, W. T.; Park, C. B. Numerical Investigation of Nucleating-Agent-Enhanced Heterogeneous Nucleation. Ind. Eng. Chem. Res. 2010, 49, 12783–12792.

[178] Lee, S. H.; Zhang, Y.; Kontopoulou, M.; Park, C. B.; Wong, A.; Zhai, W. Optimization of Dispersion of Nanosilica Particles in a PP Matrix and Their Effect on Foaming. Intern. Polym. Process. 2011, 26, 388–398.

[179] Zhai, W.; Park, C. B.; Kontopoulou, M. Nanosilica Addition Dramatically Improves the Cell Morphology and Expansion Ratio of Polypropylene Heterophasic Copolymer Foams Blown in Continuous Extrusion. Ind. Eng. Chem. Res. 2011, 50, 7282–7289.

[180] Chen, C.; Pang, H.; Liu, Z.; Li, Y.-B.; Chen, Y.-H.; Zhang, W.-Q.; Ji, X.; Tang, J.-H. Enhanced foamability of isotactic polypropylene composites by polypropylene-graft-carbon nanotube. J. Appl. Polym. Sci. 2013, 130, 961–968.

[181] Libster, D.; Aserin, A.; Garti, N. Advanced nucleating agents for polypropylene. Polym. Adv. Technol. 2007, 18, 685–695.

[182] Wang, W.; Zhou, S.; Xin, Z.; Shi, Y.; Zhao, S.; Meng, X. Preparation and foaming mechanism of foamable polypropylene based on self-assembled nanofibrils from sorbitol nucleating agents. J. Mater. Sci. 2016, 51, 788–796.

[183] Saniei, M.; Tran, M.-P.; Bae, S.-S.; Boahom, P.; Gong, P.; Park, C. B. From micro/nano structured isotactic polypropylene to a multifunctional low-density nanoporous medium. RSC Adv. 2016, 6, 108056–108066.

[184] Miyamoto, R.; Yasuhara, S.; Shikuma, H.; Ohshima, M. Preparation of micro/nanocellular polypropylene foam with crystal nucleating agents. Polym. Eng. Sci. 2014, 54, 2075–2085.

[185] Gong, W.; Gao, J.; Jiang, M.; He, L.; Yu, J.; Zhu, J. Influence of cell structure parameters on the mechanical properties of microcellular polypropylene materials. J. Appl. Polym. Sci. 2011, 122, 2907–2914.

[186] Bureau, M. N.; Gendron, R. Mechanical-Morphology Relationship of PS Foams. J. Cell. Plast. 2003, 39, 353–367.

[187] Zhao, J.; Zhao, Q.; Wang, C.; Guo, B.; Park, C. B.; Wang, G. High thermal insulation and compressive strength polypropylene foams fabricated by high-pressure foam injection molding and mold opening of nano-fibrillar composites. Mater. Des. 2017, 131, 1–11.

[188] Chen, L.; Schadler, L. S.; Ozisik, R. An experimental and theoretical investigation of the compressive properties of multi-walled carbon nanotube/poly(methyl methacrylate) nanocomposite foams. Polymer 2011, 52, 2899–2909.

[189] Ogunsona, E.; Ogbomo, S.; Nar, M.; D`Souza Nandika Anne. Thermal and Mechanical Effects in Polystyrene-Montmorillonite Nanocomposite Foams. Cell. Polym. 2011, 30, 79–94.

[190] Shen, J.; Han, X.; Lee, L. J. Nanoscaled Reinforcement of Polystyrene Foams using Carbon Nanofibers. J. Cell. Plast. 2016, 42, 105–126.

[191] Mörl, M.; Steinlein, C.; Kreger, K.; Schmidt, H.-W.; Altstädt, V. Improved compression properties of polypropylene extrusion foams by supramolecular additives. J. Cell. Plast. 2018, 54, 483-498.

[192] Ouederni, M.; Phillips, P. J. Influence of morphology on the fracture toughness of isotactic polypropylene. J. Polym. Sci. B: Polym. Phys. 1995, 33, 1313–1322.

[193] Schmidt, H.-W.; Smith, P.; Blomenhofer, M. Polypropylene Resin Compositions. WO 02/46300 A2, 2002.

[194] Mäder, D.; Hoffmann, K.; Schmidt, H.-W. ß Crystaline Polypropylenes. WO 03/102069 A1, 2003

[195] Schmidt, H.-W.; Blomenhofer, M.; Stoll, K.; Meier, H.-R. Resin Compositions. WO 04/072168 A2, 2004

8. Acknowledgement

First of all, I want to thank my advisor, Prof. Hans-Werner Schmidt for the opportunity to conduct the research for this thesis at the department of Macromolecular Chemisty I at the University of Bayreuth. I very much appreciate the interesting topic, my well-equipped lab and the multitude of analytical techniques available. Furthermore, I particularly thank him for supporting me with scientific discussions and advice.

In addition, I thank the Deutsche Forschungsgemeinschaft (DFG) for their financial support. This work was funded as part of the project B4 *"Morphologiekontrolle teilkristalliner Polymere durch supramolekulare Polymeradditive"* within the framework of the collaborative research center (SFB) 840 *"From particulate nanosystems to mesotechnology"*.

I particularly want to thank Dr. Klaus Kreger for his support, for many fruitful discussions and for sharing his vast knowledge, particularly on BTAs, with me.

I thank the technical employees Jutta Failner and Sandra Ganzleben for the synthesis of bis- and trisamides and for their assistance in compounding of *i*-PP.

I want to thank my cooperation partners Kasper van der Zwan, Dr. Christoph Zehe, Prof. Jürgen Senker, Merve Demir, Dr. Michaela Mörl and Prof. Volker Altstädt for our very good cooperation, of which many results are contained in this thesis, and many fruitful discussions. I very much appreciate them for sharing their knowledge on crystal structure determination and polymer processing with me.

I thank Petra Weiss and Christina Wunderlich to assist me with all kinds of administrative issues. I also very much appreciate Alexander Kern and Dr. Christian Neuber for their support related with IT-issues.

My thank goes to Beate Förster and Martina Heider for introducing me to SEM and for STEM and EDX measurements. I want to thank Markus Hund for introducing me to AFM and for his constant support related to this technique. Also I am grateful for Dr. Winfried Kretschmer to support me with SEC measurements.

My thank for their practical work goes to my interns Alexander Krimalowski, Andreas Frank, Dominik Dörr, Michael Ertl and Mirco Eckardt.

My special thanks go to my labmates Bastian Klose, Christian Probst, Daniel Kremer, Johannes Heigl and Markus Drummer for providing a good working atmosphere, sharing the ups and downs of my thesis, critical questions and fruitful discussions. Also, I'd like to thank the whole department of Macromolecular Chemistry I for the pleasant working atmosphere, many small assistances and common leisure activities.

(Eidesstattliche) Versicherungen und Erklärungen

(§ 9 Satz 2 Nr. 3 PromO BayNAT)

Hiermit versichere ich eidesstattlich, dass ich die Arbeit selbständig verfasst und keine anderen als die von mir angegebenen Quellen und Hilfsmittel benutzt habe (vgl. Art. 64 Abs. 1 Satz 6 BayHSchG).

(§ 9 Satz 2 Nr. 3 PromO BayNAT)

Hiermit erkläre ich, dass ich die Dissertation nicht bereits zur Erlangung eines akademischen Grades eingereicht habe und dass ich nicht bereits diese oder eine gleichartige Doktorprüfung endgültig nicht bestanden habe.

(§ 9 Satz 2 Nr. 4 PromO BayNAT)

Hiermit erkläre ich, dass ich Hilfe von gewerblichen Promotionsberatern bzw. -vermittlern oder ähnlichen Dienstleistern weder bisher in Anspruch genommen habe noch künftig in Anspruch nehmen werde.

(§ 9 Satz 2 Nr. 7 PromO BayNAT)

Hiermit erkläre ich mein Einverständnis, dass die elektronische Fassung meiner Dissertation unter Wahrung meiner Urheberrechte und des Datenschutzes einer gesonderten Überprüfung unterzogen werden kann.

(§ 9 Satz 2 Nr. 8 PromO BayNAT)

Hiermit erkläre ich mein Einverständnis, dass bei Verdacht wissenschaftlichen Fehlverhaltens Ermittlungen durch universitätsinterne Organe der wissenschaftlichen Selbstkontrolle stattfinden können.

…….

Ort, Datum, Unterschrift